UNIVERSITAT DE BARCELONA

Processament de perfils de precipitació obtinguts amb radar Doppler

Albert Garcia Benadí

Tesi doctoral

Processament de perfils de precipitació obtinguts amb radar Doppler

Albert Garcia Benadí

UNIVERSITAT DE BARCELONA

Processament de perfils de precipitació obtinguts amb radar Doppler

Programa de doctorat en Física

Autor: Albert Garcia Benadí

Director i Tutor: Dr Joan Bech Rustullet

Barcelona, setembre 2022

UNIVERSITAT DE BARCELONA

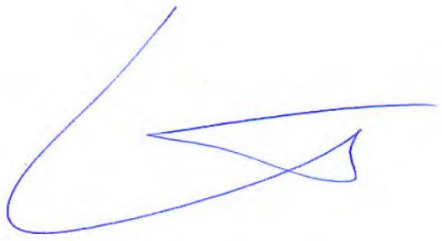

AGRAÏMENTS

Aquesta tesi és el resultat del treball realitzat durant 5 anys, on no ha estat fàcil compaginar la carrera acadèmica, professional i familiar. Aquest esforç ha estat possible gràcies al recolzament i suport de la meva família: la meva dona, Silvia, a la meva filla Emma i al meu fill Arnau. Sense vosaltres això no hagués estat possible i és en vosaltres on resideix el mèrit.

No vull oblidar les persones que m'han forjat durant tota la meva vida: els meus pares (Jesús i Maria Dolors), el meu germà (Òscar), els meus avis (Abuelo i Maria, en Coco i la Irene), tiets, tietes, cosins i cosines. No puc ficar-vos a tots ni totes ja que sinó aquest document es pot allargar fins a límits insospitats. Amb el vostre suport incondicional m'heu ensenyat la importància de la família i de la superació personal.

Als amics de debò que sempre han estat allà, malgrat que a vegades la vida ens ha portat per camins completament diferents, però per molt de temps que passi al trobar-nos sembla que ens vam veure ahir i d'on destaco en Joaquín, Ferreiro, Jordi, Joan, Callau, Fraire, Manel, Fran i molts d'altres. I la pinya que he trobat en la meva vida professional i amb la que he crescut tant personalment com professionalment i d'on destaco l'Antoni, en Pep i en Javi. Tampoc puc oblidar a l'equip de veterans del CHVNG, que sense adonar-se m'han ajudat a saber el que és un equip.

En la vessant professional vull agrair tota la col·laboració dels diferents membres del Grup de Meteorologia de la UB, ja que malgrat no m'heu vist gaire sempre heu estat disposats a ajudar, així com tot el personal del grup de recerca SARTI de la UPC, que és on desenvolupo la meva tasca laboral.

Aquests estudis m'han permès conèixer persones molt interessants i fins tot establir vincles afectius amb diferents persones de l'àmbit de la Meteorologia, d'on destaco en Sergi i l'Enric, que vam ser antics doctorands d'en Joan i dels que hem fet pinya.

He deixat pel final, i no per això menys important, l'agraïment a la tasca d'en Joan, el meu director i tutor de tesi. La teva paciència i gran dedicació han permès la finalització d'aquesta tesi.

No pretenc agrair a tothom que m'ha ajudat en la tasca de la tesi, ja que podria incloure pàgines i pàgines, però no seria capaç de plasmar aquest sentiment ni mencionar tots els noms, per això demano disculpes per la meva brevetat i us ho agraeixo de tot cor.

També cal agrair a Météo-France i al Servei Meteorològic de Catalunya les dades utilitzades en aquesta tesi (observacions de windprofiler, d'estacions automàtiques i de radiosondatge) sense les quals no es podria haver completat la feina realitzada.

Certament aquest és el final d'una etapa, però desitjo que no sigui el final de la col·laboració amb el Grup de Meteorologia, que espero mantenir durant molt de temps.

Albert Garcia Benadí

Universitat de Barcelona, 27 de setembre de 2022

RESUM

En la actualitat les dades obtingudes amb instruments de teledetecció (mesures obtingudes a distància) formen una part essencial en l'àmbit de la meteorologia. Aquestes dades s'obtenen amb diversos sensors de tipus passiu (com els radiòmetres) o actiu (com els radars meteorològics) instal·lats a la superfície terrestre, en avions o en satèl·lits. Els radars meteorològics destinats a observar precipitació operen típicament en longituds d'ona de 3 a 10 cm (bandes X, C i S), realitzen escombrats d'antena en el pla horitzontal i proporcionen una valuosa informació del camp de precipitació en un radi de l'ordre de 100 km, de gran importància en la vigilància i predicció meteorològica a curt termini. La seva posta a punt i manteniment té associat un cost no negligible. Existeixen també radars perfiladors, amb antena fixa apuntant el zenit, que proporcionen perfils verticals de precipitació amb gran resolució temporal i espacial. Aquests equips sovint són portables i més econòmics, i permeten realitzar estudis dels processos microfísics que donen lloc a la precipitació, complementant la informació dels radars meteorològics tradicionals. Aquesta tesi es centra en el processament d'observacions de radars perfiladors, concretament en dos tipus d'equips diferents que mitjançant l'efecte Doppler, poden observar la velocitat terminal de caiguda de les partícules de precipitació. La tesi s'estructura en tres blocs i es presenta com a compendi de quatre articles científics.

El primer i segon bloc de la tesi es dediquen al perfilador Doppler conegut com Micro Rain Radar del fabricant alemany Metek, que opera en banda K (longitud d'ona de 1.2 cm) i permet observar precipitació. Al primer bloc es proposa un processament de les dades brutes (reflectivitat espectral) del MRR que contempla diferents algoritmes per detectar pics meteorològics en el senyal, reducció del soroll, i diverses millores per detectar de forma robusta moviments ascendents de l'aire. A partir d'aquest processament inicial es calculen diversos paràmetres derivats, que permeten estudiar la banda de fusió o "banda brillant" amb una metodologia innovadora. Es presenta un estudi concret, aplicat a un MRR instal·lat a la Facultat de Física de la Universitat de Barcelona al costat de l'estació de radiosondatge del Servei Meteorològic de Catalunya, que s'utilitza com a referència per a la caracterització de la banda brillant. La segona part és un altre estudi aplicat a observacions de MRR durant la campanya Cerdanya-2017 on es proposa una nova metodologia per a classificar diferents tipus de precipitació (com ara pluja, plugim, neu o calamarsa). La metodologia es verifica amb observacions independents de disdròmetre, model Parsivel, (instal·lat al costat del MRR), que proporciona una classificació automàtica de tipus de precipitació.

El tercer i darrer bloc de la tesi es centra en el processament d'observacions d'un perfilador de vent Doppler polsat de banda UHF (longitud d'ona d'uns 20 cm), model PCL1300 del fabricant francès Degreane. L'equip està configurat per a funcionar amb cinc feixos per a optimitzar l'estimació de perfils de vent (components horitzontal i vertical). En aquest cas, com en els altres dos blocs anteriors, també es proposa un processat de les dades brutes, però atenent la freqüència de treball, l'equip detecta tant moviments de l'aire com la presència de partícules de precipitació. El processament, a banda d'obtenir el perfil de vent, també es capaç de detectar la precipitació i estimar el tipus de precipitació. Es presenta un estudi amb observacions d'un PCL1300 de Météo-France durant la campanya Cerdanya-2017, on també s'usen dades de MRR i disdròmetre (Parsivel) per a contrastar la nova metodologia proposada.

El resultat de cada bloc abordat en aquesta tesis és un programari d'accés lliure, disponible al repositori GitHub, perquè la comunitat científica pugui reutilitzar-lo fàcilment en estudis posteriors.

ABSTRACT

Meteorological observations obtained with remote sensing instruments (measurements obtained from a distance, not in contact with the object studied) are currently an essential part of meteorology. These data are obtained with various passive (such as radiometers) or active (such as weather radar) sensors deployed on the earth's surface, on aircraft or on satellites. Weather radars for precipitation observation typically operate in wavelengths of 3 to 10 cm (X, C and S bands), perform antenna sweeps in the horizontal plane and provide valuable information on the precipitation field at ranges of the order of 100 km, which is of great importance for short-term weather monitoring and forecasting. Their set-up and maintenance are associated with a not negligible cost. There are also profiling radars, with a fixed antenna pointing at the zenith, which provide vertical precipitation profiles with high temporal and spatial resolution. This equipment is often portable and cheaper, and allows studies of the microphysical processes that give rise to precipitation, complementing the information from traditional weather radars. This thesis focuses on the processing of profiling radar observations, specifically on two different types of equipment that, by means of the Doppler effect, can observe the terminal fall velocity of precipitation particles. The thesis is structured in three blocks and is presented as a compendium of four scientific papers.

The first and second blocks of the thesis are devoted to the frequency modulated continuous wave (FMCW) vertically pointing Doppler radar profiler known as Micro Rain Radar from the German manufacturer Metek, which operates in K-band (wavelength of 1.2 cm) and allows precipitation observation. The first block proposes a processing of the raw data (spectral reflectivity) of the MRR that includes different algorithms to detect meteorological peaks in the signal, noise reduction, and several improvements to robustly detect upward movements of the air. From this initial processing, several derived parameters are calculated, which allow the study of the melting band or "bright band" with an innovative methodology. A specific study is presented, applied to a MRR installed at the Faculty of Physics of the University of Barcelona next to the radiosounding station of the Meteorological Service of Catalonia, which is used as a reference for the characterisation of the bright band. The second block is another study applied to MRR observations during the Cerdanya-2017 campaign where a new methodology is proposed to classify different types of precipitation (such as rain, drizzle, snow or hail). The methodology is verified with independent disdrometer observations, model Parsivel, (co-located with the MRR), which provides an automatic classification of precipitation type.

The third and last block of the thesis focuses on the processing of observations from a UHF-band pulsed Doppler wind profiler (wavelength about 20 cm), model PCL1300 from the French manufacturer Degreane. The equipment is configured to operate with five beams to optimise the estimation of wind profiles (horizontal and vertical components). In this case, as in the other two previous blocks, processing of the raw data is also proposed, but taking into account the operating frequency, the equipment detects both air movements and the presence of precipitation. The processing, in addition to obtaining the wind profile, is also capable of detecting precipitation and estimating the type of precipitation. A study with observations from a PCL1300 wind profiler of Météo-France, during the Cerdagne-2017 campaign is presented, where MRR and disdrometer (Parsivel) data are also used to validate the new proposed methodology.

The result of each block addressed in this thesis is an open access software, available in the GitHub repository, so that the scientific community can easily reuse it in further studies.

Acrònims

ALWPP	Processat del perfilador de vent pel laboratori de aerologia (Aerologie Laboratoire Wind profiler Processing)
AMS	American Meteorological Society
AWS	Automatic Weather Station
BB	Banda Brillant
DSD	Drop Size Distribution
FAR	Ràtio de falsa alarma (False Alarm Rate)
IEEE	Institut d'Enginyers Elèctrics i Electrònics
ML	Capa de fusió (Melting Layer)
MRR	Micro Rain Radar
ORSS	Odds Ratio Skill Score
POD	Probabilitat de detecció(Probability Of Detection)
PSD	Distribució de mides de partícules (Particle Size Distribution)
RaProM	Processat de dades del radar MRR2 (Radar Processing MRR2)
RaProM-Pro	Processat de dades del radar MRR-Pro (Radar processing MRR-Pro)
SMC	Servei Meteorològic de Catalunya
TSS	True Skill Statistic
UBWPP	Processat del perfilador de vent per la Universitat de Barcelona (Universitat Barcelona Wind profiler Processing)
WMO	World Meteorological Organization

Taula de contingut

Capítol 1

Introducció

1.1. Motivació

La meteorologia és la ciència que estudia l'atmosfera i les seves interaccions amb la superfície terrestre, la biosfera, la hidrosfera i la criosfera. Malgrat actualment té branques molt diverses, l'origen de la meteorologia està lligat íntimament a l'observació i té un clar caràcter experimental [1]. Els instruments meteorològics es poden agrupar en dos segons el seu principi bàsic de funcionament: els instrument tradicionals, que realitzen mesures *in situ*, i els de teledetecció, que fan les mesures a distància. Entre aquests darrers es distingeixen els equips de teledetecció passiva (que mesuren energia emesa pel cos estudiat) i els de teledetecció activa (que emeten energia cap al cos estudiat i en mesuren el retorn gràcies a algun procés físic com la retrodispersió o *backscattering*).

Exemples d'instruments que fan mesures *in situ* són els que es troben habitualment en estacions meteorològiques automàtiques (*Automated Weather Stations,* AWS) com ara els pluviògrafs que mesuren la intensitat de precipitació o altres equips més sofisticats com els disdròmetres que obtenen espectres de mides i velocitats de caiguda de partícules de precipitació. Exemples d'equips de teledetecció activa són el RADAR (*RAnge Detection And Ranging*) i el LIDAR (*Light Detection and Ranging* o *Laser Imaging Detection and Ranging*). El RADAR (en endavant radar) s'usa per a detectar precipitació des de mitjans del segle passat i es basa en l'emissió d'energia electromagnètica en el rang de les microones i en la detecció de l'energia retrodispersada pels hidrometeors, o eco retornat.

Amb els anys s'han desenvolupat diversos equips radar operant en diferents freqüències cosa que permet destinar-lo a aplicacions diverses com ara l'estudi de núvols, o l'obtenció de perfils de vent per part dels sistemes coneguts com a perfiladors de vent o *Windprofilers*. La freqüència de treball de cada radar determina completament les característiques físiques de la seva interacció amb els blancs, en aquest cas blancs atmosfèrics, i per tant el tipus de dispersió que cal esperar (Mie, Rayleigh o Bragg) segons la relació entre la seva mida i la longitud d'ona (Richard & Zrnić 1993; Bech & Chau 2012). Les principals aplicacions de cada banda de l'espectre electromagnètic

considerat pel IEEE es llisten a la **Taula *1*** així com el nom de la banda i el seu rang de freqüències i longituds d'ona.

Taula 1. Relació de la banda de freqüència i els valors límits en freqüència i longitud d'ona pels radars meteorològics existents.(521-2019 - IEEE Standard Letter Designations for Radar-Frequency Bands - Redline 2020)

Banda de freqüència	Rang de freqüències [GHz]	Rang de longituds d'ona [mm]	Aplicacions
VHF	*0.03 – 0.3*	1000 – 10000	Perfilador de vent (Wind Profiler)
UHF	*0.3 – 1*	300 – 1000	
L	*1 – 2*	150 – 300	Precipitació
S	*2 – 4*	80 – 150	
C	*4 – 8*	38 – 80	
X	*8 – 12*	25 – 38	
Ku	*12 – 18*	17 – 25	
K	*18 – 27*	11 – 17	
Ka	*27 – 40*	8 – 11	Observació de núvols
V	*40 – 75*	4 – 8	Comunicació
W	*75 – 110*	3 – 4	Observació de núvols
mm	*110 – 300*	1 – 3	
THz	*300 – 1000*	0.3 – 1	Radioastronomia

Per exemple els radars meteorològics destinats a observar precipitació habitualment operen en banda S, C o X (aproximadament de 10 a 3 cm de longitud d'ona), de forma que aprofiten la dispersió de Rayleigh causada per les gotes de precipitació (amb mides de l'ordre de 1 mm). Aquests radars sovint estan col·locats en torres o llocs elevats i disposen d'una antena amb una protecció esfèrica o radom (***Figura 1***).

Les antenes d'aquests radars realitzen habitualment escombrats amb un angle d'elevació fix i azimut variable (*Plan Position Indicator* o PPI) o escombrats amb l'angle d'elevació variable i azimut fix (*Range Height Indicator* o RHI). Les sèries de PPIs a diverses elevacions proporcionen valuosa informació del camp tridimensional de precipitació amb un abast típic de l'ordre de 100 km actualitzats cada pocs minuts (segons el radar de 5 a 10 minuts). Aquests radars detecten i mesuren la intensitat de la precipitació i, gràcies a l'efecte Doppler, majoritàriament mesuren també la velocitat dels ecos respecte al radar. A més, actualment molts d'ells estan dotats de capacitats polarimètriques, que els permeten fer les mesures en més d'un pla de polarització, ampliant les variables estimades, no disponibles en radars de polarització simple, que tan sols mesuren al pla horitzontal. Un exemple rellevant de noves variables calculables amb mesures polarimètriques és la classificació d'hidrometeors [4].

Figura 1. Radar meteorològic Doppler de banda C del Servei Meteorològic de Catalunya ubicat a La Panadella [Font: pàgina web de l'Ajuntament de Montmaneu]

Aquests radars actualment són essencials per a fer tasques de vigilància i predicció a molt curt termini de la precipitació (*nowcasting*) i comporten un elevat cost d'instal·lació i manteniment.

Basats en el mateix principi del radar meteorològic Doppler, existeix un altre tipus d'instrument complementari dels anteriors però de característiques força diferents. Es tracta dels radars perfiladors Doppler, els quals tenen una antena fixa apuntant verticalment, que per tant no realitza ni PPIs ni RHIs, sinó que proporciona sèries temporals de perfils sobre l'instrument, però sovint amb major resolució especial i temporal que els radars anteriors. Amb aquestes característiques aquest tipus de radar permeten estudiar la microfísica de la precipitació i descriure detalladament la seva evolució temporal amb l'altura (Arulraj & Barros 2021; Brast & Markmann 2019; Campistron & Réchou 2012; Makino et al. 2019; Seidel et al. 2019).

Aquesta tesi està orientada a millorar el processament i aplicació de dos tipus de radars Doppler perfiladors verticals operant en banda K i UHF, el Micro Rain Radar, destinat a l'observació de precipitació, i el perfilador de vent UHF PCL1300 (**Figura 2**).

***Figura 2**. Micro Rain Radar, fabricat per Metek (esquerre, font: J. Bech) i Perfilador de vent PCL1300, fabricat per Degreane (dreta, font: J.M. Donier), en la campanya de la Cerdanya-2017, situat a Das (La Cerdanya).*

En el cas del MRR, en operar en banda K, la seva principal funció és determinar la distribució de velocitats verticals dels hidrometeors en un instant de temps. A partir del senyal obtingut no tan sols es pot obtenir la velocitat radial Doppler i el factor de reflectivitat equivalent com en altres radars convencionals sinó que, assumint els hidrometeors cauen en velocitat terminal, es pot calcular directament la distribució de mides de gotes N(D) i a partir d'aquí altres variables derivades com ara el factor de reflectivitat o la intensitat de pluja. Amb aquest equip en el passat s'han realitzat estudis de gran interès millorant el processament original del fabricant, com ara la metodologia de millora de l'aliàsing proposada per Maahn & Kollias (2012). Entre d'altres treballs destacables es pot citar els d'Adirosi et al. (2016; 2020) on es relacionen les observacions del MRR amb disdròmetres situats a la superfície per interpretar processos microfísics associats al perfil de precipitació.

Per altra banda el perfilador de vent PCL1300 operant en banda UHF permet calcular no només la velocitat dels hidrometeors sinó que també obté la velocitat de l'aire. Això proporciona un perfil de vent, tant del component horitzontal com vertical, hi hagi o no precipitació. Aquest equip s'ha usat en el passat en nombroses campanyes experimentals de recerca. Entre els estudis realitzats destaca la metodologia de processament proposada per Campistron & Réchou (2012) que va permetre obtenir, a banda del camp de vents, el flux d'energia cinètica per tal de ser usat en estudis d'erosió causada per la pluja.

La motivació de la tesi és la millora de diversos aspectes del processament de radars perfiladors Doppler per tal d'ampliar les seves aplicacions. Entre d'altres aspectes es proposen metodologies per a la millor caracterització de la banda de fusió o banda brillant i una classificació simplificada d'hidrometeors, basada únicament en mesures de polarització simple, tant per radars en banda K com per perfiladors de vent de banda UHF.

1.2. Estat de l'art

1.2.1. Banda Brillant

L'American Meteorological Society (AMS 2022) defineix la Banda Brillant (en endavant BB) com: "*Radar signature of the melting layer; a narrow horizontal layer of stronger radar reflectivity in precipitation at the level in the atmosphere where snow melts to form rain*". Per tant la BB, és l'interval d'altures on la precipitació canvia d'estat, modificant el seu estat de sòlid a líquid per mitjà de la fusió de la neu (veure exemple a la **Figura 3**). La importància de la correcta detecció de la BB evita la sobreestimació de la quantitat de pluja i ofereix dades robustes per aplicacions radar en models hidrològics i de predicció (Demir & Krajewski 2013; Seo & Krajewski 2020).

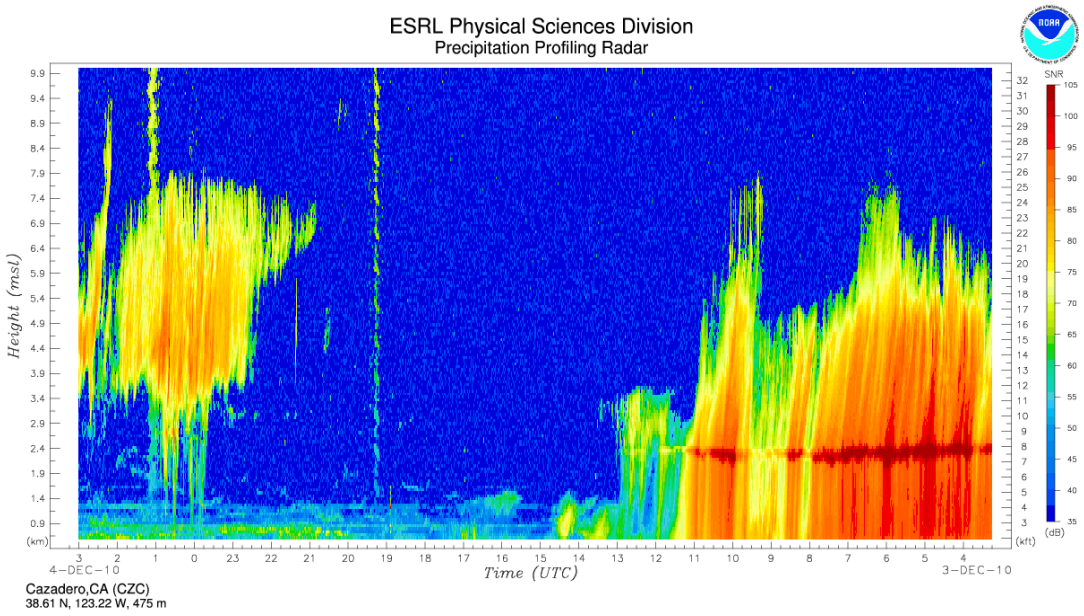

Figura 3. *Exemple de Banda Brillant observada amb un perfilador de banda S de la NOAA [font https://psl.noaa.gov/data/obs/datadisplay/]*

Inicialment la determinació de la BB es realitza per mitjà del perfil de la reflectivitat radar (Fabry & Zawadzki 1995; Sánchez-Diezma et al. 2000), però en radars de mira vertical el perfil de reflectivitat no és suficient, ja que es poden obtenir gradients elevats deguts a soroll, interferència o la presència de virga que alteren aquest càlcul. Per evitar-ho, i aprofitant la valuosa informació que aporten els perfiladors Doppler en mesurar directament velocitats radials coincidents amb velocitats verticals dels hidrometeors, a més del perfil de reflectivitat, s'usa també el perfil de velocitats de caiguda [17–19] - veure **Figura 4**. Amb aquesta doble informació la detecció de la BB millora, però encara hi ha cassos on un lleuger moviment d'ascens de l'aire provoca que el perfil de velocitat no variï com s'espera i això crea una falsa detecció.

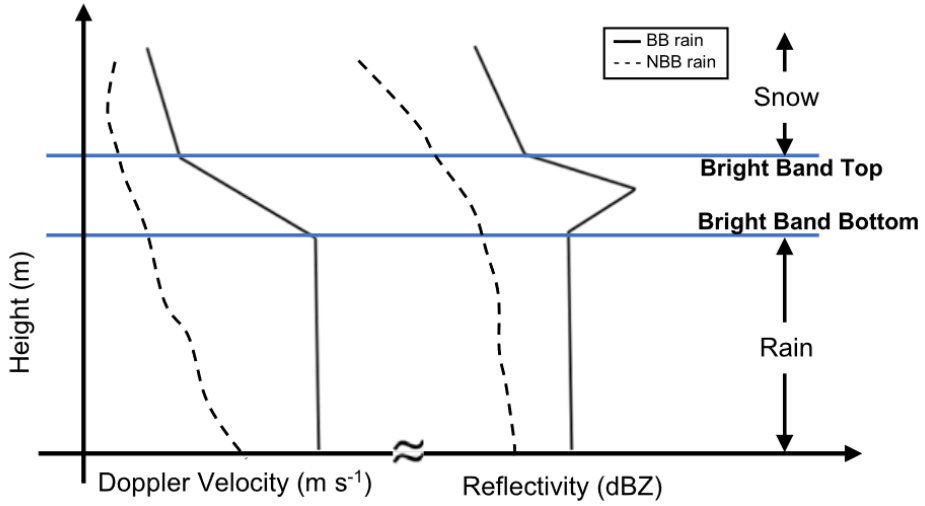

Figura 4. *Esquema de determinació de banda brillant vers el perfil de la reflectivitat equivalent i la velocitat vertical* (Font: Lin et al. 2020).

1.2.2. Tipus de precipitació

La precipitació és un dels fenòmens més rellevants en la meteorologia atenent la seva importància en la gestió del cicle de l'aigua, vigilància meteorològica i predicció a curt termini de pluges fortes, per citar alguns exemples. El tipus d'hidrometeor amb que es presenta la precipitació té una gran importància donada la seva varietat. Per exemple, la ***Taula 2*** mostra diversos hidrometeors precipitants llistats al Manual d'Observadors del Servei Meteorològic de Catalunya (Gázquez et al. 2011) per a facilitar la seva observació a nivell de superfície.

Taula 2. Selecció d'hidrometeors precipitants llistats al Manual d'Observadors de l'SMC (Gázquez et al. 2011) actualitzat amb les definicions de calamarsa i pedra llistades a la web de l'SMC (SMC, 2022).

Hidrometeor	(terme anglès)	Descripció
Plugim	*Drizzle*	Precipitació força uniforme, constituïda exclusivament per multitud de gotes menudes d'aigua de diàmetre inferior a 0,5 mm i molt properes les unes de les altres.
Pluja	*Rain*	La pluja és formada per gotes líquides de diàmetre variable entre 0,5 i 3 mm, que poden assolir un màxim de 7 mm, que s'originen per la coalescència de petites gotes. També es considera pluja en els casos que el diàmetre de les gotes sigui inferior a 0,5 mm, però que cauen molt disperses.
Calamarsa	*Small hail*	Precipitació en forma de grans d'aigua solidificada, mig transparents, rodons, rarament cònics, de 2 a 5 mm de diàmetre i que estan formats per capes concèntriques de gel.
Pedra	*Hail*	Són trossos de glaç irregulars, d'una grandària superior als 5 mm. Arriben a assolir mides superiors als 50 mm en casos excepcionals.
Aiguaneu	*Mixed*	Precipitació uniforme de neu a mig fondre o de neu i aigua barrejades
Neu	*Snow*	És el tipus de precipitació sòlida més comú. Es tracta d'una precipitació força uniforme de cristalls hexagonals microscòpics o esquelets d'aigua sòlida, que cauen individualment o, de vegades, reunits en borrallons o flocs (volves, si són molt lleus) d'un sostre continu de núvols.

Des de fa anys s'han desenvolupat altres classificacions per exemple basades en observacions radar tenint present la velocitat de caiguda de l'hidrometeor i la seva mida (Atlas et al. 1973) o la distribució de mida de les gotes de pluja o partícules precipitants [23], sovint designada com *Drop Size Distribution* (DSD) o *Particle Size Distribution* (PSD). Una vegada determinat el tipus d'hidrometeor també es pot fer una altra classificació important, relativa al règim de la precipitació, per determinar si es tracta de

precipitació convectiva o estratiforme [24]. Aquesta classificació es pot realitzar examinant propietats de la DSD assumint certes funcions de distribució, per exemple el diàmetre característic de la gota D_0, i el paràmetre N_w (Dolan et al. 2018; Thurai et al. 2016) - veure **Figura 5**.

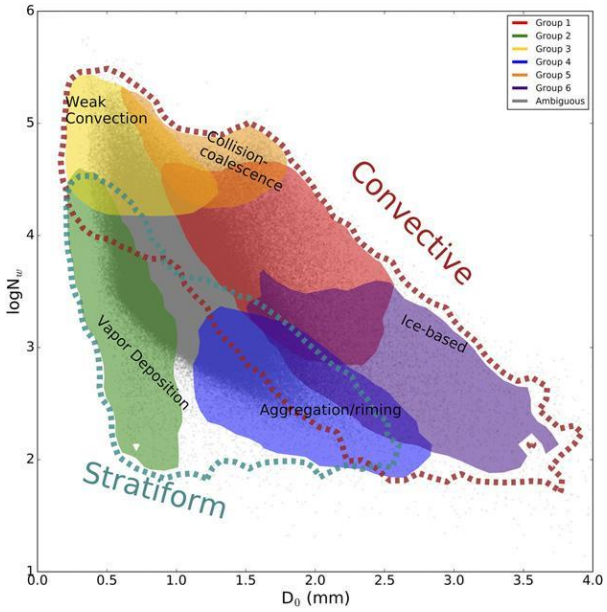

Figura 5. *Tipus de precipitació i fenòmens microfísics associats a la precipitació en funció dels paràmetres D_0 i N_w [Figure 12 de* Dolan et al. 2018*]*

1.3. Objectius

Els objectius de la tesi es poden descriure com objectius generals (OG) i objectius específics (OE). Aquest objectius ens permeten identificar la finalitat de cada bloc de la tesi.

1.3.1. Objectiu generals

Durant la tesi s'han d'assolir alguns objectius generals que es detallen com:

- **OG.1. Estudi de l'estructura de la Banda Brillant.** Es proposa revisar el coneixement actual de la BB i dissenyar eines mitjançant observacions radar per a millorar-ne la seva caracterització.
- **OG.2 Classificació d'hidrometeors amb perfiladors Doppler.** Es planteja revisar els mètodes de classificació d'hidrometeors amb perfiladors Doppler i plantejar mètodes millorats. Complementàriament, partint d'aquesta classificació, es proposa obtenir pel cas de precipitació líquida, la seva distribució de gotes de pluja (DSD).

1.3.2. Objectiu específics

Per tal d'assolir els objectius generals s'han plantejat uns objectius específics, que acoten el ventall proposat en l'objectiu general. Aquest objectius específics són:

- **OE.1. Desenvolupament d'una metodologia de caracterització de la Banda Brillant amb Micro Rain Radar**. El procés de fusió d'hidrometeors en la BB provoca una variacions característiques en les distribucions de velocitats de caiguda. La metodologia ha d'incloure un processat de les dades brutes on s'implementi un sistemàtica de la detecció de la senyal sobre el soroll així com mantenir una coherència en la continuïtat respecte la vertical. Una vegada implantades aquestes eines ja es pot implementar a metodologia de la detecció de la BB tenint en compte els diferents moments de la reflectivitat espectral.

- **OE.2 Desenvolupament d'una metodologia simplificada de classificació d'hidrometeors amb Micro Rain Radar.** La metodologia ha d'incloure diversos hidrometeors precipitants (***Taula 2***). Es planteja usar com a punt de partida la relació de la velocitat de caiguda i el factor de reflectivitat (Atlas et al. 1973) en comparació amb les distribucions de velocitat detectada per l'equip.

- **OE.3. Caracterització de perfils verticals d'hidrometeors durant la campanya Cerdanya-2017.** La campanya experimental Cerdanya-2017 disposava de diversos equips on s'han utilitzat per comprovar diverses implicacions de la orografia i per fer-ho es necessari aplicar la sistemàtica de la classificació desenvolupada a la tesi.

- **OE.4. Desenvolupament d'una metodologia de classificació d'hidrometeors amb perfilador de vent.** El perfilador de vent pot mesurar no tan sols el camp de vent (sense precipitació) sinó també detectar la precipitació i el seu moviment. La sistemàtica a desenvolupar ha de ser capaç de diferenciar la precipitació i la implementació d'una classificació tenint en compte el mateix principi determinat en el OE.1.

- **OE.5. Desenvolupament d'una metodologia de verificació de perfils d'hidrometeors amb observacions properes a la superfície.** La metodologia anterior ha de ser testada amb diferents observacions realitzades per equips de superfície que permetin validar la prèvia classificació.

- **OE.6. Difusió dels resultats de la tesi mitjançant programari d'accés lliure.** Els diferents programes realitzats com a resultat dels anteriors objectius es deixaran en un repositori de lliure accés per a la comunitat científica. A més els programes es crearan en un llenguatge que sigui gratuït i de fàcil accés perquè la comunitat els pugui adaptar a les seves necessitats.

1.4. Estructura de la tesi

La tesi s'organitza en cinc capítols i es presenta com a compendi de quatre publicacions.

En el Capítol 1 es fa aquesta introducció, on es detalla la motivació de la tesi, l'estat de l'art, els objectius generals i específics i per acabar es detalla l'estructura de la tesi.

En els propers 3 capítols és on es presenta el gruix de la feina realitzada durant el doctorat.

En el Capítol 2 es detalla una nova metodologia per la detecció de la BB vàlida per qualsevol equip, però implementada pel MRR. Es presenta l'article:

> Garcia-Benadí, A.; Bech, J.; Gonzalez, S.; Udina, M.; Codina, B. A New Methodology to Characterise the Radar Bright Band Using Doppler Spectral Moments from Vertically Pointing Radar Observations. *Remote Sens.* **2021**, *13*, 4323. https://doi.org/10.3390/rs13214323

En el Capítol 3 es desenvolupa una metodologia de classificació del tipus de hidrometeor basada en la relació entre la velocitat terminal de caiguda d'una partícula vers els seu diàmetre que s'implementarà pel MRR. Paral·lelament s'utilitzarà la nova metodologia per donar uns resultats per la campanya de la Cerdanya-2017. Es presenten dos articles:

> Garcia-Benadi, A.; Bech, J.; Gonzalez, S.; Udina, M.; Codina, B.; Georgis, J.-F. Precipitation Type Classification of Micro Rain Radar Data Using an Improved Doppler Spectral Processing Methodology. *Remote Sens.* **2020**, *12*, 4113. https://doi.org/10.3390/rs12244113

> González, S.; Bech, J.; Garcia-Benadí, A.; Udina, M.; Codina, B.; Trapero, L.; Paci, A.; Georgis, J.F. Vertical structure and microphysical observations of winter precipitation in an inner valley during the Cerdanya-2017 field campaign.Atmospheric Research. Volume 264, **2021**, 105826, https://doi.org/10.1016/j.atmosres.2021.105826

En el Capítol 4 es proposa una metodologia pel processament d'observacions de perfilador de vent i càlcul de variables derivades. Entre aquestes s'inclou una classificació d'hidrometeors

> Garcia-Benadi, A.; Bech, J.; Udina, M.; Campistron, B.; Paci, A. Multiple Characteristics of Precipitation Inferred from Wind Profiler Radar Doppler Spectra. Remote Sens. **2022**, 14, 5023. https://doi.org/10.3390/rs14195023

En el Capítol 5 es revisa l'assoliment de cadascun dels objectius detallats en el capítol 1 i es proposen noves vies de recerca per futurs treballs.

Per finalitzar es detallen dos Apèndixs. L'Apèndix A detalla les contribucions d'aquesta tesi en congressos i publicacions en revistes internacionals indexades. L'Apèndix B descriu breument una eina per a plotejar observacions de radiosondatge feta amb un programa en *Python* realitzat durant la tesi per examinar dades del radiosondatge del Servei Meteorològic de Catalunya llançat des de la Facultat de Física de la Universitat de Barcelona.

Capítol 2

Estudi de la Banda Brillant

2.1. Característiques de la Banda Brillant a Barcelona

2.1.1. Resum de l'article

En aquest article es desenvolupa una nova metodologia per a la caracterització de la banda brillant partint de les dades crues obtingudes amb un radar Doppler de mira vertical i de freqüència contínua i modulada. La metodologia es basa en la detecció de canvis al tercer moment de la reflectivitat espectral, que correspon al paràmetre d'asimetria (*skewness*) de la distribució de velocitats a una certa altura. Mirant l'evolució dels hidrometeors d'dalt a baix, es tracta d'observar el pas d'una asimetria positiva a negativa (just en entrar a la banda brillant, marcant el nivell superior de la BB), i posteriorment un canvi d'asimetria negativa a positiva (un cop les partícules surten de la BB). Aquest fet implica que partim de velocitats relativament baixes (a la part superior de la BB) i passem a velocitat majors (a la part inferior de la BB), fet que és consistent amb els canvis en la forma dels hidrometeors i la seva velocitat de caiguda associada.

La nova sistemàtica es comprova utilitzant 39 casos on es disposava de dades de precipitació obtingudes amb el MRR-Pro al terrat de la Facultat de Física de la Universitat de Barcelona, observacions del radiosondatge del Servei Meteorològic de Catalunya situat al costat del MRR-Pro i també d'observacions de disdròmetre.

2.1.2. Article

Garcia-Benadí, A.; Bech, J.; Gonzalez, S.; Udina, M.; Codina, B. A New Methodology to Characterise the Radar Bright Band Using Doppler Spectral Moments from Vertically Pointing Radar Observations. *Remote Sens.* **2021**, *13*, 4323. https://doi.org/10.3390/rs13214323

remote sensing

MDPI

Article

A New Methodology to Characterise the Radar Bright Band Using Doppler Spectral Moments from Vertically Pointing Radar Observations

Albert Garcia-Benadí [1,2], Joan Bech [2,3,*], Sergi Gonzalez [4], Mireia Udina [2] and Bernat Codina [2]

[1] SARTI, Universitat Politècnica de Catalunya, 08800 Vilanova i la Geltrú, Spain; albert.garcia@meteo.ub.edu
[2] Department of Applied Physics-Meteorology, University of Barcelona, 08028 Barcelona, Spain; mudina@meteo.ub.edu (M.U.); bcodina@ub.edu (B.C.)
[3] Water Research Institute (IdRA), University of Barcelona, 08028 Barcelona, Spain
[4] DT Catalonia, Agencia Estatal de Meteorología (AEMET), 08071 Barcelona, Spain; sgonzalezh@aemet.es
* Correspondence: joan.bech@ub.edu

Abstract: The detection and characterisation of the radar Bright Band (BB) are essential for many applications of weather radar quantitative precipitation estimates, such as heavy rainfall surveillance, hydrological modelling or numerical weather prediction data assimilation. This study presents a new technique to detect the radar BB levels (top, peak and bottom) for Doppler radar spectral moments from the vertically pointing radars applied here to a K-band radar, the MRR-*Pro* (Micro Rain Radar). The methodology includes signal and noise detection and dealiasing schemes to provide realistic vertical Doppler velocities of precipitating hydrometeors, subsequent calculation of Doppler moments and associated parameters and BB detection and characterisation. Retrieved BB properties are compared with the melting level provided by the MRR-*Pro* manufacturer software and also with the 0 °C levels for both dry-bulb temperature (freezing level) and wet-bulb temperature from co-located radio soundings in 39 days. In addition, a co-located Parsivel disdrometer is used to analyse the equivalent reflectivity of the lowest radar height bins confirming consistent results of the new signal and noise detection scheme. The processing methodology is coded in a Python program called RaProM-*Pro* which is freely available in the GitHub repository.

Keywords: Doppler radar; bright band; melting level; aliasing

Citation: Garcia-Benadí, A.; Bech, J.; Gonzalez, S.; Udina, M.; Codina, B. A New Methodology to Characterise the Radar Bright Band Using Doppler Spectral Moments from Vertically Pointing Radar Observations. *Remote Sens.* **2021**, *13*, 4323. https://doi.org/10.3390/rs13214323

Academic Editors: Gyuwon Lee and Alexander Ryzhkov

Received: 10 September 2021
Accepted: 20 October 2021
Published: 27 October 2021

1. Introduction

Precipitating hydrometeors undergo various processes as they fall, including water vapour condensation, coalescence, break-up or evaporation for liquid water and ice nucleation, riming, aggregation or accretion for the solid phase [1]. One of the most important processes occurs as falling particles cross the 0 °C isotherm level, also called melting level, where solid water particles begin to melt and eventually transform completely into liquid particles [2,3]. The atmospheric layer where this process takes place is known as the melting layer and may produce a characteristic radar signature, the so-called radar Bright Band (hereafter BB), a term originated from the local maxima caused by high reflectivity values visible in the equivalent reflectivity vertical profile [4]. The BB is caused by differences in the dielectric constants, shape and terminal fall speeds of liquid and solid hydrometeor precipitating particles, which lead to abrupt changes of the radar backscattered power within the BB. The most evident BB signatures are produced under stratiform cold rain conditions [5,6] as updrafts, and vertical mixing present in convective precipitation do not provide the proper conditions for BB formation.

The presence of a BB in volumetric operational weather radar observations may produce local overestimations of rainfall amounts, which has led to the development of different procedures to detect and correct BB effects [2,7–9]. This is particularly important for events with rapidly changing characteristics, for example, with quick transitions from

snow to rain [10–12], or in the development of subsequent robust applications of radar precipitation estimates, such as hydrological modelling or NWP assimilation [13–15].

Most of the above BB correction schemes for scanning weather radars are based on more specific studies, typically performed with vertically pointing radars or using the so-called quasi vertical profiles of polarimetric scanning weather radars [16], not only to detect but also to characterise, in detail, the BB. The methods proposed include the use of the signal to noise ratio (SNR), the Doppler velocity profile [3], vertical gradients of equivalent radar reflectivity or Doppler velocity [17–21], or different polarimetric variables if polarimetric radars are used [16,22,23]. Other studies examined the relationship between the 0 °C dry-bulb temperature isotherm level and the BB height [24], which requires additional data, i.e., the temperature profile, typically obtained from radiosonde observations. Recent research related to BB effects has examined cases with multiple melting ice particle layers [22], the relation of BB intensity to surface rainfall rate [25] or BB effects upon spaceborne radar observations [26,27].

The main objective of this article is to describe a new processing methodology to detect the BB with single polarisation vertically pointing Doppler radar spectral observations, based on the use of the third moment of the Doppler radar velocity spectrum, the skewness. The new detection algorithm is implemented for a compact frequency-modulated continuous-wave (FMCW) vertically pointing Doppler radar operating in the K-band. The radar model used here is an MRR-*Pro*, which also provides a processing software that, among other variables, computes the existence of a melting layer (ML) given by a probability value (from 0 to 1). The methodology proposed here also provides an alternative signal processing with an advanced new dealiasing scheme in order to deal with some cases where the original manufacturer software provides limited results. The equivalent reflectivity provided by the new signal and noise detection scheme is compared with co-located Parsivel observations. The proposed BB detection scheme is compared with the MRR manufacturer ML product and also with co-located radiosounding observations.

The paper is organised as follows. In Section 2, we detail the instrumentation used. Section 3 describes the methodology and the improvements performed to avoid the aliasing and the new technique to determine the BB. We show the results in Section 4, a discussion in Section 5 and in Section 6, we present the conclusions.

2. Instrumentation and Data Acquisition

2.1. Instrumentation

The main instrument used in this study was a K-band (24 GHz) Doppler radar, MRR (Micro Rain Radar) manufactured by Metek Gmbh, model MRR-*Pro*, located on the roof of the Faculty of Physics building of the University of Barcelona (41°23′4.34″ N, 2°7′3.05″ E). MRR-*Pro* is an updated version of previous MRR units [28]. The configuration parameters used in the study (Table 1) provided precipitation observations up to 6.4 km above the radar level with a vertical resolution of 50 m and a temporal resolution of 10 s.

Table 1. MRR-*Pro* configuration parameters used in this study.

Definition	Parameter	Units	Values
Number of Doppler bins	M	–	64
Number of height bins	N	–	128
Temporal resolution	T_i	s	10
Height bin resolution	Δh	m	50
Nyquist Velocity	v_{ny}	$m \cdot s^{-1}$	12
Interval of velocity	Δv	$m \cdot s^{-1}$	0.19

An OTT Parsivel-2 disdrometer [29], hereafter Parsivel, co-located with the MRR-*Pro*, provided precipitation particle size and fall speed spectra at the radar level. These parameters allow comparisons between the MRR-*Pro* and Parsivel for different variables, such as rainfall rate or radar reflectivity. Finally, on the same roof is located the Barcelona

radio sounding station (WMO code 08190), which performs two soundings a day (at 00 and 12 UTC) that were also used in this study.

2.2. Data Acquisition

The data files generated by the MRR-*Pro* manufacturer software are used as input files for the processing with RaProM-*Pro*. These files are in netcdf format and contain basic configuration settings of the data acquisition, the raw data (so-called spectral reflectivity, or spectrum raw according to the manufacturer) and derived parameters, such as radial velocity spectra or an estimate of existence of the melting layer. Figure 1 schematically shows a selection of the content of the files and also indicates which variables are used in the proposed methodology (shown in green), which are, essentially, configuration parameters and raw data, from which derived parameters can be calculated.

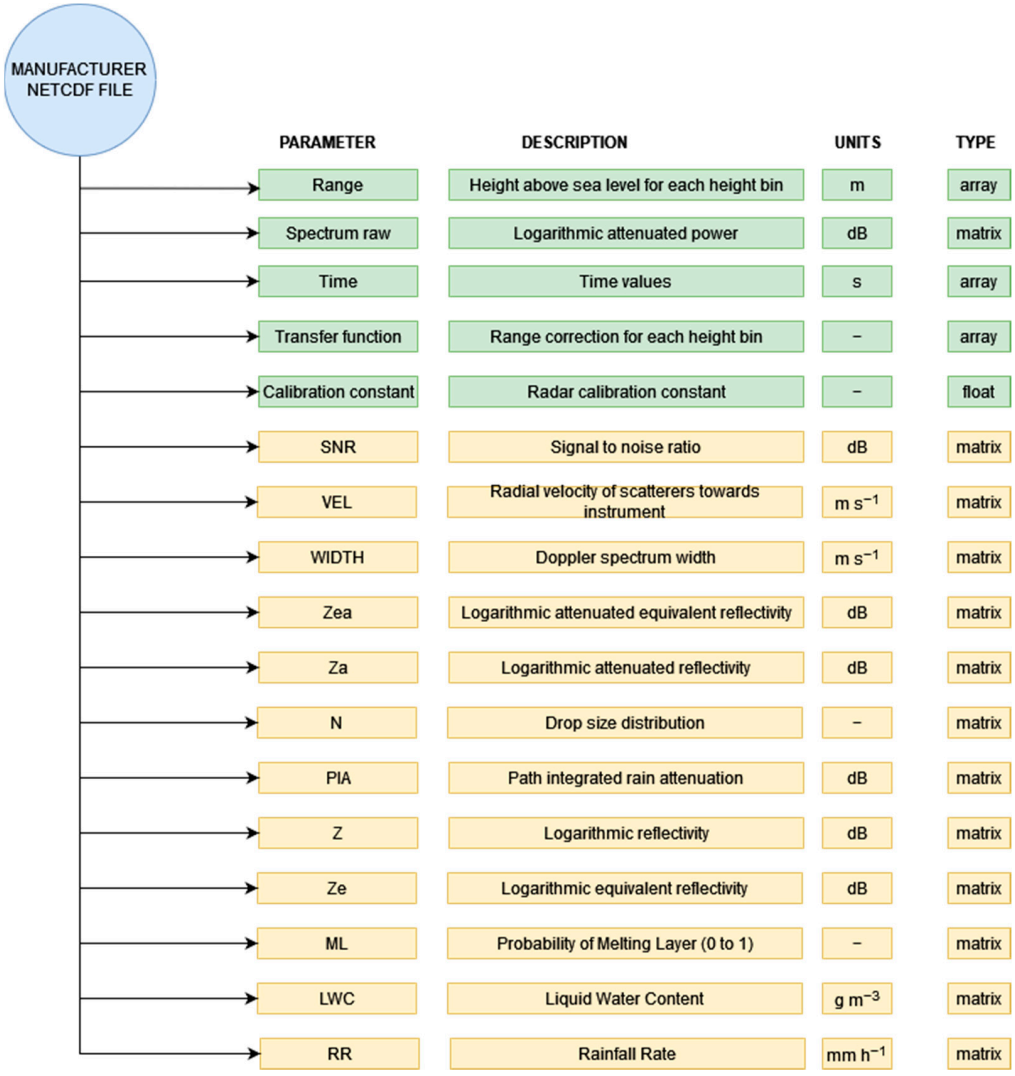

Figure 1. Description of selected parameters contained in the manufacturer's netcdf file. Parameters in green are required by the proposed methodology implemented in RaProM-*Pro*.

The parameters used by RaProM-*Pro* include, for each time step, a matrix $s(n, i)$ with the spectral raw values (labelled by the manufacturer as "spectrum raw") for all vertical levels n and Doppler frequencies i. The matrix $s(n, i)$ contains the ratio between emitted and received power after the Fourier Transform is computed by the radar and represent the intensity of the echo backscattered by the precipitation particles. The spectral values are processed with the information provided in different arrays, such as "range" (list of

heights above sea level) or "transfer function", which allows for correcting them according to their distance from the radar. Finally, a calibration constant unique to each radar unit is also provided.

To check the consistency of the new methodology proposed, additional parameters provided by the manufacturer—see [30]—are also used for comparison. These parameters include the SNR (signal to noise ratio), or the Doppler radial velocity and spectrum width and four different versions of radar reflectivity. These versions of radar reflectivity and equivalent radar reflectivity are computed in two stages. Firstly, without considering rainfall attenuation effects (in the so-called attenuated version of these variables, Za and Zea). Then, after the calculation of the drop size distribution (N), an estimate of the rainfall attenuation is calculated considering the Path Integrated rain Attenuation (PIA), which then allows the non-attenuated version of the reflectivity and equivalent reflectivity to be computed (Z, Ze). Finally, three additional parameters are considered for each height level: an estimate of the Melting Layer (ML)—expressed as a probability, a value between 0 and 1—the Liquid Water Content (LWC) and the Rainfall Rate (RR).

3. Processing Method

The processing software provided by the MRR-*Pro* manufacturer performs reasonably well in most meteorological conditions. However, in some cases, the original de-aliasing method provides limited results, as illustrated in Section 3.2. In order to develop a new de-aliasing scheme, spectral reflectivity has to be computed, so a new approach is also considered for the signal and noise processing described in this section.

The proposed processing method starts from the transformation of spectral raw data values read from the netcdf matrix S, for each level n and Doppler bin i, to their physical value given by spectral reflectivity (η), as described in two-steps in the following Equations (1) and (2):

$$s(i,n) = 10^{\left(\frac{S}{10}\right)}, \tag{1}$$

$$\eta(i,n) = s(i,n) \cdot \frac{CC}{TF(n)} \cdot n^2 \cdot \delta r, \tag{2}$$

where CC is the calibration constant, $TF(n)$ is the transfer function, δr is the height resolution, n is the number of height gates and i is the number of Doppler bins. From the spectral reflectivity, it is possible to calculate several physical parameters, such as hydrometeor velocity, equivalent radar reflectivity and the precipitation type classification, as described by [31].

The processing method consists of the following four main stages (Figure 2): (1). removal of noise and peaks detection from the raw signal, (2). dealiasing of the spectrum to improve the detection of the vertical velocity, (3). computation of attenuation path integrated (PIA) factors and (4). calculation of radar parameters using the corrected spectrum and the BB characterisation. The results are saved in a netcdf output file. Stages (2) and (4) are particularly novel. Note that Stage (1) must be performed before Stage (2) as spectral reflectivity (η), required for dealiasing, is not available in the manufacturer's netcdf file.

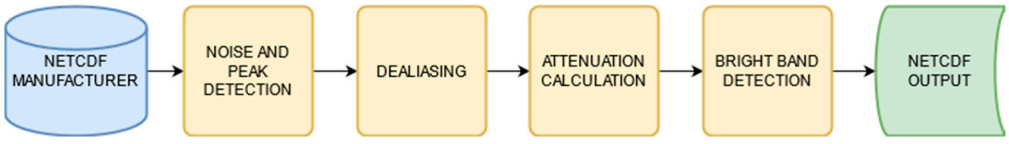

Figure 2. Flowchart of the new processing methodology.

3.1. Signal and Noise Detection

The signal and noise separation is performed considering the algorithm proposed by [32], similarly to what was described by [30], but considering two steps. The first step

consists of comparing the ratio of the squared mean spectral reflectivity and its variance with a specific threshold or limit fixed for a given integration time, given by Equation (3):

$$\frac{\overline{\eta}^2}{var(\eta)} = \frac{\left(\frac{\sum \eta_i}{n}\right)^2}{\frac{\sum (\eta_i - \overline{\eta})^2}{\sqrt{n-1}}} < Limit, \quad (3)$$

where *Limit* equals the time resolution chosen (T_i). This step is applied iteratively while the condition is verified. Each iteration implies evaluating a peak candidate, and if (3) is fulfilled, then the peak is discarded. The signal remains until the condition is false and will be considered background noise. More details of the implementation of this first step are detailed in [31].

The second step adds a new condition where the spectral reflectivity peak divided by the mean of the spectrum must be equal to or greater than a threshold value equal to 1.3 as shown in Equation (4):

$$\frac{max(\eta)}{\overline{\eta}} \geq 1.3, \quad (4)$$

in order to be considered a real signal. Note that (4) is applied after verifying (3) so that both conditions must be satisfied.

Then, the next step is the noise determination. The SNR is calculated using its definition expressed in dB, according to the manufacturer's documentation, given by Equation (5):

$$SNR = 10 \cdot \log_{10} \frac{Signal}{Noise}. \quad (5)$$

It is noted that SNR values provided by the manufacturer are substantially lower than those obtained with RaProM-*Pro*; in particular, they contain negative SNR values, i.e., signal below the noise level. This is a consequence of the different schemes applied for signal determination by the manufacturer and the methodology proposed, despite other derived variables presenting very similar values. An example is shown in Figure 3 comparing values obtained by RaProM-*Pro* and the manufacturer for equivalent reflectivity, SNR and Doppler velocity (Figure 3a–c respectively). SNR values present systematic differences around 20 dB but very similar values for the other variables, except for a few vertical velocity outliers due to the different dealiasing methods discussed below.

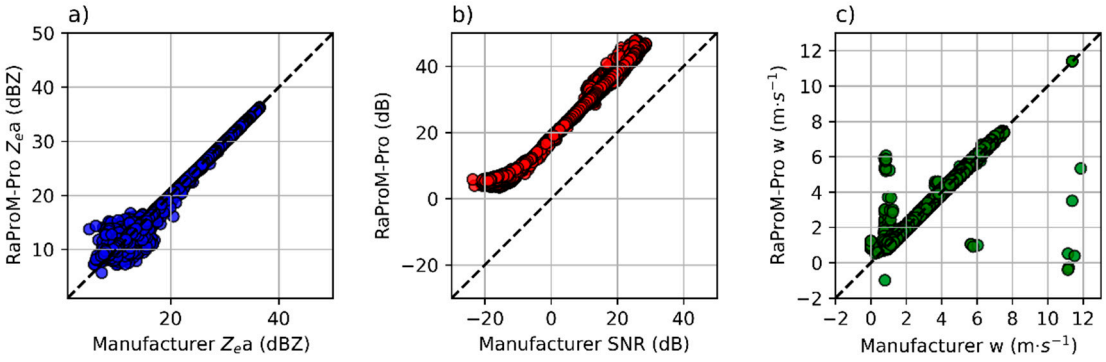

Figure 3. Scatter plots comparing the manufacturer and the RaProM-*Pro* processing. (**a**) Equivalent radar reflectivity, (**b**) signal-to-noise ratio and (**c**) Doppler vertical velocity. Data were recorded on 21 April 2020 from 10 h to 14 h UTC.

An additional analysis is performed for radar reflectivity comparing the lowest valid radar height bin (from 150 to 200 m above radar level) and the co-located Parsivel disdrometer (Figure 4) considering 1 min sampling periods. Both radar processing schemes compare very well with Parsivel values, with slight discrepancies that may be explained by instrumental differences—see [33]. More details about the signal and noise detection scheme can be found in Appendix A.

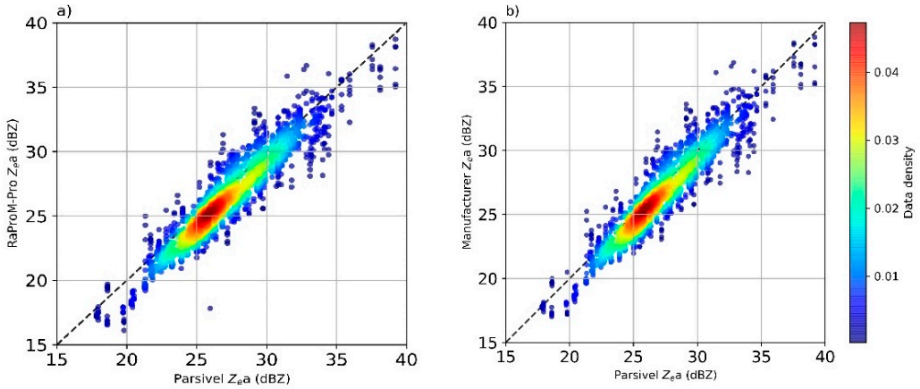

Figure 4. Scatter plots of equivalent radar reflectivity of the lowest valid height bin (150 to 200 m above radar level) of (**a**) RaProM-*Pro* and (**b**) the manufacturer processing vs. the Parsivel disdrometer located at the radar level. Coefficients of determination are equal to 0.878 (RaProM-*Pro*) and 0.879 (manufacturer) for 1195 samples. Data were recorded on 21 April 2020 from 10 h to 14 h UTC.

3.2. Dealiasing

Spectral reflectivity aliasing occurs when the target returns a signal outside the unambiguous range interval. A systematic method to correct aliasing in MRR-2 was proposed by [34] and was implemented with some modifications by [31]. The two methods are based on the estimated velocity parameters calculated from equivalent radar reflectivity in [35]. Here we propose a different approach, where only signal continuity between vertical levels is used, instead of the parameters estimated in [35]. According to the manufacturer's documentation, the radar manufacturer processing is able to detect upward movements of precipitation particles, but in some cases, this detection is not possible, and velocities are aliased. Figure 5 shows an example where the manufacturer velocity spectrum (Figure 5a) shows a suspicious pattern between 4000 and 5000 m, potentially caused by aliasing. By extending or unfolding the spectra to both sides (Figure 5b), the vertical continuity of the spectra allows a consistent dealiased spectra profile to be selected (Figure 5c).

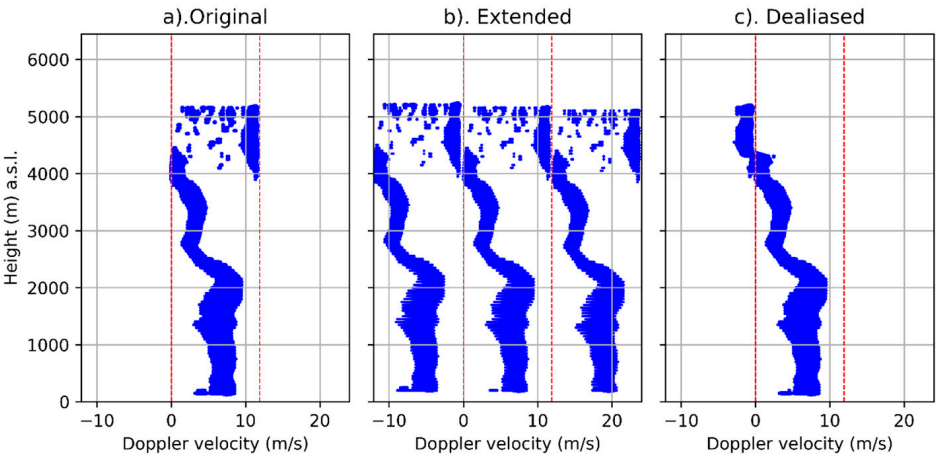

Figure 5. Example of Doppler velocity dealiasing applied with RaProM-*Pro* compared to the original data (16 May 2020, 13:45 UTC). Original Doppler spectra profile (**a**), extended Doppler spectra profile (**b**) and final dealiased Doppler spectra profile (**c**).

The dealiased spectral reflectivity allows, in this case, to detect upward movements of precipitation particles between 4000 and 5000 m. Figure 6 shows the corresponding time–height display of this case where RaProM-*Pro* detects upward movements, unlike the manufacturer original output, which indicates high downward values. More challenging cases, for example, with convective precipitation and strong windshear might not be de-

tected by the new proposed scheme, which was designed to deal with typical BB conditions (see Appendix B for more details).

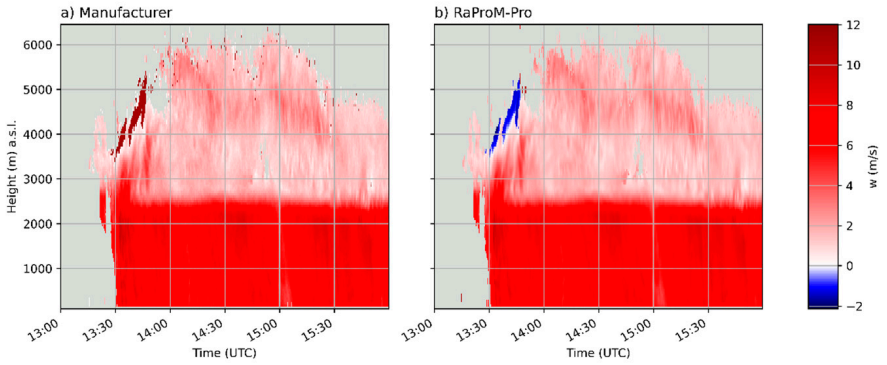

Figure 6. Time–height display of Doppler vertical velocity (positive values indicate downward direction) obtained with MRR-*Pro* on 16 May 2020 processed with: (**a**). The manufacturer's software, (**b**). RaProM-*Pro*, which includes a new dealiasing scheme.

After the dealiasing is applied, different Doppler moments from the spectral reflectivity are computed, including the equivalent radar reflectivity (dBZ), the Doppler velocity (m/s), the spectral width (m/s), the skewness and the kurtosis (Equations (6)–(10)):

$$Z_e = 10^{18} \cdot \frac{\lambda^4}{\pi^5} \cdot \frac{1}{|K|^2} \cdot \Delta v \cdot \sum \eta(v), \tag{6}$$

$$\overline{w} = \frac{\sum \eta(v,i) \cdot v(i)}{\sum \eta(v,i)} \tag{7}$$

$$\sigma = \sqrt{\frac{\sum \eta(v,i) \cdot (v(i) - w)^2}{\sum \eta(v,i)}} \tag{8}$$

$$skewness = \frac{\sum \eta(v,i) \cdot (v(i) - w)^3}{\sum \eta(v,i) \cdot \sigma^3} \tag{9}$$

$$kurtosis = \frac{\sum \eta(v,i) \cdot (v(i) - w)^4}{\sum \eta(v,i) \cdot \sigma^4} \tag{10}$$

where λ is the radar wavelength, $|K|^2$ is the dielectric factor, in this case, liquid water and Δv is the Nyquist velocity. Note that the radar reflectivity does not yet consider the possible effects of rainfall attenuation, which is computed in the next subsection.

3.3. Attenuation Calculation

Weather radars operating in attenuated frequencies, such as the K-band, may be affected by rainfall attenuation, impacting specific parameters such as radar reflectivity (Z), liquid water content (LWC) and rain rate (RR). Attenuation is calculated to determine the amount of signal loss integrated along a path (in height) by absorption and scattering by precipitating particles. PIA values are computed following an iterative process described in [36], shown schematically in Figure 7.

Essentially, drop size distributions $N'(D, n)$, at each level n, are calculated considering an attenuation factor (the PIA) multiplied by the previous (attenuated) drop size distribution $Na(D, n)$, computed from the Doppler spectra assuming Mie scattering conditions [37,38]. As these calculations are only valid for liquid precipitation particles falling at terminal fall speeds, an additional procedure that provides a hydrometeor classification type for each bin height [31] is applied so that attenuation can be used consistently only for liquid precipitation.

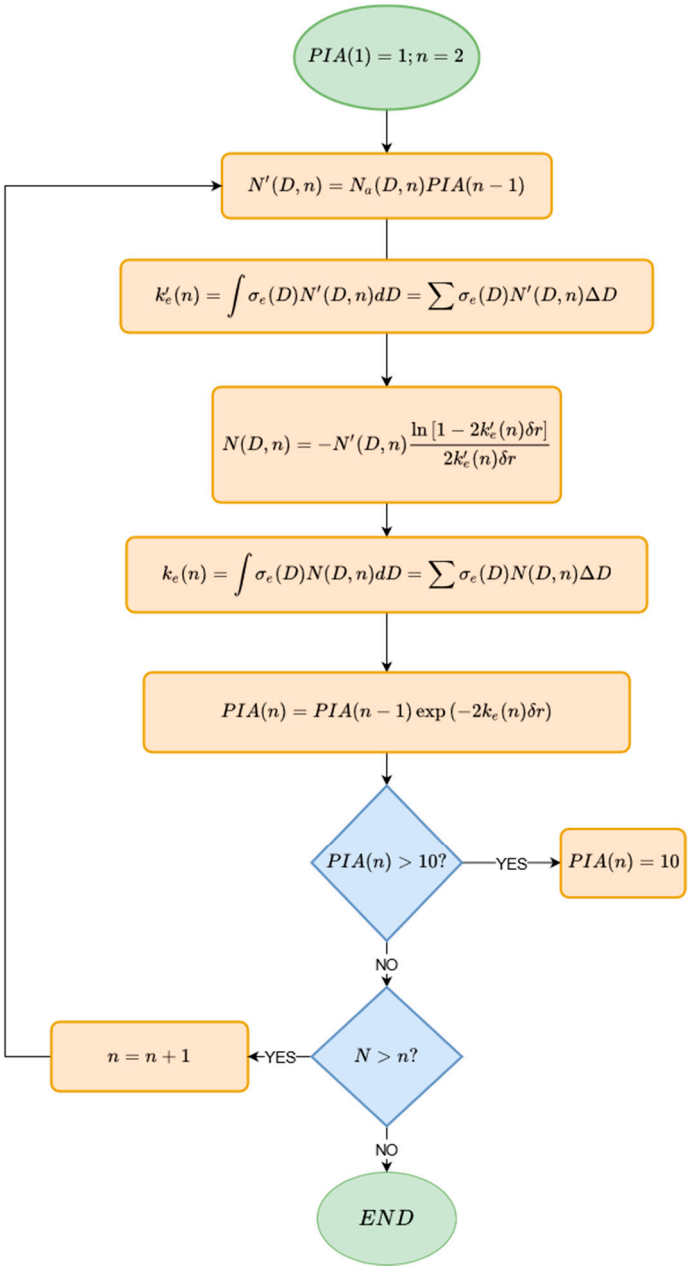

Figure 7. PIA calculation flow chart adapted from [36]. $N'(D, n)$ and $Na(D, n)$ are, respectively, the drop size distribution and the attenuated drop size distribution; k_e is the specific rain attenuation and σ_e is the single-particle extinction coefficient, calculated with the Mie theory.

As described in Figure 7, the maximum PIA value is 10, because for higher values, the scheme may not work properly. If PIA reaches the value of 10, the manufacturer processing stops calculating it for higher range bins. However, RaProM-*Pro* assigns a constant value of 10 for internal processing reasons. The final output parameter of PIA in RaProM-*Pro* is simply the PIA value expressed in dB (11), called *DBPIA*:

$$DBPIA = 10\log(PIA) \tag{11}$$

The *DBPIA* calculation is included in RaProM-*Pro* processing despite it not being applied in the BB determination procedure

Remote Sens. **2021**, *13*, 4323

3.4. Bright Band Calculation

The new methodology proposed to detect the BB is based on [39], plus a novel approach considering the vertical variation of the skewness computed from the spectrum Doppler velocity at each height. Skewness provides information about the asymmetry of the fall velocity distribution and indicates that in the BB, snowflakes or ice particles have started to melt [3,4,22]. The change of shape and aerodynamics of the solid particles as they melt modifies the averaged Doppler velocity and the spectrum shape. This change can be observed in the velocity distribution provided by the spectrum reflectivity at each height, where the maximum value changes from being tilted to the right to being tilted to the left, which implies a change of sign of the skewness. Figure 8 shows an example observed by the MRR-*Pro*, highlighting the different spectra shape above, within and below the BB calculated by RaProM-*Pro*.

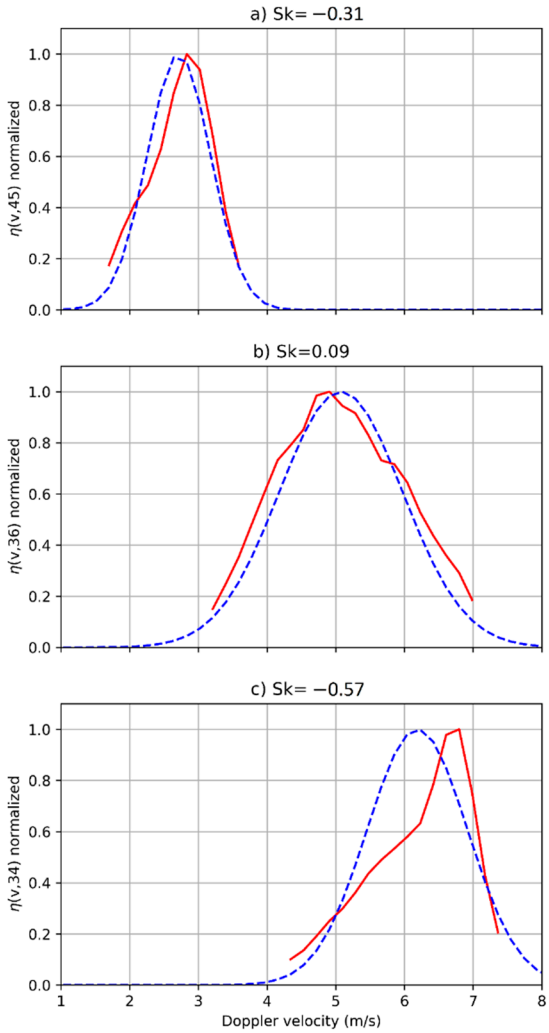

Figure 8. Examples of the Doppler velocity distribution (redsolid line) and fitted normal distribution calculated with the same average Doppler velocity and spectral width (blue dashed line) obtained at three different heights: (**a**). above the Bright Band (2350 m ASL), (**b**). within the Bright Band (1900 m ASL) and (**c**). below the Bright Band (1800 m ASL), on 5 December 2019. Skewness values (Sk) are given for each height.

The change in the shape of the spectra is clearly visible in Figure 8, where the progressive appearance of raindrops at the expense of melted solid particles (Figure 8b) modifies the Doppler velocity spectra, widening it to the right due to higher fall speeds. This leads to a symmetric or slightly right-skewed spectrum distribution, which implies a change of

the skewness from negative to positive values. Determining the height where the skewness sign changes is thus a key feature to obtain the height of the BB.

The method proposed is detailed in the flowchart shown in Figure 9, which describes, first, the BB detection approach, based on [39], and then the BB characterisation, which computes the BB top and the BB bottom. The remaining BB feature, the BBpeak, is the level located between the BB bottom and the BB top, where the skewness is maximum and should be close to the melting level. An additional checking is performed to remove BB detections of virga cases, simply verifying that precipitation reaches the ground.

The procedure is applied to each MRR-*Pro* vertical profile (in our case, available every 10 s). Then the results (BB top, BB peak and BB bottom) are smoothed temporally, considering a generalised exponential moving average [40], allowing a more continuous signal of BB characteristics, but keeping the original temporal resolution. Note that the current implementation of the scheme detects the lowest BB present in a vertical profile.

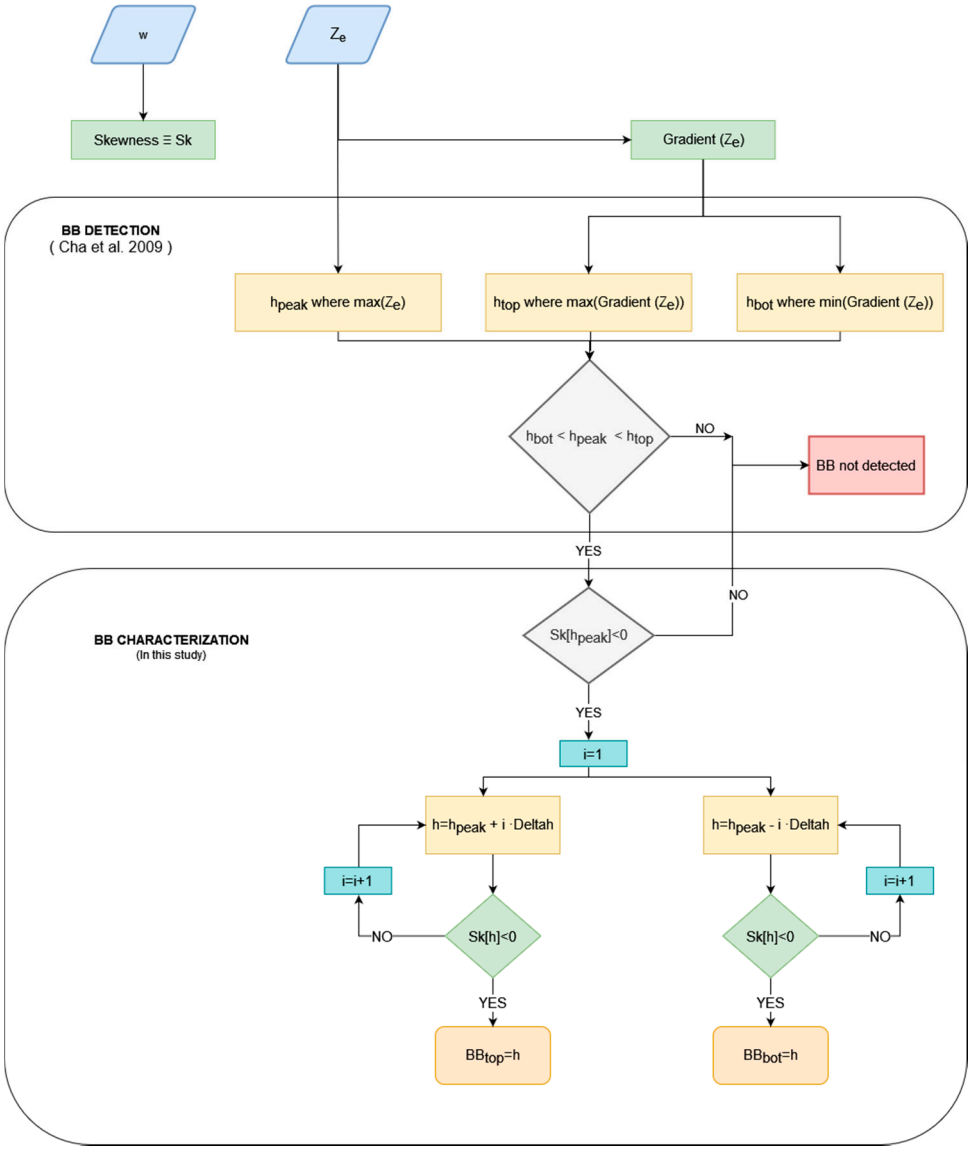

Figure 9. Bright Band (BB) detection and calculation of BB bottom (BB_{bot}) and BB top (BB_{top}). The Deltah parameter is equal to the vertical resolution of the radar data.

4. Results

The methodology presented in the previous section is illustrated in Figure 10, displaying both radiosonde data (Figure 10a) and MRR-*Pro* data (Figure 10b) for a clear BB case.

Remote Sens. **2021**, *13*, 4323

The figure shows the sounding profiles of dry-bulb, wet-bulb and dew point temperature (Figure 10a) recorded the 31 March 2020 at 12 UTC and radar equivalent reflectivity Ze from MRR-*Pro* and Parsivel observations; the latter was plotted at the lowest height level and resampled at a 10 s resolution to match MRR-*Pro* observations, from 12 to 15 UTC (Figure 10b). The sounding plot panel explicitly shows that the 0 °C wet-bulb temperature is relatively lower than the freezing level (0 °C dry-bulb temperature) due to low saturation. The wind profile is also plotted, showing west wind components below the BB, which is consistent with the precipitation fall streaks visible from the BB. Figure 10b shows consistent reflectivity values of ground measures from Parsivel and the first lowest valid height bin from the radar, for example, the alternating maxima and minima reflectivity columns. The 12 UTC melting levels and 0 °C wet-bulb temperature levels obtained with the sounding match the detected BB top and BB bottom well, respectively. This example illustrates well the ability of the new methodology to provide a temporal evolution of the BB details with a 10 s resolution.

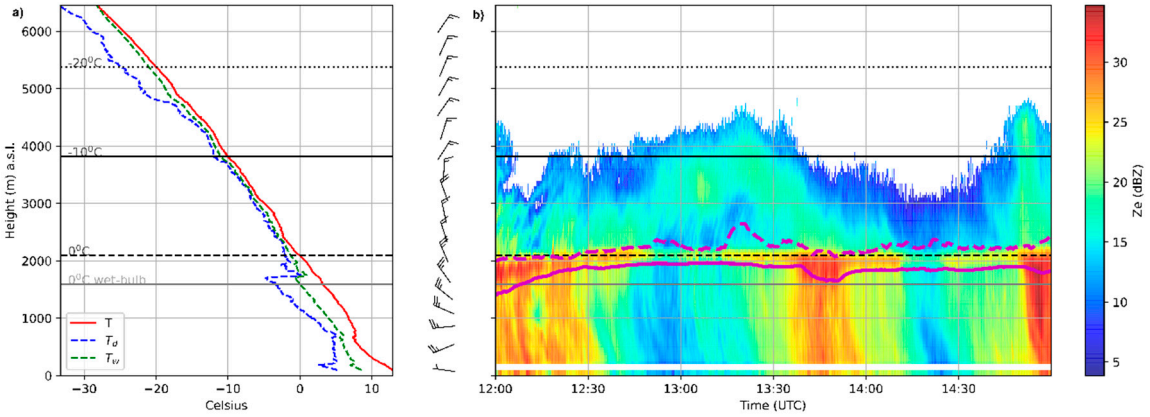

Figure 10. (**a**). Sounding profiles of dry-bulb (T), wet-bulb (T_w) and dew point (T_d) temperatures, also showing the 0 °C, −10 °C, −20 °C dry-bulb and 0 °C wet-bulb temperature levels and the wind profile, corresponding to 31 March 2020 12 UTC, (**b**). Radar equivalent reflectivity time–height display from MRR-*Pro* and Parsivel observations, the latter is plotted at the low height level, from 12 to 15 UTC 31 March 2020.

The results are presented in the following subsections, considering three different statistical comparisons. The first one is performed comparing the manufacturer's BB product and the proposed methodology. The second and third subsections compare, respectively, the new methodology and the original manufacturer product, with radio sounding observations.

4.1. Manufacturer ML Height vs. RaProM-Pro BB_{peak} Height

The previous example is the starting point to assess differences between the manufacturer's BB product and the new proposed methodology. Figure 11 shows radar reflectivity and Doppler velocity profiles processed with each methodology, also including the ML manufacturer's product and the proposed BB product. In this case, the melting layer heights computed by the manufacturer are always plotted between the estimated BB top and BB bottom, which provide a more complete description of the BB. Additionally, RaProM-*Pro* offers a more detailed description of the precipitation field (better depiction of contours and inclusion of additional weather echoes) around 15 UTC, particularly above the BB (from 4000 to 5000 m) thanks to the new noise and peak detection methodology.

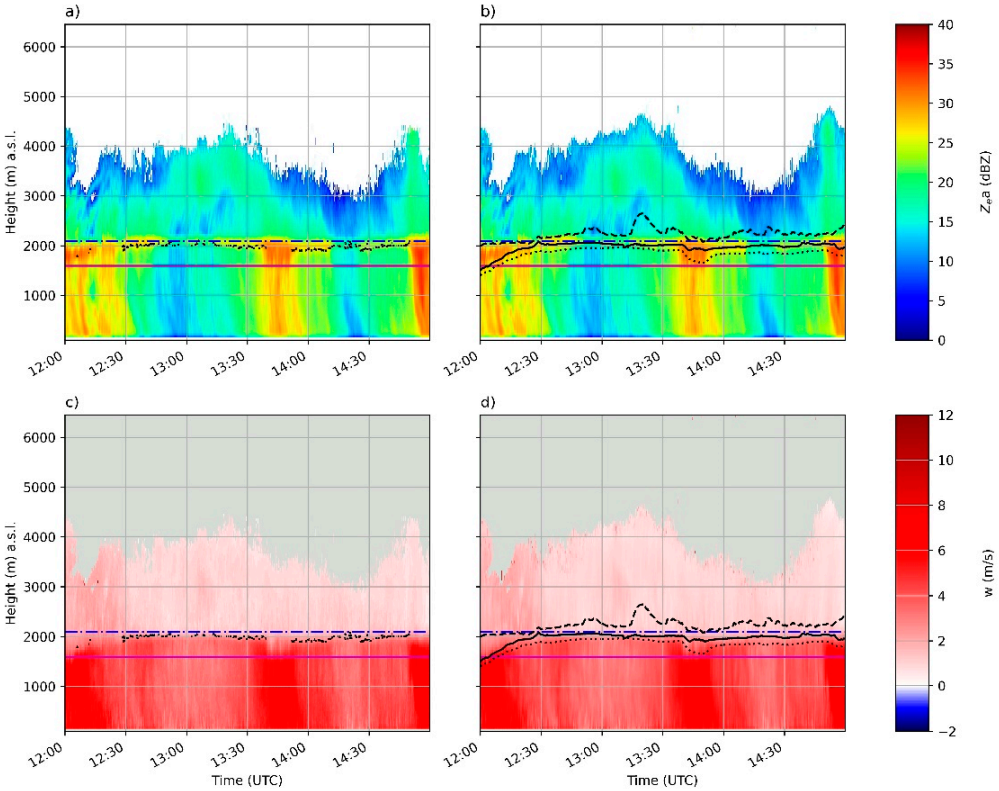

Figure 11. Time–height display of equivalent radar reflectivity—top row, panels (**a**,**b**) and Doppler velocity—bottom row, panels (**c**,**d**) calculated with the manufacturer's software (first column) and RaProM-*Pro* (second column). First and second column show, respectively, the melting level detected by the manufacturer (black dots) and the BB top, BB peak and BB bottom (dashed, continuous, and dotted black lines). The data corresponds to 31 March 2020.

A quantitative analysis is provided by comparing the melting layer (ML) height provided by the manufacturer and the BB_{peak} height calculated with RaProM-*Pro*, given by:

$$Diff\_ML = ML - BB_{peak} \quad (12)$$

The ML product is calculated using an Artificial Intelligence approach [41], providing probability values; a probability greater than 0.75 is considered a reliable ML height determination, being the maximum probability of the selected height for the melting level. The BB peak has been described in Section 3.

Figure 12 shows a histogram of *Diff_ML* for 39 days, selecting a time window of ± 1 h from the sounding launch, resulting in around 2600 cases. It displays a nearly symmetrical distribution pattern with a single-mode centred in the second negative class (from -50 to -100 m), indicating that the manufacturer's ML height is slightly lower than the BB_{peak} (the averaged value of *Diff_ML* is -89 m and the standard deviation is 180 m). More than 80% of cases do not exceed 200 m, and the tails of the distribution fall quickly, which despite some differences, reach values higher than 400 m.

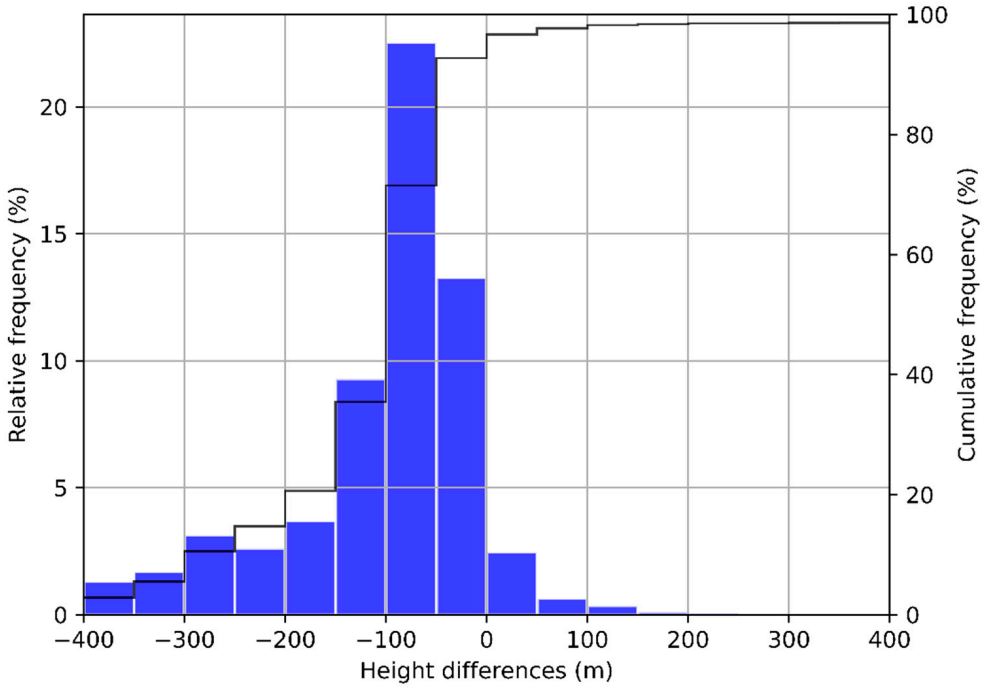

Figure 12. Histogram of differences between the melting level height provided by the manufacturer and the Bright Band peak height from RaProM-*Pro*. The height bin resolution is equal to the histogram class bin, 50 m.

4.2. Sounding Observations vs. RaProM-Pro BB Levels

The 0 °C dry-bulb temperature level (freezing level, hereafter h_0) and the 0 °C wet-bulb temperature level (hereafter $h_{w,0}$) are compared here with the BB_{top}, BB_{peak} and BB_{bot} heights. We consider the same 39 days studied in the previous subsection, with the same time intervals of ±1 h from the sounding launch time to minimise spurious differences caused by rapidly changing BB heights, leading to around 5327 cases.

The evaluation is performed using the parameters *Diff_top*, *Diff_bot*, *Diff_peak* and *Diff_Tw* defined as:

$$Diff\_top = BB_{top} - h_0 \tag{13}$$

$$Diff\_bot = BB_{bot} - h_0 \tag{14}$$

$$Diff\_peak = BB_{peak} - h_0 \tag{15}$$

$$Diff\_Tw = BB_{peak} - h_{w,0} \tag{16}$$

where BB_{top}, BB_{bot} and BB_{peak} are the heights from the BB top, BB bottom and BB peak, respectively. Note that a priori, *Diff_top* should be close to 0 as solid particles begin to melt when they reach the melting level, *Diff_bot* should be greater than 0, as it takes some time to completely melt all solid particles and, by definition, *Diff_peak*, should be between *Diff_top* and *Diff_bot*. Regarding the expected value of *Diff_Tw*, the recent study of [42] indicated that BB_{peak} heights were very similar to $h_{w,0}$, so a value close to 0 would be consistent with that result.

Figure 13a shows histograms of *Diff_top* and *Diff_bot*, indicating similar patterns but centred, respectively, below and above h_0: BB_{top} mode is between 150 and 200 m, and BB_{bot} is between −250 and −2000 m. The fact that BB_{top} occurs mostly above h_0 (so it is not close to 0 as initially expected) can be explained by the tendency of solid particles to increase aggregation just above the melting level, producing larger snowflakes and reducing the number of smaller particles [6]. This would lead to a change in the skewness spectrum, which would be detected by the proposed methodology as the BB_{top}. On the other hand,

the mode value of *Diff_bot* found is reasonable, compared with previous existing studies, such as [4].

Figure 13b shows that the *Diff_peak* histogram presents a similar pattern to *Diff_top* and *Diff_bot*, but, as expected, the mode value, more pronounced (corresponding to a more leptokurtic distribution), is centred between the previous two modes, close to 0. Finally, *Diff_*T_w presents a slightly thicker mode, with a maximum between −50 and 0 m, which is just one class below the *Diff_peak* mode.

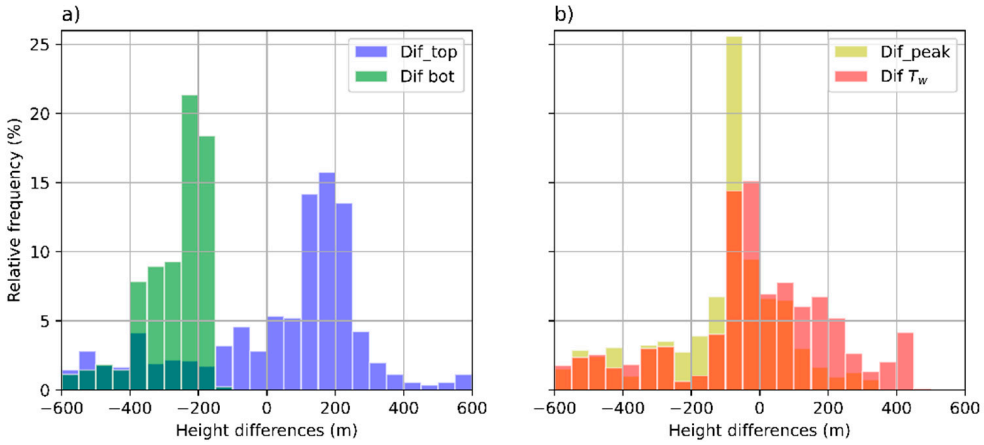

Figure 13. (**a**). Histograms of the differences between Bright Band top and Bright Band bottom heights and the sounding-derived freezing levels *Diff_top* (blue) and *Diff_bot* (green), respectively, and (**b**). histograms of differences between Bright Band peak height and the sounding-derived height of zero wet-bulb temperature, *Diff_*T_w (red) and differences between Bright Band peak height and the freezing level, *Diff_peak* (yellow). Values are analysed around ±1.5 h from the sounding launch time.

4.3. Sounding Observations vs. Manufacturer ML Levels

In this subsection, the same analysis performed in Section 4.2 is applied to the manufacturer's ML product for 1749 cases detected in the same time period considered above. However, in this case, no BB top nor bottom are considered; only a BB peak is given here by the maximum probability of the ML height product (exceeding 75% as mentioned earlier), denoted as ML_{max}. We computed the differences between the ML_{max} and sounding-derived zero dry and wet-bulb temperature heights (*Diff_peak_Man* and *Diff_Tw_Man* respectively), given by:

$$Diff\_peak\_Man = ML_{max} - h_0 \quad (17)$$

$$Diff\_Tw\_Man = ML_{peak} - h_{w,0} \quad (18)$$

The distributions of these variables are displayed in Figure 14, similarly to Figure 13b. Both variables show similar patterns and a common main mode corresponding to the same class of height differences (−150 to −100 m) and are relatively wide (three to four different height classes). Secondary modes exceeding 5% relative frequencies are found around −300 and +400 m for *Diff_peak_Man* and around −500 m for *Diff_Tw_Man*.

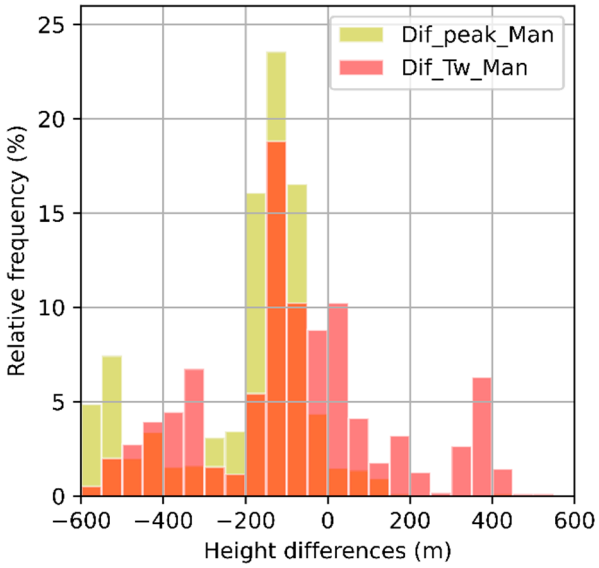

Figure 14. As in Figure 13b but for the manufacturer's ML product.

5. Discussion

According to the results shown in the previous section, the proposed BB detection and characterisation method provides some advantages.

Firstly, the new dealiasing scheme presents an improvement in some cases where the manufacturer standard processing fails. Despite the fact that the new dealiasing cannot handle very complex cases, such as those found on convective precipitation with intense turbulence, environments favourable to BB conditions, with moderate updrafts, are reasonably well identified, improving the original manufacturer's software capabilities.

Secondly, the BB detection proposed, when compared to radiosounding derived zero dry and wet-bulb temperatures, provide narrower difference height distributions compared to those obtained with the manufacturer's ML product. This suggests that, despite both schemes performing similarly, the proposed methodology gives lower differences compared to the observed freezing level. Moreover, the new method gives explicit information about the BB top and bottom, information not available from the ML manufacturer's product, and the number of detections is considerably higher (5327 vs. 1749 in the period examined).

Despite improvements in the dealiasing approach, limitations of the proposed method include the inability to correct fully folded velocity profiles and also convection with strong windshear. However, these conditions do not typically produce BBs. On the other hand, strong windshear with stratiform precipitation, leading to tilted precipitation streaks, might be a problem for the BB scheme because it examines single radar vertical profiles. Moreover, the proposed scheme cannot handle either multiple BB cases as only the lowest BB can be detected. In any case, the new method based on the vertical variability of the Doppler speed skewness provides a good basis for the further development of more sophisticated BB detection methods.

6. Summary and Conclusions

The work presents a new methodology to process spectral raw reflectivity data from a K-band vertically pointing Doppler radar, implemented for the Metek MRR-*Pro* system, and called RaProM-*Pro*, which is freely available. RaProM-*Pro* can be used complementary with the manufacturer's software and provides additional features, such as an improved signal and noise detection scheme, an advanced dealiasing method and a new Bright Band product (including top, peak and bottom levels).

The study illustrates the advantages of RaProM-*Pro*, such as the capability to detect weaker signals or the robust detection of updrafts thanks to a novel dealiasing scheme. The

derived parameters, such as radar reflectivity, mostly match the values provided by the manufacturer (R^2 of 0.992) and is also consistent with independent observations from co-located disdrometer data. The new Bright Band product, based on changes of the skewness of spectral Doppler velocities, compares favourably with the manufacturer's Melting Level product and also with collocated radio sounding observations, both qualitatively in selected examples and quantitatively, as revealed by a study considering 39 days.

Based on the current results, future work is planned to perform a long-term study of BB features in more detail, including BB occurrence, height, thickness and atmospheric conditions (dry and moist BBs).

The methodology can be used for both research and operational applications and could be adapted to other vertically pointing radars. RaProM-*Pro* is written in Python and is freely available at the GitHub repository.

Author Contributions: Conceptualisation, A.G.-B. and J.B.; methodology, A.G.-B. and J.B.; software, A.G.-B. and S.G.; data curation, A.G.-B.; writing—original draft preparation, A.G.-B. and J.B.; writing—review and editing, A.G.-B., B.J, S.G., M.U. and B.C. All authors have read and agreed to the published version of the manuscript.

Funding: This research was partly funded by the project "Analysis of Precipitation Processes in the Eastern Ebro Subbasin" (WISE-PreP, RTI2018-098693-B-C32, MINECO/FEDER) and the Water Research Institute (IdRA) of the University of Barcelona.

Data Availability Statement: The proposed methodology coded as a Python program is available at the GitHub repository (https://github.com/AlbertGBena/RaProM-Pro.git). Radiosonde data are available from the Meteorological Service of Catalonia (meteo.cat) and MRR-*Pro* and Parsivel data are available from the authors upon request.

Acknowledgments: Radiosonde data of the Meteorological Service of Catalonia were used in this study.

Conflicts of Interest: The authors declare no conflict of interest.

Appendix A

This Appendix provides additional information about the new processing methodology regarding noise and signal detection introduced in Section 3.1. Based on 3 h of precipitation data recorded from 12 to 15 UTC 31 March 2020 (Figure 11), 138,240 points (height gates) were examined. Figure A1 shows a mask of three possible cases regarding the signal and noise detection of each method: gates (pixels) with the signal detected by both methods, gates with noise detected by both methods and pixels detected only by one of the methods.

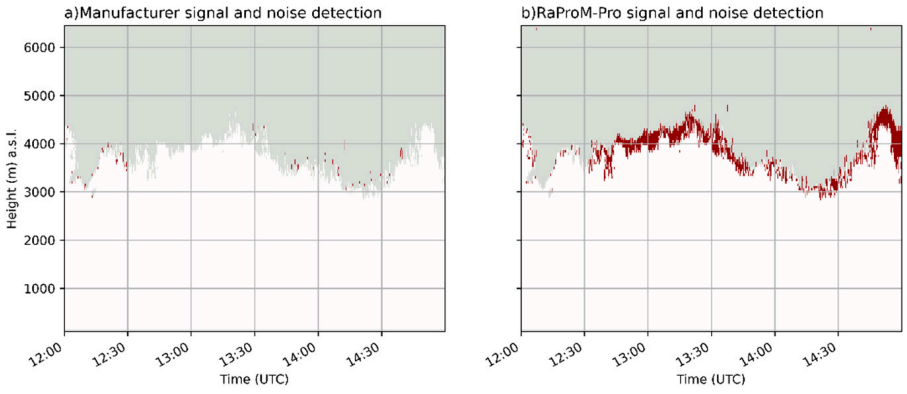

Figure A1. Signal and noise detection comparison between manufacturer and RaProm-*Pro* schemes: pixels with the signal detected by both methods (white), noise detected by both methods (grey), pixels detected only by the manufacturer (**a**) and RaProm-*Pro* (**b**) methods (red). The data were recorded from 12 to 15 UTC, 31 March 2020.

It is clear that both methods perform similarly, as most signal and noise detections are identical; only a small fraction, close or at the precipitation contours, is detected differently, being RaProM-*Pro* a bit more sensitive (about 2.8% more signal detection than the manufacturer's method, as listed in Table A1).

Table A1. Signal and noise gates detected by manufacturer versus RaProM-*Pro* methods.

Cases (12 to 15 UTC 31 March 2020)	Number	%
Total number of gates	138,240	100.00
Noise gates identified both by manufacturer and RaProM-*Pro*	57,654	41.71
RaProM-*Pro* signal gates identified as noise gates by manufacturer	4062	2.94
Manufacturer signal gates identified as noise gates by RaProM-*Pro*	166	0.12
Signal gates identified both by manufacturer and RaProM-*Pro*	76,358	55.23

Appendix B

This Appendix provides more details about the dealiasing scheme proposed.

The dealiasing scheme is based on the original work by [43,44], and it has been tested for 39 2 h events with precipitation and radiosounding data with the aim to apply it for BB detection. Other more challenging situations, such as convective precipitation with windshear or strong turbulence, where typically BB is not present, may not produce good results. Figure A2 shows one of these cases, recorded on 27 July 2019, displaying the Doppler vertical velocity provided by the manufacturer and the new dealiasing scheme.

Figure A3 (analogous to the simpler case shown in Figure 5) illustrates the steps of the dealiasing applied. Two basic concepts are considered in the scheme: Doppler bin clustering (of precipitation and non-precipitation blocks) and vertical continuity of precipitation blocks.

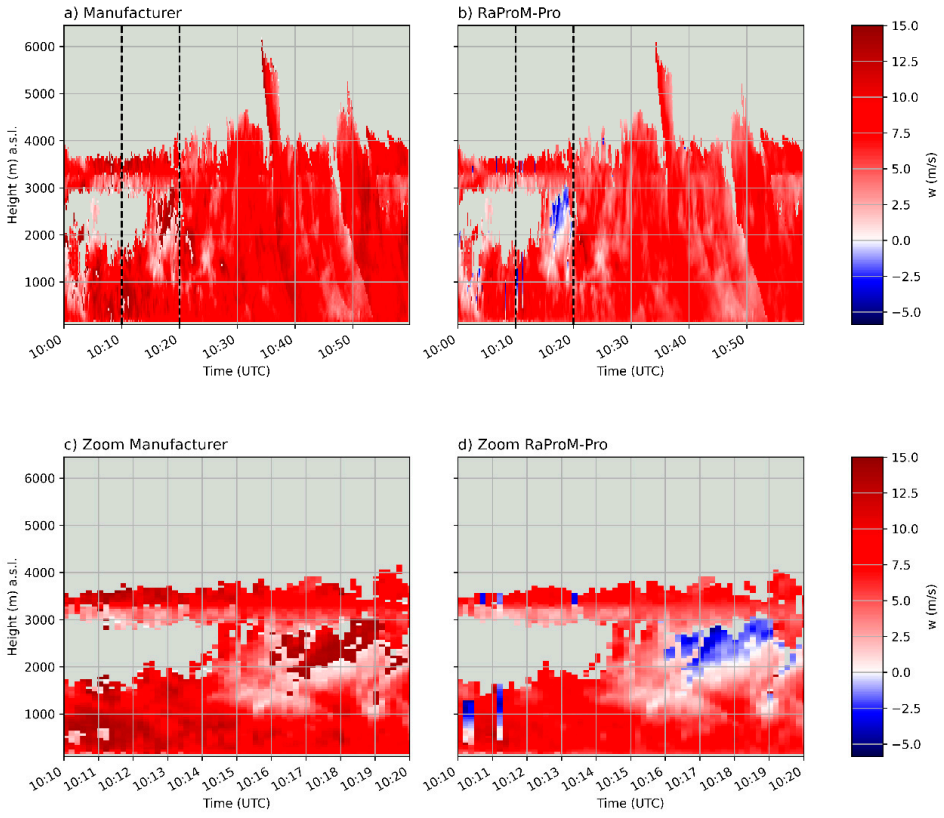

Figure A2. Time–height display of the Doppler velocity (positive values indicate downward direction) obtained with MRR-*Pro* on 27 July 2019, processed with: (**a**) the manufacturer's software, (**b**). RaProM-*Pro*. Panels (**c**,**d**) show zooms of the previous images, from 10:10 to 10:20 UTC.

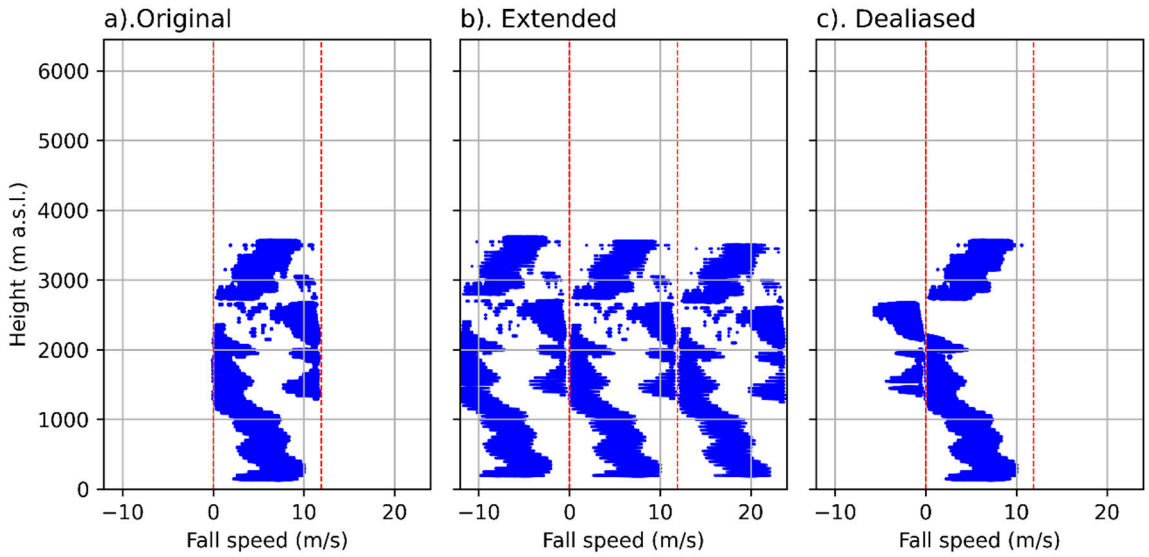

Figure A3. Doppler velocity dealiasing applied with RaProm-*Pro* compared to the original data (27 July 2019, 10:16:30 UTC). Original Doppler spectra profile (**a**), extended Doppler spectra profile (**b**) and final dealiased Doppler spectra profile (**c**).

For each height, two Doppler bin groups are identified: blocks of continuous precipitation bins and blocks of non-precipitation bins (hereafter gaps) (Figure A3a). Then, the spectra are extended to both sides of the Nyquist velocity interval, i.e., considering stronger fall speeds (adding to the right of the original spectra the spectra immediately above the central one) or upward speeds (adding to the left of the original spectra the spectra immediately below the central one). A new grouping of Doppler bins is applied to the extended spectra, providing new precipitation blocks and gaps (Figure A3b). Now three options are possible to select the dealiased velocity profile, and we assume that only one, for each height, is valid. Starting from the second lowest valid level to higher ones, the selection criteria is that the average velocity of the level considered is closest to the average velocity of the level below (Figure A3c).

In this convective case, the results seem reasonable for aliasing found from 1500 to ca. 2500 m ASL, but it is not so clear for heights above 2500 m ASL.

References

1. Tapiador, F.J.; Sánchez, J.L.; García-Ortega, E. Empirical values and assumptions in the microphysics of numerical models. *Atmos. Res.* **2019**, *215*, 214–238. [CrossRef]
2. Gray, W.R.; Cluckie, D.I.; Griffith, R.J. Aspects of melting and the radar bright band. *Meteorol. Appl.* **2001**, *8*, 371–379. [CrossRef]
3. White, A.B.; Gottas, D.J.; Strem, E.T.; Ralph, F.M.; Neiman, P.J. An Automated Brightband Height Detection Algorithm for Use with Doppler Radar Spectral Moments. *J. Atmos. Ocean. Technol.* **2002**, *19*, 687–697. [CrossRef]
4. Fabry, F.; Zawadzki, I. Long-term radar observations of the melting layer of precipitation and their interpretation. *J. Atmos. Sci.* **1995**. [CrossRef]
5. Fabry, F. *Radar Meteorology Principles and Practice*; Cambridge University Press: Cambridge, UK, 2018; ISBN 9781108460392.
6. Heymsfield, A.J.; Bansemer, A.; Poellot, M.R.; Wood, N. Observations of Ice Microphysics through the Melting Layer. *J. Atmos. Sci.* **2015**, *72*, 2902–2928. [CrossRef]
7. Bordoy, R.; Bech, J.; Rigo, T.; Pineda, N. Analysis of a method for radar rainfall estimation considering the freezing level height. *Tethys J. Weather Clim. West. Mediterr.* **2010**, 25–39. [CrossRef]
8. Hall, W.; Rico-Ramirez, M.A.; Krämer, S. Classification and correction of the bright band using an operational C-band polarimetric radar. *J. Hydrol.* **2015**, *531*, 248–258. [CrossRef]
9. Sánchez-Diezma, R.; Zawadzki, I.; Sempere-Torres, D. Identification of the bright band through the analysis of volumetric radar data. *J. Geophys. Res. Atmos.* **2000**. [CrossRef]
10. Bech, J.; Pineda, N.; Rigo, T.; Aran, M. Remote sensing analysis of a Mediterranean thundersnow and low-altitude heavy snowfall event. *Atmos. Res.* **2013**, *123*, 305–322. [CrossRef]
11. Casellas, E.; Bech, J.; Veciana, R.; Pineda, N.; Rigo, T.; Miró, J.R.; Sairouni, A. Surface precipitation phase discrimination in complex terrain. *J. Hydrol.* **2021**, *592*, 125780. [CrossRef]

12. Casellas, E.; Bech, J.; Veciana, R.; Pineda, N.; Miró, J.R.; Moré, J.; Rigo, T.; Sairouni, A. Nowcasting the precipitation phase combining weather radar data, surface observations, and NWP model forecasts. *Q. J. R. Meteorol. Soc.* **2021**, *147*, 3135–3153. [CrossRef]
13. Demir, I.; Krajewski, W.F. Towards an integrated Flood Information System: Centralized data access, analysis, and visualization. *Environ. Model. Softw.* **2013**, *50*, 77–84. [CrossRef]
14. Rossa, A.; Haase, G.; Keil, C.; Alberoni, P.; Ballard, S.; Bech, J.; Germann, U.; Pfeifer, M.; Salonen, K. Propagation of uncertainty from observing systems into NWP: COST-731 Working Group 1. *Atmos. Sci. Lett.* **2010**, *11*, 145–152. [CrossRef]
15. Seo, B.C.; Krajewski, W.F. Statewide real-time quantitative precipitation estimation using weather radar and NWP model analysis: Algorithm description and product evaluation. *Environ. Model. Softw.* **2020**, *132*, 104791. [CrossRef]
16. Ryzhkov, A.; Zhang, P.; Reeves, H.; Kumjian, M.; Tschallener, T.; Trömel, S.; Simmer, C. Quasi-Vertical Profiles—A New Way to Look at Polarimetric Radar Data. *J. Atmos. Ocean. Technol.* **2016**, *33*, 551–562. [CrossRef]
17. Tokay, A.; Hartmann, P.; Battaglia, A.; Gage, K.S.; Clark, W.L.; Williams, C.R. A field study of reflectivity and Z-R relations using vertically pointing radars and disdrometers. *J. Atmos. Ocean. Technol.* **2009**. [CrossRef]
18. Das, S.; Shukla, A.K.; Maitra, A. Investigation of vertical profile of rain microstructure at Ahmedabad in Indian tropical region. *Adv. Sp. Res.* **2010**, *45*, 1235–1243. [CrossRef]
19. Massmann, A.K.; Minder, J.R.; Garreaud, R.D.; Kingsmill, D.E.; Valenzuela, R.A.; Montecinos, A.; Fults, S.L.; Snider, J.R. The Chilean Coastal Orographic Precipitation Experiment: Observing the Influence of Microphysical Rain Regimes on Coastal Orographic Precipitation. *J. Hydrometeorol.* **2017**, *18*, 2723–2743. [CrossRef]
20. Pfaff, T.; Engelbrecht, A.; Seidel, J. Detection of the bright band with a vertically pointing K-band radar. *Meteorol. Z.* **2014**, *23*, 527–534. [CrossRef]
21. Wang, H.; Lei, H.; Yang, J. Microphysical processes of a stratiform precipitation event over eastern China: Analysis using Micro Rain Radar data. *Adv. Atmos. Sci.* **2017**. [CrossRef]
22. Li, H.; Moisseev, D. Two Layers of Melting Ice Particles Within a Single Radar Bright Band: Interpretation and Implications. *Geophys. Res. Lett.* **2020**, *47*, e2020GL087499. [CrossRef]
23. Romatschke, U. Melting Layer Detection and Observation with the NCAR Airborne W-Band Radar. *Remote Sens.* **2021**, *13*, 1660. [CrossRef]
24. Benarroch, A.; Siles, G.A.; Riera, J.M.; Perez-Pena, S. Heights of the 0 °C Isotherm and the Bright Band in Madrid: Comparison and Variability. In Proceedings of the 14th European Conference on Antennas and Propagation, EuCAP 2020, Copenhagen, Denmark, 15–20 March 2020.
25. Lin, D.; Pickering, B.; Neely, R.R., III. Relating the Radar Bright Band and Its Strength to Surface Rainfall Rate Using an Automated Approach. *J. Hydrometeorol.* **2020**, *21*, 335–353. [CrossRef]
26. Alpers, W.; Zhao, Y.; Mouche, A.A.; Chan, P.W. A note on radar signatures of hydrometeors in the melting layer as inferred from Sentinel-1 SAR data acquired over the ocean. *Remote Sens. Environ.* **2021**, *253*, 112177. [CrossRef]
27. Arulraj, M.; Barros, A.P. Automatic detection and classification of low-level orographic precipitation processes from space-borne radars using machine learning. *Remote Sens. Environ.* **2021**, *257*, 112355. [CrossRef]
28. Peters, G.; Fischer, B.; Andersson, T. Rain observations with a vertically looking Micro Rain Radar (MRR). *Boreal Environ. Res.* **2002**, *7*, 353–362.
29. Tokay, A.; Wolff, D.B.; Petersen, W.A. Evaluation of the New Version of the Laser-Optical Disdrometer, OTT Parsivel2. *J. Atmos. Ocean. Technol.* **2014**, *31*, 1276–1288. [CrossRef]
30. Metek MRR-Pro. *Description of Products. Valid for MRR-PRO Firmware VS* $\geq$ *01*; Metek Meteorologische Messtechnik GmbH: Elmshorn, Germany, 2010.
31. Garcia-Benadi, A.; Bech, J.; Gonzalez, S.; Udina, M.; Codina, B.; Georgis, J.F. Precipitation type classification of Micro Rain Radar data using an improved Doppler spectral processing methodology. *Remote Sens.* **2020**, *12*, 4113. [CrossRef]
32. Hildebrand, P.H.; Sekhon, R.S. Objective Determination of the Noise Level in Doppler Spectra. *J. Appl. Meteorol.* **1974**, *13*, 808–811. [CrossRef]
33. Adirosi, E.; Baldini, L.; Tokay, A.L.I. Rainfall and DSD parameters comparison between Micro Rain Radar, two-dimensional video and Parsivel2 disdrometers, and S-band dual-polarization radar. *J. Atmos. Ocean. Technol.* **2020**. [CrossRef]
34. Maahn, M.; Kollias, P. Improved Micro Rain Radar snow measurements using Doppler spectra post-processing. *Atmos. Meas. Tech.* **2012**, *5*, 2661–2673. [CrossRef]
35. Atlas, D.; Srivastava, R.C.; Sekhon, R.S. Doppler radar characteristics of precipitation at vertical incidence. *Rev. Geophys.* **1973**, *11*, 1–35. [CrossRef]
36. Peters, G.; Fischer, B.; Clemens, M. Rain Attenuation of Radar Echoes Considering Finite-Range Resolution and Using Drop Size Distributions. *J. Atmos. Ocean. Technol.* **2010**, *27*, 829–842. [CrossRef]
37. Prahl, S. Miepython. Available online: https://miepython.readthedocs.io/ (accessed on 1 July 2021).
38. Wiscombe, W.J. Improved Mie scattering algorithms. *Appl. Opt.* **1980**, *19*, 1505–1509. [CrossRef]
39. Cha, J.-W.; Chang, K.-H.; Yum, S.S.; Choi, Y.-J. Comparison of the bright band characteristics measured by Micro Rain Radar (MRR) at a mountain and a coastal site in South Korea. *Adv. Atmos. Sci.* **2009**, *26*, 211–221. [CrossRef]
40. Nakano, M.; Takahashi, A.; Takahashi, S. Generalized exponential moving average (EMA) model with particle filtering and anomaly detection. *Expert Syst. Appl.* **2017**, *73*, 187–200. [CrossRef]

41. Brast, M.; Markmann, P. Detecting the Melting Layer with a Micro Rain Radar Using a Neural Network Approach. *Atmos. Meas. Tech.* **2020**, *13*, 6645–6656. [CrossRef]
42. Lee, J.-E.; Jung, S.-H.; Kwon, S. Characteristics of the Bright Band Based on Quasi-Vertical Profiles of Polarimetric Observations from an S-Band Weather Radar Network. *Remote Sens.* **2020**, *12*, 4061. [CrossRef]
43. Kneifel, S.; Maahn, M.; Peters, G.; Simmer, C. Observation of snowfall with a low-power FM-CW K-band radar (Micro Rain Radar). *Meteorol. Atmos. Phys.* **2011**. [CrossRef]
44. Kneifel, S.; Kulie, M.S.; Bennartz, R. A triple-frequency approach to retrieve microphysical snowfall parameters. *J. Geophys. Res. Atmos.* **2011**, *116*, D11203. [CrossRef]

Capítol 3

Classificació d'hidrometeors mitjançant observacions de Micro Rain Radar

3.1. Desenvolupament d'una metodologia de classificació d'hidrometeors (RaProM)

3.1.1. Resum

El tipus de precipitació és una informació de gran importància per les aplicacions hidrometeorològiques i estudis de processos microfísics associats a la precipitació. En aquest treball s'ha implementat una metodologia simplificada de classificació del tipus d'hidrometeor en funció de la velocitat trobada amb el radar en incidència vertical i la velocitat que disposa l'hidrometeor en funció del seu tipus determinats gràcies a la reflectivitat equivalent (Atlas et al. 1973). Durant el desenvolupament de la metodologia s'ha realitzat un nou processament del senyal cru obtingut per l'equip on es millora la relació de senyal soroll així com es minimitza el problema de l'aliàsing amb la metodologia detallada a Maahn and Kollias (2012).

3.1.2. Article

Garcia-Benadi, A.; Bech, J.; Gonzalez, S.; Udina, M.; Codina, B.; Georgis, J.-F. Precipitation Type Classification of Micro Rain Radar Data Using an Improved Doppler Spectral Processing Methodology. *Remote Sens.* **2020**, *12*, 4113. https://doi.org/10.3390/rs12244113

remote sensing

MDPI

Article

Precipitation Type Classification of Micro Rain Radar Data Using an Improved Doppler Spectral Processing Methodology

Albert Garcia-Benadi [1,2,*], Joan Bech [1], Sergi Gonzalez [3], Mireia Udina [1], Bernat Codina [1] and Jean-François Georgis [4]

1 Department Applied Physics—Meteorology, Universitat de Barcelona, 08028 Barcelona, Spain; joan.bech@ub.edu (J.B.); mudina@meteo.ub.edu (M.U.); bcodina@ub.edu (B.C.)
2 SARTI, Universitat Politècnica de Catalunya, 08800 Vilanova i la Geltrú, Spain
3 DT Catalonia, AEMET, 08005 Barcelona, Spain; sgonzalezh@aemet.es
4 Laboratory of Aerology, University of Toulouse/CNRS, 31400 Toulouse, France; jean-francois.georgis@aero.obs-mip.fr
* Correspondence: albert.garcia@meteo.ub.edu

Received: 17 November 2020; Accepted: 14 December 2020; Published: 16 December 2020

Abstract: This paper describes a methodology for processing spectral raw data from Micro Rain Radar (MRR), a K-band vertically pointing Doppler radar designed to observe precipitation profiles. The objective is to provide a set of radar integral parameters and derived variables, including a precipitation type classification. The methodology first includes an improved noise level determination, peak signal detection and Doppler dealiasing, allowing us to consider the upward movements of precipitation particles. A second step computes for each of the height bin radar moments, such as equivalent reflectivity (Z_e), average Doppler vertical speed (W), spectral width (σ), the skewness and kurtosis. A third step performs a precipitation type classification for each bin height, considering snow, drizzle, rain, hail, and mixed (rain and snow or graupel). For liquid precipitation types, additional variables are computed, such as liquid water content (LWC), rain rate (RR), or gamma distribution parameters, such as the liquid water content normalized intercept (N_w) or the mean mass-weighted raindrop diameter (D_m) to classify stratiform or convective rainfall regimes. The methodology is applied to data recorded at the Eastern Pyrenees mountains (NE Spain), first with a detailed case study where results are compared with different instruments and, finally, with a 32-day analysis where the hydrometeor classification is compared with co-located Parsivel disdrometer precipitation-type present weather observations. The hydrometeor classification is evaluated with contingency table scores, including Probability of Detection (POD), False Alarm Rate (FAR), and Odds Ratio Skill Score (ORSS). The results indicate a very good capacity of Method3 to distinguish rainfall and snow (PODs equal or greater than 0.97), satisfactory results for mixed and drizzle (PODs of 0.79 and 0.69) and acceptable for a reduced number of hail cases (0.55), with relatively low rate of false alarms and good skill compared to random chance in all cases (FAR < 0.30, ORSS > 0.70). The methodology is available as a Python language program called RaProM at the public github repository.

Keywords: Doppler radar; noise level; precipitation type classification; rainfall parameters; spectral processing

1. Introduction

Precipitation is a key component of the hydrological cycle and a precise knowledge of the precipitating hydrometeor type is essential for remote quantitative precipitation estimates either from

scanning or from vertically pointing ground-based or spaceborne radars. Precipitation observations of vertically pointing Doppler radars allow us to estimate the fall speed of hydrometeor particles which, in general, are the sum of their terminal fall speed and vertical air velocity (Atlas et al. [1], Hauser and Amayenc [2]). As it is well known, radar sensitivity to smaller particle detection increases with shorter wavelengths but, on the other hand, attenuation by intense precipitation, particularly rainfall, increases. Thus, a compromise exists between sensitivity and attenuation effects regarding the choice of operating frequency, a crucial aspect in radar design for different applications and platforms (Battaglia et al. [3], Kollias et al. [4]).

Unlike usual ground-based scanning precipitation weather radars operating at cm frequencies (S, C or X-band), Doppler radar profilers do not provide the precipitation field over a wide area, but a high spatial and temporal resolution vertical profile over the radar location. This approach has been employed for decades to study fine-scale vertical precipitation characteristics, for instance with the NOAA Aeronomy Laboratory S-band Doppler profiler (Ecklund et al. [5]), the X-band Precipitation Occurrence Sensor System (POSS, Sheppard [6]), the K-band Micro Rain Radar (MRR, Löffler-Mang et al. [7], Peters et al. [8]), and more recently, with shorter wavelength radars traditionally used for cloud studies, such as the Ka-band ARM zenith radar (Chandra et al. [9]) or the Milešovka observatory Ka-band cloud radar (Sokol et al. [10,11]), used to derive a hydrometeor classification, including four precipitation types. A related application has been the use of lidar observations from the NASA MPLNET network to resolve weak precipitation profiles (Lolli et al. [12,13]), particularly suited for light rain, drizzle and virga, as if more intense precipitation exists, attenuation becomes too important.

Among the above-mentioned Doppler radar profilers, the MRR stands out. This has been extensively used for a wide range of applications, including microphysical analysis of rainfall characteristics using collocated ground disdrometers (Adirosi et al. [14,15], Chang et al. [16], Gonzalez et al. [17], Jass et al. [18], Luo et al. [19], Tokay et al. [20]), diurnal and precipitation characteristics at low-latitude mountains (Bendix et al. [21], Seidel et al. [22]), orographic effects and low-level seeder-feeder processes (Arulraj and Barros [23]), bright-band (BB) radar signatures (Cha et al. [24], Brast and Markmann [25]), or the monitoring of absolute calibration of C-band polarimetric weather radars (Frech et al. [26]). Many of these applications rely on the separation of the liquid to solid precipitation phase, for example above and below the BB, which is crucial for accurate quantitative precipitation estimates (Fabry and Zawadzki [27], Sanchez-Diezma et al. [28], Bordoy et al. [29]). A recent study by Makino et al. [30] described the use of MRR to predict the hydrometeor type at ground level. However, to our best knowledge, no methodology based on MRR data to partition precipitation profiles in different hydrometeor types has yet been described. Such methodologies have been developed and improved in recent years for polarimetric scanning precipitation radars (see, for instance, Ryzhkov et al. [31], Park et al. [32], Schuur et al. [33], Dolan et al. [34], Chandrasekar et al. [35], Besic et al. [36]).

MRR units produce so-called raw data files, with spectral Doppler density data, which may be processed with the MRR manufacturer software (Metek [37], hereafter Method1) to obtain derived products, such as radar reflectivity Z, Doppler fall speed w or spectral width σ. Alternatively, researchers may develop their own MRR raw data processing, such as the methodology by Maahn and Kollias [38] which improves sensitivity and Doppler dealiasing and is suited for snowfall precipitation. This methodology is freely available as a Python program, called ImproToo (hereafter Method2).

The objective of this article is threefold. First, to present a novel MRR processing methodology, called RaProM (hereafter Method3), which includes enhanced spectral processing and Doppler dealiasing, a simplified novel hydrometeor classification scheme based on the assumption that the air vertical velocity is negligible compared to the precipitation particle speed, including drizzle, rain, snow, and hail, plus additional variables depending on the precipitation type. Second, to illustrate the methodology with a detailed case study, where results are compared with those from Method1 and Method2 and other co-located instruments, such as a Particle Size and Velocity (Parsivel) disdrometer or a microwave radiometer. Third, an evaluation of the hydrometeor type classification at the lowest

MRR height bin compared with Parsivel present weather precipitation type observations recorded in 32 days.

The rest of the article is organized as follows. Section 2 introduces the instruments and location considered in this study, on the Eastern Pyrenees (NE Spain). Section 3 describes the new methodology proposed, dealing with spectral data processing with a multi peak detection procedure and details the derivation of spectral moments, hydrometeor classification and derived parameters. Section 4 presents a case study comparing, in detail, previous MRR processing methodologies and data from additional instruments and also provides the evaluation of the hydrometeor precipitation classification using contingency table scores and, finally, Section 5 presents a discussion and conclusion of the achievements and limitations of the proposed methodology and ideas for further research.

2. Instruments and Site Description

A Micro Rain Radar (MRR) is a compact frequency modulated continuous wave (FMCW) vertically pointing Doppler radar operating at 24.23 GHz, manufactured by Meteorologische Messtechnik GmbH (Metek) [37], which recently is manufacturing a newer version, the MRR-PRO. A summary of technical features of the MRR used here is given in Table 1. In this study, an MRR2 model was used and the range gate resolution was set to 100 m so observations extended up to 3.1 km above ground level. The unit was equipped with a heated antenna which prevented the accumulation of snow. Due to the relatively high operating frequency, possible attenuation by precipitation had to be checked for the data set analyzed.

Table 1. Main features from MRR.

Frequency (GHz)	24.23
Radar Type	FMCW
Number of range gates	32
Number of spectral bins	64
Range resolution (m)	10–200
Frequency sampling (kHz)	125

Other instruments used here were a laser-optical disdrometer OTT Parsivel, a microwave radiometer RPG HATPRO (MWR) and two Automatic Weather Stations (AWSs) of the Meteorological Service of Catalonia [39]—see Supplementary Materials Table S1. All these instruments were deployed for the Cerdanya-2017 field campaign at the Das aerodrome (OACI code: LECD) in the Eastern Pyrenees mountain massif from December 2016 to April 2017. Part of the study makes use of additional data collected at the same site during the period 2018 and 2019 by the MRR and Parsivel disdrometer. The location is a relatively wide valley oriented west to east, with limited radar coverage due to orographic beam blockage (Bech et al. [40], Trapero et al. [41]) so most of the MRR beam cannot be directly compared with existing ground-based weather radar observations. The Cerdanya-2017 field campaign aimed at studying various complex terrain phenomena, including cold pool formation, mountain waves and orographic precipitation—see Gonzalez et al. [17]; Udina et al. [42] for more details.

The disdrometer records hydrometeor fall speed and size spectra at ground level and other derived variables, such as hydrometeor type (e.g., rain or snow), radar reflectivity factor and precipitation intensity for liquid precipitation, among others. The microwave radiometer provides air temperature vertical profiles so the freezing level and other isotherm levels can be calculated. The two AWS are located close or near the MRR location (at the same aerodrome and nearby but a higher altitude, see Figure S1 in Supplementary Materials) and provide independent measurements of temperature, precipitation and snow depth level.

Remote Sens. **2020**, *12*, 4113 4 of 23

3. New Methodology Proposed

The methodology has two different sections. The spectral data processing is detailed in the first section, and the equations and hypotheses are treated in the second section.

3.1. Spectral Data Processing

The initial processing stage of Method3 consists in the MRR spectral data processing and follows the flow chart described in Figure 1. The first step is to transform the original signal backscattered by hydrometeors to spectral reflectivity (η) following the equation proposed by the manufacturer (Metek [37]):

$$\eta(n,i) = f(n,i) \cdot \frac{i^2}{TF(i)} \cdot \frac{C \cdot \Delta h}{10^{20}}, \quad (1)$$

where i is the range gate number ($i = 0, \ldots, 31$), n is Doppler bin number ($n = 0, \ldots, 63$), $f(n,i)$ is the original MRR signal saved in the so-called raw data files, $TF(i)$ is a transfer function specific for each height, C is the radar calibration constant and Δh is the range resolution in m. The spectral reflectivity $\eta(n,i)$ has units of m^{-1} and $TF(i)$ and C are stored in the original raw data files.

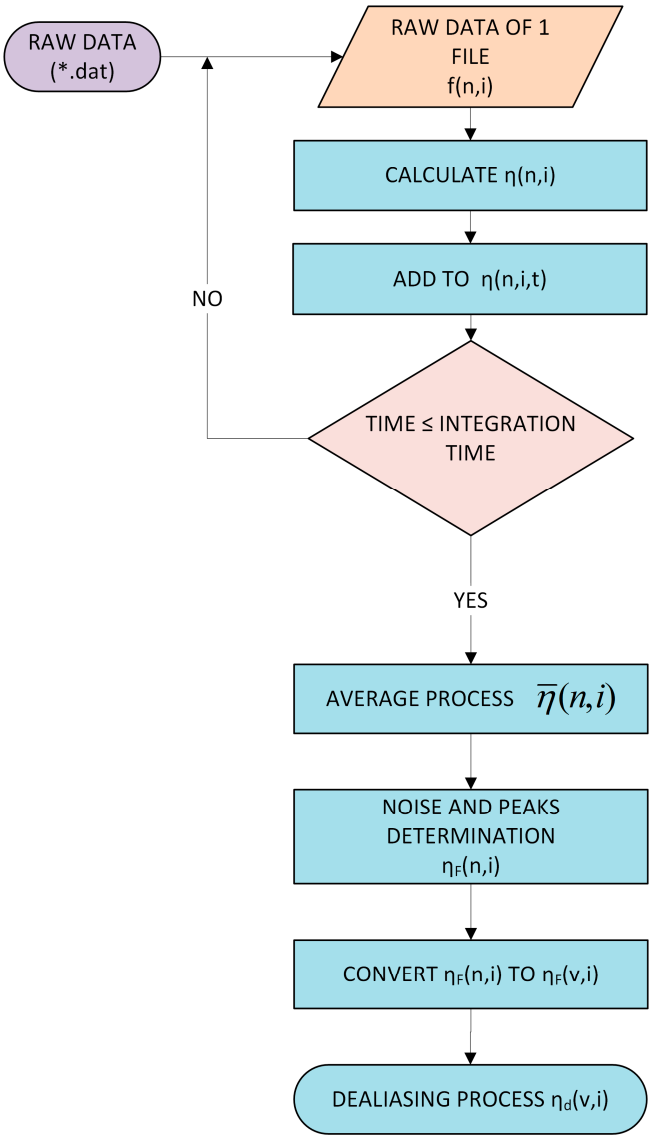

Figure 1. Flowchart of the MRR spectral data processing.

The innovations introduced in Method3 are the modification of the integration time, the average of spectra and the determination of maxima (peaks) in the signal. The integration time, usually set to 60 s, is now selectable by the user. Method3 performs the averaging of the spectrum checking that at least 50% of spectra contain a minimum valid signal. The 50% threshold is a value modifiable by the user on the code of Method3. The signal is considered valid if it verifies the Hildebrand and Sekhon [43] criterion:

$$\frac{\overline{\eta}^2}{var(\eta)} = \frac{\left(\frac{\sum \eta(n)}{N}\right)^2}{\frac{\sum(\eta-\overline{\eta})^2}{N}} < 60\,, \tag{2}$$

where $var(\eta)$ is the spectral reflectivity variance and N the number of Doppler bins considered.

The detection of the maxima of the signal at a given height consists in using all Doppler bins of the spectrum except the first and the last one, therefore all possible fall speed values are used, except the lowest and the highest. This approach allows us to recover more than one single peak of the signal more easily and provides more detail about the hydrometeor fall speed distribution potentially affected by noise in the lowest range bin, the closest one to the ground, which is excluded, as in Method1. Note that Method2, instead, excludes part of the highest and lowest Doppler bins, and discards the 3 lowest-range bins. The noise level is calculated for each height following the scheme detailed by the manufacturer [37], which implies subtracting the noise level to the signal.

Figure 2 shows two examples of noise subtraction and peak detection using Method3 applied to the lowest processed range bin (i = 1, here from 100 to 200 m a.g.l.) and the ninth range bin (i = 10, from 900 to 1000 m a.g.l.). Figure 2a,b display a single peak detection and Figure 2c,d a two peak detection. Note that these detections could not be possible with Method2, as it discards the 100 m to 200 m bin height (panels a and b) and does not consider all Doppler bins processed by Method3.

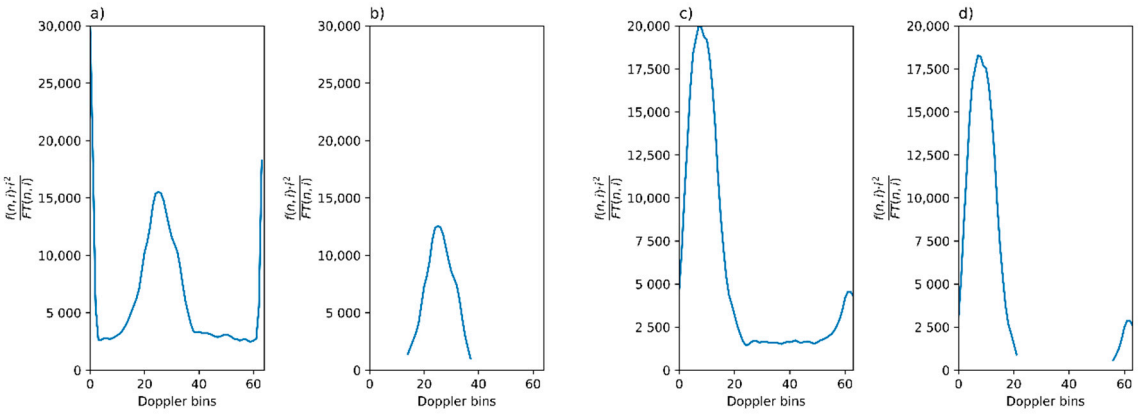

Figure 2. Examples of Method3 noise subtraction and signal detection: single peak (**a**,**b** panels) and multi-peak (**c**,**d** panels). (**a**,**c**) show the original Doppler signal from raw file and (**b**,**d**) show the noise subtraction and signal detection. The (**a**) case was recorded at the first height bin (100 to 200 m a.g.l.) and the (**c**) case at the ninth height bin (900 to 1000 m a.g.l.).

The next step is the conversion of the reflectivity spectra from n Doppler bins to velocity v according to Equation (3). Note that this transformation depends on specific MRR2 data acquisition features, such as wavelength or sampling frequency:

$$\eta(v,i) = \eta(n,i)\cdot\left(\frac{f_{sampling}}{2\cdot n_{max}\cdot i_{max}}\cdot\frac{\lambda}{2}\right)^{-1}, \tag{3}$$

where $f_{sampling}$ is 125 kHz, n_{max} is 64, i_{max} is 32 and λ is the wavelength (~1.24 cm).

The last step in the spectral processing of Method3 implements a dealiasing scheme, partly based on Kneifel et al. [44] who noticed that in some snowfall cases, MRR2 provided unrealistically high

values of hydrometeor fall speed, much higher than terminal snowflake fall speeds. This was due to two assumptions of the original manufacturer software: (i) precipitation observed was always in liquid form, so there was an inherent dependence between hydrometeor terminal fall speed versus particle diameter and (ii) only downward velocities were allowed, which is the most usual situation but is not always the case for snowflakes or convective rainfall. The snowfall case is discussed in Maahn and Kollias [38] and a dealiasing system to solve it is implemented in Method2. The dealiasing scheme proposed in Method3 consists in, for a given height, combining information from spectra of adjacent (upper and lower) height levels to determine the hydrometeors' fall speeds to extend the original speed range from 0 to 12 m/s to a dealiased range of −12 to 24 m/s. The lower-level spectra are used to expand the speed range to −12 to 0 m/s and the upper one to 12 to 24 m/s. The vertical continuity of the speed profile is used to provide the dealiased speed spectra, as illustrated in the example displayed in Figure 3. The Method2 dealiasing scheme works well for snowfall and finds possible snowflake upward movements but does not work properly for cases of intense rainfall with hydrometeor falling velocities greater than 8 m/s, unlike the proposed scheme implemented in Method3.

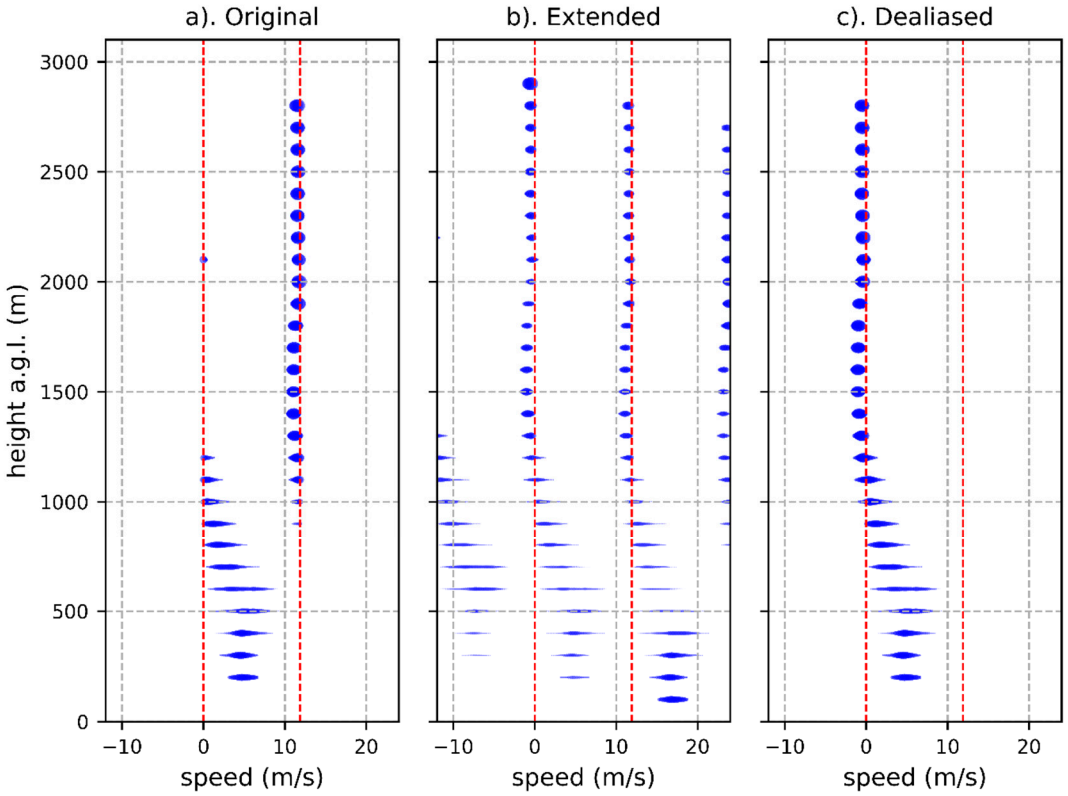

Figure 3. Spectral reflectivity after noise extraction of Doppler spectrum with Method3 on 27 March 2017 12:18 UTC. (**a**) Original spectral reflectivity after peaks and noise determination. (**b**) Extended spectral reflectivity from height bin $i-1$, i and $i+1$. (**c**) Dealiased Method3 spectral reflectivity. The blue symbol thickness is proportional to their contribution to the total Doppler spectrum for each height bin. The red dashed vertical lines indicate the original Nyquist velocity interval (from 0 to 12 m/s).

3.2. Parameters Calculation

Once Method3 spectral processing is completed, data are ready to proceed with the calculation of subsequent parameters, which is divided in two parts. The first part computes the basic Doppler radar parameters: the Doppler velocity, which is assumed here to be the hydrometeor fall speed, and the radar equivalent reflectivity factor. The second part provides an estimation of hydrometeor type and based on this, the calculation of derived parameters, such as precipitation rates for different precipitation types. Figure 4 provides an overview of parameters calculations.

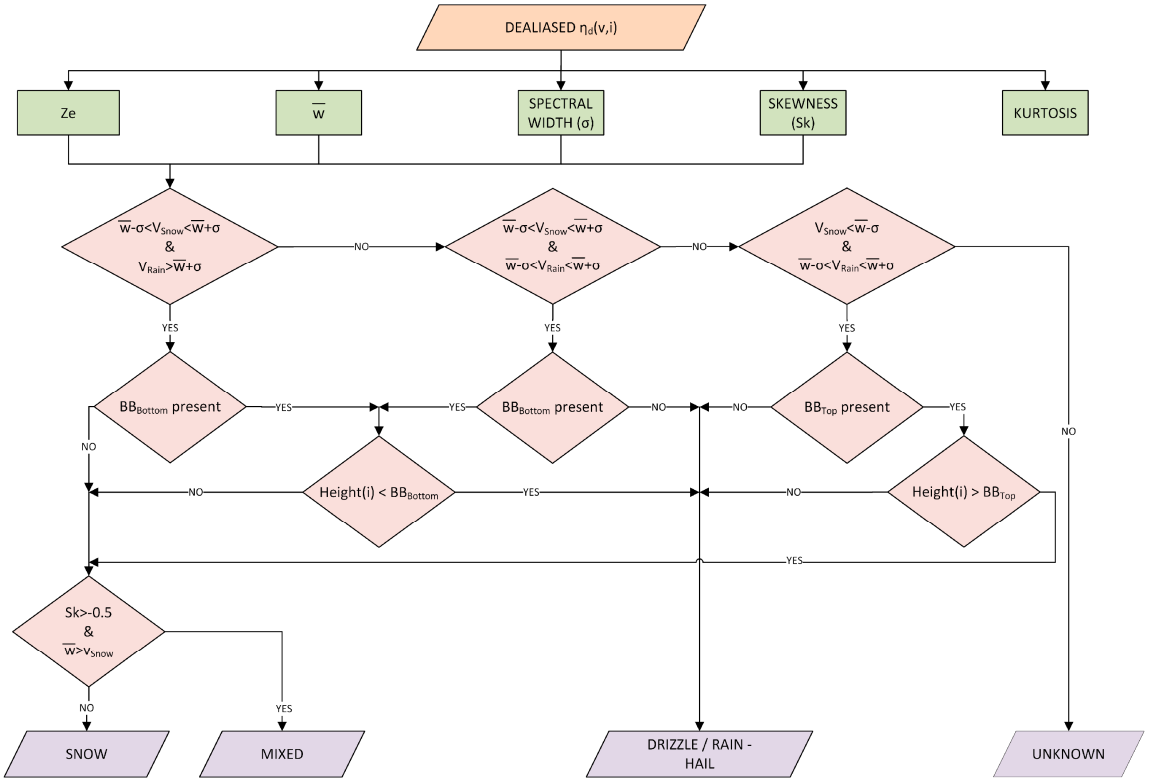

Figure 4. Flowchart of parameters calculation (effective reflectivity, fall speed, spectral width, skewness and kurtosis) and subsequent estimation without assuming any hypothesis between terminal fall speed and particle diameter of precipitation type into snow, m, drizzle/rain—hail and unknown.

3.2.1. Basic Parameters

The term basic parameters are applied here to integral parameters which can be calculated independent of the type of hydrometeor as they only depend on the spectral reflectivity. The parameters are the radar equivalent reflectivity (Z_e), the Doppler velocity, which here corresponds to the mean fall speed of hydrometeors ($\overline{w}$), and higher order moments of the Doppler speed distributions: Doppler spectral width (σ), skewness and kurtosis as described in Equations (4)–(8):

$$Z_e = 10^{18} \cdot \frac{\lambda^4}{\pi^5} \cdot \frac{1}{|K|^2} \cdot \Delta v \cdot \sum \eta(v), \tag{4}$$

$$\overline{w} = \frac{\sum \eta(v,i) \cdot v(i)}{\sum \eta(v,i)} \tag{5}$$

$$\sigma = \sqrt{\frac{\sum \eta(v,i) \cdot (v(i) - w)^2}{\sum \eta(v,i)}} \tag{6}$$

$$skewness = \frac{\sum \eta(v,i) \cdot (v(i) - w)^3}{\sum \eta(v,i) \cdot \sigma^3} \tag{7}$$

$$kurtosis = \frac{\sum \eta(v,i) \cdot (v(i) - w)^4}{\sum \eta(v,i) \cdot \sigma^4} \tag{8}$$

Note that the calculation of the radar equivalent reflectivity does not take into account possible attenuation effects which may be relevant for high precipitation rates, considering that MRR operates at the K-band. However, this can be handled in the case of liquid hydrometeors, where the path attenuation is calculated (see Section 3.2.4).

3.2.2. Hydrometeor Type Classification

As mentioned earlier, there are a number of hydrometeor classification algorithms developed mainly for scanning polarimetric weather radars, some considering up to 10 different precipitation species. Here, a simplified approach is adopted aiming to distinguish, for each height bin, 5 possible precipitation types: drizzle, rain, snow, mixed and hail. For the purpose of this paper, we consider either wet snow, a mixture of snow and rain, or graupel in the mixed category.

The classification is based on a decision tree, considering empirical relations between hydrometeor fall speed and equivalent radar reflectivity, size and particle diameter characteristics for different hydrometeors and the existence or absence of the bright band. As a starting point, the empirical relations reported by Atlas et al. [1], linking radar reflectivity and fall speeds of rain (v_{Rain}) and snow (v_{Snow}) in the absence of bright band, are considered:

$$v_{Rain} = 2.65 \cdot Ze^{0.114} \quad (9)$$

$$v_{Snow} = 0.817 \cdot Ze^{0.063} \quad (10)$$

These relationships are used to compute, given Z_e, v_{Rain} and v_{Snow}, which are the average fall speed expected for each precipitation type on those two cases. Additional parameters considered are the mean Doppler fall speed $\overline{w}$, the Doppler spectral width σ and the Skewness Sk, calculated for each height bin. Moreover, a BB detection scheme is used (Cha et al. [24]). In case there is BB, then the existence and height of its top (BB_{Top}) and bottom (BB_{Bottom}) levels are computed, following the methodology described by Wang et al. [45]. From all the above, the decision tree can be grouped in three main branches with additional conditions (Figure 4):

1. If v_{Snow} is within the interval $\overline{w} \pm \sigma$ and v_{Rain} exceeds $\overline{w} + \sigma$, then:
   - If the bin height is lower than the BB_{Bottom}, the hydrometeor is classified as: Drizzle/Rain—Hail.
   - If the bin height is equal or above the BB_{Bottom} or BB_{Bottom} is not present: Mixed: if Sk > −0.5 and $\overline{w}v_{Snow}$; Snow: otherwise.
2. If v_{Rain} and v_{Snow} are within the interval $\overline{w} \pm \sigma$, then:
   - If the bin height is below the BB_{Bottom} or BB_{Bottom} is not present: Drizzle/Rain—Hail.
   - If the bin height is above the BB_{Bottom}: Mixed: if the Sk > −0.5 and the $\overline{w}v_{Snow}$; Snow: otherwise.
3. If v_{Rain} is within the interval $\overline{w} \pm \sigma$ and v_{Snow} is lower than $\overline{w} - \sigma$, then:
   - If the bin height is below the BB_{Top} or BB_{Top} is not present: Drizzle/Rain—Hail.
   - If the bin height is above the BB_{Top}: Mixed: if the Sk > −0.5 and the $\overline{w}v_{Snow}$; Snow: otherwise.
4. Cases not included in any of the previous categories are labelled as unknown.

The category "Drizzle/Rain—Hail" is further disaggregated considering additional conditions (Figure 5). The basic criteria stem from the precipitation hydrometeor definitions. Drizzle and rain are formed only by liquid particles AMS (2020) [46,47] and are here distinguished by their skewness Sk in their fall speed distribution and for Z_e differences (ΔZ_e) between levels. According to Acquistapace et al. [48], if skewness (Sk) is lower than or equal to −0.5 and $\Delta Z_e \geq 1$ dBZ, then the hydrometeor is classified as drizzle and otherwise as rain. Hail is defined in the function of the maximum diameter on the Doppler velocity spectrum, considering here a threshold of maximum diameters greater than 5 mm. Snow and mixed class are stratified when the height is below the BB_{Bottom} as described by Kalesse et al. [49].

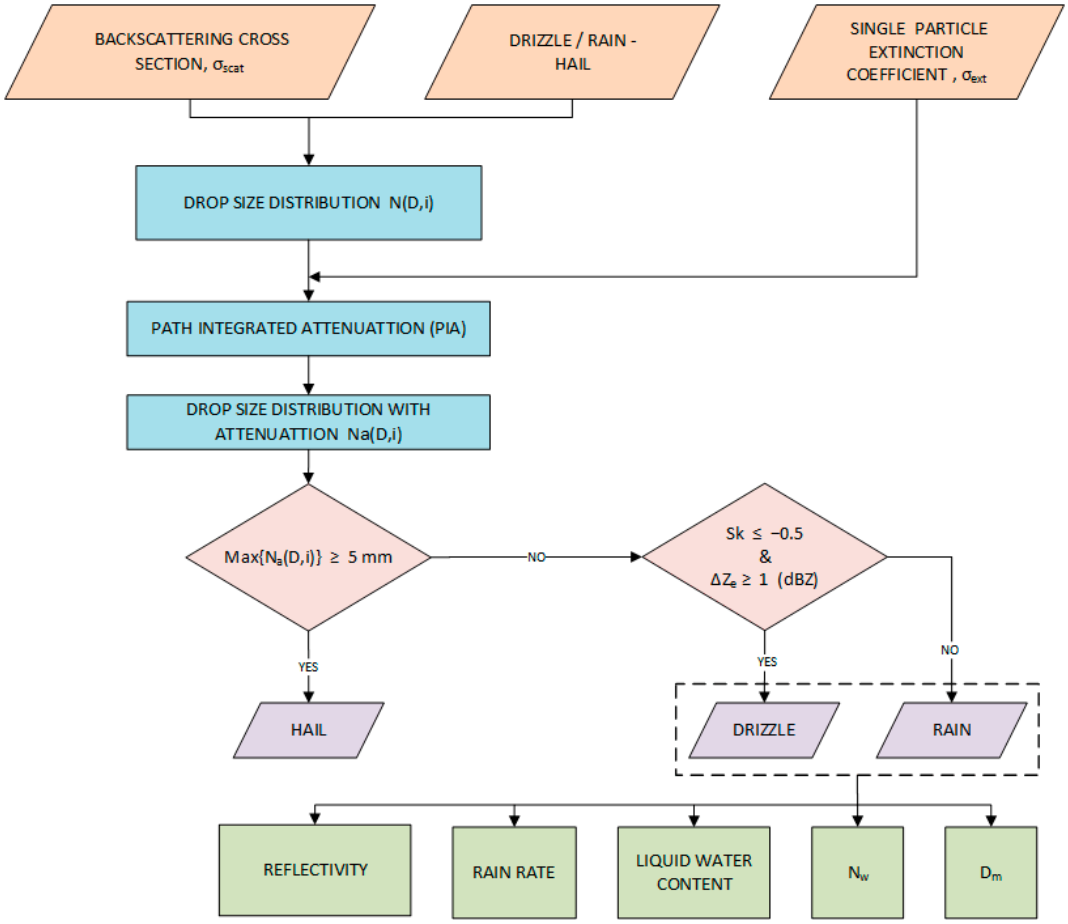

Figure 5. Flowchart of parameter calculation assuming Mie backscattering regime and the estimation of precipitation type (hail, drizzle and rain).

3.2.3. Snowfall Rate

Despite solid precipitation presents a greater variability than liquid precipitation, Matrosov and Heymsfield [50] studied the relation between equivalent radar reflectivity and snowfall rate at different wavelengths and proposed empirical relations between those variables. In particular, snowfall rate (SR) can be estimated from Z_e by inverting the Z_e–SR power–law relationship:

$$SR = \left(\frac{Z_e}{a}\right)^{1/b} \tag{11}$$

where SR is in mm/h, Z_e in mm^6 m^{-3}, a and b are the coefficients from the corresponding Z_e–SR relation and their values, for K band, are 56.00 and 1.20. It should be noted that the estimated SR might differ from actual values, given the high variability of the mass–size relation of different snow particles, as discussed in Souverijns et al. [51].

3.2.4. Rainfall Parameters from Drizzle/Rain

Rainfall parameters can be calculated if hydrometeors are in liquid phase. Section 3.2.2 details that the Drizzle/Rain types are liquid hydrometeors, thus on these types the rainfall parameters are calculated, but it is also necessary to introduce a dependence between the hydrometeor terminal fall

speed and the diameter of the hydrometeor, which implies the hydrometeor particle size distribution (N) for each n Doppler bin and height level i:

$$N_{n,i}(D_n) = \frac{\eta(D)}{\sigma_{n,i}} \tag{12}$$

where $\eta(D)$ is the spectral reflectivity as a function of the diameter and $\sigma_{n,i}$ is the Mie backscattering cross section for liquid spherical particles. Note that the initial spectral reflectivity is only a function of the fall speed using the relation between Doppler bins n. The spectral reflectivity as a function of the raindrop diameter is determined using the Gunn and Kinzer [52] expression, which relates the fall speed with the raindrop diameter plus a correction factor for the fall speed $\delta v(h)$ that takes into account air density changes with height:

$$\eta(D,i)\left[\mathrm{ms^{-1}mm^{-1}}\right] = \eta(v,i)\cdot 6.18\cdot\delta v(i\cdot\Delta h)\cdot e^{-0.6\ \mathrm{mm^{-1}}\cdot D[\mathrm{mm}]} \tag{13}$$

where D is expressed in mm and $\eta(D,i)$ is in m s^{-1} mm^{-1}. The correction factor $\delta v(h)$ is computed assuming the US Standard Atmosphere and a second order approximation following Foote and Du Toit [53]

$$\delta v(h) = \left(1 + 3.68\cdot 10^{-5}\cdot h + 1.71\cdot 10^{-9}\cdot h^2\right) \tag{14}$$

So, the corrected terminal fall speed as a function of drop diameter and height is:

$$v(D)[\mathrm{m/s}] = \delta v(h)\cdot\left(9.65 - 10.3\cdot e^{-0.6\ \mathrm{mm^{-1}}\cdot D[\mathrm{mm}]}\right) \quad \text{for } 0.109\ \mathrm{mm} \le D \le 6\ \mathrm{mm} \tag{15}$$

After the drop size distribution is determined, the Path Integrated Attenuation (PIA) is determined using the approach detailed in Metek [37], wherein the single particle extinction coefficient is necessary. The result is the drop size distribution with attenuation correction ($Na(D,i)$) which allows us to calculate the reflectivity (Z), the liquid water content (LWC), and the rain rate (RR):

$$Z = \sum Na_n\cdot {D_n}^6\cdot\Delta D \tag{16}$$

$$LWC = \rho_w\cdot\frac{\pi}{6}\cdot\sum Na_n\cdot {D_n}^3\cdot\Delta D \tag{17}$$

$$RR = \frac{\pi}{6}\cdot\sum Na_n\cdot {D_n}^3\cdot v(D)\cdot\Delta D \tag{18}$$

Following Thurai et al. [54], Method3 implements the calculation of the mean mass-weighted raindrop diameter (D_m) and the intercept parameter of the gamma distribution normalized to the liquid water content (N_w), where it is assumed that D_0 is equal to D_m:

$$D_m = \frac{\sum Na_n\cdot {D_n}^4\cdot\Delta D}{\sum Na_n\cdot {D_n}^3\cdot\Delta D} \tag{19}$$

$$N_w = \frac{256}{\pi\cdot\rho_w}\cdot\frac{LWC}{D_m^4} \tag{20}$$

These parameters are useful for discriminating between convective and stratiform rainfall, as discussed later.

4. Results

The results are divided into two parts. The first part examines a case study to assess the characteristics of Method3, compared with Method1 and Method2. In the second part, an objective validation of the hydrometeor classification is performed to show the performance of Method3 to distinguish different types of precipitation.

4.1. Case Study

The performance of the new methodology proposed (Method3) is assessed during a precipitation event, mostly stratiform, that took place on 27 March 2017. The event produced rainfall at Das AWS (4.9 mm) and 6.3 mm of equivalent rainfall amount, which fell as snow, at Malniu AWS located 1100 m aloft. These precipitation amounts are relatively modest in terms of daily amounts for the season and region (Gonzalez and Bech [55]). As the freezing level was about 750 m above ground, a substantial part of the profile observed was snow, which allows us to illustrate different features of Method3. The results are compared with Method1, Method2 and with data from other instruments—see Supplementary Materials Table S1. Comparisons may include different data subsets; for example, Method2 vs. Method3 profiles or Method3 lowest bin gate vs. disdrometer estimates.

4.1.1. Fall Speed

Precipitation fall speed profiles estimated with Method3 are displayed in Figure 6, overlaid with isotherm heights (0 °C, −10 °C and −20 °C levels), plus Parsivel fall speed at ground, indicating the consistency between the observations derived from the three independent instruments. On the one hand, a sharp increase in Method3 fall speed is generally observed below the 0 °C level, as expected when solid precipitation changes to liquid precipitation. On the other hand, the lowest Method3 height bin (100 m a.g.l.) presents fall speed values and temporal trends comparable to the Parsivel ones.

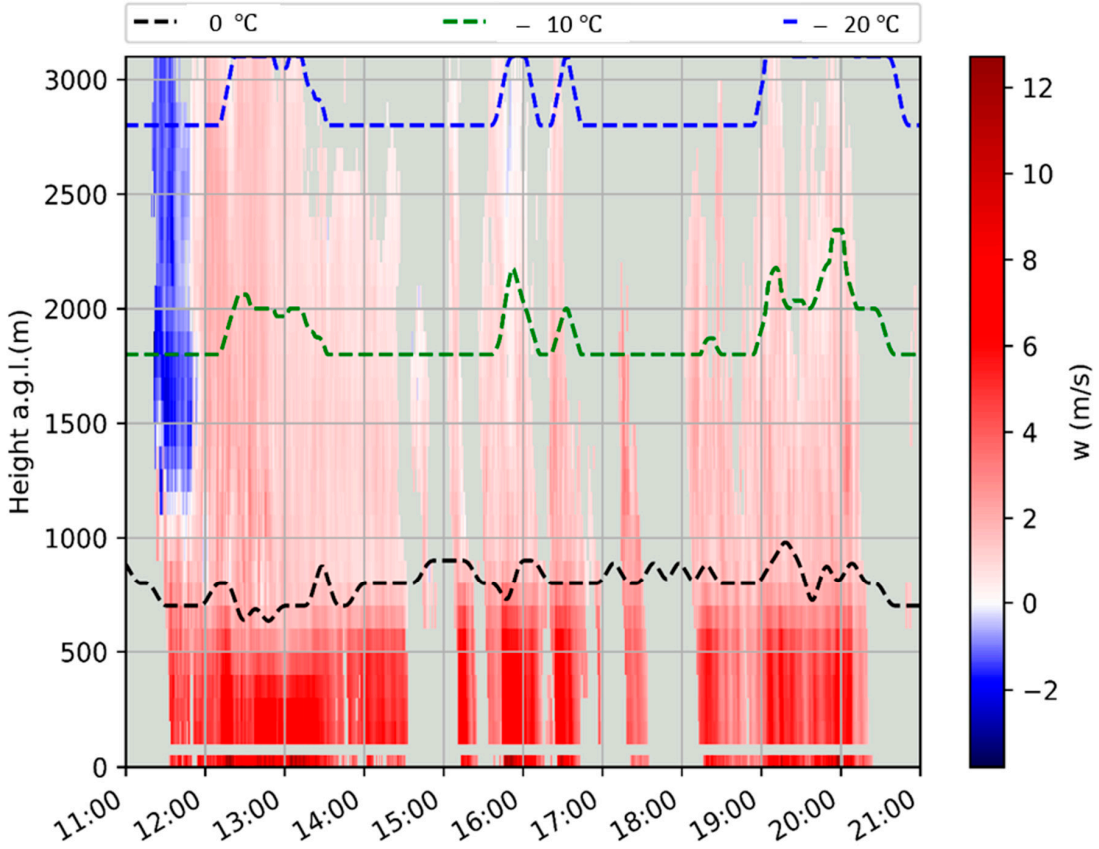

Figure 6. Fall speed height time indicator obtained from Method3 corresponding to 27 March 2017 overlaid with microwave radiometer derived isotherm levels of 0 °C, −10 °C and −20 °C and fall speed calculated from Disdrometer shown at bottom level (0 to 50 m a.g.l.). Downward fall speeds are defined positive.

The lowest range bin (100 m height) estimated with Method3 is compared with Parsivel measurements (Figure 7a). Some discrepancies are expected due to the different measurement principle

of each instrument and also the different heights compared. Both data sets compare reasonably well for speeds up to 8 m/s, and particularly well for 3 to 6 m/s fall speeds (note the higher density of data for that range, as shown in Figure 7a). All Method3 speeds are below 8 m/s, whereas disdrometer data exceed 12 m/s, so major discrepancies occur for disdrometer speeds above 8 m/s. This discrepancy could be partly due to raindrop coalescence in the lowest 100 m above ground level.

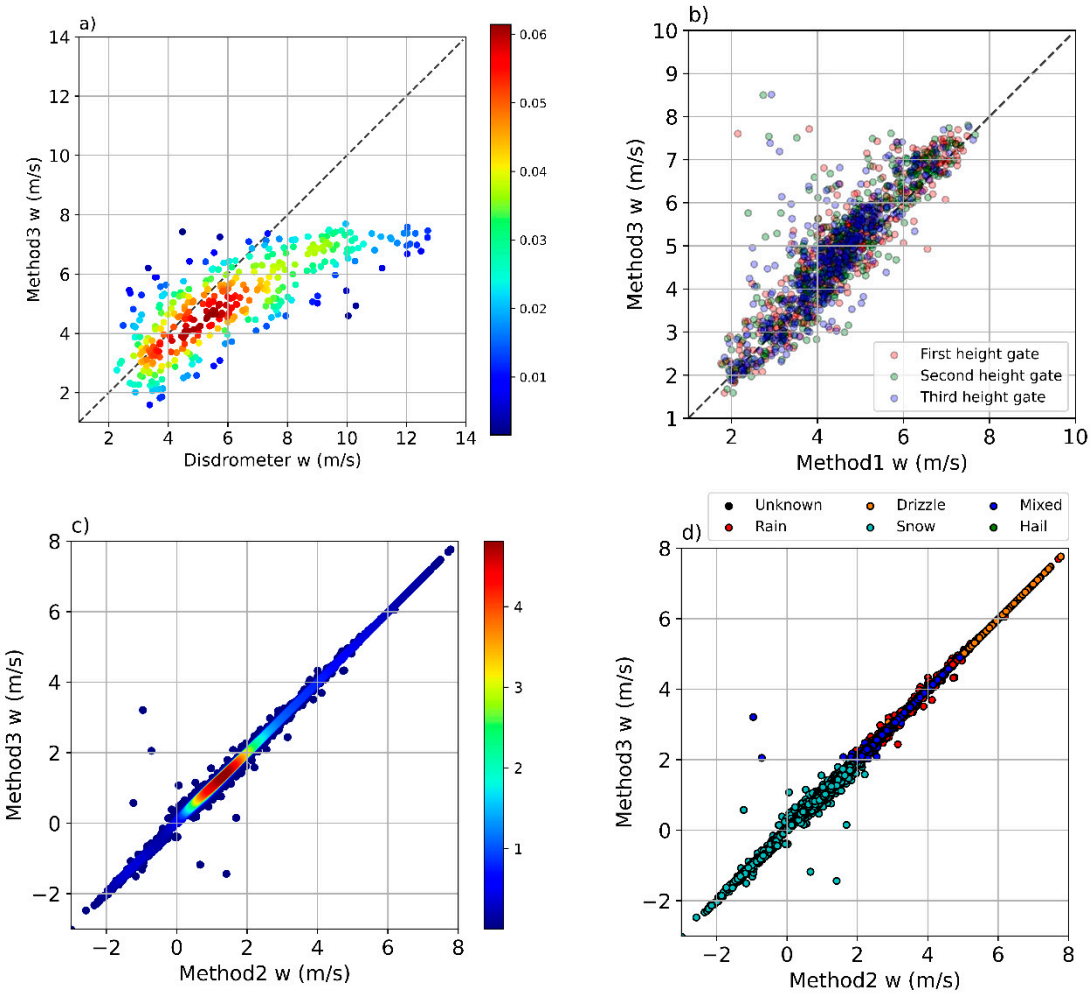

Figure 7. (**a**) Scatter plot of the proposed method (Method3) fall speed from the first height versus fall speed from disdrometer. (**b**) Fall speed comparison of the lowest three height bins between Method3 and Method1. (**c**) Scatter plot of fall speed from Method2 and Method3. (**d**) Similar to (**c**) but indicating different precipitation hydrometeor types. Color scales of panels (**a**,**c**) represent data density.

An analysis of the first three height bins obtained with Method3 is performed with a comparison with Method1 (Figure 7b). Note that Method2 cannot be included in this comparison as it discards the two lowest height bins. All negative fall speeds detected by Method1 are discarded according to the manufacturer approach, which assumes only positive values. The agreement found is generally good, with a few cases where Method3 overestimates Method1.

A comparison of profiles except for the lowest two bins not processed by Method2 is performed between Method2 and Method3 (Figure 7c). As displayed by the data density the fall speed agreement is generally good (R^2 of 0.995); however, a few cases present discrepancies, typical of the order of 1 m/s. Figure 7d shows a scatter plot between Method2 and Method3 where data are labelled to hydrometeor type classified by Method3 and illustrates that the largest discrepancies shown in Figure 7c are originated by snow and mixed cases.

The fall speed difference between the two methods, expressed here as:

$$\Delta w = w_{Method3} - w_{Method2}, \quad (21)$$

is further examined in terms of hydrometeor type according to the new hydrometeor classification methodology performed by Method3 and fall speed range, considering the different speed classes (Table 2). It can be seen that, for all classes, the absolute value of the mean error is equal or lower than 0.02 m/s. Moreover, a few snow and mixed cases present speed differences above 1 m/s. Root mean square errors are similar for all hydrometeor classes.

Table 2. Fall speed differences Δw between Method3 and Method2 stratified by speed values and hydrometeor type. Hail, mixed and unknown values were not found so only four hydrometeor classes (Rain, Drizzle, Mixed and Snow) are considered. Values listed correspond to number of height bins for each fall speed and hydrometeor class and mean error (ME) and root mean squared error (RMSE).

(m/s)	Rain	Drizzle	Mixed	Snow
$\|\Delta w\| < 1$	1142	88	1057	7441
$1 \leq \|\Delta w\| \leq 2$	0	0	0	4
$\|\Delta w\| > 2$	0	0	2	1
ME	−0.01	−0.02	0.00	0.01
RMSE	0.06	0.03	0.16	0.08

The distinct behavior of snow cases is also seen in Figure S2 in the Supplementary Materials, which shows the difference in distribution for the four hydrometeor types, shown in Table 2. Rain and mixed cases present similar quasi symmetric distribution patterns, while drizzle is much more leptokurtic and snow is platykurtic. The systematic differences between Method2 and Method3 may be due to differences in the spectral processing of the methods. However, note that these differences are very small in absolute value.

4.1.2. Equivalent Reflectivity

Equivalent reflectivity (Z_e) profiles obtained with Method3 are displayed with selected temperature levels (0 °C, –10 °C and –20 °C) retrieved from the microwave radiometer (MWR) and the reflectivity observed at ground-level by the disdrometer (Figure 8). It can be seen that the 0 °C level, around 750 m A.G.L., matches approximately with an abrupt increase in Z_e consistent with a bright band signature caused by the change from solid to liquid hydrometeors and an increase in the fall speed (shown previously). The disdrometer reflectivity is also consistent with the profiles and reproduces particularly well the timing of the local maxima (>25 dBZ).

A comparison of the reflectivities provided by Method3 at the lowest bin and the disdrometer is shown in Figure 9a, which indicates an overall agreement but a slight overestimation of the disdrometer compared to Method3 for values lower than 20 dBZ. The three lowest height bins provided by Method1 and Method3 present generally similar values (Figure 9b); however, some discrepancies are found in a few cases, mainly due to Method3 overestimating Method1. These variations appear because Method1 does not apply the dealiasing. Figure 9c shows a scatter plot comparing Method3 and Method2, which also show a good global agreement between the two methods (R^2 of 0.993), except in a few cases.

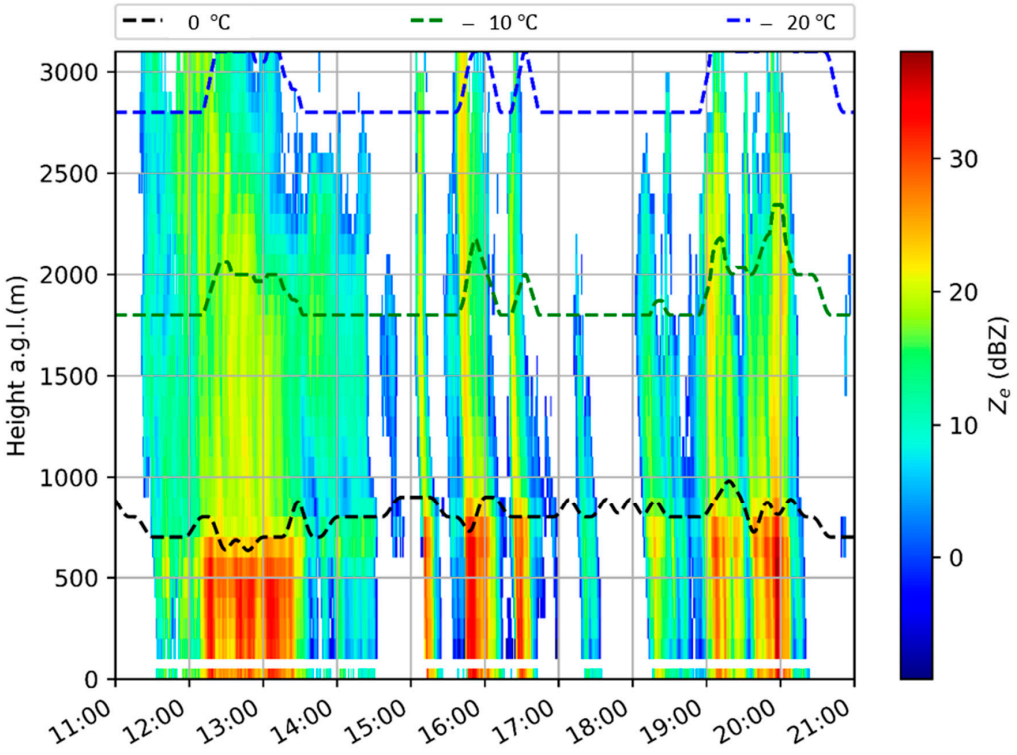

Figure 8. Equivalent reflectivity obtained from Method3 corresponding to 27 March 2017 overlaid with microwave radiometer-derived isotherm levels of 0, −10 and −20 °C and equivalent reflectivity calculated from Disdrometer, shown at bottom level (0 to 50 m a.g.l.).

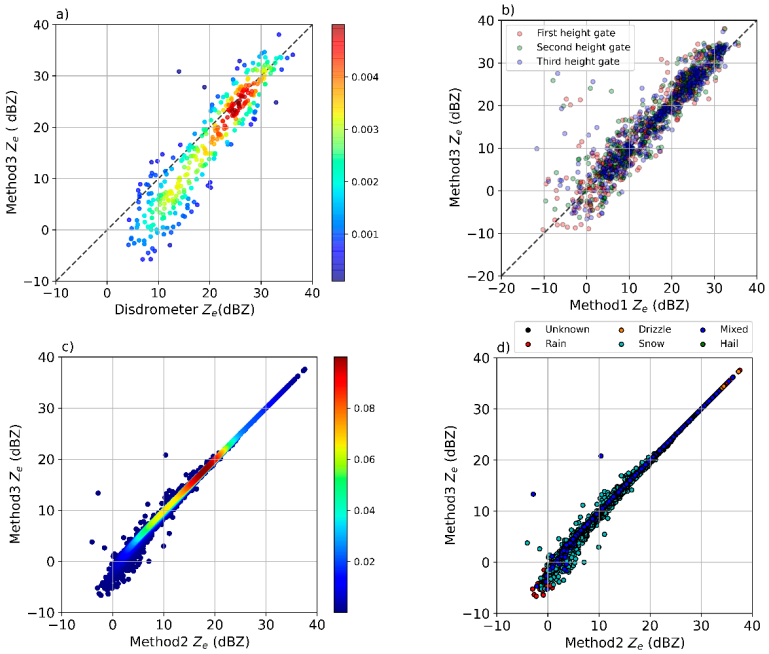

Figure 9. (**a**) Scatter plot of equivalent reflectivity (dBZ) from the Method3 lowest height bin and disdrometer data. (**b**) Comparison of equivalent reflectivity (dBZ) for the three lowest height bins from Method3 and Method1. (**c**) Scatter plot of equivalent reflectivity obtained with Method2 and Method3. (**d**) As (**c**) but indicating different precipitation hydrometeor types. Color scales of panels (**a**,**c**) represent data density.

Those discrepancies are examined in more detail by considering the difference ΔZ_e between the two methods:

$$\Delta Z_e = Z_{eMethod3} - Z_{eMethod2} \quad (22)$$

Aside from a few isolated snow and mixed cases, both snow and rain provide similar differences in terms of RMSE (~1 dB) and ME (~–0.40 dB), so Method3 provides slightly lower reflectivity values than Method2—see Table 3. Despite these similarities, the distribution of differences present distinct patterns, as highlighted in Figure S3 in the Supplementary Materials: they all present a mode value close to 0 dB but it is much less marked for snow than for others types.

Table 3. As Table 2 but for reflectivity differences ΔZ_e between Method3 and Method2.

(dBZ)	Rain	Drizzle	Mixed	Snow
$\|\Delta Z_e\| < 1$	1003	88	1023	6518
$1 \leq \|\Delta Z_e\| \leq 5$	135	0	32	914
$\|\Delta Z_e\| > 5$	4	0	4	14
ME	−0.38	−0.01	−0.14	−0.45
RMSE	1.28	0.04	0.75	0.80

4.1.3. Hydrometeor Classification

The evolution of the hydrometeor classification provided by Method3 is shown in Figure 10, overlaid with temperature levels (0, –10, –20 °C) from radiometer and Parsivel hydrometeor classification at ground level. Parsivel classification is derived from the World Meteorological Observations standard code 4677 used in surface synoptic observations (SYNOPs), grouped here as rain, drizzle, mixed, snow and hail (see details in Supplementary Materials Table S2).

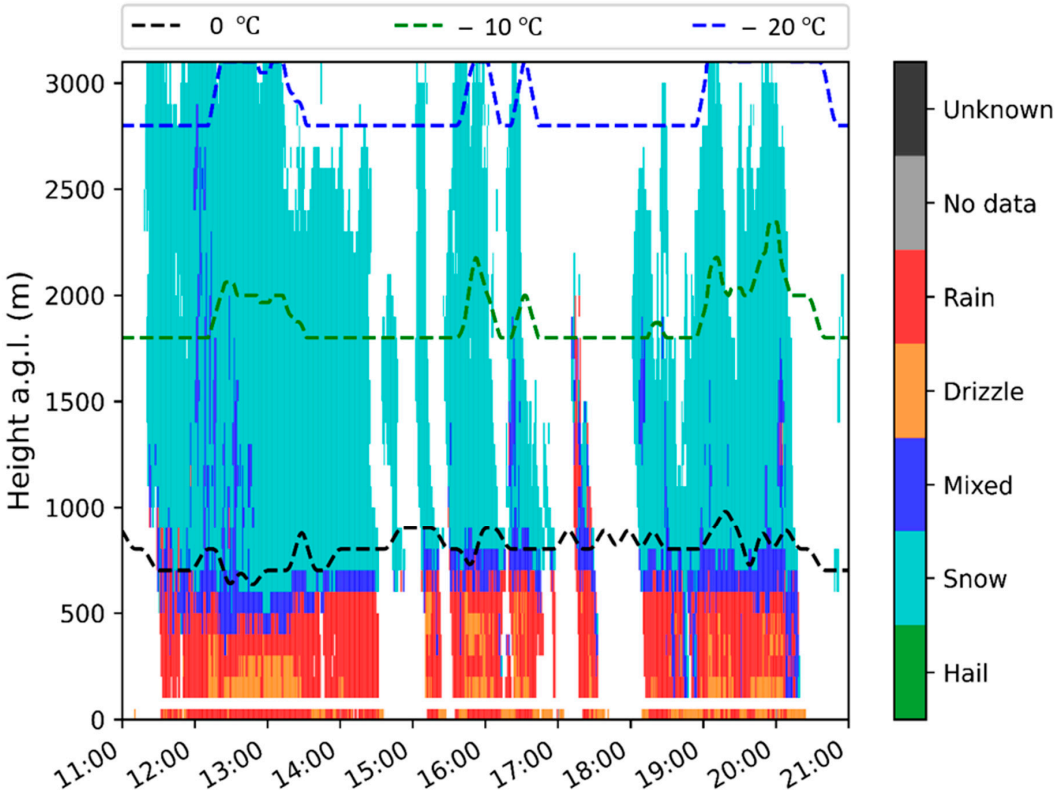

Figure 10. Hydrometeor precipitation type obtained from Method3 corresponding to 27 March 2017 overlaid with microwave radiometer derived isotherm levels of 0, −10 and −20 °C and present weather data from Disdrometer, shown at bottom level (0 to 50 m a.g.l.).

Figure 10 shows clearly that the 0 °C level is slightly above the rain level, which may be explained by the local cooling caused by heat exchange with the environment due to snow melting. From 12 to 15 UTC the freezing level increases, as does the rain level, and later decreases, a trend also followed by the rain level. It can also be seen that the disdrometer hydrometeor classification detects rain and drizzle, consistently with Method3. About 17:30 UTC a short precipitation event with liquid precipitation over the freezing level is observed. In this case, no bright band was detected and both MRR Doppler fall speed and spectrum width did not change along the precipitation profile substantially (not shown), which is consistent with the fact that it was a brief shallow convective event.

The Malniu station, located about 1100 m above ground level from Das, recorded mostly air temperatures below 0 °C and an increase in snow depth at the time the precipitation occurred (Figure S4 in Supplementary Materials), confirming that, at that height, precipitation was falling as snow, as indicated by the Method3 hydrometeor classification. On the other hand, Das station—where, initially, there was no snow on the ground—did not record any increase in snow height, as expected for a rain event.

4.1.4. Rain Rate

Rain rate obtained from the lowest bin height (100 m a.g.l.) provided by Method3 is compared to ground level rain rate, calculated with disdrometer and AWS data located at Das. Disdrometer rain rate was calculated using the raindrop number concentration per unit volume of air following Friedrich et al. [56]. The smallest raindrops detected by the disdrometer had diameters about 0.312 mm, which limits the capacity of the instrument to measure weak precipitation formed by small raindrops. This is reflected in Figure 11, which shows a comparison of concurrent 1 min rain rates obtained with Method3 and Parsivel; the latter considerably underestimates Method3 values for rates below 0.1 mm/h, but overestimates them for some cases above 1 mm/h.

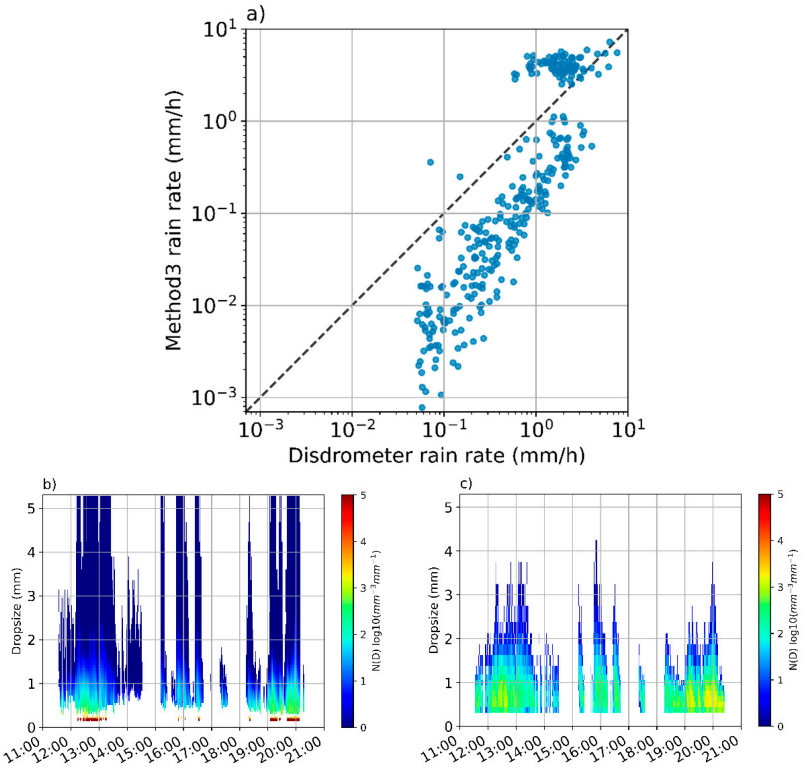

Figure 11. (**a**) Scatter plot of rain rate from disdrometer and the first height bin (100 m above disdrometer) from Method3. (**b**) Particle number concentration per unit volume from Method3 first height bin. (**c**) As (**b**) but obtained from the disdrometer.

Another comparison is performed considering 30 min averages, which is the AWS time resolution, shown in Figure 12. It displays the first (lowest) and third height bin provided by Method3 (which is the first bin available for Method2) and the AWS and disdrometer rain rates. It shows a substantial agreement between the disdrometer and the AWS data and some variability when compared to Method3 rain rates.

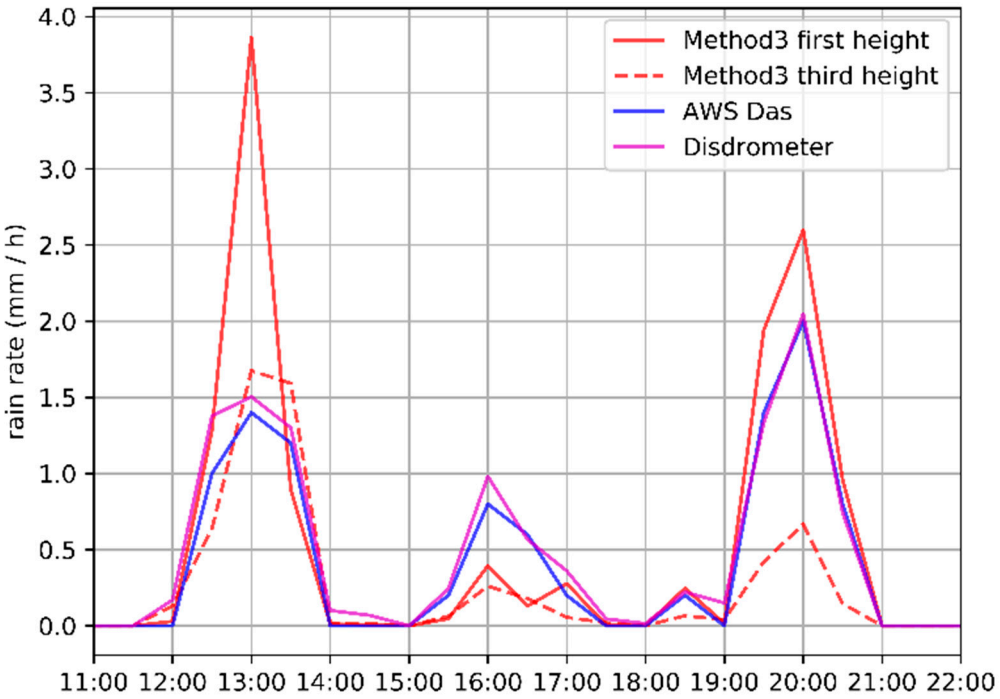

Figure 12. Rain rates during the 27 March 2017 event obtained from Method3 (first and third height bin), AWS Das and disdrometer.

4.1.5. Stratiform vs. Convective Rain

Following the criteria proposed by Thurai et al. [54], two parameters of the fitted gamma raindrop size distribution (D_m and N_w described in Section 4) are used by Method3 to classify bins identified as rainfall into three possible regimes: convective, stratiform or transition. Figure 13a illustrates the classification in the D_m and N_w space calculated from Method3 processing for all heights where rainfall is detected, confirming the predominantly stratiform character of the episode, with some periods of convective rain. Figure 13b shows a similar scatterplot comparing the lowest MRR height bin (100 m a.g.l.) and the values obtained with the disdrometer, where it is apparent that both instruments share a similar pattern but with differences that can be explained by the fact that the disdrometer has a detection limit on the smallest raindrops (~0.25 mm) and a much smaller sampling volume. This is particularly evident for $\log(N_w)$ values below 2 m^{-3} mm^{-1}. The agreement between these instruments is consistent with the recent results obtained by Adirosi et al. [15].

4.2. Hydrometeor Classification Verification

4.2.1. Verification Data and Methodology

The quality of Method3 hydrometeor classification is assessed by comparing the lowest height bin (from 100 to 200 m a.g.l.) with Parsivel present weather precipitation type at 1 min intervals. This high temporal resolution may easily introduce double penalty effects in the case of rapidly changing precipitation types, so a fuzzy verification approach is required considering neighborhoods either on the observations or on the forecast—see, for example, Ebert [57] or Trapero et al. [58] for two

dimensional fuzzy verification procedures. Here, this is evaluated as a one-dimensional data set so the neighborhood is simply a time interval around the observation time.

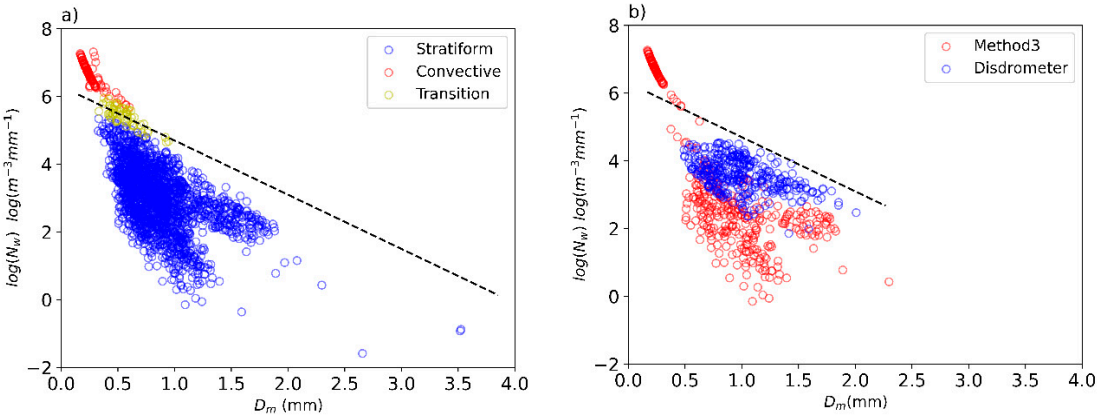

Figure 13. (**a**) N_w versus D_m for stratiform, convective and transition regimes computed for all heights during the 27 March 2017 event. (**b**) as (**a**) but only for the lowest Method3 height bin and disdrometer. As a reference, the dashed black line indicates separation between convective and stratiform regimes according to the criteria of Thurai et al. [54] with −1.6 and 6.3 for c_1 and c_2, respectively.

To choose the interval length, two aspects are considered. First, the time required for hydrometeor particles to reach the ground due to their fall speed. Second, the precipitation drift caused by horizontal wind, which hampers matching the radar observation with ground records (Collier [59], Sandford [60]). To illustrate the first aspect, we may consider that the smallest raindrop detected by Parsivel (~0.25 mm) at 200 m a.g.l., which takes about 4.5 min to reach the ground so at least a 5 min window after the observation time should be considered—other precipitation particles as snowflakes may take even more. In the case of horizontal wind, the situation is more complex, as it may be impossible to observe aloft the same observation particle recorded on the ground, particularly for the long drifts possible for winter precipitation types (Thériault et al. [61]). Moreover, the relative position (upwind or downwind) from the ground record requires us to consider positive and negative time intervals (i.e., time windows centered on the observation time). Considering these aspects, a time window of ±20 min was considered for evaluation.

A data set of 32 different days from January 2017 to October 2019 was selected (45,384 min), representing a wide variety of precipitation types and coverage of every season according to local climatology. The seasonal day distribution was: 5 winter days, 19 in spring, 4 in summer and 4 in autumn. Two examples of verification days are shown in Figure 14, a ground level transition from rain to snow, and a warm season convective event with some minutes of hail.

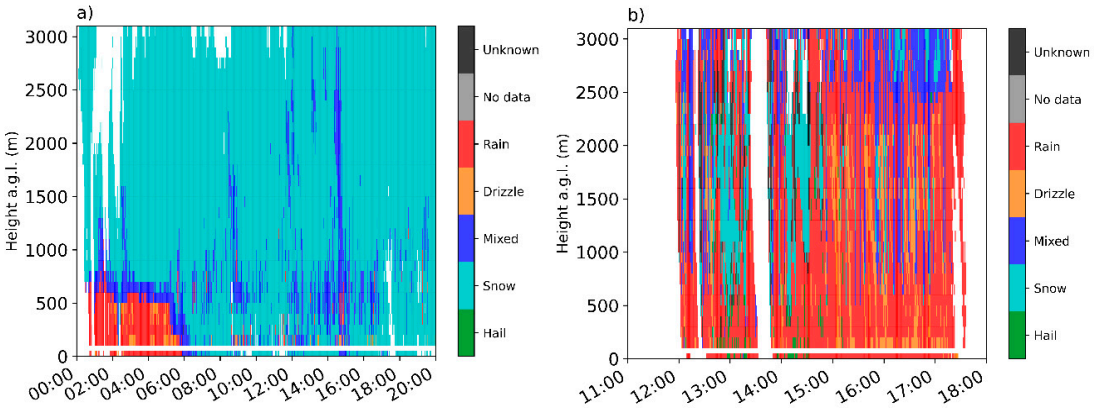

Figure 14. Hydrometeor classification by Method3 and Parsivel present weather (ground level) for: (**a**) 24 March 2018 and (**b**) 28 June 2018.

Verification scores based on a contingency table were calculated for each individual hydrometeor type, in particular the Probability of Detection (POD), the False Alarm Rate (FAR) and the Odds Ratio Skill Score (ORSS), which assess how good a forecast is compared to random chance (see Appendix A).

4.2.2. Verification Results

Table 4 shows for each precipitation type the value of POD, FAR and ORSS plus the total number of minutes of each type in the Method3 and disdrometer data sets, which share generally a similar proportion. Note that the number of hail minutes is rather limited; however, it is included to illustrate the relatively good results achieved. During the verification of the lowest bin, no cases of Method3 unclassified precipitation type arose, but they are marginally present in some bins aloft.

Table 4. Verification scores comparing Method3 precipitation type with Parsivel observations.

Class	POD	FAR	ORSS	Method3 (min)	Method3 (%)	Disdrometer (min)	Disdrometer (%)
Rain	0.99	0.29	0.99	7095	15.6	7173	15.8
Drizzle	0.69	0.26	0.72	3502	7.7	3108	6.8
Hail	0.55	0.01	0.98	49	0.1	88	0.2
Snow	0.97	0.14	0.99	3700	8.2	3897	8.6
Mixed	0.79	0.17	0.89	1001	2.2	933	2.1
No precipitation	0.94	0.05	0.99	30,037	66.2	30,185	66.5

POD values indicate that both rain and snow, and also no precipitation, are the classes best detected (above 0.93), rain being the highest (0.99) and hail the lowest (0.55). F ranges from 0.29 (rain) to 0.01 (hail) and 0.05 (no precipitation). ORSS values indicate the substantial skill of Method3 hydrometeor classification, starting drizzle from 0.72 and yielding rain, snow, and no precipitation, the best results (0.99). Overall, these results illustrate that Method3 provides a reasonable classification of the precipitation types considered.

5. Discussion and Conclusions

A new methodology has been presented for processing K-band vertically pointing Doppler radar data recorded with Micro Rain Radar (MRR) systems. The methodology, referred to here as Method3, has been compared with two previously existing processing systems, Method1 (from the manufacturer) and Method2 (detailed in Maahn and Kollias [38]), using a vertical resolution of 100 m and time resolution of 1 min.

Method3 processes as input data spectral reflectivity (MRR raw data files) and produces as output data a number of fields. The first part of Method3 processing deals with spectral density processing and includes a new peak signal selection and noise treatment approach, considering all Doppler bins but the first and the last one. Then, a dealiasing method allowing for upward velocities, similar to the one included in Method2, is applied. With this new spectral processing, Method3 is able to extend the precipitation profile to the second lowest height level; in this case 100 to 200 m above ground. Moreover, the new methodology allows us to select the integration time (set here to 60 s), for example to improve sensitivity.

In Method3, the second processing part produces different variables, which include equivalent reflectivity (Z_e), Doppler fall speed and derived parameters, such as spectral width, skewness, and kurtosis, plus a simplified precipitation-type classification. The precipitation classes considered are drizzle, rain, snow, mixed, and hail. For liquid precipitation, Mie backscattering is assumed, which allows us to provide integral parameter reflectivity (Z), liquid water content (LWC), rainfall rate (RR) and a gamma drop size distribution fit, including the computation of the normalized intercept parameter with respect to the liquid water (N_w), and the mean mass-weighted raindrop diameter (D_m). Snow rate is also calculated for snow precipitation type. Compared to previously existing MRR

processing methodologies, Method3 provides a comprehensive set of variables to study precipitation profiles to support precipitation microphysics analysis.

Method3 is illustrated with a case study comparing the results with Method2, Method3, microwave radiometer derived temperature profiles and ground data provided by a Parsivel disdrometer and two AWS, yielding consistent results. The comparison with Method2 denotes a high correlation for W and Z_e (R^2 of 0.995 and 0.993, respectively) with some exceptions for low reflectivity values, which may arise from differences in the signal detection and dealiasing. Comparisons with Method2 indicate that Method3 provides very similar patterns of fall speed and reflectivity.

Additionally, the Method3 precipitation type classification is compared with Parsivel present weather observations using contingency table scores. Results indicate a very good capacity of Method3 to distinguish rainfall and snow (PODs equal or greater than 0.97), satisfactory results for mixed and drizzle (PODs of 0.79 and 0.69) and acceptable for a reduced number of hail cases (0.55), with relatively low rate of false alarms and good skill compared to random chance in all cases (FAR < 0.30, ORSS > 0.70).

The methodology presented in this article has been implemented in Python and is freely available in the repository github as RaProM (https://github.com/AlbertGBena/RaProM). The parameters calculated in Method3 and the new hydrometeor classification proposed will facilitate the analysis of precipitation profiles for the MRR data-user community. Future work planned includes the extension of Method3 to process MRR-PRO data and the application to a larger data set to further verify the results presented here.

Supplementary Materials: The following are available online at http://www.mdpi.com/2072-4292/12/24/4113/s1. Figure S1: Location of the study area, Figure S2: Histograms of differences in fall speed between Method3 and Method2 for different hydrometeor types, Figure S3: As Figure S2 but for equivalent reflectivity, Figure S4: Temperature and snow depth from two AWS (Malniu and Das), Table S1: Summary of details of instruments used, and Table S2: WMO precipitation type classification grouping criteria.

Author Contributions: Conceptualization, A.G.-B. and J.B.; methodology, A.G.-B. and J.B.; software, A.G.-B. and S.G.; data curation, A.G.-B.; writing—original draft preparation, A.G.-B. and J.B.; writing—review and editing, A.G.-B., J.B., S.G., M.U., B.C. and J.-F.G. All authors have read and agreed to the published version of the manuscript.

Funding: This research was funded by the Spanish Government through projects CGL2015-65627-C3-1-R, CGL2015-65627-C3-2-R (MINECO/FEDER), CGL2016-81828-REDT and RTI2018-098693-B-C32 (AEI/FEDER).

Acknowledgments: The Cerdanya-2017 field campaign was a research effort organized by the University of the Balearic Islands, the University of Barcelona, METEO-FRANCE and the Meteorological Service of Catalonia. METEO-FRANCE/CNRM/GMEI/LISA, 4 M and TRAMM teams for the data acquisition during the campaign, especially Jean-Marie Donier and Alexandre Paci from CNRM.

Conflicts of Interest: The authors declare no conflict of interest.

Appendix A

The comparison between Method3 precipitation type and disdrometer present weather observations is performed considering a contingency table for each precipitation type, where "hits" represent the number of events (precipitation type) forecast by Method3 and observed by the disdrometer, "misses" the events not forecast, "false alarms" the forecast events that did not occur and "correct negatives" the events that did not occur correctly forecast. Scores used are Probability of Detection (POD), indicating the fraction of correct forecast events, False Alarm Rate (FAR), indicating fraction of "no event"' incorrectly forecast, and Odds ratio skill score (ORSS), indicating forecast skill compared to random chance, which are given by:

$$POD = \frac{hits}{hits + misses} \tag{A1}$$

$$FAR = \frac{false\ alarms}{correct\ negatives + false\ alarms} \tag{A2}$$

$$ORSS = \frac{hits \cdot correct\ negatives - misses \cdot false\ alarms}{hits \cdot correct\ negatives + misses \cdot false\ alarms} \quad \text{(A3)}$$

where best (worst) score values are, respectively, 1, 0, and 1 (0, 1, and 0).

References

1. Atlas, D.; Srivastava, R.C.; Sekhon, R.S. Doppler radar characteristics of precipitation at vertical incidence. *Rev. Geophys.* **1973**, *11*, 1–35. [CrossRef]
2. Hauser, D.; Amayenc, P. A new method for deducing hydrometeor-size distributions and vertical air motions from Doppler radar measurements at vertical incidence. *J. Appl. Meteorol.* **1981**, *20*, 547–555. [CrossRef]
3. Battaglia, A.; Kollias, P.; Dhillon, R.; Roy, R.; Tanelli, S.; Lamer, K.; Grecu, M.; Lebsock, M.; Watters, D.; Mroz, K.; et al. Spaceborne Cloud and Precipitation Radars: Status, Challenges, and Ways Forward. *Rev. Geophys.* **2020**, *58*, e2019RG000686. [CrossRef] [PubMed]
4. Kollias, P.; Clothiaux, E.E.; Miller, M.A.; Albrecht, B.A.; Stephens, G.L.; Ackerman, T.P. Millimeter-wavelength radars: New frontier in atmospheric cloud and precipitation research. *Bull. Am. Meteorol. Soc.* **2007**, *88*, 1608–1624. [CrossRef]
5. Ecklund, W.L.; Williams, C.R.; Johnston, P.E.; Gage, K.S. A 3-GHz profiler for precipitating cloud studies. *J. Atmos. Ocean. Technol.* **1999**, *16*, 309–322. [CrossRef]
6. Sheppard, B.E. Measurement of Raindrop Size Distributions Using a Small Doppler Radar. *J. Atmos. Ocean. Technol.* **1990**, *7*, 255–268. [CrossRef]
7. Löffler-Mang, M.; Kunz, M.; Schmid, W. On the performance of a low-cost K-band Doppler radar for quantitative rain measurements. *J. Atmos. Ocean. Technol.* **1999**, *16*, 378–387. [CrossRef]
8. Peters, G.; Fischer, B.; Andersson, T. Rain observations with a vertically looking Micro Rain Radar (MRR). *Boreal Environ. Res.* **2002**, *7*, 353–362.
9. Chandra, A.; Zhang, C.; Kollias, P.; Matrosov, S.; Szyrmer, W. Automated rain rate estimates using the Ka-band ARM zenith radar (KAZR). *Atmos. Meas. Tech. Discuss.* **2015**, *7*, 1807–1833. [CrossRef]
10. Sokol, Z.; Minářová, J.; Novák, P. Classification of hydrometeors using measurements of the ka-band cloud radar installed at the Milešovka Mountain (Central Europe). *Remote Sens.* **2018**, *10*, 1674. [CrossRef]
11. Sokol, Z.; Minářová, J.; Fišer, O. Hydrometeor distribution and linear depolarization ratio in thunderstorms. *Remote Sens.* **2020**, *12*, 2144. [CrossRef]
12. Lolli, S.; D'Adderio, L.; Campbell, J.; Sicard, M.; Welton, E.; Binci, A.; Rea, A.; Tokay, A.; Comerón, A.; Barragan, R.; et al. Vertically Resolved Precipitation Intensity Retrieved through a Synergy between the Ground-Based NASA MPLNET Lidar Network Measurements, Surface Disdrometer Datasets and an Analytical Model Solution. *Remote Sens.* **2018**, *10*, 1102. [CrossRef]
13. Lolli, S.; Vivone, G.; Lewis, J.R.; Sicard, M.; Welton, E.J.; Campbell, J.R.; Comerón, A.; D'Adderio, L.P.; Tokay, A.; Giunta, A.; et al. Overview of the New Version 3 NASA Micro-Pulse Lidar Network (MPLNET) Automatic Precipitation Detection Algorithm. *Remote Sens.* **2019**, *12*, 71. [CrossRef]
14. Adirosi, E.; Baldini, L.; Roberto, N.; Gatlin, P.; Tokay, A. Improvement of vertical profiles of raindrop size distribution from micro rain radar using 2D video disdrometer measurements. *Atmos. Res.* **2016**, *169*, 404–415. [CrossRef]
15. Adirosi, E.; Baldini, L.; Tokay, A.L.I. Rainfall and DSD parameters comparison between micro rain radar, two-dimensional video and parsivel2 disdrometers, and S-band dual-polarization radar. *J. Atmos. Ocean. Technol.* **2020**, *37*, 621–640. [CrossRef]
16. Chang, W.Y.; Lee, G.W.; Jou, B.J.D.; Lee, W.C.; Lin, P.L.; Yu, C.K. Uncertainty in measured raindrop size distributions from four types of collocated instruments. *Remote Sens.* **2020**, *12*, 1167. [CrossRef]
17. Gonzalez, S.; Bech, J.; Udina, M.; Codina, B.; Paci, A.; Trapero, L. Decoupling between precipitation processes and mountain wave induced circulations observed with a vertically pointing K-band doppler radar. *Remote Sens.* **2019**, *11*, 1034. [CrossRef]
18. Jash, D.; Resmi, E.A.; Unnikrishnan, C.K.; Sumesh, R.K.; Sreekanth, T.S.; Sukumar, N.; Ramachandran, K.K. Variation in rain drop size distribution and rain integral parameters during southwest monsoon over a tropical station: An inter-comparison of disdrometer and Micro Rain Radar. *Atmos. Res.* **2019**, *217*, 24–36. [CrossRef]
19. Luo, L.; Xiao, H.; Yang, H.; Chen, H.; Guo, J.; Sun, Y.; Feng, L. Raindrop size distribution and microphysical characteristics of a great rainstorm in 2016 in Beijing, China. *Atmos. Res.* **2020**, *239*, 104895. [CrossRef]

20. Tokay, A.; Hartmann, P.; Battaglia, A.; Gage, K.S.; Clark, W.L.; Williams, C.R. A field study of reflectivity and Z-R relations using vertically pointing radars and disdrometers. *J. Atmos. Ocean. Technol.* **2009**, *26*, 1120–1134. [CrossRef]
21. Bendix, J.; Rollenbeck, R.; Reudenbach, C. Diurnal patterns of rainfall in a tropical Andean valley of southern Ecuador as seen by a vertically pointing K-band Doppler radar. *Int. J. Climatol.* **2006**, *26*, 829–846. [CrossRef]
22. Seidel, J.; Trachte, K.; Orellana-Alvear, J.; Figueroa, R.; Célleri, R.; Bendix, J.; Fernandez, C.; Huggel, C. Precipitation Characteristics at Two Locations in the Tropical Andes by Means of Vertically Pointing Micro-Rain Radar Observations. *Remote Sens.* **2019**, *11*, 2985. [CrossRef]
23. Arulraj, M.; Barros, A.P. Improving quantitative precipitation estimates in mountainous regions by modelling low-level seeder-feeder interactions constrained by Global Precipitation Measurement Dual-frequency Precipitation Radar measurements. *Remote Sens. Environ.* **2019**, *231*, 111213. [CrossRef]
24. Cha, J.-W.; Chang, K.-H.; Yum, S.S.; Choi, Y.-J. Comparison of the bright band characteristics measured by Micro Rain Radar (MRR) at a mountain and a coastal site in South Korea. *Adv. Atmos. Sci.* **2009**, *26*, 211–221. [CrossRef]
25. Brast, M.; Markmann, P. Detecting the Melting Layer with a Micro Rain Radar Using a Neural Network Approach. *Atmos. Meas. Tech. Discuss.* **2019**. [CrossRef]
26. Frech, M.; Hagen, M.; Mammen, T. Monitoring the Absolute Calibration of a Polarimetric Weather Radar. *J. Atmos. Ocean. Technol.* **2017**, *34*, 599–615. [CrossRef]
27. Fabry, F.; Zawadzki, I. Long-Term Radar Observations of the Melting Layer of Precipitation and Their Interpretation. *J. Atmos. Sci.* **1995**, *52*, 838–851. [CrossRef]
28. Sánchez-Diezma, R.; Zawadzki, I.; Sempere-Torres, D. Identification of the bright band through the analysis of volumetric radar data. *J. Geophys. Res. Atmos.* **2000**, *105*, 2225–2236. [CrossRef]
29. Bordoy, R.; Bech, J.; Rigo, T.; Pineda, N. Analysis of a method for radar rainfall estimation considering the freezing level height. *J. Mediterr. Meteorol. Climatol.* **2010**, *7*, 25–39. [CrossRef]
30. Makino, K.; Shiina, T.; Ota, M. A Precipitation Classification System Using Vertical Doppler Radar Based on Neural Networks. *Radio Sci.* **2019**, *54*, 20–33. [CrossRef]
31. Ryzhkov, A.V.; Schuur, T.J.; Burgess, D.W.; Heinselman, P.L.; Giangrande, S.E.; Zrnic, D.S. The Joint Polarization Experiment: Polarimetric Rainfall Measurements and Hydrometeor Classification. *Bull. Am. Meteorol. Soc.* **2005**, *86*, 809–824. [CrossRef]
32. Park, H.S.; Ryzhkov, A.V.; Zrnić, D.S.; Kim, K.E. The hydrometeor classification algorithm for the polarimetric WSR-88D: Description and application to an MCS. *Weather Forecast.* **2009**, *24*, 730–748. [CrossRef]
33. Schuur, T.J.; Park, H.S.; Ryzhkov, A.V.; Reeves, H.D. Classification of precipitation types during transitional winter weather using the RUC model and polarimetric radar retrievals. *J. Appl. Meteorol. Climatol.* **2012**, *51*, 763–779. [CrossRef]
34. Dolan, B.; Rutledge, S.A.; Lim, S.; Chandrasekar, V.; Thurai, M. A robust C-band hydrometeor identification algorithm and application to a long-term polarimetric radar dataset. *J. Appl. Meteorol. Climatol.* **2013**, *52*, 2162–2189. [CrossRef]
35. Chandrasekar, V.; Keränen, R.; Lim, S.; Moisseev, D. Recent advances in classification of observations from dual polarization weather radars. *Atmos. Res.* **2013**, *119*, 97–111. [CrossRef]
36. Besic, N.; Figueras i Ventura, J.; Grazioli, J.; Gabella, M.; Germann, U.; Berne, A. Hydrometeor classification through statistical clustering of polarimetric radar measurements: A semi-supervised approach. *Atmos. Meas. Tech.* **2016**, *9*, 4425–4445. [CrossRef]
37. METEK. *MRR Physical Basics Valid for MRR Service Version ≥ 5.2.0.9*; Technical Manual; METEK: Elmshorn, Germany, 2015.
38. Maahn, M.; Kollias, P. Improved Micro Rain Radar snow measurements using Doppler spectra post-processing. *Atmos. Meas. Tech.* **2012**, *5*, 2661–2673. [CrossRef]
39. Prohom, M.; Puig, O. 18. Weather Observation Network and Climate Change Monitoring in Catalonia, Spain. In *Planning to Cope with Tropical and Subtropical Climate Change*; De Gruyter Open Poland: Berlin, Germany; Boston, MA, USA, 2016; pp. 322–335. ISBN 9783110480795.
40. Bech, J.; Codina, B.; Lorente, J.; Bebbington, D. The Sensitivity of Single Polarization Weather Radar Beam Blockage Correction to Variability in the Vertical Refractivity Gradient. *J. Atmos. Ocean. Technol.* **2003**, *20*, 845–855. [CrossRef]

41. Trapero, L.; Bech, J.; Rigo, T.; Pineda, N.; Forcadell, D. Uncertainty of precipitation estimates in convective events by the Meteorological Service of Catalonia radar network. *Atmos. Res.* **2009**, *93*, 408–418. [CrossRef]
42. Udina, M.; Bech, J.; Gonzalez, S.; Soler, M.R.; Paci, A.; Miró, J.R.; Trapero, L.; Donier, J.M.; Douffet, T.; Codina, B.; et al. Multi-sensor observations of an elevated rotor during a mountain wave event in the Eastern Pyrenees. *Atmos. Res.* **2020**, *234*, 104698. [CrossRef]
43. Hildebrand, P.H.; Sekhon, R.S. Objective Determination of the Noise Level in Doppler Spectra. *J. Appl. Meteorol.* **1974**, *13*, 808–811. [CrossRef]
44. Kneifel, S.; Kulie, M.S.; Bennartz, R. A triple-frequency approach to retrieve microphysical snowfall parameters. *J. Geophys. Res. Atmos.* **2011**, *16*, 116. [CrossRef]
45. Wang, H.; Lei, H.; Yang, J. Microphysical processes of a stratiform precipitation event over eastern China: Analysis using micro rain radar data. *Adv. Atmos. Sci.* **2017**, *34*, 1472–1482. [CrossRef]
46. American Meteorological Society, Cited 2020 Drizzle. Glossary of Meteorology. Available online: https://glossary.ametsoc.org/wiki/Drizzle (accessed on 8 September 2020).
47. American Meteorological Society, Cited 2020 Rain. Glossary of Meteorology. Available online: https://glossary.ametsoc.org/wiki/Rain (accessed on 8 September 2020).
48. Acquistapace, C.; Löhnert, U.; Maahn, M.; Kollias, P. A new criterion to improve operational drizzle detection with ground-based remote sensing. *J. Atmos. Ocean. Technol.* **2019**, *36*, 781–801. [CrossRef]
49. Kalesse, H.; Szyrmer, W.; Kneifel, S.; Kollias, P.; Luke, E. Fingerprints of a riming event on cloud radar Doppler spectra: Observations and modeling. *Atmos. Chem. Phys.* **2016**. [CrossRef]
50. Matrosov, S.Y.; Heymsfield, A.J. Empirical relations between size parameters of ice hydrometeor populations and radar reflectivity. *J. Appl. Meteorol. Climatol.* **2017**, *56*, 2479–2488. [CrossRef]
51. Souverijns, N.; Gossart, A.; Lhermitte, S.; Gorodetskaya, I.V.; Kneifel, S.; Maahn, M.; Bliven, F.L.; van Lipzig, N.P.M. Estimating radar reflectivity—Snowfall rate relationships and their uncertainties over Antarctica by combining disdrometer and radar observations. *Atmos. Res.* **2017**, *196*, 211–223. [CrossRef]
52. Gunn, R.; Kinzer, G.D. The terminal velocity of fall for water droplets in stagnant air. *J. Meteorol.* **1949**, *6*, 243–248. [CrossRef]
53. Foote, G.B.; Du Toit, P.S. Terminal Velocity of Raindrops Aloft. *J. Appl. Meteorol.* **1969**, *8*, 249–253. [CrossRef]
54. Thurai, M.; Gatlin, P.N.; Bringi, V.N. Separating stratiform and convective rain types based on the drop size distribution characteristics using 2D video disdrometer data. *Atmos. Res.* **2016**, *169*, 416–423. [CrossRef]
55. Gonzalez, S.; Bech, J. Extreme point rainfall temporal scaling: A long term (1805–2014) regional and seasonal analysis in Spain. *Int. J. Climatol.* **2017**, *37*, 5068–5079. [CrossRef]
56. Friedrich, K.; Kalina, E.A.; Masters, F.J.; Lopez, C.R. Drop-size distributions in thunderstorms measured by optical disdrometers during VORTEX2. *Mon. Weather Rev.* **2013**, *141*, 1182–1203. [CrossRef]
57. Ebert, E.E. Fuzzy verification of high-resolution gridded forecasts: A review and proposed framework. *Meteorol. Appl.* **2008**, *15*, 51–64. [CrossRef]
58. Trapero, L.; Bech, J.; Duffourg, F.; Esteban, P.; Lorente, J. Mesoscale numerical analysis of the historical November 1982 heavy precipitation event over Andorra (Eastern Pyrenees). *Nat. Hazards Earth Syst. Sci.* **2013**, *13*, 2969–2990. [CrossRef]
59. Collier, C.G. The impact of wind drift on the utility of very high spatial resolution radar data over urban areas. *Phys. Chem. Earth Part B Hydrol. Ocean. Atmos.* **1999**, *24*, 889–893. [CrossRef]
60. Sandford, C. Correcting for wind drift in high resolution radar rainfall products: A feasibility study. *J. Hydrol.* **2015**, *531*, 284–295. [CrossRef]
61. Thériault, J.M.; Stewart, R.E.; Henson, W. Impacts of terminal velocity on the trajectory of winter precipitation types. *Atmos. Res.* **2012**, *116*, 116–129. [CrossRef]

3.2. Aplicació de RaProM a les observacions de la campanya Cerdanya-2017

3.2.1. Resum

Estudis anteriors s'havien dedicat a l'anàlisi de diversos episodis de precipitació de la campanya experimental Cerdanya-2017, sense entrar en l'anàlisi del tipus d'hidrometeor en els perfils de precipitació. No obstant, el resultat de la nova metodologia presentada a l'apartat 3.1. ha permès aplicar-la a l'anàlisi d'observacions de MRR de la campanya experimental Cerdanya 2017, introduint aquesta nova informació, de gran interès en episodis amb transicions de precipitació en superfície (pluja a neu o neu a pluja) com els que s'examinen a l'article.

3.2.2. Article

González, S.; Bech, J.; Garcia-Benadí, A.; Udina, M.; Codina, B.; Trapero, L.; Paci, A.; Georgis, J.F. Vertical structure and microphysical observations of winter precipitation in an inner valley during the Cerdanya-2017 field campaign. Atmospheric Research. Volume 264, **2021**, 105826, https://doi.org/10.1016/j.atmosres.2021.105826

Atmospheric Research 264 (2021) 105826

Contents lists available at ScienceDirect

Atmospheric Research

journal homepage: www.elsevier.com/locate/atmosres

Vertical structure and microphysical observations of winter precipitation in an inner valley during the Cerdanya-2017 field campaign

Sergi González [a,b,*], Joan Bech [b], Albert Garcia-Benadí [b,c], Mireia Udina [b], Bernat Codina [b], Laura Trapero [d], Alexandre Paci [e], Jean-François Georgis [f]

[a] DT Catalonia, Agencia Estatal de Meteorología (AEMET), Barcelona, Spain
[b] Department of Applied Physics - Meteorology, University of Barcelona, Barcelona, Spain
[c] SARTI, Universitat Politècnica de Catalunya, Vilanova i la Geltrú, Spain
[d] Snow and Mountain Research Center of Andorra (CENMA-IEA), Andorra Research Institute, Andorra
[e] Centre National de Recherches Météorologiques (CNRM), Université de Toulouse, METEO-FRANCE, CNRS, Toulouse, France
[f] Laboratoire d'Aérologie, Université de Toulouse, CNRS, Toulouse, France

ARTICLE INFO

Keywords:
Mountain precipitation
Inner valley
Micro Rain Radar
Parsivel disdrometer
Microphysical processes
Pyrenees
Cerdanya-2017

ABSTRACT

Precipitation processes at windward and leeward sides of the mountains have been object of study for many decades. Instead, inner mountain valleys, where usually most mountain population lives, have received considerably less attention. This article examines precipitation processes during a winter field campaign in an inner valley of the Pyrenees (NE Spain) using, among other instruments, a K-band vertically pointing Doppler radar (Micro Rain Radar) and a laser-based optical disdrometer (Parsivel). A decoupling is found between the stalled air of the valley and the air of the free atmosphere above the mountain crest level, evidenced by an increase of turbulence and spectral width of precipitation particles. Wind shear layer may promote riming and aggregation of the ice and snow particles. Two main rainfall regimes are found during the campaign: (1) stratiform rainfall mostly produced by water vapour deposition processes, although sometimes riming and aggregation become important, and (2) weak convection with slight dominance of collision-coalescence processes. Precipitation characteristics at the bottom of the valley show typical continental features such as low Liquid Water Content, despite the valley is only about 100 km from the sea. This study demonstrates that inner valley may present distinct precipitation features with respect to windward and leeward precipitation.

1. Introduction

Orographic interaction with precipitating clouds depends on multiple factors (Houze, 2012; Roe, 2005). Static stability, moisture content or vertical profile and strength of the air flow affect orographic precipitation (Medina et al., 2005). The specific geometry of the air flow orientation with respect to terrain is also very important (Roe, 2005). Those interactions are commonly explained from the point of view of the windward vs. leeward duality. In the simplest conceptual idealized model, precipitation is enhanced by forced ascent on the windward side of a two-dimensional mountain and appears a precipitation shadow on the leeside where air sinks. Further investigations have demonstrated that interactions between air flow and precipitation can be much more complex. Several mesoscale and microscale processes modify the precipitation growth, intensity, distribution and phase (Aikins et al., 2016; Garvert et al., 2007; Geerts et al., 2011; Houze et al., 2017; Medina and Houze, 2003). An example is the presence of a persistent wind shear layer observed upstream of major mountain ranges in stable stratified low-level flow (Medina et al., 2005; Medina and Houze, 2015). This layer increases turbulence, which has been observed to enhance the precipitation over the windward slopes. Another notable example of orographic complexity is caused by the forced updrafts that trigger shallow convective systems (Konwar et al., 2014; Murata et al., 2020), where the process of coalescence produces a large number of relatively small raindrops. This process is fundamental to produce high amounts of orographic precipitation in areas such as the Western Ghats of India (Das et al., 2017; Konwar et al., 2014) or Cherrapunji (Murata et al., 2020). Note that the latter location holds the world record for rainfall amounts at several temporal durations between two days and two years (Galmarini et al., 2004; Gonzalez and Bech, 2017).

* Corresponding author at: DT Catalonia, AEMET. C/ Arquitecte Sert, 1, E-08003 Barcelona, Spain.
E-mail address: sgonzalezh@aemet.es (S. González).

https://doi.org/10.1016/j.atmosres.2021.105826
Received 21 April 2021; Received in revised form 23 August 2021; Accepted 23 August 2021
Available online 27 August 2021

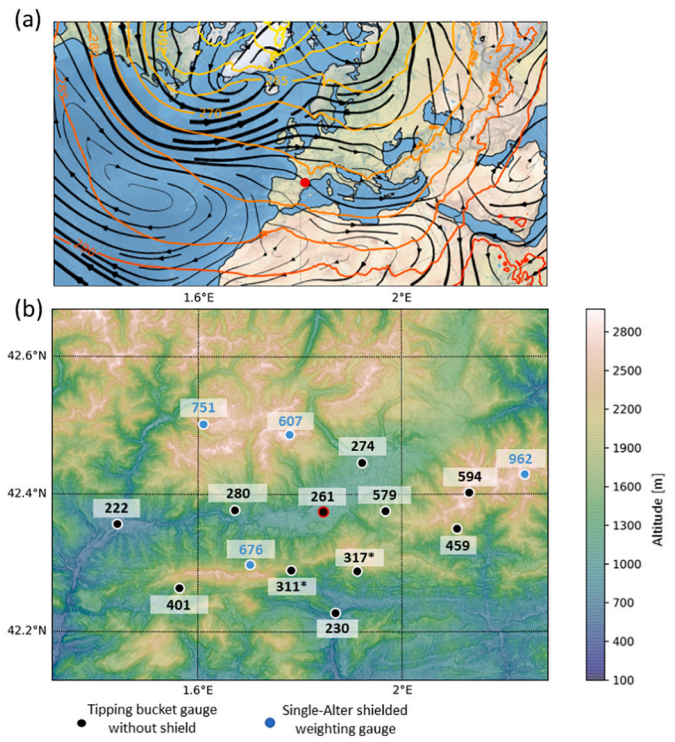

Fig. 1. (a) Location of the Cerdanya valley (red circle) at the eastern side of Pyrenees mountain massif in south-west Europe with the 850 hPa temperature (contours) and wind (streamlines proportional to the wind speed) averaged from Jan to Apr 2017 using ERA5 data. (b) Map of the Cerdanya valley showing precipitation (mm) corrected for undercatch wind effects during the C2017 field campaign recorded at single-Alter shielded weighting gauges (blue solid circles) and tipping bucket heated gauges (black solid circles). Precipitation records at gauges without collocated wind measurements (indicated by the * symbol) were not corrected. The main observing site is located at LECD aerodrome (black circle with red contour; 260.9 mm, 1097 m *asl*). Malniu (606.7, 2230 m *asl*) is located at the north-northwest of LECD. (For interpretation of the references to colour in this figure legend, the reader is referred to the web version of this article.)

Many mountain systems have several regions that cannot be described using the simple windward or leeward model (Prat and Barros, 2010). This is the case of inner valleys, characterized by being surrounded by other valleys with different orientations, which produces a relative isolation with respect to the synoptic wind flow. Inner valleys have received considerably less attention than windward and leeward slopes. As far as we know, only Prat and Barros (2010) have focused on the characterization of precipitation processes of inner regions, studied in the mountains in the Great Smoky Mountains in the Southern Appalachians. Additionally, other precipitation studies have been performed on inner valleys, specifically at the Tropical Andes (Kumar et al., 2020; Seidel et al., 2019). Inner valleys present an additional challenge to the study of the precipitation processes: conventional ground-based weather radars become blocked by the surrounding mountains preventing low-level in-valley measurements (Bech et al., 2007; Bech et al., 2003; Prat and Barros, 2010; Trapero et al., 2009). In addition, spaceborne radar precipitation estimates from satellites such as the Core Observatory satellite of the Global Precipitation Measurement (GPM) mission are affected by ground clutter hampering near-ground measurements (Maahn et al., 2014) and this cluttering may be even worse in valleys due to the proximity of mountain slopes (Arulraj and Barros, 2021). Because of these limitations, ground-based vertical-profiling radars –able to provide high temporal (1 min) and vertical spatial (100 m) resolutions– become a suitable tool to study precipitation in inner valleys together with in-situ precipitation measurements such as rain-gauges and disdrometers.

The main scientific objective of this paper is to present an analysis of winter precipitation observations measured in an inner valley, studying their vertical variability and dominant microphysical processes in order to expand the current limited literature on the topic. In particular, we want to assess if the isolation of an inner valley in the Pyrenees Mountains may lead to more continental conditions than expected given the proximity to the Mediterranean Sea. For this purpose, we carried out a field campaign at the Cerdanya Valley in the eastern Pyrenees from December 2016 to April 2017. A dedicated network of non-conventional meteorological instrumentation was deployed including, among others, a Micro-Rain Radar and a Parsivel disdrometer. A description of the area of interest is presented in Section 2 and the instrumentation used in this study is described in Section 3. Section 4 presents the results of the campaign describing the precipitation events (Section 4.1), the vertical profiles during the snowfall events (Section 4.2), the drop size distribution of the rainfall events (Section 4.3), and the analysis of two selected case studies (Section 5). Main conclusions and outlook for future work are described in Section 6.

2. Region of study

The Pyrenees mountain massif is an important ecoregion in south-western Europe with a high level of biodiversity and endemic species. From the human perspective, it is a strategic region for energy production (López-Moreno et al., 2002), tourism (Lasanta et al., 2007) and water management in north-eastern Spain (López-Moreno et al., 2014). Precipitation is therefore an essential resource in this area that has been extensively investigated from the climatic point of view (Buisan et al., 2015; Lemus-Canovas et al., 2019; Pérez-Zanón et al., 2017) and mesoscale factors associated to heavy rainfall events (Trapero et al., 2013a, 2013b).

Located on the Eastern Pyrenees, the Cerdanya is a wide inner valley (~15 km at the minor axis and 35 km at the major axis) corresponding to the higher basin of the Segre River, a tributary of the Ebro river basin (Fig. 1). Unlike most valleys of the Pyrenees with N-S orientation, the Cerdanya is oriented from east-northeast to west-southwest. The bottom of the valley, where most instruments were located is at 1100 m above sea level (*asl*). The valley narrows to the west-southwest and is surrounded by mountain ranges at northwest and southeast with mountain peaks exceeding 2000 m *asl*. Therefore it is a quite enclosed valley. Several small valleys drain to the wide Cerdanya valley in addition to the surrounding slopes causing frequent thermal inversions in the bottom of the valley in winter (Conangla et al., 2018; Miró et al., 2018; Pagès et al., 2017).

The Cerdanya valley has a large precipitation gradient with altitude. The lowest inner areas of the valley have yearly averages about 600 mm yr^{-1} while in the surrounding mountains the precipitation may exceed 1400 mm yr^{-1} (Xercavins, 1985), thus presenting a classical rain shadow pattern. Unlike other neighbouring Mediterranean areas, the summer in the Cerdanya valley is the wet season and winter is historically considered the dry season. However, this climatology may be biased due to underestimation of solid precipitation in rain gauges as described in previous studies (Buisán et al., 2017; Rasmussen et al., 2012). Snow days show a great dependence with altitude. In the inner valley, there are less than 20 days of snow a year while there are more than 40 days of snow a year in the surrounding mountains, especially in the northern mountains more exposed to the winter northerlies (Xercavins, 1985).

3. Instrumentation and methodology

From December 2017 to May 2017, a field campaign was conducted to study cold pools, mountain waves, rotors and precipitation in this mountainous terrain area (see f.e. Gonzalez et al., 2019; Udina et al., 2020). During the campaign, named Cerdanya-2017 (hereafter C2017),

Table 1
Precipitation events observed during the C2017, indicating the date and time of the event, the duration, type of hydrometeor on surface (snow, mixed, rain or virga), depth of the precipitation column over 10 dBZ (Shallow: < 2500 m, Borderline: 2500–3000 m, Tall: >3000 m), continuity of the precipitation into the event and availability of Parsivel measurements (A: available; NA: not available; P: partially available).

Event	Year	Month	Start day	Start time	End day	End time	Duration (h)	Type	Depth	Continuity	Parsivel
1	2017	1	10	10:30	10	13:30	3	Snow to Mixed	Tall - Borderline-Shallow	Continuous	A
2	2017	1	10	19:00	11	1:00	6	Snow	Borderline -Shallow	Continuous	A
3	2017	1	13	3:00	13	18:00	15	Virga-Snow	Borderline - Shallow	Scattered	A
4	2017	1	14	2:00	14	22:00	10	Virga-Snow	Borderline -Shallow	Scattered	A
5[a]	2017	1	14	22:00	16	15:00	41	Snow	Tall -Borderline	Continuous	A
6	2017	1	25	14:00	26	15:00	25	Snow	Tall -Shallow	Scattered	NA
7	2017	1	27	7:00	28	6:00	23	Snow	Tall - Borderline	Continuous	NA
8	2017	1	28	17:00	28	20:00	3	Virga	Borderline	Isolated	NA
9	2017	2	2	7:00	2	20:00	13	Rain	Tall - Shallow	Scattered	NA
10	2017	2	3	8:00	3	13:00	5	Snow to Mixed	Tall - Shallow	Scattered	NA
11	2017	2	3	20:00	4	8:00	12	Snow to Rain	Shallow	Scattered	NA
12	2017	2	4	15:00	5	11:00	20	Rain	Shallow - Borderline - Tall	Scattered	NA
13	2017	2	5	13:00	6	7:00	18	Snow	Tall - Borderline	Continuous	NA
14	2017	2	6	17:00	7	0:00	7	Rain	Shallow	Continuous	NA
15	2017	2	7	18:00	8	1:00	7	Rain or Mixed	Tall -Borderline	Scattered	NA
16	2017	2	8	3:00	8	6:00	3	Virga	Tall	Isolated	NA
17	2017	2	11	14:00	12	3:00	13	Rain or Mixed	Borderline	Scattered	NA
18	2017	2	12	13:00	12	15:00	2	Virga	Borderline	Isolated	NA
19	2017	2	12	19:00	14	7:00	36	Rain or Mixed	Tall-Borderline-Shallow	Scattered	NA
20	2017	2	24	2:00	24	3:00	1	Rain	Borderline	Isolated	NA
21	2017	2	28	17:00	28	19:00	2	Probably Mixed	Tall	Isolated	NA
22	2017	3	3	18:00	4	4:00	10	Rain to Mixed	Tall	Continuous	NA
23	2017	3	4	16:30	4	18:00	1.5	Snow	Tall	Isolated	NA
24[b]	2017	3	6	5:00	6	10:00	5	Rain	Borderline	Scattered	NA
25	2017	3	7	15:00	7	20:00	5	Rain	Borderline	Scattered	NA
26	2017	3	8	2:00	8	5:00	3	Virga	Shallow	Scattered	NA
27	2017	3	12	2:00	12	22:30	10.5	Rain and Virga	Tall	Scattered	NA
28	2017	3	22	22:00	23	12:00	14	Rain Mixed and Snow	Tall - Borderline	Scattered	A
29	2017	3	24	8:00	25	18:00	34	Rain Mixed and Snow	Tall-Borderline-Shallow	Scattered	A
30	2017	3	27	12:00	27	21:00	9	Rain	Borderline-Tall	Scattered	NA
31	2017	3	31	10:00	31	14:00	4	Virga	Tall	Scattered	NA
32	2017	3	31	18:00	31	21:00	3	Rain	Tall	–	NA
33	2017	4	1	2:00	2	1:00	23	Virga	Tall-Shallow	Scattered	NA
34	2017	4	5	18:00	5	21:00	3	Rain-Shower	Borderline - Shallow	–	NA
35	2017	4	8	17:00	8	18:00	1	Rain-Shower	Tall	Isolated	NA
36	2017	4	9	14:00	9	15:00	1	Rain-Shower	Tall	Isolated	NA
37	2017	4	13	17:00	13	18:00	1	Rain-Shower	Tall	Isolated	NA
38	2017	4	14	15:00	14	20:00	5	Virga	Tall	Scattered	NA
39	2017	4	15	13:00	15	16:00	3	Rain	Tall	Continuous	NA
40	2017	4	23	16:00	23	19:00	3	Rain	Tall	Scattered	NA
41	2017	4	25	5:00	27	16:00	59	Rain to Snow	Tall-Borderline	Scattered	P
42[b]	2017	4	30	3:00	30	23:00	20	Rain	Tall-Borderline-Shallow	Scattered	A

[a] Examined in Gonzalez et al. (2019).
[b] Examined in this study.

different instrumentation was deployed including Automatic Weather Stations (AWSs), located throughout the valley, and other instruments located at Das aerodrome (ICAO code: LECD; coordinates: 42.386° N 1.867° E at 1097 m *asl*). The following precipitation specific instruments were installed in the C2017 field campaign.

3.1. Rain Gauges

The campaign took advantage of the previous AWSs managed by the official meteorological services that operates in the area: the Spanish Meteorological Service (AEMET), the Catalan Meteorological Service (SMC), the Andorran Study Institute (IEA) and the French Meteorological Service (METEO-FRANCE). An additional network of AWS managed by the CNRM observation group (CNRM/GMEI) was also deployed. There were rain gauges of two different kinds in the area: tipping-bucket gauges and weighting gauges. Rain gauges may have several sources of error, including systematic ones like wind deviation, wetting, evaporation and splashing (WMO, 2014). These errors are expected to be relatively small, generally less than 10% for liquid precipitation (WMO, 1994) and measure is considered without corrections. However, the same is not true with solid precipitation, when the error may achieve 80%, especially when the wind is strong (Kochendorfer et al., 2017a, 2017b; Rasmussen et al., 2012). When solid precipitation occurred, measures were corrected using the transference functions developed by Buisán et al. (2017) for unshielded tipping-bucket gauges, and by Kochendorfer et al. (2017a, 2017b) for single-Alter-shielded weighting gauges.

3.2. Parsivel disdrometer

Particle Size Velocity (Parsivel; Löffler-Mang and Joss, 2000) manufactured by OTT, Germany, is an optical laser disdrometer based on the attenuation of a laser beam obscured by falling precipitation particles. From the reduction of the output voltage and the signal duration, Parsivel determines the particle size and velocity assuming that particles are raindrop spheroids. Parsivel classifies hydrometeors in 32 diameter bins and 32 velocity bins, obtaining a matrix with the quantity of particles measured for each of the $32 \times 32 = 1024$ bins every 60 s as it was configured during this campaign. The disdrometer used during the C2017 was a first generation Parsivel. The main limitation of this instrument is the underestimation of small-size drops that presents (Wen et al., 2017). To minimize this effect, liquid precipitation measured by the disdrometer was corrected following the methodology described by Raupach and Berne (2015) and, additionally, rainfall rates below 0.2

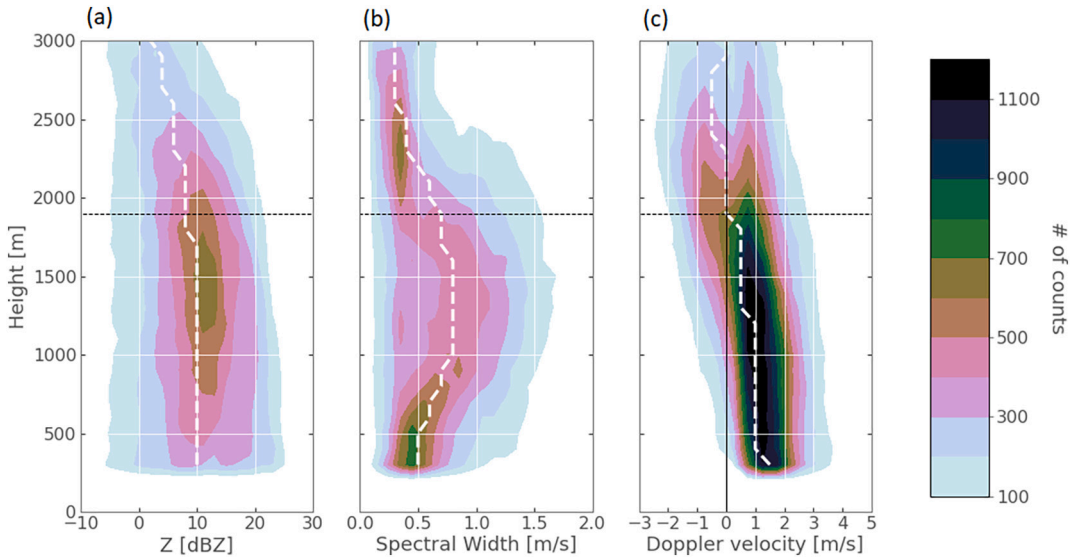

Fig. 2. (a) Radar reflectivity, (b) spectral width and (c) Doppler velocity vs. height (*agl*) measured by the MRR during snowfall events in the C2017. The white dashed line represents the median and the horizontal black line indicates the mountain top height.

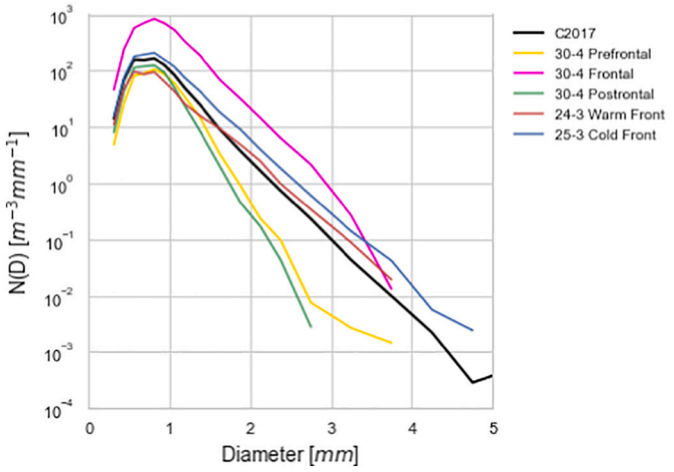

Fig. 3. DSD of liquid precipitation during the C2017 (black) and selected periods of the campaign measured by Parsivel.

Table 2
Median, standard deviation and percentiles of raindrop size distribution parameters of the rainfall precipitation during the C2017 derived from Parsivel measurements.

	D_m (mm)	$Log(N_w)$ (mm^{-1} m^{-3})	LWC (g m^{-3})	R (mm h^{-1})	Z (dBZ)	λ (mm^{-1})	μ
Mean	1.17	3.64	0.090	3.2	21.7	15.2	10.9
Std	0.35	3.70	0.120	4.3	8.2	14.7	10.9
min	0.56	0.77	0.006	0.2	3.5	1.2	−2.4
25%	0.94	3.01	0.012	0.4	14.6	5.9	3.8
50%	1.12	3.38	0.038	1.3	21.7	10.5	7.8
75%	1.35	3.77	0.125	4.3	28.6	19.1	14.4
MAX	5.23	4.52	1.303	45.2	43.1	173.7	122.0

mm h^{-1} were filtered to avoid spurious measurements. Other limitations are splashing or wind effects that also affects to other precipitation instruments. In this article, we used Parsivel to characterize the precipitation phase and the Drop Size Distribution (DSD) of the rainfall events using the manufacturer algorithm. The total number of Parsivel records available between January and April 2017 was 51,093 min, of which 1760 min corresponded to liquid precipitation.

3.3. Micro Rain Radar

Micro Rain Radar (MRR; Peters et al., 2005) manufactured by Metek, Germany, is a portable meteorological Doppler radar profiler that operates using a FMCW (Frequency Modulated Continuous Wave) scheme in K-band (24.230 GHz). MRR operates transmitting a microwave signal and measuring the backscattered radiation by the falling particles every 10 s. The Doppler spectra is divided in 32 height bins. During the C2017 campaign, the MRR was configured to obtain 60-s averages with a height bins resolution of 100 m. To improve the sensibility of light precipitation and snow typical of winter precipitation and to avoid aliasing errors produced by ascending movements of small raindrops and snowflakes, the postprocess scheme developed by Maahn and Kollias (2012) was applied. This processing has been applied in the past to study winter and polar storms and precipitation (e.g. Durán-alarcón et al., 2018; Gonzalez et al., 2019; Gorodetskaya et al., 2015; Minder et al., 2015; Souverijns et al., 2017; Stark et al., 2013). Additionally, the recent methodology developed by Garcia-Benadi et al. (2020) has been used to classify the different hydrometeor types of selected case studies.

3.4. Variables evaluated

In rainfall microphysics, the Drop Size Distribution (DSD) has been described by a gamma function (Rosenfeld and Ulbrich, 2003; Tokay and Short, 1996; Ulbrich and Atlas, 1998). However, a normalized version of this function has been suggested to minimize the correlation between the function parameters (Bringi et al., 2003; Cao and Zhang, 2009; Testud et al., 2001; Willis, 1984):

$$N(D) = N_w f(\mu)\left(\frac{D}{D_m}\right)^{\mu} exp\left(-(4+\mu)\left(\frac{D}{D_m}\right)\right), \quad (1)$$

where *N(D)* is the raindrop concentration per unit volume (m^{-3} mm^{-1}), *D* is the raindrop diameter (mm), f(μ) is defined as

$$f(\mu) = \frac{6}{4^4}\frac{(4+\mu)^{\mu+4}}{\Gamma(\mu+4)}, \quad (2)$$

and it is function of the shape parameter (μ) and the gamma function (Γ),

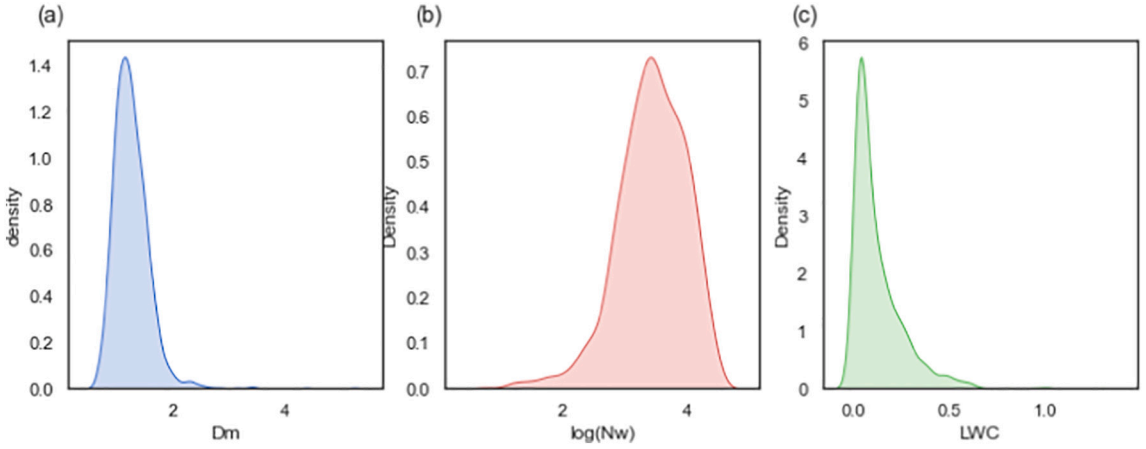

Fig. 4. Kernel Density Estimate of (a) D_m (mm), (b) log(N_w) (dimensionless) and (c) LWC (g m^{-3}) of rainfall measured by Parsivel during the C2017.

Table 3
Comparison between raindrop size distribution parameter in different published studies.

Paper	Location	Region or area	Precipitation	Dm	Log(N_w)	LWC	Observations
This study	*Cerdanya valley, Spain*	*Extratropical inner valley*	*Total winter*	*1.17*	*3.64*	*0.09*	
Casanovas et al., 2021	Sierras de Cordoba, Argentina	Extratropical continental mountain slope and plain	Mountain summer	1.55	3.19	0.14	
			Transition summer	1.69	3.09	0.17	
			Plain summer	1.79	3.02	0.19	
Das et al., 2017	Western Gaths	Tropical mountain slope	Mixed Convective - Stratiform	1.5	–	0.58	
			Stratiform	1.3	–	0.21	
			Convective	1.8	–	1.34	
			Shallow	1.1	–	0.24	
Dolan et al., 2018	Various places	Global	Total annual	1.13	3.95	0.23	Evaluates D0 instead of Dm
		High latitudes		1.00	4.12	–	
		Mid latitudes		1.18	3.79	–	
		Low latitudes		1.18	3.94	–	
Hachani et al., 2017	Cévennes-Vivarais region, France	Extratropical mountain slope and plain	Total annual	~1.1	~3.95	–	Median values
Ji et al., 2019	Beijing, China	Extratropical plain near mountain	Stratiform	1.03	3.57	0.08	
			Convective	2.05	3.61	1.08	
Martner et al., 2008	California, USA	Extratropical coastal mountain slope	BB winter	1.25–1.27	3.62–3.75	0.21–0.29	BB = Bright Band
			NBB winter	0.73–0.77	3.89–4.03	0.22–0.31	NBB = Non Bright Band
Seidel et al., 2019	Cuenca, Ecuador	Tropical inner valley	Stratiform	1.07	3.46	–	
			Convective	1.66	3.76	–	
	Huaraz, Perú	Tropical inner valley	Stratiform	0.93	3.74	–	
			Convective	1.21	4.69	–	
Suh et al., 2021	Southern South Korea	Extratropical coast	Stratiform	0.96–1.09	3.68–4.02	–	
			Convective	1.47–1.58	3.83–3.97	–	
Villalobos-Puma et al., 2020	Mantaro basin, Perú	Tropical inner valley	Stratiform	1.04	2.88	0.08	
			Convective	2.98	3.73	0.70	
Wen et al., 2016	Jiangning, China	Extratropical plain	Total	1.15	4.09	0.49	
			Stratiform	1.16	3.78	0.15	
			Convective	1.41	4.37	1.50	
			Shallow	0.64	4.97	0.21	

N_w is the generalized interception (m^{-3} mm^{-1}) defined as

$$N_w = \frac{4^4}{\pi\rho_w}\left(\frac{LWC}{D_m^4}\right), \tag{3}$$

where ρ_w is the liquid water density (10^6 g m^{-3}), LWC is the liquid water content (g m^{-3}) given by

$$LWC = 10^{-9}\frac{\pi}{6}\rho_w \int D^3 N(D) dD \tag{4}$$

and D_m is the mean volume of drops (mm) defined as

$$D_m = \frac{M_4}{M_3}, \tag{5}$$

where M_n is the n-th moment of the DSD formulated as $M_n = \int D^n N(D) dD$.

These three parameters are commonly evaluated in many studies and are used here to compare the microphysical properties of the liquid precipitation during C2017 with a selection of different worldwide studies in *Section 4.3*. As Dolan et al. (2018) presents their results in terms of median volume of the drops D_0 (mm) instead of D_m, we also calculated this variable:

$$D_0 = \frac{3.67+\mu}{4+\mu} D_m. \tag{6}$$

Finally, we calculated two more parameters: the radar reflectivity factor and the rain rate. The radar reflectivity factor (Z; mm^6 m^{-3}) is related with the power of the electromagnetic signal backscattered by the hydrometeors and is defined as

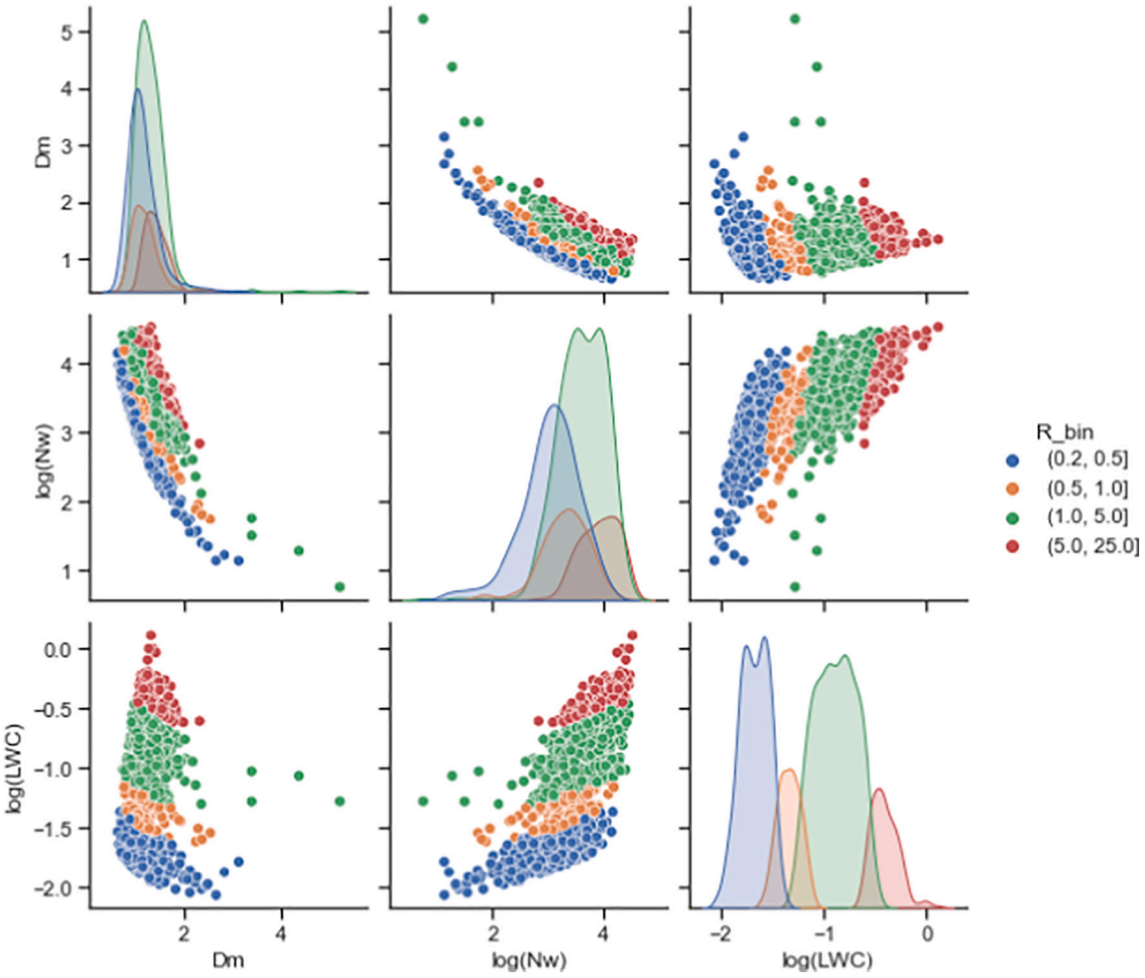

Fig. 5. Kernel Density Estimate (plots in the diagonal) and correlation (remaining plots) between D_m (mm), log(N_w) (dimensionless) and LWC (g m^{-3}) for stripped rain rate (mm h^{-1}) of rainfall measured by Parsivel during the C2017.

$$Z = \int D^6 N(D) dD. \tag{7}$$

The Rain Rate (R; mm h^{-1}) is expressed by

$$R = 3.6{\cdot}10^{-3} \frac{\pi}{6} \int v(D) D^3 N(D) dD \tag{8}$$

where $v(D)$ (m s^{-1}) is the fall drop velocity (downward values defined positive) approximated using the empirical equation of Atlas et al. (1973):

$$v(D) = 9.65 - 10.30\ exp(-0.6D) \tag{9}$$

4. Precipitation during C2017

4.1. Characterization of the precipitation events

During the field campaign, precipitation in the area of study ranged from 230 to 962 mm, with lower amounts at valley stations and higher ones at mountain stations (Fig. 1). Note that precipitation at LECD (260.9 mm, 1097 m *asl*) is less than half the amount recorded at Malniu (606.7 mm, 2230 m *asl*), exhibiting the usual precipitation-shadow pattern observed in the area. As usual in winter, many cyclonic systems crossed the region producing most of the precipitation during C2017. This produced a mean flow from the northwest (Fig. 1a), perpendicular to the mountain systems that enclose the valley.

Different winter precipitation events were intensively observed during C2017. We define here precipitation event as a period with similar precipitation characteristics and related with the same synoptic structure (e.g. frontal passage) and spaced by at least 3 h without precipitation with another event. Note that during the event the precipitation can be continuous or discontinuous. According to this definition, 42 precipitation events were observed and analysed using the data obtained with the MRR, which operated during all the campaign, and with the Parsivel, when it was available. Ceilometer, microwave radiometer (MWR) and AWSs measurements were used also to support the analysis of the different events. The ceilometer and the MWR were used to retrieve the cloud base and the top of melting layer height, respectively. These instruments have limitations under heavy precipitation conditions (Costa-Surós et al., 2013; Knupp et al., 2009) but most precipitation rate during C-2017 was weak or moderate. Table 1 shows a brief description of the events occurred during the campaign.

Events were classified by the type of ground precipitation (rain, snow, mixed) and also virga, recorded at LECD aerodrome (1097 m *asl*). The classification was performed using the MRR profiles and Parsivel information, in particular the automatic WMO SYNOP Present Weather precipitation classification provided by the disdrometer (OTT, 2016; Appendix D). When Parsivel was unavailable, ground precipitation type was estimated using temperature and humidity observations from the LECD AWS, similarly as described in Casellas et al. (2021). Most of the precipitation events included mixed precipitation or transition between rain and snow. Six events were classified as only snow events, and fifteen events were classified as only rain events. When reflectivity values showed precipitation above the ground but zero in the MRR bottom bins

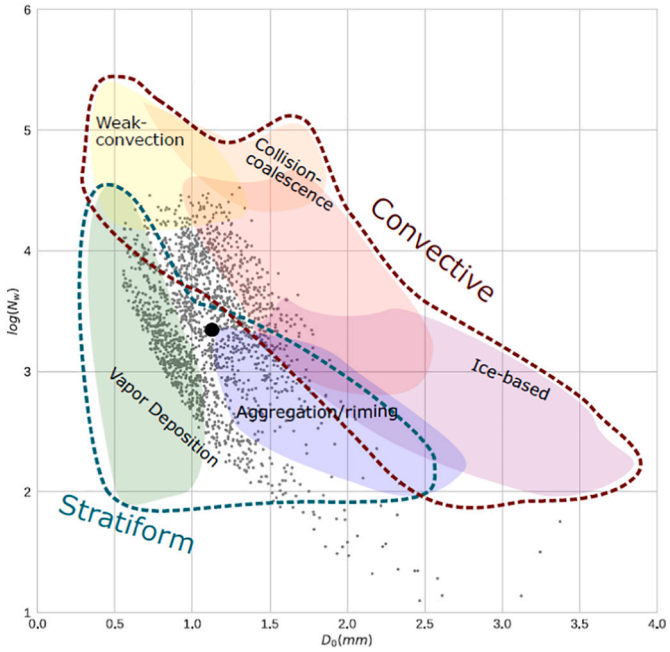

Fig. 6. Distribution of the raindrop size distribution measurements during the C2017 campaign in the D_0-log(N_w) space overlapped to Dolan et al. (2018) dominant precipitation processes and convective and stratiform rainfall regimes. The average value of D_0 and log(N_w) during C2017 is marked with a black dot.

the event was classified as a virga; there were six events with this feature. Only snowfall episodes took place in January and February while only rainfall episodes occurred from February to April, prevailing at the end of the campaign. Transition events were frequent during all the campaign, including late snow periods at the end of the campaign (event #41). These late events with transition features were characterized by frontal passages which strongly modify low level temperature.

Most events showed discontinuous precipitation considering 1-min temporal resolution. Only seven events displayed continuous precipitation and most of these occurred on January. There are also differences between the beginning and the end of the campaign according to depth of the precipitating clouds. In January and early February, precipitating columns tended to be shallow with tops below 2500 m above ground level (*agl*). Instead, in April deep precipitating columns dominated with tops above the 3000 m *agl* that the MRR could measure during C2017.

4.2. Vertical structure of solid precipitation

To investigate the vertical structure of the precipitation over the inner valley, a statistical analysis of reflectivity, spectral width and Doppler velocity has been conducted. The phase transition of the hydrometeors during rainfall and transition events that occurs at the melting layer aloft does not allow to systematically observe the vertical structure of the measured variables during the winter campaign. To prevent the inhomogeneity of the hydrometeors and their impact on the profile analysis we used only the measures during snowfall events. This ensures that changes observed are due only to changes in microphysical processes and mesoscale or microscale circulations in the inner valley.

Fig. 2 shows the averaged vertical structure of the precipitation during during snow events in the C2017 campaign. Similar plots were produced for the whole campaign for rain, mixed and virga events (see Fig. S1 in the Supplementary Information). Reflectivity is related with both quantity and size of the hydrometeors. A downward increase in the reflectivity profile typically indicates snow particles growth. Doppler velocity measures the hydrometeor vertical motions. Snowflakes have a low terminal velocity, of around 1 m s^{-1}, and allow to trace the vertical movement of the air using the Doppler velocity measured by radar profilers such as MRR or similar instruments (Geerts et al., 2011; Gonzalez et al., 2019; Toloui et al., 2014). Similarly, the spectral width associated with solid precipitation particles gives an indication of the turbulence of the air.

Fig. 2a shows that measured reflectivity at 3000 m *agl* during snow events is comprised between −5 and 10 dBZ, averaging 3 dBZ. Reflectivity increases downward until it reaches the height of the mountains, or the crest level, around 1900 m *agl*. Below, reflectivity remains almost constant with values comprised between −5 and 25 dBZ, averaging 10 dBZ. Fig. 2b shows low values of spectral width, between 0.2 and 0.7 m s^{-1} above 2500 m *agl* and averaging 0.3 m s^{-1}. Between 2500 and 700 m *agl* it is noticeable a layer with greater values of spectral width, averaging 0.7 m s^{-1} between 1100 and 1600 m *agl*. However, this layer presents high variability with values ranging between 0.3 and reaching up to 1.6 m s^{-1} in the most extreme cases. Below 700 m *agl*, spectral width decreases averaging 0.5 m s^{-1} with maximum values of 1 m s^{-1} at the lowest bin. Doppler velocity of the hydrometeors (Fig. 3c) may be both upward (negative values) or downward (positive values) up to ±2 ms^{-1} above the mountain crest level, averaging 0 m s^{-1} above 2600 m *agl*. Doppler velocity steadily increases below averaging downward velocities of 1 m s^{-1} in the last 1300 m.

The statistical analysis of the vertical profile of the snowfall events over the Cerdanya valley shows the general pattern of the microphysical processes and small-scale circulations that occur in this area during the C2017. Snow crystals generally emerge and grow above the crest mountain level. Those crystals are affected by vertical air currents, which can be either upward or downward. Below the mountain peaks at 1900 m *agl*, crystals have grown to full size and downward velocities start to dominate. It is remarkable the structure that generates an increase of the turbulence below the mountain crest level. This structure has been identified in previous studies as a shear layer on windward slopes (Medina et al., 2005). In inner mountains, it decouples the stalled air of the valley and the air of the free atmosphere above the mountains

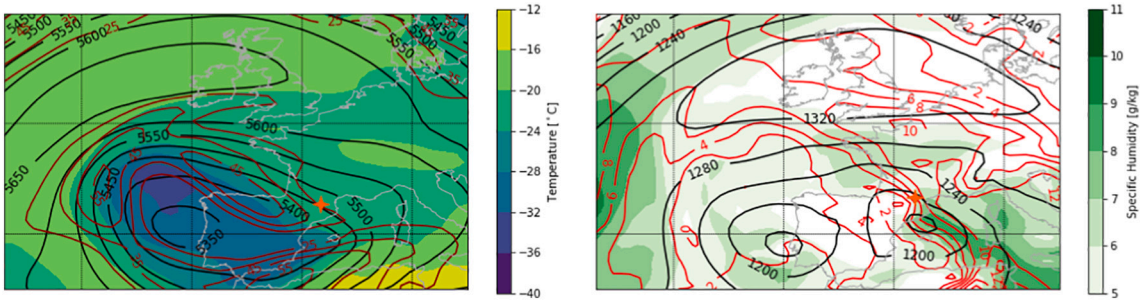

Fig. 7. Synoptic setting on 25 March 2017 at 00:00 UTC. (a) Geopotential height (black lines, mgp) and temperature (shaded) at 500 hPa, and wind speed at 300 hPa (red lines, m s^{-1}). (b) Geopotential height (black lines, mgp), temperature (red lines, °C) and specific humidity (shaded) at 850 hPa. Red star indicate the location of LECD aerodrome. (For interpretation of the references to colour in this figure legend, the reader is referred to the web version of this article.)

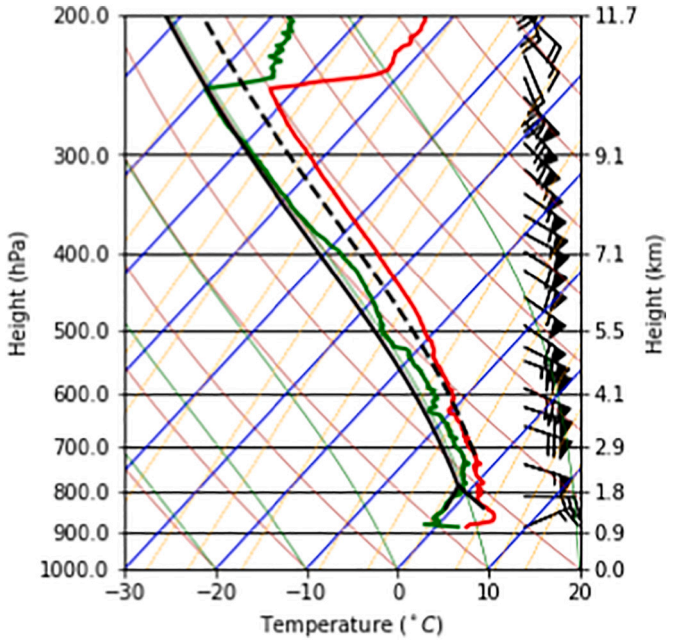

Fig. 8. Sounding launched at LECD on 24 March 2017 at 22:34 UTC showing air temperature (red line), dew point (green line), vertical evolution of an averaged air parcel with the features of the first 100 m (black continuous line) and vertical evolution of an air parcel starting from the convective condensation level (black dashed line). (For interpretation of the references to colour in this figure legend, the reader is referred to the web version of this article.)

(Gonzalez et al., 2019). The air of the free atmosphere above crest level flows according the synoptic setting at mid-levels. Instead, stalled air of the valley bottom can only flow along the basin main axis as suggested by the wind direction measured at LECD AWS during the snow events (Fig. S2). Notice that the main wind direction at LECD flows from a very different direction than climatological wind at 850 hPa (Fig. 1a). Increase of spectral width in the shear layer is not linked with an increase of the reflectivity at the same level, suggesting that, unlike other observations of winter precipitation over mountainous areas (Aikins et al., 2016), turbulence generated by the shear layer does not favour snowfall growth. The steady increase of downward Doppler velocity may indicate an increase of riming below the mountain crest level. Alternatively, it might also be related with the absence of the vertical currents into the stalled valley air.

4.3. Raindrop size distributions

Raindrop size distribution have also been investigated during C2017. To examine the ground level microphysical properties of the liquid precipitation during the campaign, we considered all data classified as rainfall by Parsivel processing. Selected examples of DSDs during the campaign are shown in Fig. 3 showing the diversity of DSDs observed during the campaign: some events present larger tails than others, indicating the presence of larger hydrometeors (e.g. 25 March cold front vs. 30 April postfrontal). Other events present a larger concentration of hydrometeors for all diameters suggesting a convective character of the rainfall event (e.g. 20 April frontal). On the contrary, events with low values of mid to large hydrometeors indicate light stratiform rain or drizzle (eg. 30 April prefrontal and postfrontal). Those events are further discussed in Section 5.

Table 2 shows the mean values, the standard deviation and some percentiles for different parameters of the DSD and Fig. 4 shows the distribution of D_m, $\log(N_w)$ and LWC. Despite they present asymmetric distributions, the mean values of D_m and $\log(N_w)$ are relatively similar to the median values, unlike LWC, which are much more different. We compared the mean values with a selection of different worldwide studies (Table 3) described in the following subsections.

4.3.1. Properties of the Dm

The mean D_m during C2017 was 1.17 mm with an interquartile range between 0.94 and 1.35 mm. Values of D_m are characteristic of the average precipitation in mid-latitudes (Dolan et al., 2018). Those values are similar to stratiform precipitation in extratropics both in mountain and in plain or coastal areas where reported values in the literature examined range from 0.96 to 1.16 mm (Hachani et al., 2017; Ji et al., 2019; Suh et al., 2021; Wen et al., 2016). Martner et al. (2008), who studied winter precipitation in mountain coastal areas of California distinguishing between Bright Band (BB) and Non-Bright Band (NBB) cases, reported values of 1.25–1.27 mm and 0.73–0.77 mm for BB and NBB cases, respectively. Those results differ substantially from the others reported in extratropical areas.

In the tropics, stratiform precipitation presents a larger D_m (1.3 mm) in tropical mountain slopes of India (Das et al., 2017), but in inner valleys of the Andean mountains values are enclosed between 0.93 and 1.07 mm, similar than in mid-latitudes (Seidel et al., 2019; Villalobos-Puma et al., 2020). Indeed, total precipitation in low latitudes present similar mean D_m than mid-latitudes (Dolan et al., 2018).

Convective precipitation presents larger values of D_m over 1.5 mm (see for example Casanovas et al., 2021; Das et al., 2017; Suh et al., 2021; Villalobos-Puma et al., 2020). However, convective precipitation usually accounts for a small fraction of total occurrence of precipitation in mid-latitudes (although not precipitation depth), having a small impact in the averaged diameter of the total precipitation.

4.3.2. Properties of the Log(N_w)

Mean value of $\log(N_w)$ during C2017 was 3.64 with an interquartile range of 3.01 and 3.76. This is slightly below the values obtained by Dolan et al. (2018) for precipitation in mid-latitudes (3.79). It is also similar to other observations of stratiform precipitation in different regions at low-latitudes and mid-latitudes such as 3.46 and 3.74 at Central Andes (Seidel et al., 2019), 3.74 in East China (Wen et al., 2016), 3.53 in Northern China (Ji et al., 2019) and 3.62 in coastal California for BB winter precipitation (Martner et al., 2008). The latter study is relevant as NBB precipitation presents higher values of $\log(N_w)$ associated with orographically forced condensation-coalescence processes in shallow clouds (Martner et al., 2008). Convective and shallow clouds, including NBB precipitation, presents greater $\log(N_w)$, often higher than 4.00 near mountains, except in some extratropical sites where convective precipitation is related to ice-based processes (Casanovas et al., 2021).

4.3.3. Properties of the LWC

Averaged LWC was 0.090 g m^{-3} with an interquartile range of 0.012 and 0125 g m^{-3}, with a substantial difference between the average and median values, due to the high asymmetry of the LWC distribution (Fig. 4). LWC values found are far below the world wide mean (0.23 g m^{-3}) calculated by Dolan et al. (2018) and below measures with maritime influence; for example, 0.21–0.29 g m^{-3} by Martner et al. (2008) for BB winter precipitation in California coastal mountains, 0.21 g m^{-3} by (Konwar et al., 2014) for stratiform precipitation in Western Gaths in India and 0.15 g m^{-3} by Wen et al. (2016) for precipitation in East China. Convective precipitation on those places presents much higher values, over 0.5 g m^{-3}. Instead, mean LWC during C2017 is similar to the 0.08 g m^{-3} measured in Beijing by Ji et al. (2019) and in the Mantaro basin (Perú) by Villalobos-Puma et al. (2020). This reflects the continental characteristics of the Cerdanya valley that despite being relatively near to the sea (i.e. it is closer than Jiangning in Wen et al.) is well isolated by the surrounding mountains.

4.3.4. Inner valley characteristics

The previous results suggest that C2017 winter rainfall was dominated by stratiform precipitation. The absence of a very large quantity of

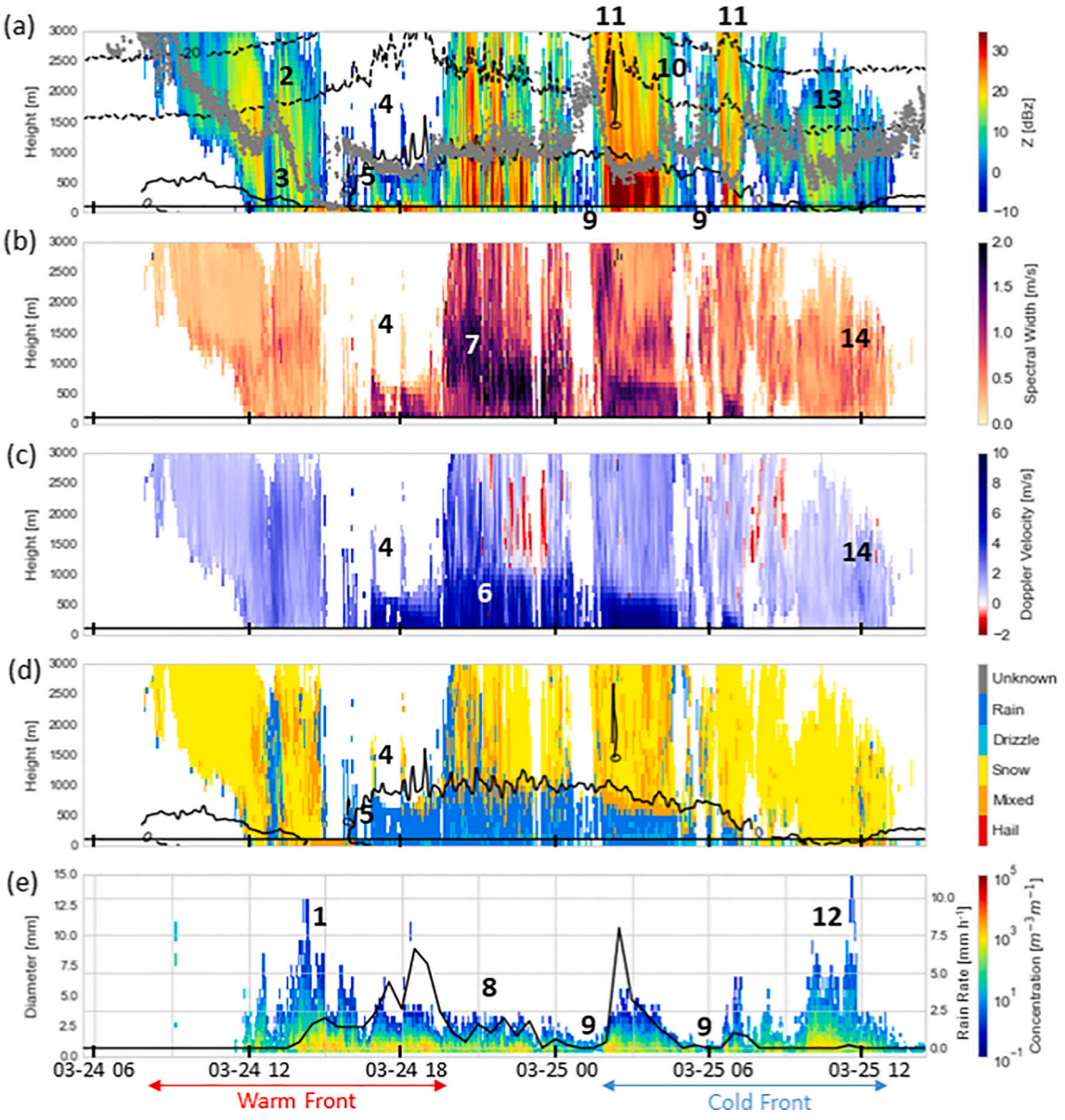

Fig. 9. Time series of the 24–25 March case study. (a) Radar reflectivity from MRR (above black horizontal line) and Parsivel (below black horizontal line). (b) Spectral Width from MRR. (c) Particle Doppler fall velocity from MRR. (d) Type of precipitation derived from MRR (above black horizontal line) and Parsivel (below black horizontal line). (e) Parsivel particle concentration as a function of the widest hydrometeor diameter and rain rate recorded by the LECD AWS. Dotted black lines and the grey points in (a) indicate isotherm levels derived from MWR and cloud base height derived from ceilometer, respectively. Black line in (d) indicates the MRR derived zero degrees isotherm. Numeric labels are text references.

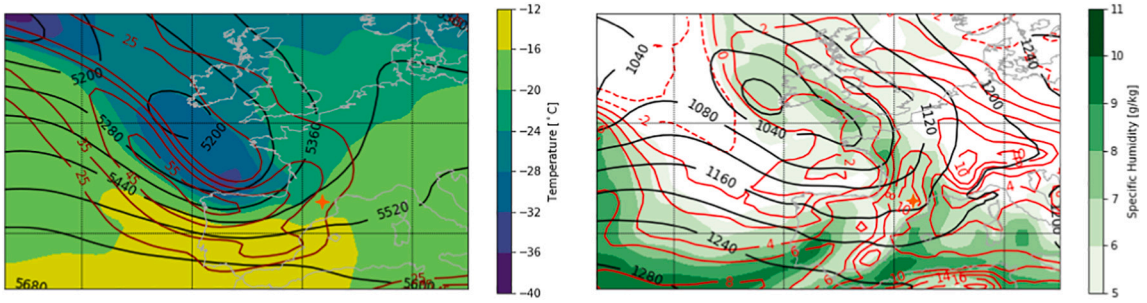

Fig. 10. As in Fig. 7 but for 30 April 2017 at 12:00 UTC.

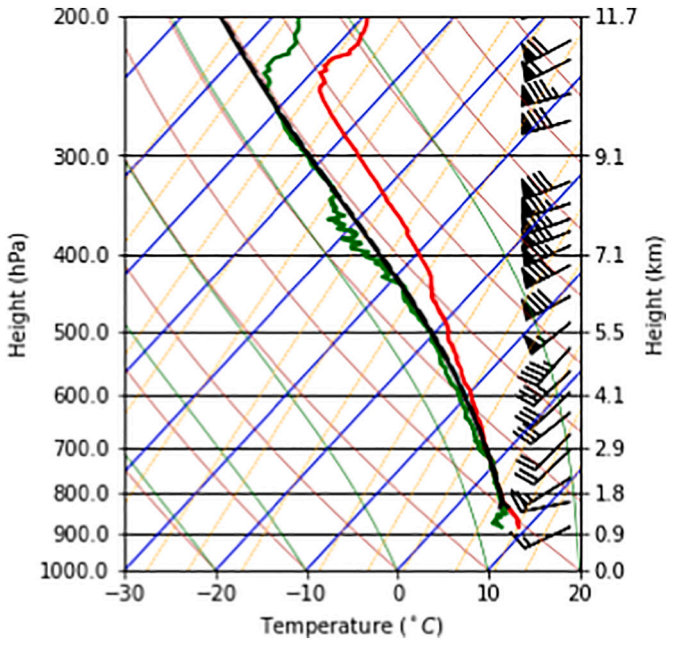

Fig. 11. As in Fig. 8 but for 30 April 2017 at 18:09 UTC.

very small raindrops indicates that shallow convection and coalescence processes do not dominate the winter precipitation of the valley (Martner et al., 2008). Instead, water vapour deposition and stratiform cold-ice processes are likely playing a major role. However, disdrometric characteristics measured during C2017 presented a large variability, indicating that not all precipitation was stratiform. Indeed Table 1 lists a few spring convection events in April (events #34, #35, #36 and #37).

Fig. 5 shows the relation between D_m, N_w and LWC grouped by rain rate computed with Parsivel. As rain rate increases, mean values of D_m, N_w and LWC also increase. However, distributions are overlapped for N_w and especially D_m. As stated in other studies (e.g. Bringi et al., 2003; Dolan et al., 2018), D_m–log(LWC) and log(N_w)–log(LWC) linear correlations are positive, and D_m–log(N_w) correlation is negative. However, the distribution of the parameters in the winter campaign is more similar to those in high-latitudes than those in mid-latitudes as evidenced by the near absence of measures of D_0 over 2 mm reported by Dolan et al. (2018).

To contextualize the measures obtained during C2017 we have represented in Fig. 6 all records on the D_0–log(N_w) space overlaid with the diagram made by Dolan et al. (2018) showing dominant precipitation mechanisms derived from their principal component analysis of global data (their Fig. 12). Note that most measures are located in the stratiform section of the plot, which is consistent with the disdrometric parameter values discussed at the beginning of this section. Fig. 6 suggests that the predominant rainfall regime during C2017 was stratiform precipitation, highly influenced by vapour deposition and aggregation and riming processes, but some convective events were also present. The later do not exhibit neither the characteristics of typical summer deep convection (ice-based processes) nor those of warm and weak convection (collision-coalescence processes). Instead, they are associated with moderate convection resulting in modest drop sizes of about 1 mm and moderate values of log(Nw) around 4.

5. Vertical structure of precipitation in selected case studies

Previous section showed the general features of precipitation during the campaign. However, these features change with from event to event and sometimes even within the same precipitation event. To illustrate inter-event variability, we selected two different cases of well-observed storms during the C2017 (with all the instruments available). A particularly interesting case of heavy snowfall was already investigated by Gonzalez et al. (2019), illustrating how precipitation profiles and disdrometric measurements of snow were decoupled from the mountain induced circulations despite the increased turbulence caused by an atmospheric rotor during a mountain wave event. They suggested that conditions that induce the decoupling are caused by low liquid water content and lack of dendritic form, that reduced both riming and aggregation. Here, we present a case with transition from snow to rain occurred between 24 and 25 March 2017, exhibiting an interesting sequence of different hydrometeors. This event was also studied by Soula et al. (2021), but focused in the analysis of winter thunderstorms during C2017. The second case analysed, which occurred at the end of the campaign on 30 April 2017, shows an early spring transition event with scattered liquid precipitation.

5.1. Case of 24–25 March 2017

5.1.1. Synoptic setting and vertical structure of the atmosphere

This case was characterized by a cut-off low located west to the Iberian Peninsula with a 500 hPa cold core of −33 °C at 12:00 UTC on 24 March. The interaction between the trough of the cut-off low and the Atlas Mountains produced a secondary low over the Mediterranean Sea north of Algeria that headed north to Catalonia (García-Moya et al., 1989). As the low advanced to our area of study, the system established a backward warm front that crossed the Cerdanya from the northeast and a warm and a moist flux that impinged to the Pyrenees from the southeast (Fig. 7). The two vortex systems whirled in a merry-go-round system producing a Fujiwhara effect (Fujiwhara, 1921). At the end of the day, a well-organized storm in a coma shape and isolated of the main low could be appreciated in the satellite images (Fig. S3). Finally, on 25 March at 12:00 UTC, cold front of the vortex crossed the Pyrenees.

One sounding was launched on 24 March at 22:34 UTC, coinciding with the moment of the strongest flux after the crossing of the warm front (Fig. 8 and S4). The temperature profile shows a single and homogeneous layer with conditional unstable stratification close to the surface up to 10 km *asl.* Moisture is high, especially below 4000 m *asl.* Wind is also strong and homogeneous in both direction and velocity, with around 30 m s^{-1} from the ESE over the 2000 m *asl.*

5.1.2. Microphysical and mesoscale evolution

Fig. 9 shows the evolution of the vertical structure of the low-level precipitation at the Cerdanya valley. The first stage of the event, from 9:00 to 17:00 UTC on 24 March was characterized by the arrival of cloud structures associated to the warm front. This arrival was observed by the ceilometer and the MRR as a progressive decrease of the cloud base and the onset of precipitation nearby the ground. Precipitation was observed as virga before 12:00 UTC and by the Parsivel as snow from 12:00 to 17:00 UTC. Effective reflectivity measured by Parsivel increased at 15:00 UTC when large precipitation particles were observed, probably snow aggregates (see label 1 in Fig. 9). A progressive increase of the temperature over 1000 m *agl* was observed from 10:00 UTC by the MWR (label 2). However, it is noticeable the decrease of the temperature at low levels at the same time (label 3). We hypothesize that the low-level cooling occurred due to the latent heat absorbed during the sublimation process of the solid precipitation (analysed in detail at Section 5.1.3). The wet snow accumulated over the MRR antenna dish attenuated the signal from 16:00 UTC when vertical profiles became unavailable (label 4). As evidenced by the DSD, precipitation continued first in solid phase and later in liquid phase. Signal was recovered at 20:00 UTC when snow over the antenna melted.

From 17:00 UTC on 24 March to 8:00 UTC on 25 March surface precipitation phase changed to rain and precipitation intensity increased to values over 2.5 mm h^{-1}. This stage initiated with a sudden increase of the low-level temperature at low levels that occurred when the air close to the ground became saturated (label 5). When the MRR signal was recovered, it is observed the increase of the downward Doppler velocity

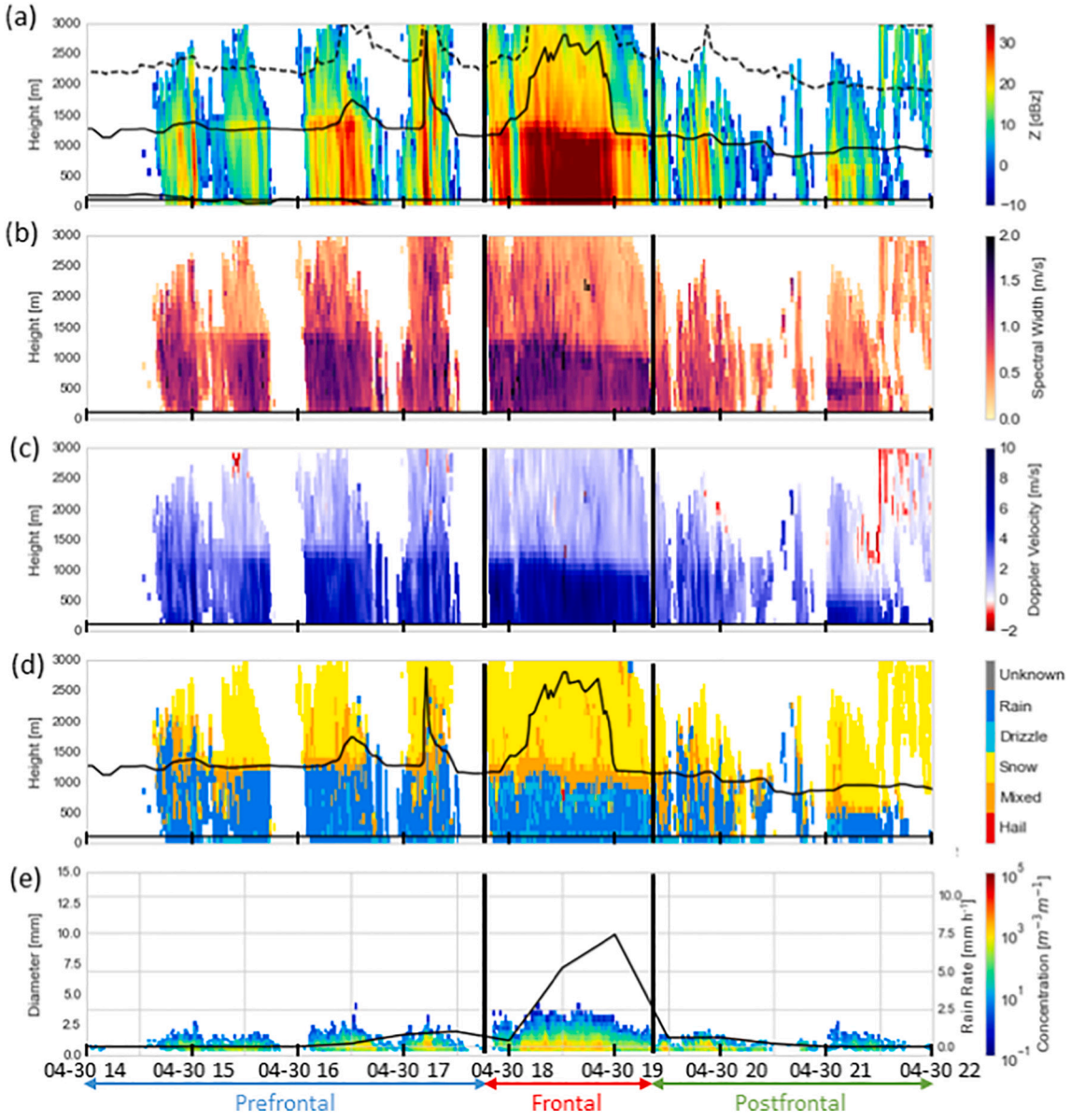

Fig. 12. As in Fig. 9 but for 30 April 2017.

of the precipitation particles as they melt with values over 4 m s^{-1} (label 6). It is noticeable as well, an increase of the spectral width over 2 m s^{-1} during this part of the event (label 7), approximately at the crest level suggesting the influence of a wind shear layer favoured by the decoupling of the stalled air of the valley and the air of the free atmosphere. The increase of the spectral width indicates enhanced turbulence that caused riming on the particles, which favoured the triggering of lightning flashes in the neighbourhood (Soula et al., 2021). DSD of the surface precipitation was homogeneous during this stage; raindrops were generally small, and the bigger ones did not exceed 4 mm (label 8). They decreased during the periods when precipitation was interrupted, probably reaching to the Parsivel only wind-blown small drops from the vicinity (label 9). From 02:00 UTC on 25 March atmospheric temperature steadily decreased indicating the passage of the cold front (label 10). Unlike the warm front, temperature dropped at a similar rate in the whole layer analysed. It can be noticed that the DSD of the rainfall during the cold front is similar to the one in the warm front, with the same D_m and only a small change in N_w, being higher during the warm front (Fig. 3). During this stage it was also observed a characteristic signature of the temperature profiles when the precipitation was enhanced: the presence of a warm bias of the temperature caused by the emission of the water at similar frequencies used by the MWR (Knupp et al., 2009) (label 11).

At 8:00 UTC on 25 March, precipitation phase changed again over LECD becoming snow. Parsivel measured large particles, probably snow aggregates (label 12). This is consistent with the height of the precipitation growing located between −10 and −20 °C (label 13). Around −15 °C, the conditions for dendritic growth increase (Kobayashi, 1967) and particles are more sensible to aggregating owing to mechanical entanglement (Rauber, 1987). Turbulence decreased during this stage, nonetheless, small areas of increased turbulence concur with greater downward Doppler velocities and increased aggregation (label 14). These areas may correspond to overturning cells with larger mechanical aggregation of dendrites (Aikins et al., 2016).

5.1.3. *Effect of the sublimation during the warm front passage*

Here, we study the role of the sublimation on the low-level cooling during the passage of the warm front. As observed at the surface station at LECD, temperature decreased 5.5 °C in 5 h, from 5.3 °C at 11:30 UTC to −0.2 °C at 16:30 UTC (Fig. S5). Similarly, relative humidity increased

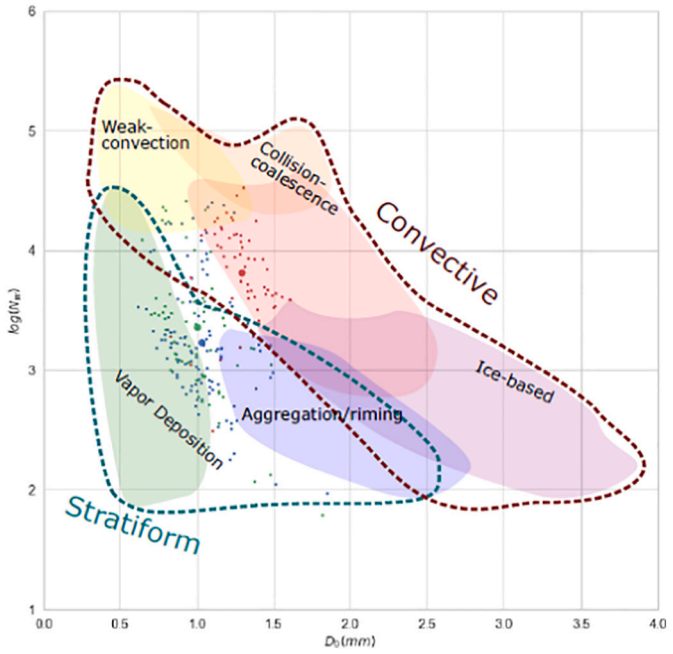

Fig. 13. As in Fig. 6 but for the measurements on 30 April 2017. Blue dots indicate pre-frontal precipitation, red dots indicate frontal precipitation and green dots indicate post-frontal precipitation. Big dots indicate the mean value of each period. (For interpretation of the references to colour in this figure legend, the reader is referred to the web version of this article.)

63% from 36% to 99%, while pressure remained almost constant at around 980 hPa. This corresponds to an increase of 2 g of water vapour per kg of air. Assuming that the increase of the humidity is produced entirely by sublimation of the solid particles falling from aloft, the absorption of latent heat would produce a cooling of 5.6 °C that is compatible with the observations. This process implies that air exchange is suppressed, which is a good assumption in an enclosed inner valley with low ventilation. This is further confirmed by low wind observations recorded at the bottom of the valley.

5.2. Case of 30 April 2017

5.2.1. Synoptic setting and vertical structure of the low troposphere

This event was characterized by a trough over the North Atlantic crossing rapidly from west to east the Iberian Peninsula. Downstream side of the trough with a diffluent pattern was located over our area of study at 12:00 UTC (Fig. 10). A deep surface low associated to the trough deepened south-west to the British Islands. The associated synoptic cold front crossed the Iberian Peninsula from west to east, reaching to eastern Pyrenees in the afternoon.

Two soundings were launched during this event. The first one was released at 12:05 UTC before the front passage and the second at 18:09 UTC when the front was crossing the area of study. Thermodynamic conditions previous to the front (Fig. S6) showed the presence of a moist and well-mixed layer more than 3000 m deep over the ground. Separated by a stable layer, there was a very dry and almost neutrally stratified layer above. Satellite images showed the presence of trapped lee waves before the front caused by this inversion. In the second sounding inside the front (Fig. 11 and S7), the separation between layers became suppressed. The front, which was modified at low levels by the mountains, produced an important moistening and cooling on the inversion layer. Furthermore, in this layer temperature dropped strongly. However, at low levels the front barely changed the vertical temperature profile, and only increased slightly the stratification stability. Similarly, to the previous case, a single layer with conditional instable stratification was developed. Wind blew from the WSW at all tropospheric levels, with small shear at low levels but increasing at middle and upper levels.

5.2.2. Microphysical and mesoscale evolution

Fig. 12 shows the evolution of this event. The weather station at LECD (Fig. S8) measured a progressive decrease of the temperature owing to the cold front passage falling 9 °C in 12 h. Over the station the decrease was less pronounced and started later. As previously stated, large increases in MWR temperature (sudden rise of more than 10 °C) are probably due by the emission of raindrops in the reception bands of the MWR (Knupp et al., 2009). Melting layer was well observed, evidenced by a sudden increase of the Doppler velocity and spectral width. It was located around 1200 m *agl* height until 18:30 and steadily decreased afterwards. This level is close to the crest level, but no clear evidence of a wind shear layer favoured by the decoupling of the air valley and the free atmosphere is found unlike the previous case study.

We divided the event in three stages: prefrontal stage, frontal stage and postfrontal stage. At the prefrontal stage, precipitation started with light and intermittent showers of less than 2 mm h^{-1}. Parsivel measured low surface concentration of small drops of less than 2 mm. As the main frontal band approached, reflectivity increased, and the surface median drop size and concentration increased. The frontal stage, between 18:00 and 19:00 UTC, was the period of highest precipitation intensity that reached 7.5 mm h^{-1} in 30 min. During this period the reflectivity of the whole column increased, especially below the melting layer, exceeding 35 dBZ. Surface raindrop concentration largely increased and drop particles reached 4 mm. After 19 UTC the precipitation decreased, and the concentration and size of the hydrometeors as well. During the dissipating stage raindrops did not exceed 2 mm diameter. Melting layer height decreased to 700 m. Precipitation continued intermittently until

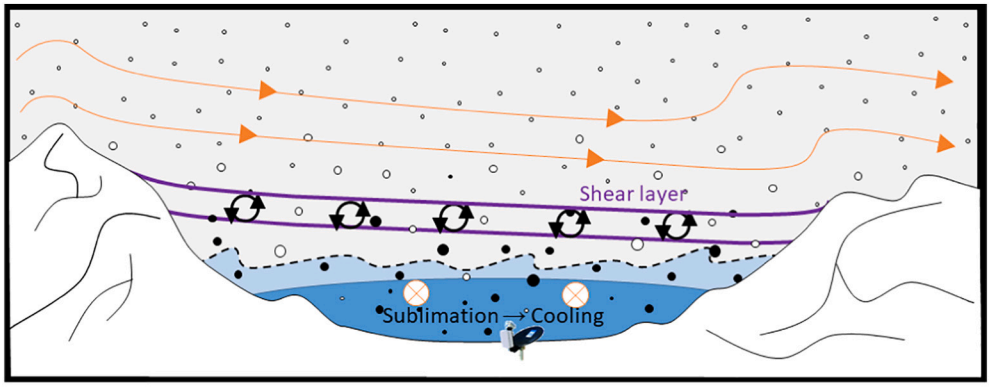

Fig. 14. Conceptual model of winter precipitation in Cerdanya valley from the study of MRR profiles showing the most relevant features: unrimed ice and snow particles (white circles), rimed ice and snow particles (black circles), free atmosphere layers (orange lines), shear layer (purple lines) that decouples the free atmosphere and the stagnant valley air at the valley bottom (dark blue layer) and the cloud base (dashed black line). Around the shear layer turbulence increases, and snow particles grow downward and become rimed by the turbulence. Near the valley floor, snow particles sublimate, cooling the bottom air layer. (For interpretation of the references to colour in this figure legend, the reader is referred to the web version of this article.)

22:00 UTC but virga was observed by MRR afterwards.

Fig. 13 shows the Parsivel measurements during this event into a D_0–log(N_w) space diagram. During the front passage, D_0 remained in a narrow range of 0.7–1.5 mm. Log(N_w) had a greater variation ranging between 2.5 and 4.5. During the event two main microphysical processes were observed. In the prefrontal and postfrontal stages, stratiform precipitation dominated, especially by vapour deposition process, presenting a similar DSD at both stages (Fig. 3). However, in the frontal stage convective precipitation dominated, with much higher N(D) for all drop diameters (Fig. 3), and although there was no clear dominating process, collision-coalescence may had played a major role. Although precipitation occurred far from the coast, ice-based processes seemed to be supressed only during the convective period.

6. Concluding remarks

Throughout this article we examined the precipitation data obtained in a wide inner valley of the Pyrenees during the Cerdanya-2017 field campaign. The analysis of the MRR average profiles during the snow events, shows the presence of a persistent shear layer over the valley that decouples the stalled air of the valley and the free atmosphere over the mountains (Gonzalez et al., 2019; Medina et al., 2005). Generally, shear layer increases the turbulence of the air promoting riming of the ice and snow particles as suggested by the patterns observed on average MRR profiles during the campaign. However, occasionally, as in the case studied by Gonzalez et al. (2019), precipitating ice particles may not be affected by riming on these conditions. Other relevant precipitation processes are revealed by the vertical MRR profiles and MWR profiles and the surface data during snow and mixed events such as the cooling effect of the sublimation during the passage of the warm front in the 24 March event. A summary of the effects of the wind shear layer located at crest level and sublimation at the valley bottom upon solid precipitation processes during C2017 is illustrated in a schematic conceptual model shown in Fig. 14.

During the rain periods at the bottom of the valley, our results show that LWC is relatively low compared with other experimental campaigns on mountain environments in similar latitudes, despite its proximity to the Mediterranean Sea. This is probably due to the geographic conditions of the enclosed inner valley, which prevents the advection of moist flows from both Atlantic and Mediterranean. Two principal regimes of rainfall are found during the campaign: (1) stratiform rainfall mainly produced by water vapour deposition processes, although sometimes riming and aggregation become important, and (2) weak convection with slight dominance of collision-coalescence processes. The second one occurs mainly during the frontal passage of 30 April, and during the early spring convective events.

Compared to previous field campaigns devoted to study winter precipitation in mountain areas, the analysis of precipitation events during C2017 contributes to improve our understanding on winter precipitation microphysical processes in an inner valley. The results of this paper suggest that (1) despite being close to the sea, the inner valley favours a cold continental environment and (2) the presence of the wind shear layer may decouple the stalled air of the valley from the free atmosphere inducing turbulent overturning cells that enhances snow growth. Future work could include the comparison of observed vertical precipitation profiles presented and discussed here with those of numerical model prediction systems to assess their capacity in describing the complexities of winter precipitation in inner valleys.

Funding sources

This work was funded by the Spanish Agencia Estatal de Investigación (AEI) and Fondo Europeo al Desarrollo Regional (FEDER) [grant numbers CGL2015-65627-C3-1-R, CGL2015-65627-C3-2-R, CGL2016-81828-REDT, RTI2018-098693-B-C32] the Water Research Institute (IdRA) of the University of Barcelona and the Generalitat de Catalunya through the ANTALP Research Group [grant number 2017 SGR 1102].

Declaration of Competing Interest

The authors declare that they have no known competing financial interests or personal relationships that could have appeared to influence the work reported in this paper.

Acknowledgments

The Cerdanya-2017 field campaign is a research effort organized by the University of the Balearic Islands, the University of Barcelona. We want to acknowledge the three anonymous reviewers, which through their comments helped to substantially improve the final form of this manuscript.

Appendix A. Supplementary data

Supplementary data to this article can be found online at https://doi.org/10.1016/j.atmosres.2021.105826.

References

Aikins, J., Friedrich, K., Geerts, B., Pokharel, B., 2016. Role of a cross-barrier jet and turbulence on winter orographic snowfall. Mon. Weather Rev. 144, 3277–3300. https://doi.org/10.1175/MWR-D-16-0025.1.

Arulraj, M., Barros, A.P., 2021. Automatic detection and classification of low-level orographic precipitation processes from space-borne radars using machine learning. Remote Sens. Environ. 257, 112355. https://doi.org/10.1016/j.rse.2021.112355.

Atlas, D., Srivastava, R.C., Sekhon, R.S., 1973. Doppler radar characteristics of precipitation at vertical incidence. Rev. Geophys. 11, 1–35. https://doi.org/10.1029/RG011i001p00001.

Bech, J., Codina, B., Lorente, J., Bebbington, D., 2003. The sensitivity of single polarization weather radar beam blockage correction to variability in the vertical refractivity gradient. J. Atmos. Ocean. Technol. 20, 845–855. https://doi.org/10.1175/1520-0426(2003)020<0845:TSOSPW>2.0.CO;2.

Bech, J., Gjertsen, U., Haase, G., 2007. Modelling weather radar beam propagation and topographical blockage at northern high latitudes. Q. J. R. Meteorol. Soc. 133, 1191–1204. https://doi.org/10.1002/qj.98.

Bringi, V.N., Chandrasekar, V., Hubbert, J., Gorgucci, E., Randeu, W.L., Schoenhuber, M., 2003. Raindrop size distribution in different climatic regimes from disdrometer and dual-polarized radar analysis. J. Atmos. Sci. 60, 354–365. https://doi.org/10.1175/1520-0469(2003)060<0354:RSDIDC>2.0.CO;2.

Buisan, S.T., Saz, M.A., López-Moreno, J.I., 2015. Spatial and temporal variability of winter snow and precipitation days in the western and central Spanish Pyrenees. Int. J. Climatol. 35, 259–274. https://doi.org/10.1002/joc.3978.

Buisán, S.T., Earle, M.E., Collado, J.L., Kochendorfer, J., Alastrué, J., Wolff, M., Smith, C. D., López-Moreno, J.I., 2017. Assessment of snowfall accumulation underestimation by tipping bucket gauges in the Spanish operational network. Atmos. Meas. Tech. 10, 1079–1091. https://doi.org/10.5194/amt-10-1079-2017.

Cao, Q., Zhang, G., 2009. Errors in estimating raindrop size distribution parameters employing disdrometer and simulated raindrop spectra. J. Appl. Meteorol. Climatol. 48, 406–425. https://doi.org/10.1175/2008JAMC2026.1.

Casanovas, C., Salio, P., Galligani, V., Dolan, B., Nesbitt, S.W., 2021. Drop size distribution variability in central Argentina during relampago-cacti. Remote Sens. 13, 2026. https://doi.org/10.3390/rs13112026.

Casellas, E., Bech, J., Veciana, R., Pineda, N., Rigo, T., Miró, J.R., Sairouni, A., 2021. Surface precipitation phase discrimination in complex terrain. J. Hydrol. 592, 125780. https://doi.org/10.1016/j.jhydrol.2020.125780.

Conangla, L., Cuxart, J., Jiménez, M.A., Martínez-Villagrasa, D., Miró, J.R., Tabarelli, D., Zardi, D., 2018. Cold-air pool evolution in a wide Pyrenean valley. Int. J. Climatol. 38, 2852–2865. https://doi.org/10.1002/joc.5467.

Costa-Surós, M., Calbó, J., González, J.A., Martin-Vide, J., 2013. Behavior of cloud base height from ceilometer measurements. Atmos. Res. 127, 64–76. https://doi.org/10.1016/J.ATMOSRES.2013.02.005.

Das, S.K., Konwar, M., Chakravarty, K., Deshpande, S.M., 2017. Raindrop size distribution of different cloud types over the Western Ghats using simultaneous measurements from Micro-Rain Radar and disdrometer. Atmos. Res. 186, 72–82. https://doi.org/10.1016/j.atmosres.2016.11.003.

Dolan, B., Fuchs, B., Rutledge, S.A., Barnes, E.A., Thompson, E.J., 2018. Primary modes of global drop size distributions. J. Atmos. Sci. 75, 1453–1476. https://doi.org/10.1175/JAS-D-17-0242.1.

Durán-alarcón, C., Boudevillain, B., Genthon, C., Grazioli, J., Souverijns, N., Van Lipzig, N.P.M., Gorodetskaya, I., Berne, A., 2018. The vertical structure of precipitation at two stations in East Antarctica derived from micro rain radars. Cryosph. Discuss. 1–24. https://doi.org/10.5194/tc-2018-153.

Fujiwhara, S., 1921. The natural tendency towards symmetry of motion and its application as a principle in meteorology. Q. J. R. Meteorol. Soc. 47, 287–292. https://doi.org/10.1002/qj.49704720010.
Galmarini, S., Steyn, D.G., Ainslie, B., 2004. The scaling law relating world point-precipitation records to duration. Int. J. Climatol. 24, 533–546. https://doi.org/10.1002/joc.1022.
Garcia-Benadi, A., Bech, J., Gonzalez, S., Udina, M., Codina, B., Georgis, J.F., 2020. Precipitation type classification of micro rain radar data using an improved doppler spectral processing methodology. Remote Sens. 12, 1–23. https://doi.org/10.3390/rs12244113.
García-Moya, J.A., Jansà, A., Díaz-Pabon, R., Rodríguez, E., 1989. Factor influencing the Algerian sea cyclogenesis. In: WMO|TD, 298, pp. 87–94.
Garvert, M.F., Smull, B., Mass, C., 2007. Multiscale Mountain waves influencing a major orographic precipitation event. J. Atmos. Sci. 64, 711–737. https://doi.org/10.1175/jas3876.1.
Geerts, B., Miao, Q., Yang, Y., 2011. Boundary layer turbulence and orographic precipitation growth in cold clouds: evidence from profiling airborne radar data. J. Atmos. Sci. 68, 2344–2365. https://doi.org/10.1175/JAS-D-10-05009.1.
Gonzalez, S., Bech, J., 2017. Extreme point rainfall temporal scaling: a long term (1805–2014) regional and seasonal analysis in Spain. Int. J. Climatol. 37, 5068–5079. https://doi.org/10.1002/joc.5144.
Gonzalez, S., Bech, J., Udina, M., Codina, B., Paci, A., Trapero, L., 2019. Decoupling between precipitation processes and mountain wave induced circulations observed with a vertically pointing K-band Doppler Radar. Remote Sens. 11, 1034. https://doi.org/10.3390/RS11091034.
Gorodetskaya, I.V., Kneifel, S., Maahn, M., Thiery, W., Schween, J.H., Mangold, A., Crewell, S., Van Lipzig, N.P.M., 2015. Cloud and precipitation properties from ground-based remote-sensing instruments in East Antarctica. Cryosphere 9, 285–304. https://doi.org/10.5194/tc-9-285-2015.
Hachani, S., Boudevillain, B., Delrieu, G., Bargaoui, Z., 2017. Drop size distribution climatology in Cévennes-Vivarais region, France. Atmosphere (Basel) 8, 233. https://doi.org/10.3390/atmos8120233.
Houze, R.A., 2012. Orographic effects on precipitating clouds. Rev. Geophys. 50, RG1001 https://doi.org/10.1029/2011RG000365.
Houze, R.A., McMurdie, L.A., Petersen, W.A., Schwall Er, M.R., Baccus, W., Lundquist, J. D., Mass, C.F., Nijssen, B., Rutledge, S.A., Hudak, D.R., Tanelli, S., Mace, G.G., Poellot, M.R., Lettenmaier, D.P., Zagrodnik, J.P., Rowe, A.K., DeHart, J.C., Madaus, L.E., Barnes, H.C., 2017. The olympic mountains experiment (Olympex). Bull. Am. Meteorol. Soc. 98, 2167–2188. https://doi.org/10.1175/BAMS-D-16-0182.1.
Ji, L., Chen, H., Li, L., Chen, B., Xiao, X., Chen, M., Zhang, G., 2019. Raindrop size distributions and rain characteristics observed by a PARSIVEL disdrometer in Beijing, Northern China. Remote Sens. 11, 1479. https://doi.org/10.3390/rs11121479.
Knupp, K.R., Ware, R., Cimini, D., Vandenberghe, F., Vivekanandan, J., Westwater, E., Coleman, T., Phillips, D., 2009. Ground-based passive microwave profiling during dynamic weather conditions. J. Atmos. Ocean. Technol. 26, 1057–1073. https://doi.org/10.1175/2008JTECHA1150.1.
Kobayashi, T., 1967. On the variation of ice crystal habit with temperature. Phys. Snow Ice 1, 95–104.
Kochendorfer, J., Nitu, R., Wolff, M., Mekis, E., Rasmussen, R., Baker, B., Earle, M.E., Reverdin, A., Wong, K., Smith, C.D., Yang, D., Roulet, Y.A., Buisan, S., Laine, T., Lee, G., Aceituno, J.L.C., Alastrué, J., Isaksen, K., Meyers, T., Brækkan, R., Landolt, S., Jachcik, A., Poikonen, A., 2017a. Analysis of single-Alter-shielded and unshielded measurements of mixed and solid precipitation from WMO-SPICE. Hydrol. Earth Syst. Sci. 21, 3525–3542. https://doi.org/10.5194/hess-21-3525-2017.
Kochendorfer, J., Rasmussen, R., Wolff, M., Baker, B., Hall, M.E., Meyers, T., Landolt, S., Jachcik, A., Isaksen, K., Brækkan, R., Leeper, R., 2017b. The quantification and correction of wind-induced precipitation measurement errors. Hydrol. Earth Syst. Sci. 21, 1973–1989. https://doi.org/10.5194/hess-21-1973-2017.
Konwar, M., Das, S.K., Deshpande, S.M., Chakravarty, K., Goswami, B.N., 2014. Microphysics of clouds and rain over the Western Ghat. J. Geophys. Res. 119, 6140–6159. https://doi.org/10.1002/2014JD021606.
Kumar, S., Del Castillo-Velarde, C., Prado, J.M.V., Rojas, J.L.F., Gutierrez, S.M.C., Alvarez, A.S.M., Martine-Castro, D., Silva, Y., 2020. Rainfall characteristics in the mantaro basin over tropical andes from a vertically pointed profile rain radar and in-situ field campaign. Atmosphere (Basel) 11, 248. https://doi.org/10.3390/atmos11030248.
Lasanta, T., Laguna, M., Vicente-Serrano, S.M., 2007. Do tourism-based ski resorts contribute to the homogeneous development of the Mediterranean mountains? A case study in the Central Spanish Pyrenees. Tour. Manag. 28, 1326–1339. https://doi.org/10.1016/j.tourman.2007.01.003.
Lemus-Canovas, M., Lopez-Bustins, J.A., Trapero, L., Martin-Vide, J., 2019. Combining circulation weather types and daily precipitation modelling to derive climatic precipitation regions in the Pyrenees. Atmos. Res. 220, 181–193. https://doi.org/10.1016/j.atmosres.2019.01.018.
Löffler-Mang, M., Joss, J., 2000. An optical disdrometer for measuring size and velocity of hydrometeors. J. Atmos. Ocean. Technol. 17, 130–139. https://doi.org/10.1175/1520-0426(2000)017<0130:AODFMS>2.0.CO;2.
López-Moreno, J.I., Beguería, S., García-Ruiz, J.M., 2002. Influence of the Yesa reservoir on floods of the Aragón River, central Spanish Pyrenees. Hydrol. Earth Syst. Sci. 6, 753–762. https://doi.org/10.5194/hess-6-753-2002.
López-Moreno, J.I., Zabalza, J., Vicente-Serrano, S.M., Revuelto, J., Gilaberte, M., Azorin-Molina, C., Morán-Tejeda, E., García-Ruiz, J.M., Tague, C., 2014. Impact of climate and land use change on water availability and reservoir management: scenarios in the Upper Arago'n River, Spanish Pyrenees. Sci. Total Environ. 493, 1222–1231. https://doi.org/10.1016/j.scitotenv.2013.09.031.
Maahn, M., Kollias, P., 2012. Improved Micro Rain Radar snow measurements using Doppler spectra post-processing. Atmos. Meas. Tech. 5, 2661–2673. https://doi.org/10.5194/amt-5-2661-2012.
Maahn, M., Burgard, C., Crewell, S., Gorodetskaya, I.V., Kneifel, S., Lhermitte, S., Van Tricht, K., Van Lipzig, N.P.M., 2014. How does the spaceborne radar blind zone affect derived surface snowfall statistics in polar regions? J. Geophys. Res. 119, 13,604–13,620. https://doi.org/10.1002/2014JD022079.
Martner, B.E., Yuter, S.E., White, A.B., Matrosov, S.Y., Kingsmill, D.E., Ralph, F.M., 2008. Raindrop size distributions and rain characteristics in California coastal rainfall for periods with and without a radar bright band. J. Hydrometeorol. 9, 408–425. https://doi.org/10.1175/2007JHM924.1.
Medina, S., Houze, R.A., 2003. Air motions and precipitation growth in Alpine storms. Q. J. R. Meteorol. Soc. 129, 345–371. https://doi.org/10.1256/qj.02.13.
Medina, S., Houze, R.A., 2015. Small-scale precipitation elements in midlatitude cyclones crossing the California Sierra Nevada. Mon. Weather Rev. 143, 2842–2870. https://doi.org/10.1175/MWR-D-14-00124.1.
Medina, S., Smull, B.F., Houze, R.A., Steiner, M., 2005. Cross-barrier flow during orographic precipitation events: results from MAP and IMPROVE. J. Atmos. Sci. 62, 3580–3598. https://doi.org/10.1175/JAS3554.1.
Minder, J.R., Letcher, T.W., Campbell, L.S., Veals, P.G., Steenburgh, W.J., 2015. The evolution of lake-effect convection during landfall and orographic uplift as observed by profiling radars. Mon. Weather Rev. 143, 4422–4442. https://doi.org/10.1175/MWR-D-15-0117.1.
Miró, J.R., Peña, J.C., Pepin, N., Sairouni, A., Aran, M., 2018. Key features of cold-air pool episodes in the northeast of the Iberian Peninsula (Cerdanya, eastern Pyrenees). Int. J. Climatol. 38, 1105–1115. https://doi.org/10.1002/joc.5236.
Murata, F., Terao, T., Chakravarty, K., Syiemlieh, H.J., Cajee, L., 2020. Characteristics of orographic rain drop-size distribution at Cherrapunji, Northeast India. Atmosphere (Basel) 11, 777. https://doi.org/10.3390/ATMOS11080777.
OTT Hydromet GmbH, 2016. Operating Instructions Present Weather Sensor OTT Parsivel 2.
Pagès, M., Pepin, N., Miró, J.R., 2017. Measurement and modelling of temperature cold pools in the Cerdanya valley (Pyrenees), Spain. Meteorol. Appl. 24, 290–302. https://doi.org/10.1002/met.1630.
Pérez-Zanón, N., Sigró, J., Ashcroft, L., 2017. Temperature and precipitation regional climate series over the central Pyrenees during 1910–2013. Int. J. Climatol. 37, 1922–1937. https://doi.org/10.1002/joc.4823.
Peters, G., Fischer, B., Münster, H., Clemens, M., Wagner, A., 2005. Profiles of raindrop size distributions as retrieved by Microrain Radars. J. Appl. Meteorol. 44, 1930–1949. https://doi.org/10.1175/JAM2316.1.
Prat, O.P., Barros, A.P., 2010. Ground observations to characterize the spatial gradients and vertical structure of orographic precipitation - experiments in the inner region of the Great Smoky Mountains. J. Hydrol. 391, 141–156. https://doi.org/10.1016/j.jhydrol.2010.07.013.
Rasmussen, R., Baker, B., Kochendorfer, J., Meyers, T., Landolt, S., Fischer, A.P., Black, J., Thériault, J.M., Kucera, P., Gochis, D., Smith, C., Nitu, R., Hall, M., Ikeda, K., Gutmann, E., 2012. How well are we measuring snow: the NOAA/FAA/NCAR winter precipitation test bed. Bull. Am. Meteorol. Soc. 93, 811–829. https://doi.org/10.1175/BAMS-D-11-00052.1.
Rauber, R.M., 1987. Characteristics of cloud ice and precipitation during wintertime storms over the mountains of northern Colorado. J. Clim. Appl. Meteor. 26, 488–524. https://doi.org/10.1175/1520-0450(1987)026<0488:COCIAP>2.0.CO;2.
Raupach, T.H., Berne, A., 2015. Correction of raindrop size distributions measured by Parsivel disdrometers, using a two-dimensional video disdrometer as a reference. Atmos. Meas. Tech. 8, 343–365. https://doi.org/10.5194/amt-8-343-2015.
Roe, G.H., 2005. Orographic precipitation. Annu. Rev. Earth Planet. Sci. 33, 645–671. https://doi.org/10.1146/annurev.earth.33.092203.122541.
Rosenfeld, D., Ulbrich, C.W., 2003. Cloud microphysical properties, processes, and rainfall estimation opportunities. Meteorol. Monogr. 30, 237–258. https://doi.org/10.1175/0065-9401(2003)030<0237:CMPPAR>2.0.CO;2.
Seidel, J., Trachte, K., Orellana-Alvear, J., Figueroa, R., Célleri, R., Bendix, J., Fernandez, C., Huggel, C., 2019. Precipitation characteristics at two locations in the tropical Andes by means of vertically pointing micro-rain radar observations. Remote Sens. 11, 2985. https://doi.org/10.3390/rs11242985.
Soula, S., Pineda, N., Georgis, J.F., Leroy, A., Vanpoucke, I., Montanyà, J., Casellas, E., Gonzalez, S., Bech, J., 2021. On the conditions for winter lightning at the Eagle Nest Tower (2537 m asl) during the Cerdanya-2017 field experiment. Atmos. Res. 247, 105208. https://doi.org/10.1016/j.atmosres.2020.105208.
Souverijns, N., Gossart, A., Lhermitte, S., Gorodetskaya, I.V., Kneifel, S., Maahn, M., Bliven, F.L., van Lipzig, N.P.M., 2017. Estimating radar reflectivity - snowfall rate relationships and their uncertainties over Antarctica by combining disdrometer and radar observations. Atmos. Res. 196, 211–223. https://doi.org/10.1016/j.atmosres.2017.06.001.
Stark, D., Colle, B.A., Yuter, S.E., 2013. Observed microphysical evolution for two East Coast winter storms and the associated snow bands. Mon. Weather Rev. 141, 2037–2057. https://doi.org/10.1175/MWR-D-12-00276.1.
Suh, S.H., Kim, H.J., Lee, D.I., Kim, T.H., 2021. Geographical characteristics of raindrop size distribution in the southern parts of South Korea. J. Appl. Meteorol. Climatol. 60, 157–169. https://doi.org/10.1175/JAMC-D-20-0102.1.
Testud, J., Oury, S.P., Black, R.A., Amayenc, P., Dou, X., 2001. The concept of "'normalized'" distribution to describe raindrop spectra: a tool for cloud physics and cloud remote sensing. J. Appl. Meteorol. 40, 1118–1140. https://doi.org/10.1175/1520-0450(2001)040<1118:TCONDT>2.0.CO;2.

Tokay, A., Short, D.A., 1996. Evidence from tropical raindrop spectra of the origin of rain from stratiform versus convective clouds. J. Appl. Meteorol. 35, 355–371. https://doi.org/10.1175/1520-0450(1996)035<0355:EFTRSO>2.0.CO;2.

Toloui, M., Riley, S., Hong, J., Howard, K., Chamorro, L.P., Guala, M., Tucker, J., 2014. Measurement of atmospheric boundary layer based on super-large-scale particle image velocimetry using natural snowfall. Exp. Fluids 55, 1737. https://doi.org/10.1007/s00348-014-1737-1.

Trapero, L., Bech, J., Rigo, T., Pineda, N., Forcadell, D., 2009. Uncertainty of precipitation estimates in convective events by the Meteorological Service of Catalonia radar network. Atmos. Res. 93, 408–418. https://doi.org/10.1016/j.atmosres.2009.01.021.

Trapero, L., Bech, J., Duffourg, F., Esteban, P., Lorente, J., 2013a. Mesoscale numerical analysis of the historical November 1982 heavy precipitation event over Andorra (Eastern Pyrenees). Nat. Hazards Earth Syst. Sci. 13, 2969–2990. https://doi.org/10.5194/nhess-13-2969-2013.

Trapero, L., Bech, J., Lorente, J., 2013b. Numerical modelling of heavy precipitation events over Eastern Pyrenees: analysis of orographic effects. Atmos. Res. 123, 368–383. https://doi.org/10.1016/j.atmosres.2012.09.014.

Udina, M., Bech, J., Gonzalez, S., Soler, M.R., Paci, A., Miró, J.R., Trapero, L., Donier, J. M., Douffet, T., Codina, B., Pineda, N., 2020. Multi-sensor observations of an elevated rotor during a mountain wave event in the Eastern Pyrenees. Atmos. Res. 234, 104698. https://doi.org/10.1016/j.atmosres.2019.104698.

Ulbrich, C.W., Atlas, D., 1998. Rainfall microphysics and radar properties: analysis methods for drop size spectra. J. Appl. Meteorol. 37, 912–923. https://doi.org/10.1175/1520-0450(1998)037<0912:RMARPA>2.0.CO;2.

Villalobos-Puma, E., Martinez-Castro, D., Flores-Rojas, J.L., Saavedra-Huanca, M., Silva-Vidal, Y., 2020. Diurnal cycle of raindrops size distribution in a valley of the peruvian central Andes. Atmosphere (Basel) 11, 38. https://doi.org/10.3390/ATMOS11010038.

Wen, L., Zhao, K., Zhang, G., Xue, M., Zhou, B., Liu, S., Chen, X., 2016. Statistical characteristics of raindrop size distributions observed in East China during the asian summer monsoon season using 2-D video disdrometer and micro rain radar data. J. Geophys. Res. 121, 2265–2282. https://doi.org/10.1002/2015JD024160.

Wen, L., Zhao, K., Zhang, G., Liu, S., Chen, G., 2017. Impacts of instrument limitations on estimated raindrop size distribution, radar parameters, and model microphysics during mei-yu season in east China. J. Atmos. Ocean. Technol. 34, 1021–1037. https://doi.org/10.1175/JTECH-D-16-0225.1.

Willis, P.T., 1984. Functional fits to some observed drop size distributions and parameterization of rain. J. Atmos. Sci. 41, 1648–1661. https://doi.org/10.1175/1520-0469(1984)041<1648:FFTSOD>2.0.CO;2.

WMO, 1994. World Meteorological Organization Guide to Hydrological Practices, 5th ed. (Geneva, Switzerland).

WMO, 2014. Measurement of precipitation. In: Guide to Meteorological Instruments and Methods of Observation. World Meteorological Organization (WMO), Geneva, Switzerland, pp. 186–221.

Xercavins, A., 1985. Els climes del Pirineu Oriental: des de les terres gironines fins a la Catalunya Nord i Andorra. Doc. d'Anàlisi Geogr. 7, 81–102.

Capítol 4

Classificació d'hidrometeors mitjançant observacions de perfilador de vent

4.1. Desenvolupament d'una metodologia de classificació d'hidrometeors (UBWPP)

4.1.1. Resum

L'equip sobre el que s'ha desenvolupat la metodologia de classificació d'hidrometeors és un radar polsat de mira vertical que treballa en freqüència ultra alta (UHF) de la marca Degreane, model PCL1300, dissenyat com a perfilador de vent. En aquest cas l'equip genera un senya mitjançant un emissor i rep l'energia retrodispersada, tant de les molècules d'aire com de les partícules d'hidrometeors precipitants. Aquest emissor és modular, i s'utilitzen 5 mòduls que es posicionen en diferents angles respecte la vertical i l'azimut, que permet no només calcular el perfil del vent vertical sinó que també estima la velocitat meridional i zonal. Un avantatge important de l'equip és la manca d'atenuació per precipitació, ja que la seva longitud d'ona és molt més gran que la mida dels hidrometeors.

El processat proposat és una alternativa a dos ja existents: un per part del fabricant, i l'altre elaborat pel *Laboratoire d'Aerologie* de la Universitat de Toulouse, amb el nom d'ALWPP (Campistron & Réchou 2012). Cap de les metodologies anteriors detectava el tipus de precipitació de forma explícita de forma que cal destacar l'avenç aconseguit amb la nova metodologia proposada.

El resultats s'han comprovat amb diferents instruments situats prop de l'equip tals com el Micro Rain Radar (MRR2), disdròmetre Parsivel i estacions automàtiques.

4.1.2. Article

Garcia-Benadi, A.; Bech, J.; Udina, M.; Campistron, B.; Paci, A. Multiple Characteristics of Precipitation Inferred from Wind Profiler Radar Doppler Spectra. Remote Sens. **2022**, 14, 5023. https://doi.org/10.3390/rs14195023

remote sensing

MDPI

Article

Multiple Characteristics of Precipitation Inferred from Wind Profiler Radar Doppler Spectra

Albert Garcia-Benadi [1,2], Joan Bech [2,3,*], Mireia Udina [2], Bernard Campistron [4] and Alexandre Paci [5]

1 SARTI, Universitat Politècnica de Catalunya, 08800 Vilanova i la Geltrú, Spain
2 Department of Applied Physics—Meteorology, University of Barcelona, 08028 Barcelona, Spain
3 Water Research Institute, University of Barcelona, 08007 Barcelona, Spain
4 Laboratoire d'Aérologie Université Paul Sabatier, 31400 Toulouse, France
5 CNRM, University of Toulouse, METEO-FRANCE, CNRS, 38400 Toulouse, France
* Correspondence: joan.bech@ub.edu

Abstract: A methodology to process radar wind profiler Doppler spectra is presented and implemented for an UHF Degreane PCL1300 system. First, double peak signal detection is conducted at each height level and, then, vertical continuity checks for each radar beam ensure physically consistent measurements. Second, horizontal and vertical wind, kinetic energy flux components, Doppler moments, and different precipitation-related variables are computed. The latter include a new precipitation type estimate, which considers rain, snow, and mixed types, and, finally, specific variables for liquid precipitation, including drop size distribution parameters, liquid water content and rainfall rate. The methodology is illustrated with a 48 h precipitation event, recorded during the Cerdanya-2017 field campaign, carried out in the Eastern Pyrenees. Verification is performed with a previously existing process for wind profiler data regarding wind components, plus precipitation estimates derived from Micro Rain Radar and disdrometer observations. The results indicated that the new methodology produced comparable estimates of wind components to the previous methodology (Bias < 0.1 m/s, RMSE ≈ 1.1 m/s), and was skilled in determining precipitation type when comparing the lowest estimate of disdrometer data for snow and rain, but did not correctly identify mixed precipitation cases. The proposed methodology, called UBWPP, is available at the GitHub repository.

Keywords: hydrometeor type estimation; Doppler; wind profiler; pulsed radar

Citation: Garcia-Benadi, A.; Bech, J.; Udina, M.; Campistron, B.; Paci, A. Multiple Characteristics of Precipitation Inferred from Wind Profiler Radar Doppler Spectra. *Remote Sens.* **2022**, *14*, 5023. https://doi.org/10.3390/rs14195023

Academic Editors: Yingzhao Ma, V. Chandrasekar, Robert Cifelli and Seppo Pulkkinen

Received: 11 August 2022
Accepted: 2 October 2022
Published: 9 October 2022

1. Introduction

Radar wind profilers (hereafter RWPs) are designed to retrieve the vertical profile of the wind, through processing Doppler spectra, typically using wavelengths between 20 cm to 6 m, where attenuation by rain can be considered negligible. Bragg and Rayleigh backscattering at these wavelengths, respectively, allows detection of atmospheric echoes caused by both clear air and hydrometeor particles, respectively [1,2]. Depending on the operating frequency, RWPs are often classified as Very High Frequency (VHF band, from 30 MHz to 300 MHz) and Ultra-high frequency (UHF band, from 300 MHz to 3 GHz). In recent decades, RWP networks have been deployed, and routinely operated, in different countries and regions, such as the USA (NOAA Profiler Network, [3]), Europe (COST-76 Action Program) [4], Japan (WINDAS) [5], Korea (KMA) [6] and China (CMA) [7].

The use of RWP includes a wide range of applications, such as evaluation of boundary layer conditions [8,9] diagnostic studies of convective clouds [10,11], windshear and turbulence in complex terrain [12,13] or, in recent years, assimilation into NWP models [14–17]. One key aspect of RWP data processing is the effect of precipitation particles in the sampled volume [18–20], which needs to be taken into account; particularly, to obtain the vertical component of the wind. In fact, previous studies, based on vertical wind components observed by RWP, estimated height of snow or precipitation rate [21,22], but, to our best

knowledge, very limited attention has been devoted so far to the use of RWP observations in retrieval of explicit precipitation types. To fill this gap, the objective of this paper is to describe a new processing methodology for RWP data, addressing, specifically, the detection of precipitation particles and their classification into a simplified precipitation type classification, including rain, snow, and mixed classes. While other instruments, such as conventional polarimetric weather radars, may provide a more complete description of hydrometeor types [23–25], we illustrate the benefits of a simplified classification with RWP data with data sets recorded during the Cerdanya-2017 field campaign in the Eastern Pyrenees mountains.

The verification of results is performed in two stages. First, results of the new method (vertical and horizontal wind) are compared with an already existing processing for RWP. Then, we use Micro Rain Radar (providing profiles of estimated precipitation type) and disdrometer observations (with ground level automatic observations of precipitation type) to produce verification statistics of rain, snow, and mixed precipitation estimates.

The structure of the rest of the paper is as follows. Section 2 describes briefly the Cerdanya-2017 field campaign instruments used in this study. Then, the new processing of RWP data is described in Section 3 and results are compared with other instruments in Section 4. A discussion is provided in Section 5 and conclusions and final remarks are presented in Section 6.

2. Field Campaign and Instrumentation

This section provides, first, a brief overview of the field campaign, region and period of study, and, then, a description of the instruments used in the study.

2.1. Cerdanya-2017 Field Campaign

The datasets used in this study were recorded during the Cerdanya-2017 field campaign, carried out during the 2016–2017 winter season in the Eastern Pyrenees, close to the Spanish, French and Andorra borders (Figure 1). The purpose of the campaign was to study different cold season meteorological phenomena influenced by complex terrain, including cold-pools, mountain waves, and orographic precipitation [13,26]. Instruments used were an UHF RWP, a Micro Rain Radar (MRR2), a disdrometer, and two automatic weather stations (AWSs). The MRR2, disdrometer, and AWS SO were installed in the Das aerodrome (see Table 1), or in the vicinity of about 2.6 km from the MRR2 (Wind Profiler and AWS S8). The instruments were around 1100 m above sea level, surrounded by mountains, with some peaks slightly exceeding 2900 m. One key difference between the RWP and the MRR is the sensitivity, which is much higher for the RWP. Sensitivities were calculated following the method described by [27], as shown in Table 2, along other characteristics explained in more detail in the following subsections.

Table 1. Location of instruments used.

Instrument (Institution)	Longitude (°)	Latitude (°)	Height ASL (m)
RWP (Météo-France)	1.83759 E	42.39688 N	1079
MRR2 (University of Barcelona)	1.86650 E	42.38643 N	1099
Disdrometer (University of Barcelona)	1.86655 E	42.38643 N	1101
AWS S0 (Meteorological Service of Catalonia)	1.86640 E	42.38605 N	1097
AWS S8 (Météo-France)	1.82980 E	42.39340 N	1088

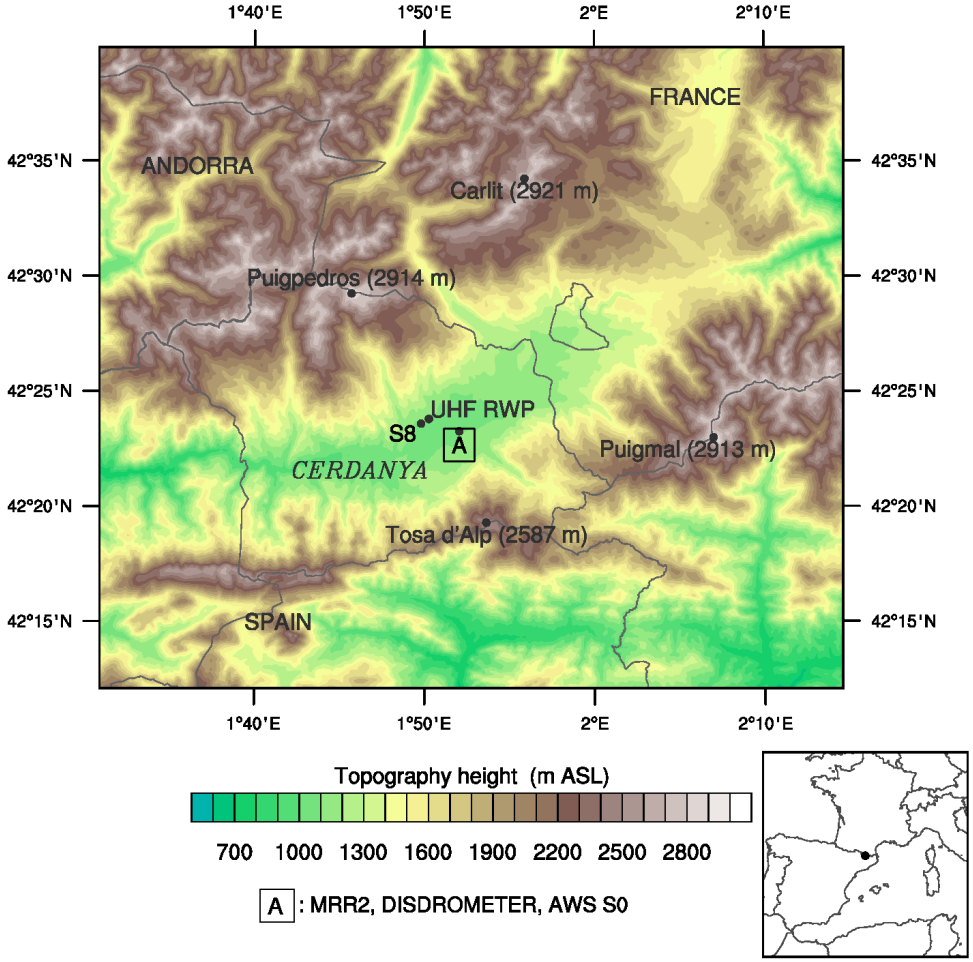

Figure 1. Topography of the Eastern Pyrenees region of study showing the location of the aerodrome (A) with most of the instrumentation: Micro Rain Radar (MRR2), Disdrometer and AWS from the Meteorological Service of Catalonia. Location of an additional Météo-France AWS (number S8) and the Ultra-High Frequency wind profiler (UHF RWP). The main mountain peaks of Carlit (2921 m ASL), Puigpedrós (2914 m ASL) and Puigmal (2913 m ASL) are also labelled, as well as Andorra, France and Spain and their borders.

Table 2. Main features of the RWP and MRR2 used in this study.

Feature	RWP	MRR2
Manufacturer, model	Degreane, PCL1300	Metek, MRR2
Frequency (GHz)	1.247	24.23
Radio band	UHF	K
Number of range gates	45	32
Number of Doppler bins	128	64
Peak power (W)	2500	0.05
Pulse width (μs)	1	—
Maximum height (km)	6.5	3.1
Minimum reflectivity at 1 km (dBZ)	−15.0	−4.7

The data used in this paper were recorded during a 48 h period, from the 24th to 25th of March 2017. This period was selected because it contained different regimes of precipitation (stratiform and convective), alternating also at different ground level hydrometeor types (with snow and rain transitions). Total precipitation recorded at AWS S0 during the event was 30 mm. Complementarily, a second three-day event (3 to 5 February 2017) also

containing different precipitation types at ground level, was examined, and can be found in the Supplementary Materials.

2.2. UHF Wind Profiler

We used a RWP model PCL1300, manufactured by the French company Degreane (see Table 2 for technical details), configured with five fixed antennas and two operating modes, depending on the pulse length used, high and low. In high mode, the range gate length was 187.5 m and the first gate was at 102 m above ground level (AGL), reaching 9102 m AGL. In low mode, the gate length was 150 m and the first gate was at 96 m AGL, reaching 6696 m AGL. In order to have the maximum vertical resolution possible, RWP data used here corresponded only to low mode. The complete update cycle of measurements was about 3 min, but, as mentioned below, the verification of precipitation type was performed averaging measurements into 5-min resolution data.

The five-beam configuration of the unit is illustrated in Figure 2. One beam was oriented vertically, and the other four were tilted towards the cardinal directions, each with the same zenithal angle (17°, i.e., with an elevation angle of 73° over the local horizontal plane). The vertical beam is numbered as beam 1 and the four beams in the cardinal directions (North, South, East and West) are numbered 2, 3, 4 and 5, respectively. Each beam has an angular width of 8.5°.

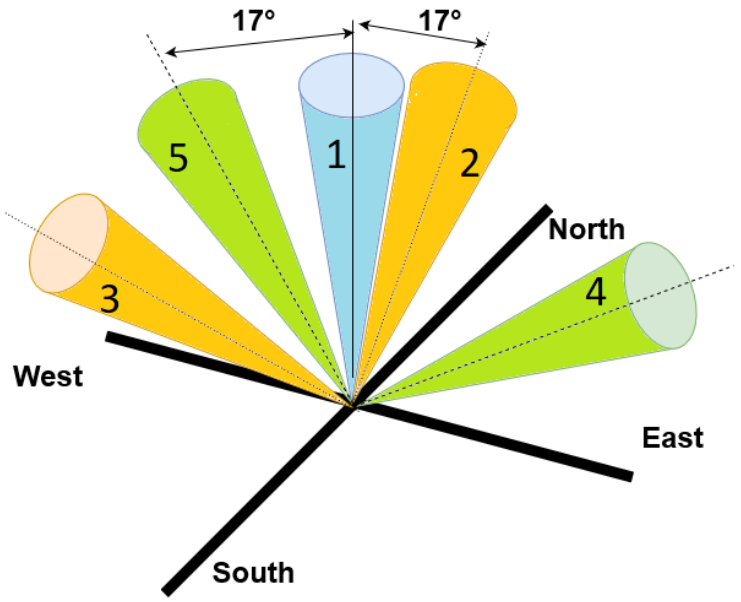

Figure 2. Scheme of wind profiler five-beam configuration with a vertical beam (blue) and four tilted beams oriented towards the four cardinal directions with constant zenithal angle (17°, not to scale). Each beam is numbered according to the labels shown (1, 2, . . .).

The manufacturer data acquisition software applied rain detection on vertical speed and reflectivity criteria to avoid speed aliasing and receiver saturation. In particular, when an abrupt increase in vertical speed was detected, the system increased the Nyquist velocity and changed speed spectra resolution from 0.18 m/s to 0.30 m/s, and the output data included a flag named *Pluie* (rain flag, in this paper).

RWP Doppler spectra of each beam were stored in raw data files (so-called .dat Degreane files). Typically, these files were processed with a methodology developed at the *Laboratoire d'Aérologie* of the *Université Paul Sabatier*, the Aerologie Laboratory Wind Profiler Processing (ALWPP), including signal peak detection and spectrum filtering, as described in [28]. The output files were processed by Météo-France and stored in netcdf files. These data are referred to, hereafter, as Method1, and contain, among other variables, horizontal and vertical wind components.

It should be noted that ALWPP was developed to retrieve wind profiles (horizontal and vertical components) plus additional rainfall variables, such as kinetic energy fluxes used for erosion studies. However, ALWPP does not contain a hydrometeor classification, unlike the proposed UBWPP. For this reason, a comparison between ALWPP and UBWPP was performed covering only wind components, but no other variables were compared with other instruments, as described below.

2.3. Micro Rain Radar

A Micro Rain Radar [29], model MRR2 (hereafter MRR2), manufactured by the German company Metek GmbH, was used. It is a frequency modulated continuous wave, vertically pointing, Doppler radar operating at K band, suitable for precipitation measurements [30]. The unit has 32 range gates and was configured with a range gate vertical resolution of 100 m, starting at 100 m AGL and reaching 3.2 km AGL–see Table 2 for a summary of technical details. Doppler spectra of each range gate were processed with the methodology described in [10], which included the computation of Doppler fall speed, equivalent radar reflectivity, and precipitation type (drizzle, rain, snow, mixed, and hail), among other variables. Vertical MRR2 profiles were available with 1-min resolution.

2.4. Disdrometer

A laser disdrometer. manufactured by the German company OTT GmbH, model Parsivel2 [31], was also used in this study. It provided particle size and fall speed spectra at ground level, and a number of derived variables, which included precipitating hydrometeor type, coded according to the World Meteorological Organization (WMO) Table 4677 specifications (WMO 2018 [32]). Disdrometer hydrometeor types were available with 1-min resolution.

2.5. Automatic Weather Stations

Two automatic weather stations (hereafter AWSs) from Météo-France and the Meteorological Service of Catalonia were also used. They provided, with 1-min temporal resolution, temperature and relative humidity measurements. These two variables were used to compute the probability of snow (assuming precipitation was present), based on the empirical formula proposed by [33], and the thresholds determined by [34,35] to distinguish rain, mixed, and snow cases. The ranges of probabilities were 0.00 to 0.39 (rain), 0.40 to 0.58 (mixed), and 0.59 to 1.00 (snow).

3. Data Processing

This section describes the new processing methodology, the University of Barcelona Wind Profiler Processing (UBWPP). Input data are the raw Doppler spectra power encoded in the so-called RWP .dat Degreane files. Further technical details about the file format are available in the Supplementary Materials, such as the RWP parameters, the automatic configuration of the RWP and signal decoding.

The main processing steps of UBWPP are detailed in Figure 3, including Signal Peak Detection, Vertical Continuity Check and Parameter Calculation. Note that the first two steps were applied to all five RWP beams, as previous methods used in radar wind profiler processing, have done [36,37].

3.1. Signal Peak Detection

The detection of signal peaks was performed for each range of height beam at a given time instant, where the signal was examined as a function of the Doppler spectrum. With the method used, at most, two maximum values were detected. A maximum value followed the definition of the signal adjusted with the convolution method [38] with smoothing filter, where the signal was adjusted to a smoother signal, but with well-defined maxima. It is important to note that at this point the rate of fall and its moments were calculated, so the value of the signal was not relevant (see Supplementary Materials). As illustrated

in Figure 4, starting from the original signal (Figure 4a) a convolution was performed (marked in red in Figure 4b), and, based on this, two modes at most were identified. The inflection points of these modes were used to identify the velocity interval of the signal identified. The resulting signal identified is shown in red in Figure 4c (the blue part of the signal was rejected). Note that the area below the identified signal was used to compute the equivalent reflectivity.

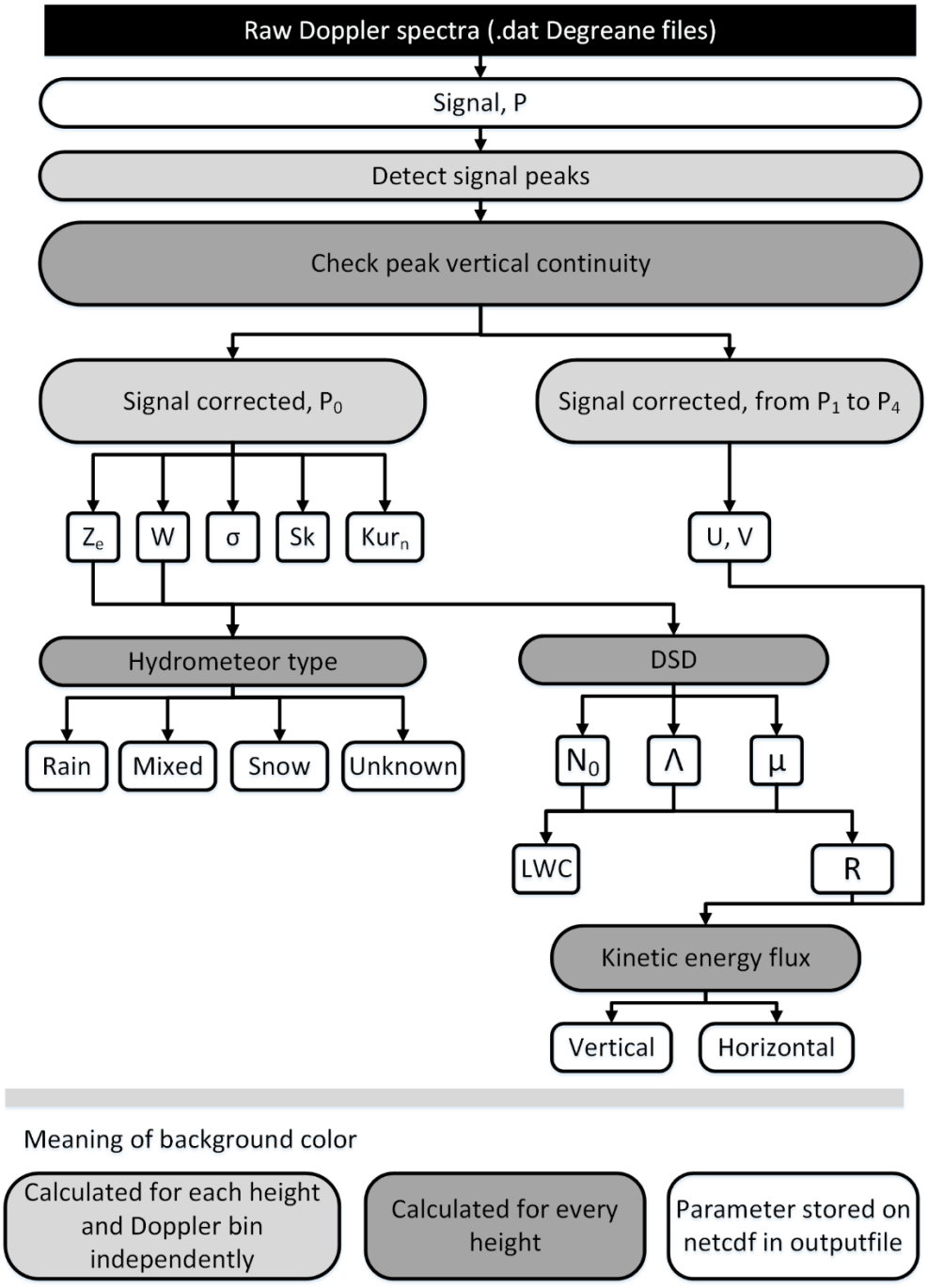

Figure 3. Flow diagram of the UBWPP Wind Profiler processing of raw Doppler spectra and output variables, see in the text for the explanation of the parameters appearing in the diagram.

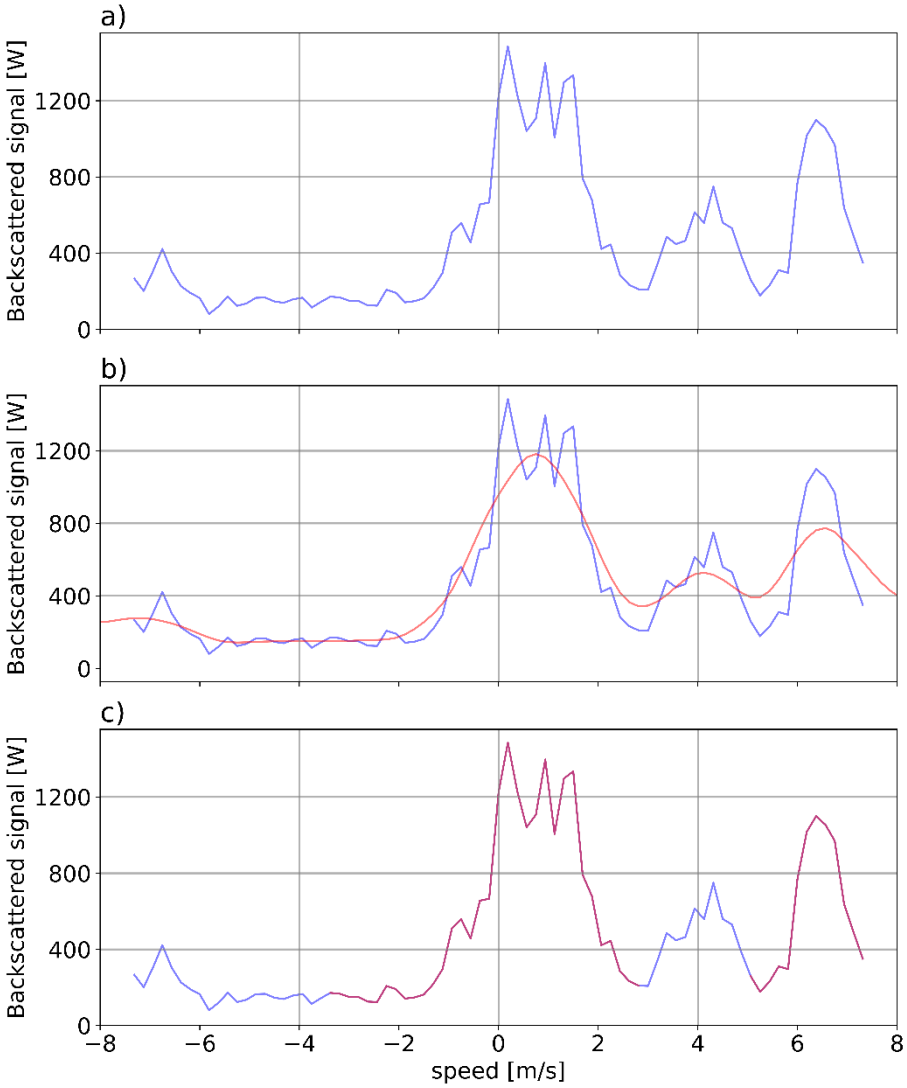

Figure 4. Signal peak detection on a vertical beam: (**a**) original signal, (**b**) convolution (in red) and original signal (in blue) (**c**) result, where part of the original signal was refused (in blue) and the rest (in red) was the corrected signal. At most two peaks were kept from the original signal. Data corresponds to Beam number 1 (vertical incidence, positive values corresponding to downward movement).

Despite this scheme considering a maximum of two peaks, which, in principle, could allow finding the true terminal velocity of hydrometeor particles in convective updrafts by simple subtraction, this was finally not implemented. The reason was that a wide variety of situations were found for both precipitation and non-precipitation Doppler spectra, for example, rain with one peak or clear-air with two peaks. Therefore, the peak spectra allowed more precise calculations (for example, of Doppler moments) but they were not used to attempt to compute true terminal speeds of hydrometeors. The process of signal peak detection illustrated in Figure 4 was not only applied to Beam 1 (vertical velocities) but to all other beams (Beams 2, 3, 4, and 5).

Considering the noise level as the minimum value from the backscattered signal, and the signal-to-noise ratio (SNR) as the ratio between the maximum signal detected by the noise detected, then:

$$SNR = 10 \cdot \log_{10} \frac{Signal_{max}}{Noise}, \quad (1)$$

3.2. Vertical Continuity Check

A check on the vertical continuity of the peak found on the previous step was performed to avoid jumps in the vertical velocity profile. These variations might be due to a malfunction, or the detection of non-meteorological targets (birds or insects). A threshold value was detailed to give physical meaning to the profile, where the speed found at one height could not exceed the limit of 5 m/s at the adjacent height. The height range in high mode was 187 m and in low mode 150 m, so, assuming this limit was deemed reasonable. An example of this process is illustrated in Figure 5, showing first the original signal (with amplitude normalized) at each height, then the peak detection, and, finally, the vertical continuity test applying the threshold mentioned above. Despite the vertical continuity test having been described explicitly for Beam 1, it was also applied to all other beams.

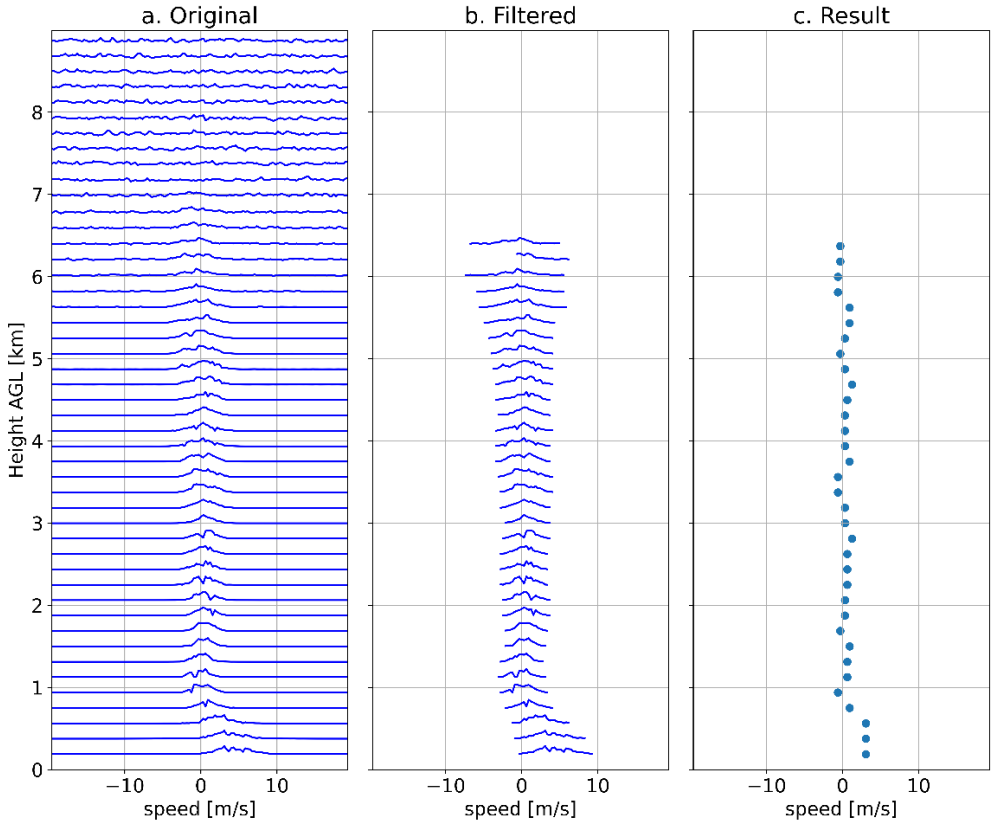

Figure 5. Example of Doppler speed profile corrected with the RWP vertical continuity test: (**a**) original signal, normalized, at each height; (**b**) signal after the peak detection was performed; (**c**) mean vertical speed for each height after applying the vertical continuity test. Data corresponds to Beam number 1 (vertical incidence, positive values corresponding to downward movement) recorded on the 25th of March 2017 3:01:44 UTC.

3.3. Parameters Calculation

Several derived parameters, including three-dimensional Wind Components, Radar Reflectivity, Drop Size Distribution, Liquid Water Content, Kinetic Energy flux, and Hydrometeor Type were calculated. Additional information about the formulae used for Doppler moments are provided in the Supplementary Materials.

3.3.1. Wind Components

In this process the radial speed was calculated for each beam, assuming the wind was constant at a given altitude during the measurement period. The relation between zonal (u), meridional (v), and vertical (w) velocity components are given by:

$$v_{r,1} = w, \tag{2}$$

$$v_{r,2} = -\cos\alpha_2 \cdot v + \sin\alpha_2 w \tag{3}$$

$$v_{r,3} = \cos\alpha_3 \cdot v + \sin\alpha_3 w \tag{4}$$

$$v_{r,4} = -\cos\alpha_4 \cdot u + \sin\alpha_4 w \tag{5}$$

$$v_{r,5} = \cos\alpha_5 \cdot u + \sin\alpha_5 w \tag{6}$$

where α_i is the angle between the vertical and the beam i, with $i = 1, \ldots 5$ according to the beam numbering described in Section 2.2., and downward vertical velocity was defined as positive.

Note that if the angle for all beams was the same, then:

$$v = \frac{v_3 - v_2}{2 \cdot \cos\alpha} \tag{7}$$

$$u = \frac{v_5 - v_4}{2 \cdot \cos\alpha} \tag{8}$$

$$w = v_1 = \frac{v_2 + v_3}{2 \cdot \sin\alpha} = \frac{v_4 + v_5}{2 \cdot \sin\alpha} \tag{9}$$

According to the last equations, the vertical speed w could be obtained 3 different ways; although UBWPP only used the direct measurement from Beam 1.

3.3.2. Radar Reflectivity

The frequency of the WPR was 1274 MHz so the wavelength was around 0.23 m and the Rayleigh scattering regime was valid for cloud droplets and raindrops. The radar reflectivity was calculated from the power received, once filtered. Equation (10) shows the radar reflectivity Z from Beam 1 (vertically pointing):

$$Z(dBZ) = 10 \cdot \log_{10} P_r - Ct + 20 \cdot \log_{10} h, \tag{10}$$

where P_r is the received power, Ct is related to the radar constant RC ($Ct = 10\log_{10}(RC)$) previously known, and h is the height above ground level, assuming the antenna height is negligible.

3.3.3. Precipitation Type

Prior to estimating the precipitation type it was necessary to distinguish clear air echoes from precipitation echoes. Therefore, a precipitation detection procedure was applied, consisting of the verification of at least one of the two following conditions: (i) the rain flag; (ii) the signal to noise ratio of the peak detected (see Section 3.1) exceeding 10 dB.

Once a precipitation echo was detected we proposed two approaches for the evaluation of the precipitation type, considering in both the following simplified classes, based o thermodynamic phase: rain (including liquid precipitation), snow (including solid precipitation) and mixed (including both solid and liquid precipitation), and unknown (when none of the former classes was detected).

The first approach was based on Atlas et al. (1973) [39] (hereafter A73) and it classifies precipitation considering the observed vertical velocity w and spectral width σ given for each hydrometeor type, according to the expected terminal velocity values for rain

v_{rain} and snow v_{snow} particles obtained from the reflectivity, as described in [39]. The equations are:

$$v_{rain} = 2.65 \cdot Z^{0.114} \quad (11)$$

$$v_{snow} = 0.817 \cdot Z^{0.063} \quad (12)$$

where velocities are expressed in m s^{-1} and Z in mm^6 m^{-3}. The method is modified to include the mixed case, containing both solid and liquid precipitation.

The second approach was based on the threshold values for different hydrometeors reported in Ralph et al. 1995 [40] (hereafter R95) where the values were modified to include the mixed case. The thresholds are detailed in Table 3.

Table 3. Precipitation type adapted from A73 and R95.

Approach	Type	Condition
A73	Rain	$\lvert v_{rain} - w \rvert < 2 \cdot \sigma$ *and* $\lvert v_{snow} - w \rvert > 2 \cdot \sigma$
	Mixed	$\lvert v_{rain} - w \rvert < 2 \cdot \sigma$ *and* $\lvert v_{snow} - w \rvert < 2 \cdot \sigma$ *and* $v_{rain} \geq w \geq v_{snow}$
	Snow	$\lvert v_{rain} - w \rvert > 2 \cdot \sigma$ *and* $\lvert v_{snow} - w \rvert < 2 \cdot \sigma$
	Unknown	*None of the above*
R95	Rain	$w \geq 3$ m s^{-1} *and* $\sigma^2 \geq 1$ m^2 s^{-2}
	Mixed	2 m $s^{-1} \leq w \leq 3$ m s^{-1}
	Snow	0.5 m $s^{-1} < w < 2$ m s^{-1} *and* $\sigma^2 < 1$ m^2 s^{-2}
	Unknown	*None of the above*

Despite both A73 and R95 echo precipitation classifications originally using different initial variables and final precipitation classes they both rely on comparing the Doppler velocity spectrum measured at vertical incidence with terminal velocity of precipitation particles. With our proposal we tried to adapt this approach considering also a mixed precipitation class, including solid and liquid precipitation.

3.3.4. Drop Size Distribution

For precipitation echoes classified as rain, the drop size distribution N(D) was computed assuming a gamma distribution [41]:

$$N(D) = N_0 \cdot D^{\mu} \cdot e^{-\Lambda \cdot D} \quad (13)$$

where D is the drop diameter (in m), N_0 is the intercept (in $m^{-(\mu+4)}$) that can be interpreted as the number density per unit drop diameter, Λ is the slope (in m^{-1}) associated with the gradient of the distribution, and μ the shape parameter (dimensionless). This last parameter follows the quadratic expression derived by [42] as explained in [28]:

$$\Lambda = 50.0 \cdot \mu^2 + 1200.0 \cdot \mu + 3390.0 \quad (14)$$

As the shape parameter μ has no analytical equation, it must be solved using the vertical speed, expressed in terms of a_i (from i = 1, 2 and 3) coefficients [43].

$$W(D) = a_1 - a_2 \cdot e^{-a_3 \cdot D} \quad (15)$$

and the mean vertical speed obtained after integration over all diameter from 0 to infinity. In this analysis the vertical air speed is considered negligible.

$$< W > = a_1 - a_2 \cdot \left(1 + \frac{a_3}{\Lambda}\right)^{-(\mu+7)} \quad (16)$$

Thus, the value of μ is calculated using the intersection of two functions (f_1, and f_2), derived from Equation (16). The analytical solution is obtained giving values to μ between -6.9 to 30 with a resolution of 0.01.

$$f_1 = \frac{-1}{\mu + 7} \cdot \ln\left(\frac{a_1 - w}{a_2}\right) \tag{17}$$

$$f_2 = \ln\left(1 + \frac{a_3}{\Lambda}\right) \tag{18}$$

where the units of a_1 and a_2 are m s^{-1}, and for a_3 are m^{-1}. These parameters are function of the density, except a_3:

$$a_1 = 9.65 \cdot \frac{\rho_0}{\rho}^{0.4}, \tag{19}$$

$$\alpha_2 = 10.3 \cdot \frac{\rho_0}{\rho}^{0.4}, \tag{20}$$

$$a_3 = 600, \tag{21}$$

The rain rate R is computed assuming that the mean drop size distribution $N(D)$, follows a gamma function and integrating over all diameters [39]:

$$R = N_0 \cdot \Gamma(\mu + 4) \cdot \frac{\pi}{6} \cdot \left(a_1 \cdot \Lambda^{-(\mu+4)} - a_2 \cdot (\Lambda + a_3)^{-(\mu+4)}\right), \tag{22}$$

3.3.5. Liquid Water Content

The liquid water content (*LWC*) is the liquid water amount contained in a unit volume, which is proportional to the third moment of the DSD. Supposing a spherical shape, the density is ρ_w equal to 10^6 in g m^{-3}, the *LWC* units are g m^{-3}, and is given by:

$$LWC = \rho_w \cdot \frac{\pi}{6} \cdot N_0 \cdot \frac{\Gamma(\mu + 4)}{\Lambda^{\mu+4}} \tag{23}$$

3.3.6. Kinetic Energy Flux

The rain kinetic energy flux crossing a horizontal surface of unit area during a unit of time is decomposed in vertical and horizontal components. The horizontal kinetic energy flux *HKEF* is a function of the horizontal wind speed:

$$HKEF = \rho_w \cdot V^2 \cdot \frac{R}{2} \tag{24}$$

where V is the module of the horizontal wind and R is the rain rate. The unit of *HKEF* is g s^{-3}. The vertical kinetic energy flux VKEF (also in g s^{-3}) is a function of the vertical speed:

$$\begin{aligned} VKEF = \rho_w \cdot N_0 \cdot \Gamma(\mu + 4) \cdot \frac{\pi}{12} \\ \cdot \left[a_1^3 \cdot \Lambda^{-(\mu+4)} - a_2^3 \cdot (\Lambda + 3 \cdot a_3)^{-(\mu+4)} + 3 \cdot a_1 \cdot a_2^2\right. \\ \left. \cdot (\Lambda + 2 \cdot a_3)^{-(\mu+4)} - 3 \cdot a_2 \cdot a_1^2 \cdot (\Lambda + a_3)^{-(\mu+4)}\right] \end{aligned} \tag{25}$$

These equations were derived and used in [28] to estimate rainfall kinetic energy with radar data, complementing previous studies of soil erosion effects of rainfall made with disdrometric measurements [44].

4. Results

The results of the new methodology are illustrated for the Cerdanya-2017 field campaign precipitation case recorded from March 24 to 25th March 2017 [26], where the passage of a warm and a cold front produced several hydrometeor type transitions at ground level alternating with stratiform and shallow convective precipitation.

The verification is described in two distinct parts: wind components and precipitation type.

Wind components were computed with the Aerologie Laboratory Wind Profiler Processing (ALWPP) [28] (Method1), and compared with the new proposed methodology named University of Barcelona Wind Profiler Processing (UBWPP), hereafter Method2. MRR2 data is also used to compare the vertical wind estimates. The purpose of this comparison is to ensure that Method2 is able to properly compute wind components, using Method1 as a benchmark.

Then a comparison of Hydrometeor type obtained with Method2 is performed with MRR2 (profiles), and disdrometer and AWS data (at ground level).

4.1. Vertical Speed

The vertical speed wind component is an essential variable to perform the estimation of precipitation type; therefore, here we compared the average estimates performed with RWP (Method1 and Method2) and MRR2, processed according to [10] and homogenizing both the temporal and spatial resolution to Method1 (Figure 6). Some differences are expected between RWP and MRR2 estimates, due to the different frequencies of operation (UHF vs. K band) and, to a lesser extent in this case, to the siting of the two instruments, given the mostly stratiform character of the event. MRR2 can only observe precipitation particles while RWP detects both precipitation and clear air wind.

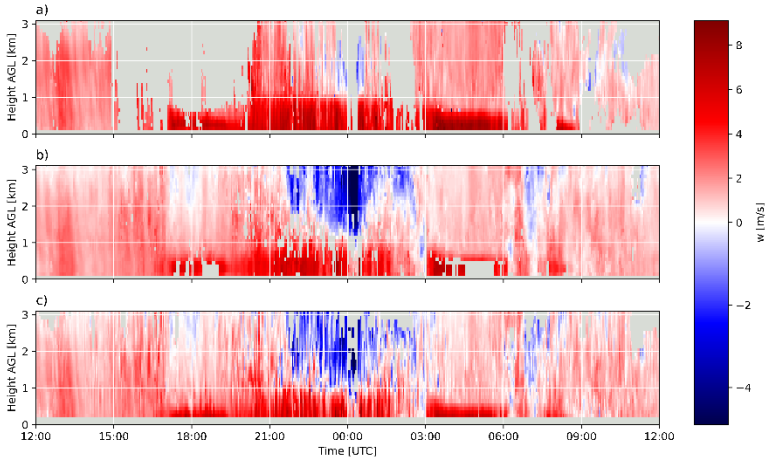

Figure 6. Vertical speed (downward defined positive) estimates for 24th to 25th March 2017. (**a**) MRR2, (**b**) RWP (Method1) and (**c**) RWP (Method2).

Figure 6 shows clear similarities between the estimates of the two instruments and between Method1 and Method2. An overall agreement was found in the pattern distribution, with a clear sharp gradient, indicating a melting layer signature, around 1 km AGL at 00 UTC (more evident for the MRR2, Figure 6a), and also negative speeds (updrafts, in blueish colors) around 00 UTC, much more clearly (in intensity in duration) in both RWP estimates. The better ability of the RWP to observe updrafts was expected for UHF measurements able to measure Bragg backscattering caused by air molecules unlike K band measurements, which only detect updrafts if precipitation particles are present.

A more detailed comparison between Method1 and Method2 is shown in the scatter plot and frequency distributions of Figure 7, distinguishing RWP echoes labelled with the rain flag from the rest. Distribution patterns of rainy and non-rainy conditions for Method1 and Method2 are very similar, unimodal and wider vs bimodal with the main mode centered at 0 m/s, respectively. The global analysis of 29820 points indicated a Mean Error (ME) (Method2–Method1) of −0.04 m/s, a Root Mean Square Error (RMSE) of 0.39 m/s, and a correlation coefficient of 0.86.

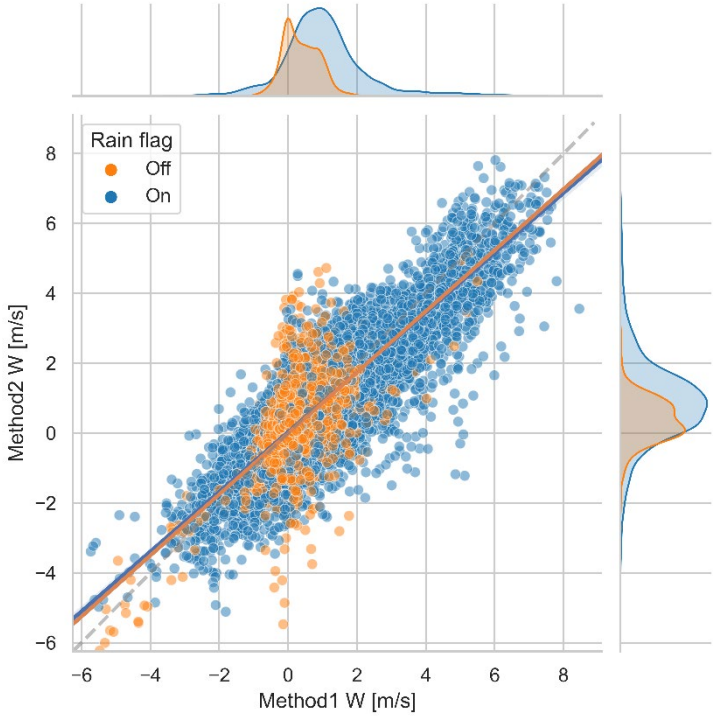

Figure 7. Vertical speed from ALWPP (Method1) vs UBWPP (Method2) showing wind profiler echoes in rainy (20127 samples, in blue) and non-rainy (9693 samples, in orange) conditions, the corresponding linear regression (also in blue and orange) and the diagonal (dashed) line. The top and right panels show the normalized distributions of rainy and non-rainy conditions for Method1 and Method2, respectively.

4.2. Horizontal Wind

Figure 8 shows scatter plots of Method1 vs Method2 for both zonal (U) and meridional (V) wind components (left column) plus histograms of differences between the two methods (right column). Note the similar patterns found in the zonal and meridional distributions and the symmetrical and unbiased (<0.1 m/s) shape of the distributions of differences. Statistical analysis of 24201 samples indicated ME, RMSE and correlation coefficients for zonal (meridional) components of −0.034 m/s, 1.089 m/s and 0.99 (0.088 m/s, 1.154 m/s and 0.96), respectively.

4.3. Precipitation Type

The precipitation type estimation produced with Method2 was evaluated by comparing profiles of equivalent height obtained from MRR2 [10], and ground level disdrometer and AWS data.

Figure 9 provides an overview of precipitation type estimated by the MRR2 (upper panel) and Method2 (lower panel), in this case based on the A73 approach - note that the number of classes was different for each method. The overall pattern was similar, starting with snow (first as virga, reaching the ground around 12 UTC), later with a brief rain shaft and more snow, then (beginning sometime between 16 and 17 UTC) with rain below the melting level and snow above, and finally snow (about 8 UTC). Moreover, a radio-sounding, launched at the Das aerodrome on the 24th of March at 22.34 UTC (see Supplementary Material) indicated that the freezing level was about 0.8 km AGL, consistent with results displayed in Figure 9. The different bin vertical resolution of the two instruments and the distance between them might partly explain the differences in freezing levels. Moreover, despite the general pattern of precipitation types estimated from both instruments being similar, the higher sensitivity of the RWP revealed more precipitation areas, such as those above 0.5 km AGL, from 16 to 20 UTC 24 March 2017.

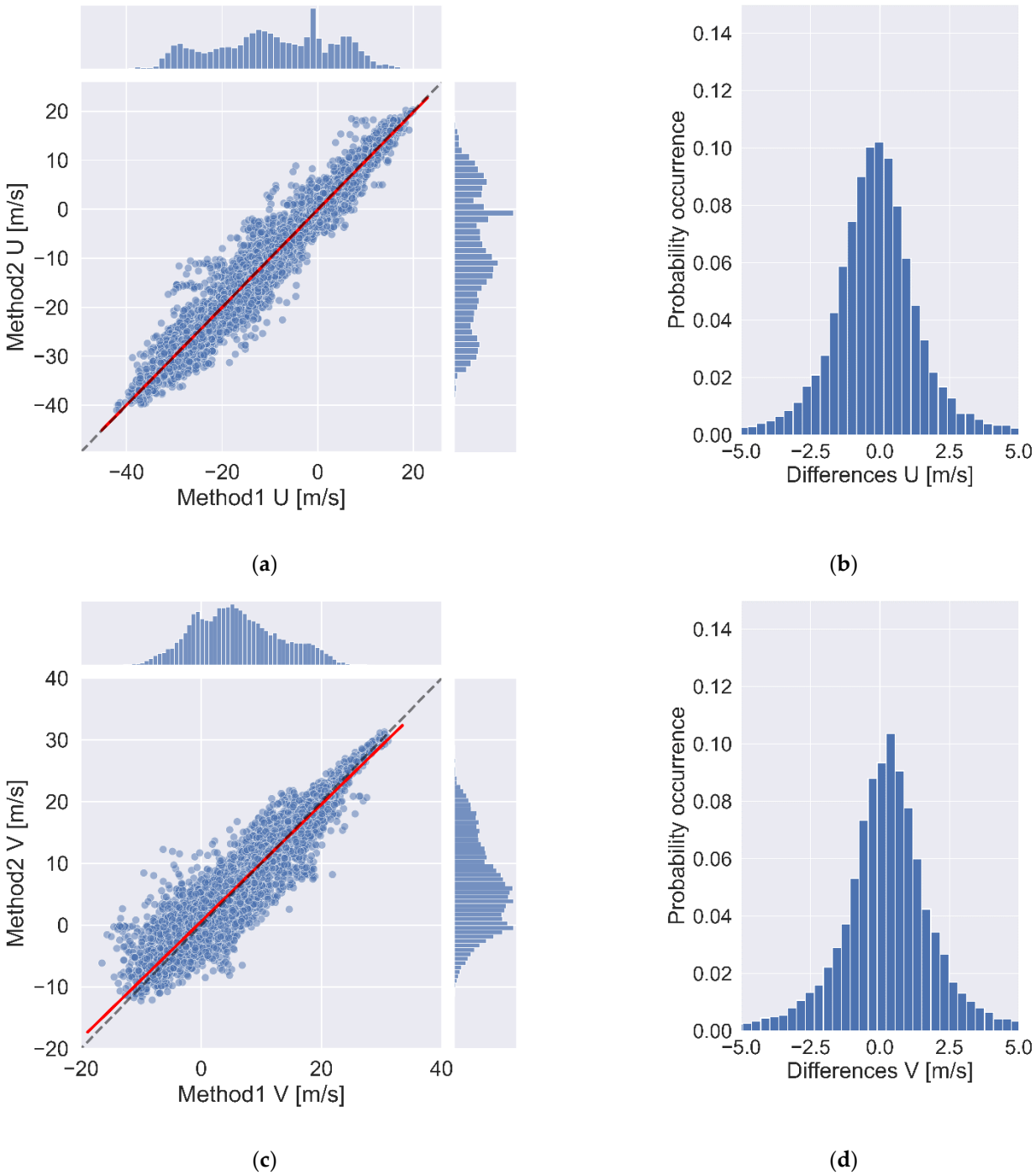

Figure 8. Scatterplots and distributions of differences between ALWPP (Method1) and UBWPP (Method2) for zonal component U, panels (**a**,**b**), and meridional component V, panels (**c**,**d**). Scatter plots show correlation (red) and perfect correlation in diagonal (dashed) lines.

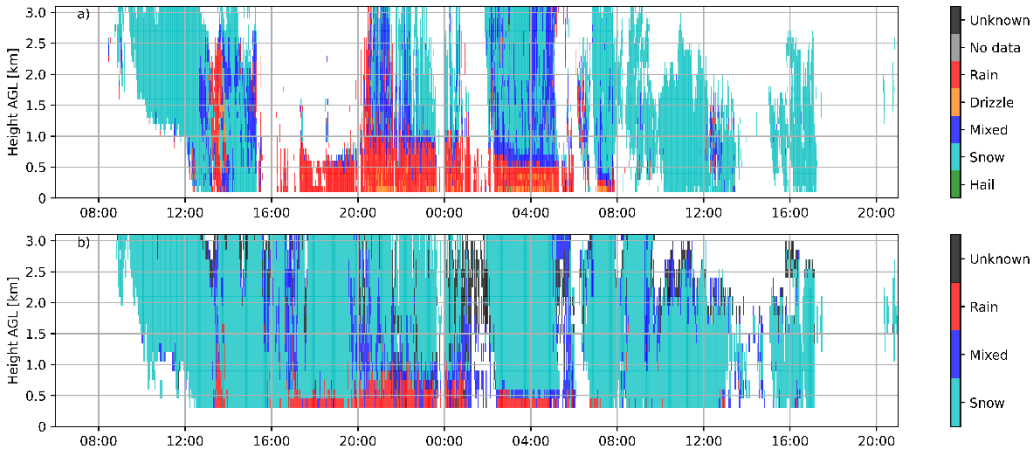

Figure 9. Precipitation type estimation during the 24 and 25 March 2017 event. (**a**) MRR2 observations with 6 classes and (**b**) RWP Method2, using A73, with 5 classes. Note RWP data has been clipped to the MRR2 maximum height. White areas indicate clear air echoes.

A quantitative comparison was performed with disdrometer data and AWS estimates. As Method2 detected five types of precipitation (rain, mixed, snow, no data and unknown) and the disdrometer provided a more complete list of hydrometeor types (WMO Table 4677), the latter had to be properly grouped to perform the comparison. Table 4 lists the WMO codes selected to match the Method2 precipitation types. Note that the Unknown class was assigned to hail, despite this hydrometeor mpt being observed in the datasets examined, so this class should be further verified.

Table 4. Correspondence between precipitation types observed by the disdrometer (WMO Table 4677) and precipitation types estimated with Method2.

Disdrometer Precipitation Type	WMO Table 4677 Values	Method2 Precipitation Type
Drizzle	From 51 to 53	Rain
Drizzle with rain	From 58 to 59	
Rain	From 61 to 65	
Rain, drizzle with snow	From 68 to 69	Mixed
Snow	From 71 to 75	Snow
Snow grains	77	
Soft hail	From 87 to 88	
Hail	From 89 to 90	Unknown

The comparison between Method2 and disdrometer and AWS station data also had to deal with their different temporal resolutions. For practical reasons, Method2 precipitation type, originally with 3.5-min temporal resolution were transformed into 5-min resolution data. Then, AWS and disdrometer data, originally with 1-min resolution, were converted to 5-min resolution with an ad-hoc procedure, described in Appendix A. The number of resulting cases is listed in Table 5.

Table 5. Number of each precipitation type cases for Method2 (A73 and R95) and disdrometer observations after the 5-min time resolution re-binning.

Precipitation Type	Method2 with A73	Method2 with R95	Disdrometer
Rain	113	124	158
Mixed	46	60	37
Snow	118	109	85
Unknown	5	2	-
Total	282	295	280

Finally, to interpret the comparison between the different datasets it must be taken into account that the Das aerodrome (where the MRR2, disdrometer and AWS S0 were) was about 3 km from the RWP site (see Figure 1). Moreover, the lowest RWP precipitation type computed with Method2 was about 300 m above ground level (AGL) and the measures from AWS and disdrometer were about 1.5 m above ground level.

Figure 10 displays the Method2 precipitation type estimated at the lowest range gate (background colors), disdrometer observations, and AWS derived estimates at S0. It was apparent that the overall match was reasonably good, capturing the global initial snow, rain, and final snow periods. AWS S8 provided very similar results (not shown).

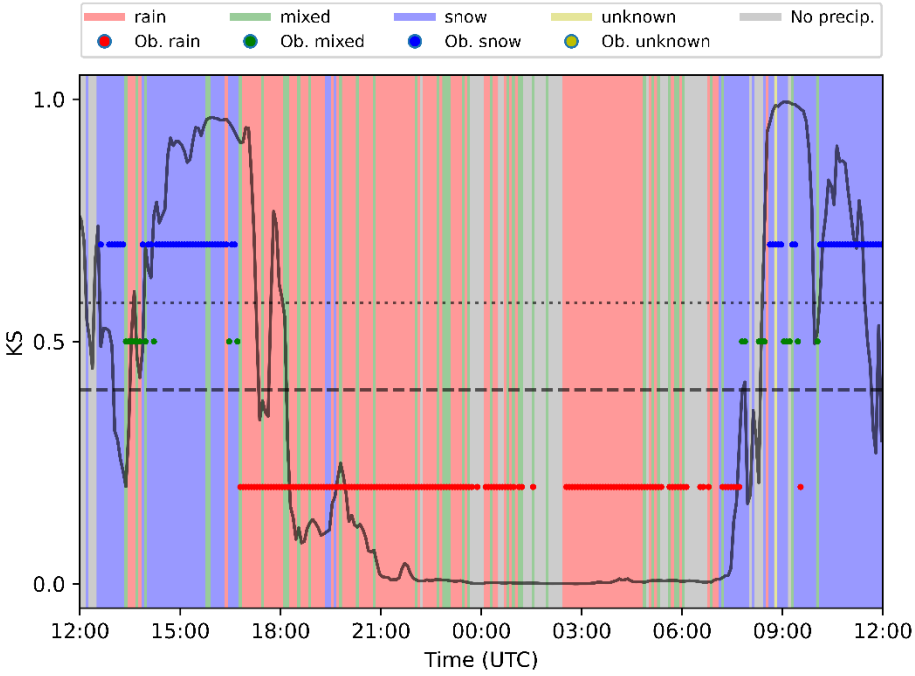

Figure 10. Precipitation type estimated from different sources for the 24 to 25 March 2017 event showing precipitation type estimates from Method2 (vertical, colored stripes), disdrometer observations (small colored circles), and AWS derived Koistinen-Saltikoff (KS) probability of snow (thick black line) at AWS S0 with reference lines for values separating the rain and mixed classes (dashed black line) and the mixed and snow classes (black dotted line). For the sake of simplicity disdrometer colored circles are shown at fixed KS probabilities within the corresponding class.

A quantitative comparison between precipitation type derived from Method2 and disdrometer data was performed with verification scores considering categorical events for the occurrence of the different classes. Scores computed were Probability of Detection (POD), False Alarm Ratio (FAR), Odds ratio skill score (ORSS) and the True Skill Statistic (TSS). A complete description of these scores is given by [45] and formulae used here are detailed in Appendix B.

The quantitative analysis of Method2 precipitation type was performed for both the so-called Atlas and Ralph approaches described in Section 3. For both approaches a range of time windows (additional time before and after the nominal time) were considered in the evaluation, to handle the effect of possible temporal mismatches accounting for the time necessary for the precipitation particle to reach the ground, which could be exacerbated by the presence of strong horizontal wind. Verification scores, considering time windows with intervals of 0, 5, and 10 min, are shown in Table 6 for Rain, Mixed, Snow, and No Precipitation cases.

Table 6. Verification scores of Method2 precipitation type at the lowest height bin compared with disdrometer observations. Time interval windows of 0, 5 and 10 min were considered for both A73 and R95 precipitation type approaches. Perfect values for each verification score are given in parentheses.

Approach	Parameter	Time Interval (min)	POD (1)	FAR (0)	ORSS (1)	TSS (1)
A73	Rain	0	0.78	0.10	0.94	0.68
	Mixed		0.19	0.81	0.41	0.10
	Snow		0.90	0.40	0.93	0.66
	No Precipitation		0.91	0.08	0.98	0.83
	Rain	5	0.79	0.10	0.95	0.70
	Mixed		0.24	0.76	0.57	0.16
	Snow		0.92	0.35	0.95	0.68
	No Precipitation		0.92	0.08	0.98	0.84
	Rain	10	0.79	0.10	0.95	0.69
	Mixed		0.31	0.69	0.68	0.23
	Snow		0.93	0.32	0.95	0.97
	No Precipitation		0.92	0.08	0.98	0.84
R95	Rain	0	0.88	0.05	0.99	0.83
	Mixed		0.33	0.78	0.57	0.21
	Snow		0.77	0.44	0.83	0.54
	No Precipitation		0.88	0.07	0.98	0.81
	Rain	5	0.88	0.05	0.99	0.84
	Mixed		0.55	0.52	0.81	0.44
	Snow		0.82	0.37	0.88	0.60
	No Precipitation		0.89	0.07	0.98	0.82
	Rain	10	0.89	0.05	0.99	0.84
	Mixed		0.59	0.55	0.84	0.48
	Snow		0.83	0.34	0.90	0.62
	No Precipitation		0.89	0.07	0.98	0.82

Results for both A73 and R95 showed skilled distinguishing of No Precipitation echoes, and, therefore, Method2 was able to discriminate between Precipitation and No Precipitation echoes, yielding the best scores of all classes (POD $\geq$ 0.88, FAR $\leq$ 0.07, ORSS $\geq$ 0.98, TSS $\geq$ 0.81). Rain and Snow were reasonably well classified, A73 being better with Snow and R95 with Rain. Mixed types were generally not well classified, with PODs systematically lower than FARs and ORSS and TSS well below 1.

5. Discussion

As seen in Section 4.1., the new methodology UBWPP (Method2) provided very similar estimates of vertical wind component w to those obtained by the existing ALWPP methodology (Method1), with a correlation index of 0.86. Small differences were found, mainly due to signal processing treatment (Method2 being occasionally slightly less sensitive than Method1), and also due to the vertical continuity check (allowing Method2 to detect vertical speeds greater than 6 m/s, undetected by Method1). An example of the

latter can be seen around 5 UTC on 25 March (Figure 6). The comparison of horizontal wind components between Method1 and Method2 also provided very similar results, with correlation coefficients equal to, or greater than, 0.96.

Regarding precipitation impact upon vertical wind components, a key question in this study, the comparison between Method1 and Method2, also showed that, in rainy conditions (Figure 7, rain flag on), the w distribution displayed a double peak, with a main peak close to zero and a secondary peak close to 1 m/s. In non-rainy conditions (rain flag off), the two distributions were unimodal with mode close to 1 m/s (Figure 7). This is a well-known pattern in RWP observations in cases of rain, as air and rain particles exhibit two distinct peaks, confirming that Method2 was able to detect them.

An additional comparison of Method1 versus Method2 horizontal and vertical wind components during a three-day period provided similar results to the case examined here (see Supplementary Materials).

Further insight into the effect of rain on vertical wind estimates is provided by Figure 11, which shows a contour frequency altitude diagram for rainy and non-rainy conditions, where frequency is shown in absolute terms (counts) with a common color scale that allows comparison between the two panels. As expected, in rainy conditions (Figure 11a) the distribution was asymmetric and the Doppler spectra widened, particularly at lower levels (<1 km AGL). This was likely due to the presence of raindrops that, as they approach the ground, increase their size, probably due to collision and coalescence processes either with other raindrops or with lower-level cloud droplets, reaching higher speeds (>5 m/s) and tilting the distribution to positive speeds, with the mode of the distribution (reddish colors) clearly tilted at lower levels (<3 km AGL). On the contrary, non-rainy conditions (Figure 11b) showed a more symmetrical distribution, in this case with slightly longer cues to the right at lower levels consistent with shallow convection, and the distribution mode close to 0 m/s.

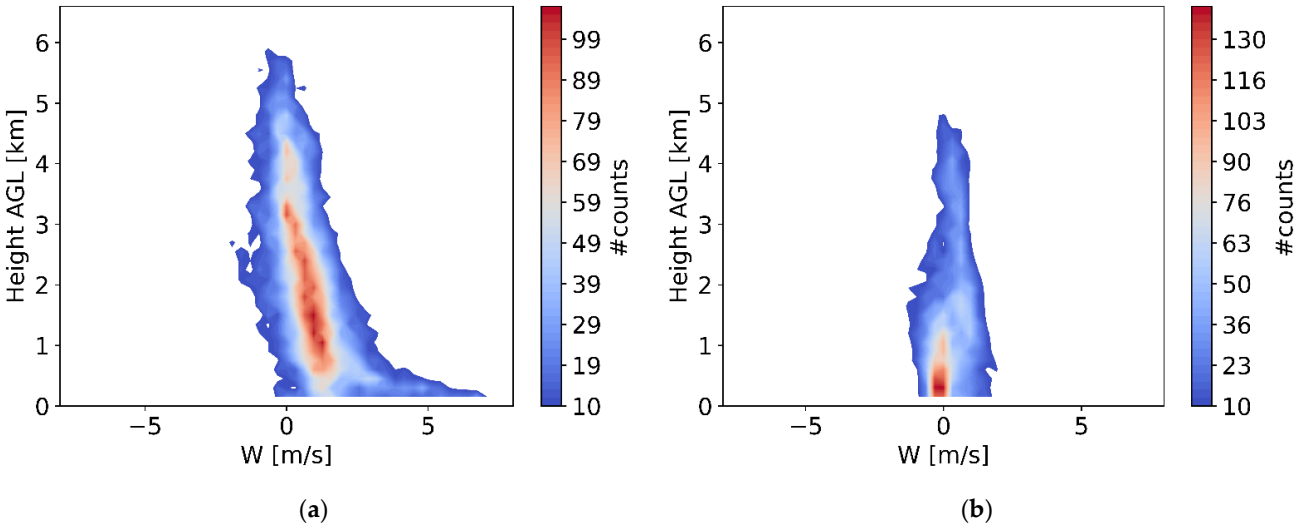

Figure 11. Contour frequency altitude diagram of vertical speed computed with RWP Method2 for 24 to 25 March 2017 considering: (**a**) rainy conditions (rain flag on), (**b**). non-rainy conditions (rain flag off). Frequencies of counts are shown in absolute terms.

The quantitative analysis of Method2 precipitation classification described in Section 4.3. considering two approaches (A73 and R95), provided mostly satisfactory results in terms of verification scores. No Precipitation and Snow echoes were very well identified by A73, with PODs ranging from 0.91 to 0.92 and 0.90 to 0.93, respectively, while for Rain, PODs were a bit lower, 0.78 to 0.79 from A73, and FARs were generally low, not exceeding 0.40 for snow echoes. Mixed echoes were poorly classified, despite the visual

inspection of Figure 9, displaying them in the transition level between snow and rain, as expected. However, both their POD and FAR were unsatisfactory.

The approach based on R95 also provided good results regarding the identification of Rain, Snow, and No Precipitation echoes, with PODs ranging from 0.77 to 0.89 and FARs not exceeding 0.44 for snow echoes. Mixed echoes were better classified than using A73, with PODs ranging from 0.33 to 0.59 and FARs 0.55 to 0.78.

Based on Table 6 (ORSS and TSS scores), A73 performed best at detecting Snow and No Precipitation echoes and R95 provided the best results for rain echoes and Mixed cases, despite the latter still having important deficiencies. Therefore, depending on the application required, one or the other approach might be more advantageous.

The fact that the mixed class at ground level was mostly associated with snow to rain and rain to snow transitions, and the disdrometer and the RWP were not collocated, might have influenced this discrepancy. It should be noted that the mixed class definition based on A73 was successfully tested for MRR2 and the disdrometer collocated during the Cerdanya-2017 field campaign [10].

To further illustrate the event examined, from 24 to 25 March 2017, a selection of variables computed with Method2 and the A73 approach are shown in Figure 12 (radar reflectivity, fall velocity, horizontal wind, and precipitation type). The passage of a warm front with an associated vortex circulation on 24 March was well captured by the wind profile (shifting from south to west) and the onset of precipitation, mostly as rain at ground level. A few hours later, at around 3 UTC 25 March, a cold front brought convective developments (a reflectivity tower exceeding 5.5 km AGL) and stronger eastern winds at all levels, shifting later to the south-west, with the arrival of the colder air mass which implied a transition from rain to snow at ground level. More details of this event can be found in [26].

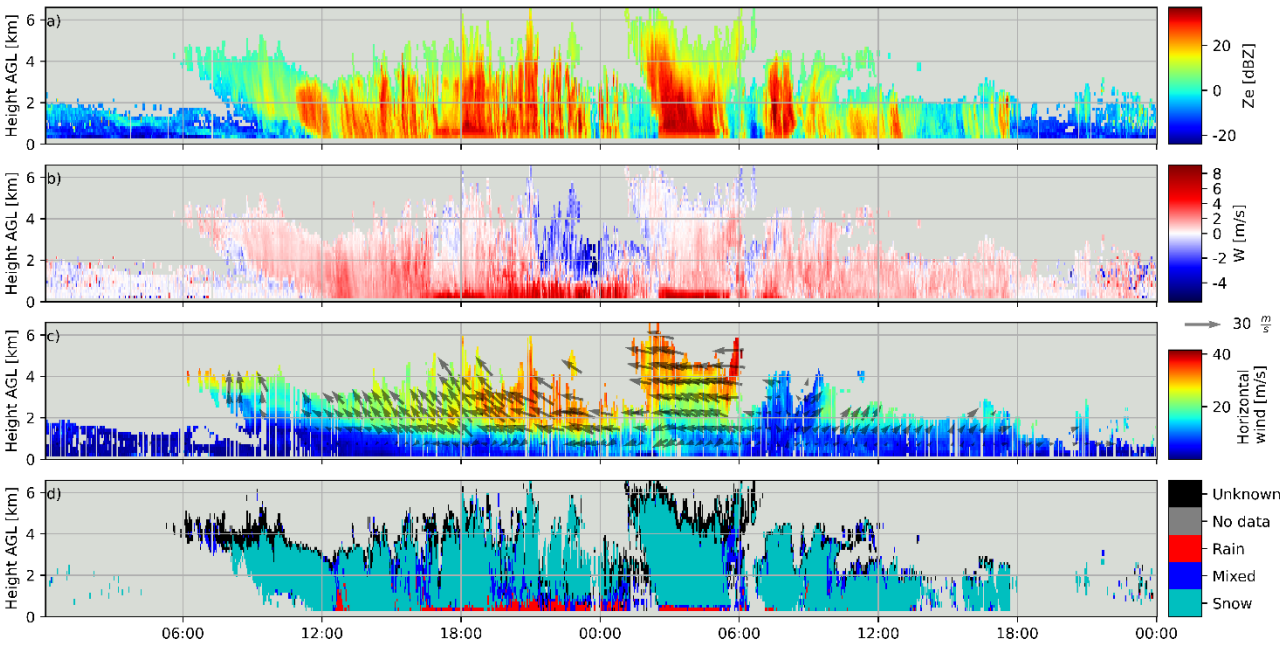

Figure 12. Method2 (A73 approach) processing applied to RWP observations recorded from 24 to 25 March 2017. (**a**) radar reflectivity, (**b**) vertical fall speed, (**c**) horizontal wind, module and direction and (**d**) precipitation type.

6. Conclusions

A new processing methodology of wind profiler Doppler spectra called UBWPP (Method 2) has been described, addressing the computation of horizontal and vertical wind components, and other variables such as radar reflectivity, spectral width, vertical and horizontal kinetic energy, refractive index, liquid water content, drop size distribution

parameters, and a simplified precipitation type classification (including rain, snow, and mixed classes).

The performance of Method2 was assessed using observations of a PCL1300 Degreane UHF wind profiler plus other datasets recorded during the Cerdanya-2017 field campaign. A 48h precipitation event was selected for this purpose as it included different ground-level snow to rain transitions.

Quantitative comparisons with a previously existing methodology to compute horizontal and vertical wind components provided satisfactory results. Nearby disdrometer, automatic weather stations, and Micro Rain Radar observations were used to evaluate the Method2 precipitation type. Despite some limitations in the comparison procedure, qualitative and quantitative results based on contingency table verification scores indicated an overall good performance of the estimated precipitation for snow and rain types showing promise for further application, unlike mixed types, that were not correctly diagnosed.

Future work is planned to review the mixed precipitation class definition and evaluate Method2 with a larger dataset with co-located instruments such as a disdrometer, a Micro Rain Radar, or a polarimetric weather radar. A larger observational data set should be used not only to confirm current results, but also to assess the feasibility of expanding precipitation types; for example, including hail cases.

A version of Method2 written in Python is publicly available at the GitHub repository with the name UBWPP (https://github.com/AlbertGBena/UBWPP (accessed on 30 September 2022)).

Supplementary Materials: The following are available online at https://www.mdpi.com/article/10.3390/rs14195023/s1, Supplementary Material S1: File Header of the Degreane wind profiler PCL1300; Supplementary Material S2: Calculation of selected parameters contained in the Degreane file header; Supplementary Material S3: Decoding of Degreane dat files; Supplementary Material S4: Overview of Radar Wind Profiler Doppler processing; Supplementary Material S5: Moments description; Supplementary Material S6: Evaluation of additional events; Supplementary Material S7: Additional information on 24 March 2017 event.

Author Contributions: Conceptualization, A.G.-B. and J.B.; methodology, A.G.-B. and J.B.; software, A.G.-B., M.U. and B.C.; data curation, A.G.-B.; writing—original draft preparation, A.G.-B. and J.B.; writing—review and editing, A.G.-B., J.B., M.U., B.C. and A.P. All authors have read and agreed to the published version of the manuscript.

Funding: This research was funded by the Spanish Government through projects CGL2015-65627-C3-1-R, CGL2015-65627-C3-2-R (MINECO/FEDER), CGL2016-81828-REDT and RTI2018-098693-B-C32 (AEI/FEDER), and the Water Research Institute (IdRA) of the University of Barcelona.

Data Availability Statement: Data Availability Statement: Data from the Cerdanya-2017 field campaign is publicly available at https://cerdanya.sedoo.fr/catalogue/ (accessed on 8 August 2022).

Acknowledgments: The Cerdanya-2017 field campaign was a research effort organized by the University of the Balearic Islands, the University of Barcelona, METEO-FRANCE and the Meteorological Service of Catalonia (SMC). We thank METEO-FRANCE/CNRM/GMEI/LISA, 4 M and TRAMM teams for the data acquisition during the campaign, especially Jean-Marie Donier from CNRM, and SMC for providing Das automatic weather station data. We also thank deeply the help regarding wind profiler technical processing from Phillip Currier from the company Degreane, manufacturer of the wind profiler used. This research was funded by the Spanish Government through projects CGL 2009-12797-C03-02 and CGL 2009-12797-C03-03 and the Water Research Institute (IdRA) of the University of Barcelona.

Conflicts of Interest: The authors declare no conflict of interest.

Appendix A

This appendix details the method to reclassify the hydrometeor type from disdrometer records, in 1-min resolution, to 5-min resolution, to match the wind-profiler estimates resolution. Figure A1 shows how the five 1-min resolution (m1 to m5) hydrometeor types (Type1 to Type5) are transformed into one of the possible five hydrometeor classes: Rain, Snow, Mixed or No Precipitation. The first possibility considered is that all five 1-min types are the same ("F All Types") which obviously yields the same hydrometeor type. The second one considers the number of rain (R) and snow (S) minutes are the same which produces a Mixed type. The third possibility considers that there are more than three 1-min types equal to no precipitation which produces a No Precipitation type. Then two symmetric groups of conditions are considered in case all 1-min types are not equal to snow or rain, leading to various possibilities. Table A1 lists examples of the hydrometeor reclassification.

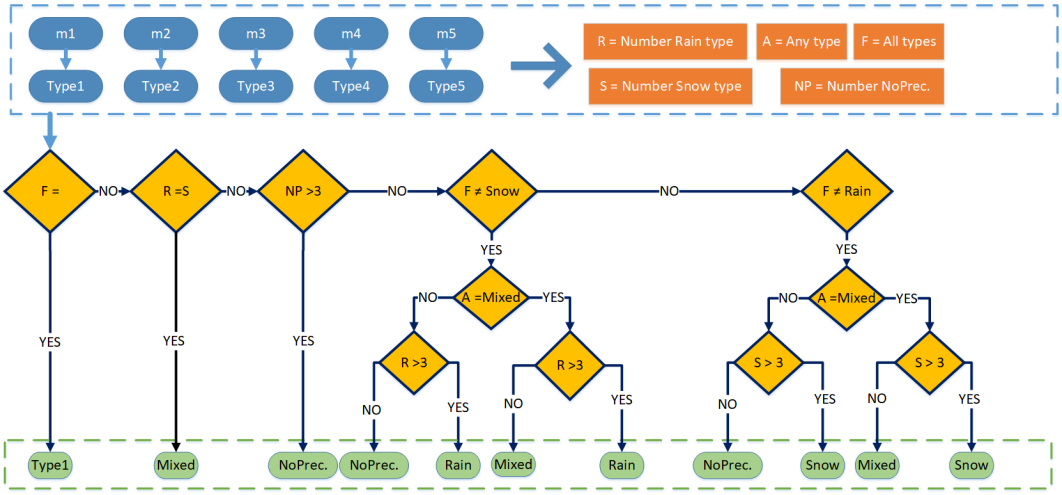

Figure A1. Flow diagram showing the hydrometeor reclassification from 1-min to 5-min periods.

Table A1. Examples of precipitation type reclassification from 1-min to 5-min resolution.

Case	5-min Interval of 1-min Types					Type Chosen
	m1	m2	m3	m4	m5	
1	Rain	Rain	Rain	Rain	Rain	Rain
2	Snow	Snow	Snow	Snow	Snow	Snow
3	Rain	Rain	Rain	Rain	Mixed	Rain
4	Snow	Snow	Snow	Snow	Mixed	Snow
5	Rain	Rain	NoPrec	Snow	Snow	Mixed
6	Rain	Rain	Rain	Snow	Snow	Mixed
7	Snow	Snow	Snow	Rain	Rain	Mixed
8	NoPrec	NoPrec	NoPrec	Rain	Rain	NoPrec
9	Rain	Rain	Rain	Rain	Snow	Mixed
10	Snow	Snow	Snow	Snow	Rain	Mixed
11	Rain	Rain	Rain	Mixed	Mixed	Mixed

Appendix B

The verification scores used are based on a traditional 2 × 2 contingency table where "hits" represent the number of events (precipitation types) correctly forecast, "misses" the number of events not forecast, "false alarms" the number of forecast events that didn't occur and "correct negatives" the correctly forecast events that didn't occur. Scores considered here are Probability of Detection (POD), False Alarm Ratio (FAR), Odds ratio skill score

(ORSS) and the True Skill Statistic, also known as Hanssen and Kuipers discriminant or Peirce's skill score, (TSS), given by the following equations:

$$POD = \frac{hits}{hits + misses} \tag{A1}$$

$$FAR = \frac{false\ alarms}{hits + false\ alarms} \tag{A2}$$

$$ORSS = \frac{hits \cdot Correct\ negatives - misses \cdot false\ alarms}{hits \cdot Correct\ negatives + misses \cdot false\ alarms} \tag{A3}$$

$$TSS = \frac{hits}{hits + misses} - \frac{false\ alarms}{Correct\ negatives + false\ alarms} \tag{A4}$$

References

1. Yamamoto, M. New Observations by Wind Profiling Radars. In *Doppler Radar Observations—Weather Radar, Wind Profiler, Ionospheric Radar, and Other Advanced Applications*; Bech, J., Chau, J., Eds.; InTech: London, UK, 2012; ISBN 978-953-51-0496-4.
2. Lehmann, V.; Brown, W. Radar Wind Profiler. In *Springer Handbook of Atmospheric Measurements*; Foken, T., Ed.; Springer: Cham, Switzerland, 2021; pp. 901–933. ISBN 978-3-030-52171-4.
3. Molod, A.; Salmun, H.; Dempsey, M. Estimating Planetary Boundary Layer Heights from NOAA Profiler Network Wind Profiler Data. *J. Atmos. Ocean. Technol.* **2015**, *32*, 1545–1561. [CrossRef]
4. Nash, J.; Oakley, T.J. Development of COST 76 Wind Profiler Network in Europe. *Phys. Chem. Earth Part B Hydrol. Ocean. Atmos.* **2001**, *26*, 193–199. [CrossRef]
5. Ishihara, M.; Kato, Y.; Abo, T.; Kobayashi, K.; Izumikawa, Y. Characteristics and Performance of the Operational Wind Profiler Network of the Japan Meteorological Agency. *J. Meteorol. Soc. Jpn. Ser. II* **2006**, *84*, 1085–1096. [CrossRef]
6. Kim, K.-H.; Kim, M.-S.; Seo, S.-W.; Kim, P.-S.; Kang, D.-H.; Kwon, B.H. Quality Evaluation of Wind Vectors from UHF Wind Profiler Using Radiosonde Measurements. *J. Environ. Sci. Int.* **2015**, *24*, 133–150. [CrossRef]
7. Liu, B.; Guo, J.; Gong, W.; Shi, L.; Zhang, Y.; Ma, Y. Characteristics and Performance of Wind Profiles as Observed by the Radar Wind Profiler Network of China. *Atmos. Meas. Tech.* **2020**, *13*, 4589–4600. [CrossRef]
8. Gonzalez, S.; Bech, J.; Udina, M.; Codina, B.; Paci, A.; Trapero, L. Decoupling between Precipitation Processes and Mountain Wave Induced Circulations Observed with a Vertically Pointing K-Band Doppler Radar. *Remote Sens.* **2019**, *11*, 1034. [CrossRef]
9. Zhang, Y.; Guo, J.; Yang, Y.; Wang, Y.; Yim, S. Vertical Wind Shear Modulates Particulate Matter Pollutions: A Perspective from Radar Wind Profiler Observations in Beijing, China. *Remote Sens.* **2020**, *12*, 546. [CrossRef]
10. Garcia-Benadi, A.; Bech, J.; Gonzalez, S.; Udina, M.; Codina, B.; Georgis, J.F. Precipitation Type Classification of Micro Rain Radar Data Using an Improved Doppler Spectral Processing Methodology. *Remote Sens.* **2020**, *12*, 4113. [CrossRef]
11. Wang, D.; Giangrande, S.E.; Feng, Z.; Hardin, J.C.; Prein, A.F. Updraft and Downdraft Core Size and Intensity as Revealed by Radar Wind Profilers: MCS Observations and Idealized Model Comparisons. *J. Geophys. Res. Atmos.* **2020**, *125*, e2019JD031774. [CrossRef]
12. Politovich, M.K.; Goodrich, R.K.; Morse, C.S.; Yates, A.; Barron, R.; Cohn, S.A. The Juneau Terrain-Induced Turbulence Alert System. *Bull. Am. Meteorol. Soc.* **2011**, *92*, 299–313. [CrossRef]
13. Udina, M.; Bech, J.; Gonzalez, S.; Soler, M.R.; Paci, A.; Miró, J.R.; Trapero, L.; Donier, J.M.; Douffet, T.; Codina, B.; et al. Multi-Sensor Observations of an Elevated Rotor during a Mountain Wave Event in the Eastern Pyrenees. *Atmos. Res.* **2020**, *234*, 104698. [CrossRef]
14. Wang, C.; Chen, M.; Chen, Y. Impact of Combined Assimilation of Wind Profiler and Doppler Radar Data on a Convective-Scale Cycling Forecasting System. *Mon. Weather Rev.* **2022**, *150*, 431–450. [CrossRef]
15. Degelia, S.K.; Wang, X.; Stensrud, D.J.; Turner, D.D. Systematic Evaluation of the Impact of Assimilating a Network of Ground-Based Remote Sensing Profilers for Forecasts of Nocturnal Convection Initiation during PECAN. *Mon. Weather Rev.* **2020**, *148*, 4703–4728. [CrossRef]
16. Schraff, C.; Reich, H.; Rhodin, A.; Schomburg, A.; Stephan, K.; Periáñez, A.; Potthast, R. Kilometre-scale Ensemble Data Assimilation for the COSMO Model (KENDA). *Q. J. R. Meteorol. Soc.* **2016**, *142*, 1453–1472. [CrossRef]
17. Liu, D.; Huang, C.; Feng, J. Influence of Assimilating Wind Profiling Radar Observations in Distinct Dynamic Instability Regions on the Analysis and Forecast of an Extreme Rainstorm Event in Southern China. *Remote Sens.* **2022**, *14*, 3478. [CrossRef]
18. Ralph, F.M.; Neiman, P.J.; Ruffieux, D. Precipitation Identification from Radar Wind Profiler Spectral Moment Data: Vertical Velocity Histograms, Velocity Variance, and Signal Power–Vertical Velocity Correlations. *J. Atmos. Ocean. Technol.* **1996**, *13*, 545–559. [CrossRef]
19. Radenz, M.; Bühl, J.; Lehmann, V.; Görsdorf, U.; Leinweber, R. Combining Cloud Radar and Radar Wind Profiler for a Value Added Estimate of Vertical Air Motion and Particle Terminal Velocity within Clouds. *Atmos. Meas. Tech.* **2018**, *11*, 5925–5940. [CrossRef]

20. Tsai, S.-C.; Chu, Y.-H.; Chen, J.-S. Identification of Concurrent Clear-Air and Precipitation Doppler Profiles for VHF Radar and an Incorporating Study of Strongly Convective Precipitation with Dual-Polarized Microwave Radiometer. *Atmosphere* **2022**, *13*, 557. [CrossRef]
21. Lundquist, J.D.; Neiman, P.J.; Martner, B.; White, A.B.; Gottas, D.J.; Ralph, F.M. Rain versus Snow in the Sierra Nevada, California: Comparing Doppler Profiling Radar and Surface Observations of Melting Level. *J. Hydrometeorol.* **2008**, *9*, 194–211. [CrossRef]
22. Valdivia, J.M.; Scipión, D.E.; Milla, M.; Silva, Y. Multi-Instrument Rainfall-Rate Estimation in the Peruvian Central Andes. *J. Atmos. Ocean. Technol.* **2020**, *37*, 1811–1826. [CrossRef]
23. Ryzhkov, A.V.; Schuur, T.J.; Burgess, D.W.; Heinselman, P.L.; Giangrande, S.E.; Zrnic, D.S. The Joint Polarization Experiment: Polarimetric Rainfall Measurements and Hydrometeor Classification. *Bull. Am. Meteorol. Soc.* **2005**, *86*, 809–824. [CrossRef]
24. Besic, N.; Ventura, J.F.I.; Grazioli, J.; Gabella, M.; Germann, U.; Berne, A. Hydrometeor Classification through Statistical Clustering of Polarimetric Radar Measurements: A Semi-Supervised Approach. *Atmos. Meas. Tech.* **2016**, *9*, 4425–4445. [CrossRef]
25. Chen, Y.; Liu, X.; Bi, K.; Zhao, D. Hydrometeor Classification of Winter Precipitation in Northern China Based on Multi-Platform Radar Observation System. *Remote Sens.* **2021**, *13*, 5070. [CrossRef]
26. González, S.; Bech, J.; Garcia-Benadí, A.; Udina, M.; Codina, B.; Trapero, L.; Paci, A.; Georgis, J.-F. Vertical Structure and Microphysical Observations of Winter Precipitation in an Inner Valley during the Cerdanya-2017 Field Campaign. *Atmos. Res.* **2021**, *264*, 105826. [CrossRef]
27. O'Hora, F.; Bech, J. Improving Weather Radar Observations Using Pulse-Compression Techniques. *Meteorol. Appl.* **2007**, *14*, 389–401. [CrossRef]
28. Campistron, B.; Réchou, A. Rain Kinetic Energy Measurement with a UHF Wind Profiler: Application to Soil Erosion Survey of a Volcanic Tropical Island. In Proceedings of the 13th International Workshop on Technical and Scientific Aspects of MST Radars, Kühlungsborn, Germany, 19–23 March 2012; pp. 47–51. Available online: https://www.iap-kborn.de/MST13/files/mst13proceedings.pdf (accessed on 8 August 2022).
29. Peters, G.; Fischer, B.; Andersson, T. Rain Observations with a Vertically Looking Micro Rain Radar (MRR). *Boreal Environ. Res.* **2002**, *7*, 353–362.
30. Chang, W.Y.; Lee, G.W.; Jou, B.J.D.; Lee, W.C.; Lin, P.L.; Yu, C.K. Uncertainty in Measured Raindrop Size Distributions from Four Types of Collocated Instruments. *Remote Sens.* **2020**, *12*, 1167. [CrossRef]
31. Tokay, A.; Wolff, D.B.; Petersen, W.A. Evaluation of the New Version of the Laser-Optical Disdrometer, OTT Parsivel2. *J. Atmos. Ocean. Technol.* **2014**, *31*, 1276–1288. [CrossRef]
32. World Meteorological Organization. *Manual on Codes—International Codes, Volume I.1, Annex II to the WMO Technical Regulations: Part A—Alphanumeric Codes*; World Meteorological Organization: Geneva, Switzerland, 2019; ISBN 978-92-63-10306-2.
33. Koistinen, J.; Saltikoff, E. Experience of Customer Products of Accumulated Snow, Sleet and Rain. *COST75 Adv. Weather Radar Syst.* **1998**, *397*, 406.
34. Casellas, E.; Bech, J.; Veciana, R.; Pineda, N.; Miró, J.R.; Moré, J.; Rigo, T.; Sairouni, A. Nowcasting the Precipitation Phase Combining Weather Radar Data, Surface Observations, and NWP Model Forecasts. *Q. J. R. Meteorol. Soc.* **2021**, *147*, 3135–3153. [CrossRef]
35. Casellas, E.; Bech, J.; Veciana, R.; Pineda, N.; Rigo, T.; Miró, J.R.; Sairouni, A. Surface Precipitation Phase Discrimination in Complex Terrain. *J. Hydrol.* **2021**, *592*, 125780. [CrossRef]
36. Anandan, V.K.; Balamuralidhar, P.; Rao, P.B.; Jain, A.R.; Pan, C.J. An Adaptive Moments Estimation Technique Applied to MST Radar Echoes. *J. Atmos. Ocean. Technol.* **2005**, *22*, 396–408. [CrossRef]
37. Allabakash, S.; Yasodha, P.; Bianco, L.; Reddy, S.V.; Srinivasulu, P. Improved Moments Estimation for VHF Active Phased Array Radar Using Fuzzy Logic Method. *J. Atmos. Ocean. Technol.* **2015**, *32*, 1004–1014. [CrossRef]
38. Price-Whelan, A.M.; Sipőcz, B.M.; Günther, H.M.; Lim, P.L.; Crawford, S.M.; Conseil, S.; Shupe, D.L.; Craig, M.W.; Dencheva, N.; Ginsburg, A.; et al. The Astropy Project: Building an Open-Science Project and Status of the v2.0 Core Package. *Astron. J.* **2018**, *156*, 123. [CrossRef]
39. Atlas, D.; Srivastava, R.C.; Sekhon, R.S. Doppler Radar Characteristics of Precipitation at Vertical Incidence. *Rev. Geophys.* **1973**, *11*, 1–35. [CrossRef]
40. Ralph, F.M.; Neiman, P.J.; van de Kamp, D.W.; Law, D.C. Using Spectral Moment Data from NOAA's 404-MHz Radar Wind Profilers to Observe Precipitation. *Bull. Am. Meteorol. Soc.* **1995**, *76*, 1717–1739. [CrossRef]
41. Ulbrich, C.W. Natural Variations in the Analytical Form of the Raindrop Size Distribution. *J. Clim. Appl. Meteorol.* **1983**, *22*, 1764–1775. [CrossRef]
42. Chu, Y.-H.; Su, C.-L. An Investigation of the Slope–Shape Relation for Gamma Raindrop Size Distribution. *J. Appl. Meteorol. Climatol.* **2008**, *47*, 2531–2544. [CrossRef]
43. Gunn, R.; Kinzer, G.D. The Terminal Velocity of Fall for Water Droplets in Stagnant Air. *J. Meteorol.* **1949**, *6*, 243–248. [CrossRef]
44. Cerro, C.; Bech, J.; Codina, B.; Lorente, J. Modeling Rain Erosivity Using Disdrometric Techniques. *Soil Sci. Soc. Am. J.* **1998**, *62*, 731–735. [CrossRef]
45. Jolliffe, I.T.; Stephenson, D.B. *Forecast Verification: A Practitioner's Guide in Atmospheric Science*; John Wiley & Sons: Hoboken, NJ, USA, 2012; ISBN 978-1-119-96000-3.

Capítol 5

Conclusions

En aquest darrer capítol de la tesi es presenten les conclusions de la recerca realitzada en el període doctoral. El treball desenvolupat partia dels objectius generals detallats al Capítol 1, que eren:

- **OG.1. Estudi de l'estructura de la Banda Brillant**.
- **OG.2 Classificació d'hidrometeors amb perfiladors Doppler**.

Aquests objectius de la tesi s'havien desglossat en sis objectius específics. Per aquest motiu a l'apartat següent de conclusions finals es detallarà l'assoliment de cada objectiu específic individualment. Finalment, es comentaran algunes línies de recerca per a possibles futurs treballs.

5.1. Conclusions finals

- **OE.1. Desenvolupament d'una metodologia de caracterització de la Banda Brillant amb Micro Rain Radar**.

S'ha creat una metodologia per la caracterització de la banda brillant, on es determina l'altura del nivell inferior, pic i superior de la BB mitjançant l'estudi del tercer moment de la distribució de velocitats. La base teòrica és que en la BB les partícules de neu grans es fusionen i donen lloc a d'altres més petites, aquestes després per agregació es convertiran en més grans i augmentarà la seva velocitat. Aquest fet, des del punt de vista de l'espectre de velocitat provocarà un canvi en la asimetria de la distribució de velocitats i justament aquest fenomen és el que caracteritzarà els nivells de la BB. Una de les avantatges d'aquesta nova metodologia és la possibilitat de detectar BB en casos de moviment ascendent moderat, on la sistemàtica de Cha et al. (2009) no detecta el gradient en el perfil de velocitats.

La metodologia s'ha comprovat en 39 dies utilitzant un producte d'estimació de la BB elaborat pel fabricant del MRR i les dades del radiosondatge (prenent com a referència l'altura corresponent als 0 ºC, o nivell de la isoterma zero i que anomenarem

com isozero). Els resultats obtinguts indiquen que els nivells inferior i superior de la BB es troben uns 200 metres al voltant de la isozero, i que l'altura del pic de la BB es troba a uns 50 m per sota de la isozero. Per altra banda en la comparativa amb la metodologia del fabricant vers les dades del sondatge es detecta que el valor del nivell de fusió (*melting level*) es troba uns 200 m per sota la isozero. Cal destacar que la nova metodologia presenta una BB contínua en el temps, en contra del fabricant que indica ocasionalment valors aïllats i aparentment poc realistes. Aquest fet afavoreix que el nombre d'altures respecte el temps en la nova metodologia sigui àmpliament superior a la del fabricant (5000 deteccions de la nova metodologia versus 1800 del fabricant). Cal senyalar que en la metodologia del fabricant s'entreveu que la detecció de falsos positius és molt superior a la metodologia proposada, que es més conservadora.

Aquesta metodologia s'ha implantat pel radar de mira vertical Micro Rain Radar del fabricant Metek, model MRR-Pro, en el programa *RaProM-Pro*. Aquest programa inclou altres millores com ara un processat propi del soroll que millora la capacitat de detecció de la senyal, sobretot a altures elevades, guanyant un 2,8% de sensibilitat. També millora la continuïtat del perfil vertical de velocitats, i per tant dels perfils del factor de reflectivitat, incloent el procés per evitar l'aliàsing. S'ha realitzat una adaptació de la pròpia atenuació degut a la precipitació. Tots els resultats es presenten en un arxiu en format parametritzat (netcdf).

- **OE.2 Desenvolupament d'una metodologia de classificació d'hidrometeors amb Micro Rain Radar.**

La classificació d'hidrometeors parteix de la relació entre la velocitat vertical vers la reflectivitat obtinguda (Atlas et al. 1973), que ens permet diferenciar diferents tipus d'hidrometeors: pedra, neu, mixt, plugim i pluja (*hail, snow, mixed and rain*) a partir de les seves velocitats de caiguda mitjana i la seva desviació típica.

Una vegada es detecta la precipitació en fase líquida (plugim i pluja), aplicant la hipòtesi que la velocitat és terminal s'implementa la relació diàmetre vers velocitat de caiguda (Gunn & Kinzer 1949) i obtenim la seva distribució de mides (DSD) a partir de la reflectivitat espectral i de la seva secció transversal de cada partícula, obtinguda amb l'aproximació de Mie ja que la longitud d'ona del radar és de l'ordre de la mida de les gotes. Amb la DSD ja podem calcular altres paràmetres de la precipitació com la intensitat de pluja (*Rain Rate*, RR) i la quantitat de aigua líquida (*Liquid Water Content*, LWC).

La nova metodologia s'ha validat mitjançant un estudi de 32 dies en l'interval de gener de 2017 a octubre de 2019 distribuïts per estacions on tenim 5 casos d'hivern, 19 de primavera, 4 d'estiu i 4 de tardor. Pel criteri d'avaluació s'han emprat taules de contingència utilitzant diferents paràmetres d'on destaquem, la probabilitat de detecció POD i ràtio de falsa alarma FAR, amb les dades del tipus d'hidrometeor obtingudes en superfície per un disdròmetre Parsivel. El POD obtingut per la pluja i la neu és superior al 97% amb un FAR no superior al 30%, que ens permet validar la metodologia, almenys a nivell de superfície.

Aquesta metodologia s'ha implantat pel radar de mira vertical Micro Rain Radar del fabricant Metek, model MRR2, amb la generació d'un programa propi *RaProM*. Les dades font que utilitza el *RaProM* són les dades crues obtingudes per l'equip emmagatzemades en codi ASCII. Pel programa s'ha implementat una sistemàtica per la detecció de la senyal vers el soroll (Hildebrand & Sekhon 1974) i s'ha implementat la

metodologia proposada en Maahn & Kollias (2012) per evitar l'aliàsing. El resultat del programa és un arxiu multi paramètric (netcdf).

- **OE.3. Caracterització de perfils verticals d'hidrometeors durant la campanya Cerdanya-2017.**

En aquest objectiu específic s'ha aplicat la metodologia del RaProM a tots els perfils verticals generats pel MRR2 durant la campanya de la Cerdanya 2017. Aquesta cobreix el període de desembre de 2016 a maig de 2017 en la zona del Pirineu Oriental, en una vall interior relativament ampla (vall de la Cerdanya) corresponent a la conca alta del riu Segre. La zona cobreix una extensió d'un 15 km per 35 km i està rodejada per carenes que superen els 2000 m d'altitud i diversos pics que superen 2800 m.

Les dades obtingudes i processades pel MRR2 juntament amb els altres instruments ubicats en la zona, tal com el MWR han facilitat la detecció de diversos fenòmens. Entre aquests destaca el desacoblament dels processos de precipitació i les circulacions induïdes per les ones de muntanya [29], així com la detecció de processos de refredament per efecte de la sublimació durant el pas d'un front càlid i els efectes de la capa de cisallament del vent respecte els cims vers la sublimació al fons de la vall.

- **OE.4. Desenvolupament d'una metodologia de classificació d'hidrometeors amb perfilador de vent.**

En el Capítol 4 s'ha implementat una metodologia de classificació simplificada d'hidrometeors, contemplant pluja, mixt, neu i desconegut (tipus de precipitació no identificat). Aquesta metodologia està basada en els llindars en la velocitat terminal de caiguda de partícules precipitants dels treballs d'Atlas et al. (1973) i Ralph et al. (1995)). Cal tenir present que els resultats experimentals del treball d'Atlas s'obtenen a partir d'un radar centimètric i les dades d'en Ralph es basen en dades obtingudes amb un perfilador de vent de banda VHF.

Per a poder aplicar la metodologia s'ha dissenyat un programa, que un cop llegides les dades en cru, implementa un nou mètode de detecció de la senyal i on s'aplica la continuïtat espai-temporal de les mesures per evitar senyals no meteorològics. Una de les dificultats superades ha estat la detecció de la precipitació, ja que l'equip pot detectar moviments d'aire i no necessàriament de precipitació com succeeix en el cas del MRR.

La validació del mètode, anomenat UBWPP, s'ha realitzat en dues fases. A la primera s'ha comprovat que el resultat de la sistemàtica de detecció de senyal i continuïtat en la velocitat vertical i les components del vent horitzontal no es desviaven dels resultat dels mateixos paràmetres obtinguts amb un programa del *Aerologie Laboratoire* (ALWPP).

La segona fase ha consistit en la validació de la classificació mitjançant mesures de superfície, semblant al detallat al Capítol 3, obtingudes amb un disdròmetre i on el sistema de validació ha consistit en resultats de la taula de contingència. Sobre els resultats obtinguts s'observa que la No precipitació es detecta amb un POD Superior al 0.88 i un FAR inferior a 0.08, i és aquest resultat el que valida la metodologia per la detecció de precipitació. Sobre la classificació els valors obtinguts per la neu i pluja són satisfactoris (POD >0.78 i FAR< 0.40) d'on es destaca que la metodologia d'Atlas es millor en la detecció de neu i per contra la metodologia de Ralph és millor en la detecció

de pluja. Malauradament en el tipus mixt no s'aconsegueixen bons resultats (POD de l'ordre de 0.20 i FAR de l'ordre 0.80). Aquesta discrepància pot ser deguda a que la primera altura on es determina el tipus de classificació, en mode baix del perfilador que és el que disposa d'una resolució espacial menor de 150 m, és la tercera sobre el dispositiu, per tant la comparació es realitza amb mesures de superfície vers tipus detectats a 450 m. Aquest fet implica que l'hidrometeor a 450 m sobre el nivell de terra sí podria estar en fase mixta però degut a la temperatura superficial pot haver canviat d'estat. Per exemple, en l'episodi del dia 24 al 25 de març de 2017 a nivell de superfície únicament es detecten 37 casos de mixt, localitzats en la zona de transició que indica el perfilador de vent, tal com es veu en la següent **Figura 6**.

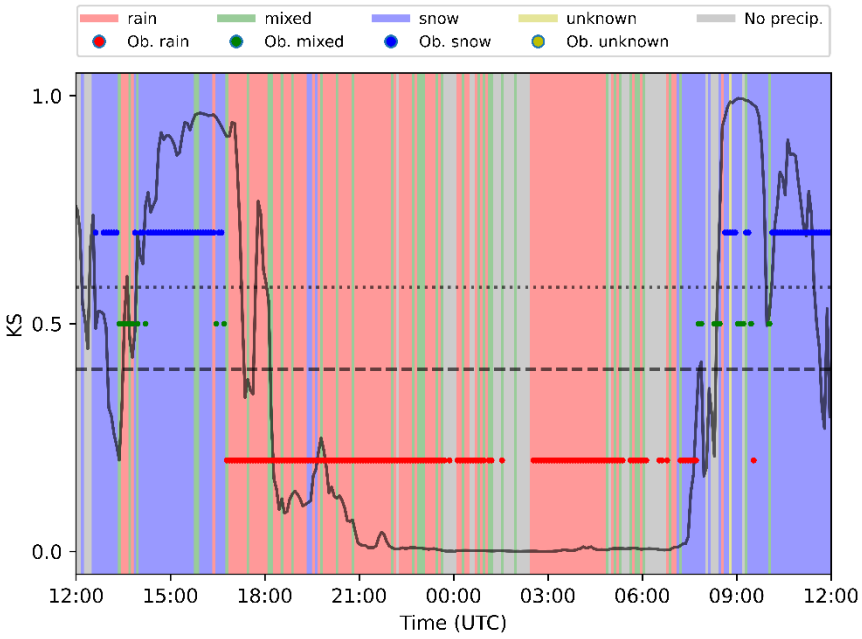

***Figura 6**. Estimació del tipus de precipitació per l'episodi del 24 al 25 de març de 2017. El color de fons és la classificació del perfilador de vent. Els cercles és la classificació en superfície realitzada pel disdròmetre. La línia negra contínua representa la probabilitat de neu derivada de les dades de les estacions automàtiques seguint el treball de* Koistinen & Saltikoff (1998)*, la línia discontínua és la probabilitat KS màxima de trobar neu, i la puntejada és la probabilitat mínima de trobar pluja.*

Aquesta metodologia és la primera vegada que s'aplica sobre un perfilador de vent, i amb el resultats obtinguts es dona a peu a l'ampliació de les aplicacions del dispositiu.

- **OE.5. Desenvolupament d'una metodologia de verificació de perfils d'hidrometeors amb observacions properes a la superfície.**

En els capítols 3 i 4 la metodologia proposada s'ha comparat amb mesures proporcionades per un disdròmetre Parsivel, en superfície. En els dos casos s'han adaptat els tipus de classificació del disdròmetre, mitjançant el paràmetre 4677 (Taula codificada d'observacions sinòptiques de l'Organització Meteorològica Mundial), als tipus d'hidrometeor determinats tant pel MRR com pel UHF.

Com la comparativa es realitza en dos altures diferents s'ha creat una finestra temporal d'estudi comuna, tenint en compte el component horitzontal del vent, així com l'interval de temps des de la primera altura de detecció del radar de mira vertical i la superfície.

En el cas del MRR aquest finestra temporal s'ha pogut aplicar sense problemes degut a que la resolució temporal del MRR i el disdròmetre és la mateixa, 1 minut. En el cas del perfilador de vent la resolució temporal entre els equips és diferent, de 3.5 minuts pel perfilador de vent i d'un minut pel disdròmetre. Aquesta diferència de resolució s'ha resolt mitjançant una integració a un interval definit, en aquest cas de 5 minuts. Al definir l'interval s'han de fer la mitjana dels valors qualitatius i per això es detalla una sistemàtica de mitjana exposada en la **Figura 7**.

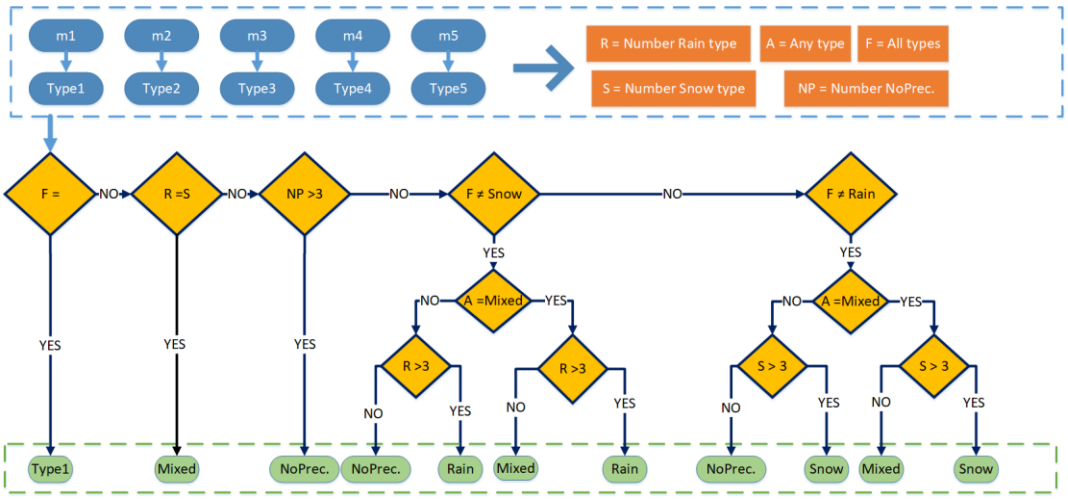

***Figura 7**. Diagrama de flux que detalla la reclassificació del tipus d'hidrometeor al passar d'una resolució de 1 minut a 5 minuts*

Els resultats de la detecció de precipitació i no precipitació en els dos capítols és molt elevada, amb una probabilitat de detecció (POD) superior al 0.95, fet que té molt rellevància sobretot en el Capítol 4 ja que el perfilador de vent no s'havia contemplat com equip per mesurar la precipitació.

- **OE.6. Difusió dels resultats de la tesi mitjançant programari d'accés lliure.**

En cada un dels objectius s'ha posat a disposició de la comunitat científica el codi per poder generar les seves dades, mitjançant el repositori de github, completament obert i lliure, on la seva ubicació és:

Processament de Micro Rain Radar, de Metek model MRR2:

https://github.com/AlbertGBena/RaProM

Processament de Micro Rain Radar, de Metek model MRR-Pro:

https://github.com/AlbertGBena/RaProM-Pro

Processament de Perfilador de vent, de Degreane PCL1300:

https://github.com/AlbertGBena/UBWPP

Processament i visualització del radiosondatge del Servei Meteorològic de Catalunya:

https://github.com/AlbertGBena/RadiosoundingDataReading

El motiu de deixar-ho obert és que el codi es pugui anar millorant i la comunitat disposi de més eines per continuar les seves investigacions. Gràcies als programes en obert els investigadors poden tractar les dades a partir d'alguns dels productes generats i modificar el programa per les seves necessitats particulars.

Cal senyalar que durant el període de la tesi els programes han anat evolucionant afegint diferents noves funcions, arrel de peticions d'usuaris, habitualment institucions meteorològiques com per exemple la GPM-GV de la NASA Wallops Flight Facility i el LIM (Leipzig Institute for Meteorology) entre d'altres. Entre les peticions realitzades es pot citar l'ampliació de paràmetres de sortida (que es calculaven internament però no s'enregistraven), tals com la DSD amb 3 coordenades (temps, espectre i altura), la DSD suposant que tot l'espectre està en fase líquida, millora la correcció de l'altitud, etc.

5.2. Futurs treballs

Per a futurs treballs seria recomanable comprovar els resultats dels diferents programes amb major nombre de casos a ser possible en zones diferents a les latituds mitjanes. Així s'analitzaria com es comporten les metodologies per condicions diferents amb valors extrems de velocitat vertical, casos de convecció tropical, rangs de temperatura diferents als considerats, etc..

Un dels sistemes de validació utilitzats és amb les mesures en superfície. Com validació inicial és vàlida, però seria necessari l'anàlisi del tipus de hidrometeor a totes les altures. Aquesta comparativa es podria dur a terme mitjançant la comparació amb dades de radars polarimètrics. Per aquesta tasca caldria utilitzar conjunts d'equips propers on els volums mostrejats fossin el més semblant possible. A més es podria plantejar la incorporació de noves classes de precipitació.

Bibliografia

Adirosi, E.; Baldini, L.; Roberto, N.; Gatlin, P.; Tokay, A. Improvement of vertical profiles of raindrop size distribution from micro rain radar using 2D video disdrometer measurements. Atmos. Res. 2016, 169, Part, 404–415, doi:https://doi.org/10.1016/j.atmosres.2015.07.002.

Adirosi, E.; Baldini, L.; Tokay, A. Rainfall and DSD Parameters Comparison between Micro Rain Radar, Two-Dimensional Video and Parsivel2 Disdrometers, and S-Band Dual-Polarization Radar. J. Atmos. Ocean. Technol. 2020, 37, 621–640, doi:10.1175/JTECH-D-19-0085.1.

Arulraj, M.; Barros, A.P. Automatic detection and classification of low-level orographic precipitation processes from space-borne radars using machine learning. Remote Sens. Environ. 2021, 257, 112355, doi:https://doi.org/10.1016/j.rse.2021.112355.

Atlas, D.; Srivastava, R.C.; Sekhon, R.S. Doppler radar characteristics of precipitation at vertical incidence. Rev. Geophys. 1973, 11, 1–35, doi:10.1029/RG011i001p00001.

Brast, M.; Markmann, P. Detecting the Melting Layer with a Micro Rain Radar Using a Neural Network Approach. Atmos. Meas. Tech. Discuss. 2019, doi:10.5194/amt-2019- 248.

Campistron, B.; Réchou, A. Rain kinetic energy measurement with a UHF wind profiler: application to soil erosion survey of a volcanic tropical island. In Proceedings of the 13th international workshop on technical and scientific aspects of MST radars; Germany, 2012; p. En ligne.

Cha, J.W.; Chang, K.H.; Yum, S.S.; Choi, Y.J. Comparison of the bright band characteristics measured by Micro Rain Radar (MRR) at a mountain and a coastal site in South Korea. In Proceedings of the Advances in Atmospheric Sciences; 2009; Vol. 26, pp. 211–221.

Demir, I.; Krajewski, W.F. Towards an integrated Flood Information System: Centralized data access, analysis, and visualization. Environ. Model. Softw. 2013, 50, 77–84, doi:https://doi.org/10.1016/j.envsoft.2013.08.009.

Dolan, B.; Fuchs, B.; Rutledge, S.A.; Barnes, E.A.; Thompson, E.J. Primary Modes of Global Drop Size Distributions. J. Atmos. Sci. 2018, 75, 1453–1476, doi:10.1175/JAS-D-17-0242.1.

Fabry, F.; Zawadzki, I. Long-term radar observations of the melting layer of precipitation and their interpretation. J. Atmos. Sci. 1995, doi:10.1175/1520-0469(1995)052<0838:LTROOT>2.0.CO;2.

Gázquez Picón, A.; Toda Savll, J.; Bech, J.; Pineda, N. Manual per als observadors del Servei Meteorològic e Catalunya; 2011; ISBN 978-84-393-8762-6.

Gonzalez, S.; Bech, J.; Udina, M.; Codina, B.; Paci, A.; Trapero, L. Decoupling between precipitation processes and mountain wave induced circulations observed with a vertically pointing K-band doppler radar. Remote Sens. 2019, doi:10.3390/rs11091034.

Gunn, R.; Kinzer, G.D. The terminal velocity of fall for water droplets in stagnant air. J. Meteorol. 1949, 6, 243–248, doi:10.1175/1520-0469(1949)006<0243:TTVOFF>2.0.CO;2.

Hildebrand, P.H.; Sekhon, R.S. Objective Determination of the Noise Level in Doppler Spectra. J. Appl. Meteorol. 1974, 13, 808–811, doi:10.1175/1520-0450(1974)013<0808:ODOTNL>2.0.CO;2.

Houze, R.A. Stratiform Precipitation in Regions of Convection: A Meteorological Paradox? Bull. Am. Meteorol. Soc. 1997, 78, 2179–2196, doi:10.1175/1520-0477(1997)078<2179:SPIROC>2.0.CO;2.

Koistinen, J.; Saltikoff, E. Experience of customer products of accumulated snow, sleet and rain. COST75 Adv. Weather Radar Syst. 1998, 397, 406.

Lin, D.; Pickering, B.; III, R.R.N. Relating the Radar Bright Band and Its Strength to Surface Rainfall Rate Using an Automated Approach. J. Hydrometeorol. 2020, 21, 335– 353, doi:10.1175/JHM-D-19-0085.1.

Lolli, S.; Vivone, G.; Lewis, J.R.; Sicard, M.; Welton, E.J.; Campbell, J.R.; Comerón, A.; D'Adderio, L.P.; Tokay, A.; Giunta, A.; et al. Overview of the New Version 3 NASA Micro-Pulse Lidar Network (MPLNET) Automatic Precipitation Detection Algorithm. Remote Sens. 2019, 12, 71, doi:10.3390/rs12010071.

Maahn, M.; Kollias, P. Improved Micro Rain Radar snow measurements using Doppler spectra post-processing. Atmos. Meas. Tech. 2012, 5, 2661–2673, doi:10.5194/amt-5- 2661-2012.

Makino, K.; Shiina, T.; Ota, M. A Precipitation Classification System Using Vertical Doppler Radar Based on Neural Networks. Radio Sci. 2019, doi:10.1029/2018RS006567.

Massmann, A.K.; Minder, J.R.; Garreaud, R.D.; Kingsmill, D.E.; Valenzuela, R.A.; Montecinos, A.; Fults, S.L.; Snider, J.R. The Chilean Coastal Orographic Precipitation Experiment: Observing the Influence of Microphysical Rain Regimes on Coastal Orographic Precipitation. J. Hydrometeorol. 2017, 18, 2723–2743, doi:10.1175/JHM-D-17-0005.1.

Ralph, F.M.; Neiman, P.J.; van de Kamp, D.W.; Law, D.C. Using Spectral Moment Data from NOAA's 404-MHz Radar Wind Profilers to Observe Precipitation. Bull. Am. Meteorol. Soc. 1995, 76, 1717–1739, doi:10.1175/1520-0477(1995)076<1717:USMDFN>2.0.CO;2.

Richard, D.; Zrnić, D. Doppler Radar and Weather Observations; Elsevier, 1993; ISBN9780122214226.

Sánchez-Diezma, R.; Zawadzki, I.; Sempere-Torres, D. Identification of the bright band through the analysis of volumetric radar data. J. Geophys. Res. Atmos. 2000, doi:10.1029/1999JD900310.

Seidel, J.; Trachte, K.; Orellana-Alvear, J.; Figueroa, R.; Célleri, R.; Bendix, J.; Fernandez, C.; Huggel, C. Precipitation characteristics at two locations in the tropical andes by means of vertically pointing micro-rain radar observations. Remote Sens. 2019, doi:10.3390/rs11242985.

Seo, B.C.; Krajewski, W.F. Statewide real-time quantitative precipitation estimation using weather radar and NWP model analysis: Algorithm description and product evaluation. Environ. Model. Softw. 2020, 132, 104791, doi:10.1016/j.envsoft.2020.104791.

Sverre, P. Introduction to meteorology. By Sverre Petterssen, New York (McGraw-Hill),1958. Pp. ix, 327, 213 Figs.; 14 Tables; 52s. 6d. Q. J. R. Meteorol. Soc. 1959, 85, 78–78, doi:10.1002/qj.49708536319.

Thurai, M.; Gatlin, P.N.; Bringi, V.N. Separating stratiform and convective rain types based on the drop size distribution characteristics using 2D video disdrometer data. Atmos. Res. 2016, 169, 416–423, doi:10.1016/j.atmosres.2015.04.011.

White, A.B.; Gottas, D.J.; Strem, E.T.; Ralph, F.M.; Neiman, P.J. An automated brightband height detection algorithm for use with Doppler radar spectral moments. J. Atmos. Ocean. Technol. 2002, doi:10.1175/1520-0426(2002)019<0687:AABHDA>2.0.CO;2.

Yamamoto, M. New Observations by Wind Profiling Radars. In Doppler RadarObservations - Weather Radar, Wind Profiler, Ionospheric Radar, and Other Advanced Applications; Bech, J;Chau, J., Ed.; InTech, 2012 ISBN 978-953-51-0496-4.

Zrnić, D.S.; Ryzhkov, A.; Straka, J.; Liu, Y.; Vivekanandan, J. Testing a Procedure forAutomatic Classification of Hydrometeor Types. J. Atmos. Ocean. Technol. 2001, 18,892–913, doi:10.1175/1520-0426(2001)018<0892:TAPFAC>2.0.CO;2.

Apèndix A. Contribucions derivades de la tesi

En aquest apèndix s'inclouen una llista de les contribucions fetes a la comunitat científica en el període del curs del doctorat respecte la tesi que es presenta.

A.1. Articles

- Acquistapace, C.; Coulter, R.; Crewell, S.; Garcia-Benadí, A.; Gierens, R.; Labbri, G.; Myagkov, A.; Risse, N.; Schween, J. **EUREC4A's Maria S. Merian ship-based cloud and micro rain radar observations of clouds and precipitation.** *Earth Syst. Sci. Data, vol. 14, no. 1, pp. 33–55, Jan. 2022*. < https://doi.org/10.5194/essd-14-33-2022 >

- Garcia-Benadí, A.; Bech, J.; Udina, M; Campistron, B and Paci, A. **Multiple Characteristics of Precipitation Inferred from Wind Profiler Radar Doppler** Spectra. Remote Sensing. 2022; 14(19):5023. <https://doi.org/10.3390/rs14195023>

- Garcia-Benadí, A.; Bech, J.; González , S.; Udina, M.; Codina, B. **A new methodology to characterise the radar bright band using doppler spectral moments from vertically pointing radar observations.** *Remote sensing*. 2021. Volum: 13. Número: 21. Pàgs.: 4223:1 ~ 4223:20. <https://doi.org/10.3390/rs13214323>

- Garcia-Benadí, A.; Bech, J.; González , S.; Udina, M.; Codina, B.; Georgis, J.-F. **Precipitation type classification of micro rain radar data using an improved Doppler spectral processing methodology.** *Remote sensing*. 2020. Volum: 12. Número: 24. Pàgs.: 4113:1 ~ 4113:23. <https://doi.org/10.3390/rs12244113>

- Ghada, W.; Casellas, E.; Herbinger, J.; Garcia-Benadí, A.; Bothmann, L.; Estrella, N.; Bech, J.; Menzel, A. **Stratiform and convective rain classification using machine learning models and micro rain radar**. Remote sensing. 2022. Volum: 14. Número: 18, article 4563. <https://doi.org/10.3390/rs14184563 >

- González , S.; Bech, J.; Garcia-Benadí, A.; Udina Sistach, Mireia; Codina, B.; Trapero, L.; Georgis, J.-F. **Vertical structure and microphysical observations of winter precipitation in an inner valley during the Cerdanya-2017 field campaign.** *Atmospheric research*. 2021. <https://doi.org/10.1016/j.atmosres.2021.105826>

A.2. Presentacions i pòsters en congressos

- Bech, J.; Udina, M.; González , S.; Garcia-Benadí, A.; Altube, P.; Mercader, J.; Arús, J.; Casellas, E. **Preliminary results of the analysis of precipitation processes in the Eastern Ebro Subbasin (WISE-PreP) field campaign within HILIAISE**. *EMS Annual Meeting Abstracts, vol. 18 (2021)*. Copernicus Office. 2021. Pàgs.: 1 ~ 2. <https://meetingorganizer.copernicus.org/EMS2021/abstracts/displaymaterials/UP>

- Garcia-Benadí, A.; Bech, J.; Udina, M.; Campistron, B.; Paci, A. **Comparison of windprofiler and micro rain radar precipitation observations**. ERAD 2022: book of abstracts: 11th European Conference on Radar in Meteorology and Hydrology, 29th August - 02nd September 2022, Locarno, Switzerland. MeteoSwiss (Bundesamt für Meteorologie und Klimatologie MeteoSchweiz).

2022. Pàgs.: 186 ~ 187. <https://www.erad2022.ch/_files/ugd/25a7b1_23b223c508be440ca402c5a29bba166e.pdf >

- Garcia-Benadí, A.; Bech, J.; Udina, M.; Altube, P.; Fabro, F. **Feasibility analysis of monitoring a C-band weather radar reflectivity calibration using a K-band Doppler radar profiler**. *WXRCALMON 2021: 3rd Weather Radar Calibration Workshop: Météopole, Toulouse, France: November 17-19, 2021: book of abstracts*. Météo-France. 2021. Pàgs.: 12 ~ 12. <http://www.meteo.fr/cic/meetings/2021/wxrcalmon/WXRCalMon2021_book_of_abstracts.pdf>

- Garcia-Benadí, A.; González, S.; Casellas, E.; Bech, J.; Udina, M.; Codina, B. **Micro rain radar precipitation observations of cyclones Filomena and Hortense**. *MetMed 8th International Meeting on Meteorology and Climatology of the Mediterranean (online, 25-27 May 2021): abstract book*. 2021. Pàgs.: 44 ~ 44. <https://agenda.uib.es/53568/section/31183/8th-international-conference-on-meteorology-and-climatology-of-the-mediterranean.html>

- Garcia-Benadí, A.; Bech, J.; Campistron, B.; Paci, A. **Complementary observations of precipitation profiles from a windprofiler and a micro-rain radar**. 11th European Conference on Radar in Meteorology and Hydrology. 2020.

- Garcia-Benadí, A.; Bech, J.; González , S.; Del Rio, J. **Alternative processing for micro rain radar (MRR) observations**. *ERAD2018: 10th European Conference on Radar in Meteorology and Hydrology: Ede-Wageningen, The Netherlands: July 1-6, 2018: abstracts book*. 2018. Pàgs.: 786 ~ 796. <https://doi.org/10.18174/454537>

- González , S.; Bech, J.; Garcia-Benadí, A.; Udina, M.; Codina, B.; Trapero, L.; Paci, A.; Georgis, J.-F. **Precipitation microphysics analysis during winter storms in a inner valley of the Pyrenees using a K-band doppler radar and disdrometer data**. ERAD 2022: book of abstracts: 11th European Conference on Radar in Meteorology and Hydrology, 29th August - 02nd September 2022, Locarno, Switzerland. MeteoSwiss (Bundesamt für Meteorologie und Klimatologie MeteoSchweiz). 2022. Pàgs.: 271 ~ 272. <https://www.erad2022.ch/_files/ugd/25a7b1_23b223c508be440ca402c5a29bba166e.pdf>

- Udina, M.; Trapero, L.; Soler, M.R.; Bech, J.; Miró, J.; Mercader, J.; Bravo, M.; Paci, A.; Ferreres, E.; González, S.; Garcia-Benadí, A. **Downslope windstorms, mountain waves, orographic precipitation and associated processes analysis during 10-17 January 2017 in The Cerdanya-2017 field experiment**. *34th International Conference on Alpine Meteorology, Reykjavík, Iceland, 18-23 June 2017: abstracts*. Icelandic Meteorological Society. 2017. Pàgs.: 38 ~ 39. <http://vedur.org/wp-content/uploads/2017/04/ICAM2017-abstracts.pdf

Apèndix B. Sondatges llançats des de la Facultat de Física de la Universitat de Barcelona

Durant el treball del doctorat s'han analitzat les dades del sondatge del Servei Meteorològic de Catalunya que es realitza cada 12 hores des del terrat de la Facultat de Física de la Universitat de Barcelona (latitud 41° 23' 4.34'' N i longitud 2° 7' 3.05'' E). Aquestes dades han estat útils per avaluar l'alçada de la banda brillant, detallada en el Capítol 2.

Com a resultat s'ha creat un programa per realitzar dues tasques: la primera mostrar el desplaçament de la sonda sobre el territori (**Figura *B.*1**).

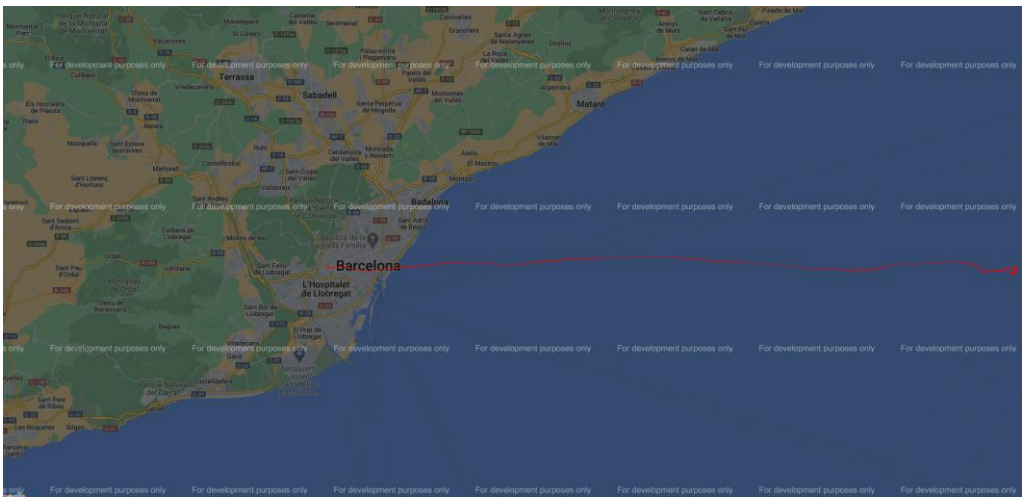

Figura B.1. Desplaçament (línia vermella) de la sonda en el llançament del dia 30 d'agost de 2022 a les 12h UTC.

La segona tasca detalla totes les dades del perfil de temperatura i temperatura del punt de rosada, així com algunes dades atmosfèriques rellevants (**Figura *B.2***).

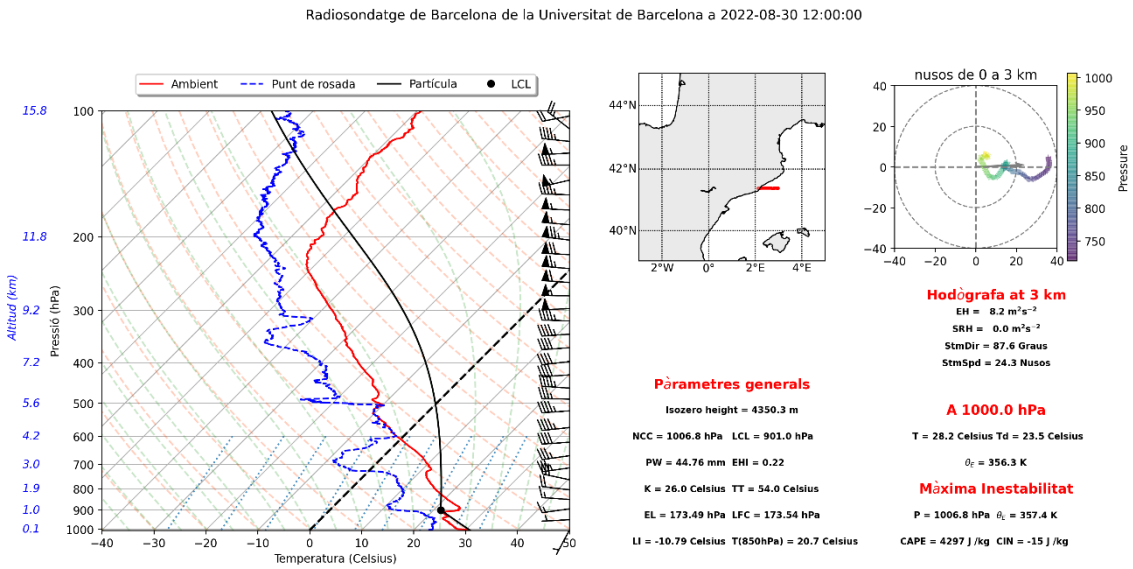

Figura B.2. Perfil de temperatura i dades atmosfèriques del llançament del dia 30 d'agost de 2022 a les 12h

L’exemple del dia 30 d’agost de 2022 es interessant ja que es van registrar pedra superior a 10 cm de diàmetre en la zona de Girona.

El programari per a realitzar aquestes tasques està disponible al repositori Github:

https://github.com/AlbertGBena/RadiosoundingDataReading